# Theoretical Studies of Structural, Electronic and Optical Properties of Graphene Based Systems

Submitted by CELAL YELGEL to the University of Exeter as a thesis for the degree of Doctor of Philosophy in Physics.

July 2013



I certify that all material in this thesis which is not my own work has been identified and that no material has previously submitted and approved for the award of a degree by this or any other university.

# Abstract

The equilibrium atomic geometry, electronic properties, electronic orbital states, and optical properties of graphene and graphene based systems have been comprehensively investigated using the density functional theory (DFT) in the framework of plane wave pseudopotential. These properties have been compared with recently found experimental results and theoretical works done by tight-binding and DFT methods.

In Chapter 1, a brief theoretical overview about the structural properties of graphene based systems has been provided. The basic concepts of semiconductor surfaces have been introduced for the study of graphene on InAs(111) surfaces.

In Chapter 2, explanations of the essential ingredients of the density functional theory and the plane wave pseudopotential theory have been provided. The main concepts of geometry optimisation in all calculations have been explained. The theory of scanning tunnelling microscopy which gives very detailed information about geometrical structures and electronic states has been described .

In Chapter 3, atomic geometry, electronic structures, and interband optical transitions for isolated monolayer graphene, bilayer graphene, ABA-stacked trilayer graphene, and graphite systems have been studied. The electron velocity and effective mass were estimated using the in-plane electronic band calculation. The modifications in the electronic properties due to increasing the number of graphene layers have been discussed. The changes in interband optical transitions have also been presented for bilayer graphene, trilayer graphene, and graphite with respect to the monolayer graphene.

In Chapter 4, a detailed theoretical study of the electronic structures of ABC-stacked trilayer and $N$-layer graphene has been presented. The nature of the trigonal warping of energy bands slightly above the Fermi level for different layer thicknesses was examined. The orbital natures of the highest occupied molecular orbital (HOMO) and lowest unoccupied molecular orbital (LUMO) states have been investigated.

In Chapter 5, the equilibrium geometry and electronic structure of multilayer graphene deposited on hexagonal boron nitride substrate have been studied. It has been found that the graphene sheet is weakly adsorbed on the boron nitride substrate. Using the in-plane electronic band calculations the carrier velocity and effective mass were estimated. The importance of the interlayer interaction and stacking patterns of multilayer graphene/boron nitride has been explained for band gap and effective mass tuning in multilayer graphene. The interband transition energies for all systems were also calculated.

In Chapter 6, the atomic geometry and electronic structure of graphene on the most stable In-vacancy InAs(111)A surface have been investigated. The effect of the substrate on electronic charge re-distribution around the graphene sheet was examined. The transparency effect of graphene has also been investigated by simulating scanning tunnelling microscopy.

Finally, the summary of results and the future works have been outlined in Chapter 7.

*for my wife...*

# Acknowledgments

First of all, I would like to express my sincerest appreciation to my supervisor, Professor G. P. Srivastava, whose thoughtful consideration and guidance has been invaluable. Without his guidance, support and inspiration during the most critical period of my PhD journey, I would not have been able to accomplish this study. To him, I wish to say 'You are a wonderful supervisor, professor and researcher!'

I would like to thank my mentor Dr. A. P. Hibbins for his nice suggestion in our regular meetings. I also want to thank Dr. R. H. Miwa (University of Uberlandia, Brazil) for his wonderful collaboration and fruitful discussion.

I would like to acknowledge the financial support from The Republic of Turkey Ministry of National Education through Recep Tayyip Erdoğan University.

I also wish to my sincere thank to my dear mother and father, whose support and encouragement. I have been able to count on everyday during my PhD, even while sometimes living halfway around the world.

Words could not express my gratitude to my wonderful wife for her companionship, unending patience, encouragement, and unwavering love. She is the woman of my dreams and I am very fortunate to found her. I therefore send my unlimited thanks to my dear wife Övgü Ceyda. Without her deep love and support , I would not be where I am today. This is why this thesis is dedicated to her.

# List of Publications

**C. Yelgel** and G. P. Srivastava, *Ab-initio Studies of Electronic and Optical Properties of Graphene and Graphene-BN Interface*, Applied Surface Science **258**, 8338 (2012).

**C. Yelgel** and G. P. Srivastava, *Energy Band Gap Modification of Graphene Deposited on a Multilayer Hexagonal Boron Nitride Substrate*, MRS Proceedings **1407**, mrsf11-1407-aa15-08 (2012).

**C. Yelgel**, G. P. Srivastava, and R. H. Miwa, *Ab initio Investigation of the Electronic Properties of Graphene on InAs(111)A*, Journal of Physics: Condensed Matter **24**, 485004 (2012).

**C. Yelgel** and G. P. Srivastava, *Atomic and Electronic Structure of Multilayer Graphene on a Monolayer Hexagonal Boron Nitride*, MRS Proceedings **1549**, mrss13-1549-o06-26 (2013).

**C. Yelgel** and G. P. Srivastava, *Electronic Structure of ABC-stacked Multilayer Graphene and Trigonal Warping: First-principles Calculations*, Carbon (2013) (submitted).

# Attended Conferences

- VII International Workshop on Semiconductor Surface Passivation, 11-15 September 2011, Kraków, Poland, (*Oral presentation*).

- 2011 Materials Research Society Fall Meeting and Exhibit, 28 November - 2 December 2011, Boston, USA, (*Poster presentation*).

- 2013 Materials Research Society Spring Meeting and Exhibit, 1-5 April 2013, San Francisco, USA, (*Poster presentation*).

# Contents


**1 Introduction** **1**

1.1 Introduction . . . . . 1

1.1.1 Graphite . . . . . 5

1.1.2 Graphene . . . . . 7

1.1.3 Hexagonal Boron Nitride . . . . . 8

1.2 Structure of Clean Semiconductor Surfaces . . . . . 9

1.2.1 The Surface Relaxiaton and Reconstruction . . . . . 10

1.2.2 Periodic Boundary conditions and slab models for surfaces 12

1.2.3 InAs(111) Surface . . . . . 14

1.3 Outline of the Thesis . . . . . 15

**2 Theoretical Techniques** **17**

2.1 Introduction . . . . . 17

2.2 Many-electron Theory . . . . . 17

2.2.1 The Adiabatic Approximation . . . . . 18

2.2.2 Wave-Function Approaches . . . . . 19

2.2.2.1 Hartree Theory . . . . . 19

2.2.2.2 Hartree-Fock Theory . . . . . 20

2.2.3 Density Functional Approach . . . . . 21

2.2.3.1 Thomas Fermi Theory . . . . . 22

2.2.3.2 Hohenberg-Kohn-Sham Theory . . . . . 23

2.2.4 Exchange Correlation Functional . . . . . 25
2.2.4.1 Local Density Approximation . . . . . 25
2.2.4.2 Generalised Gradient Approximation . . . . . 27
2.3 Electron-Ion Interaction . . . . . 28
2.3.1 All-electron methods . . . . . 29
2.3.2 Pseudopotential Method . . . . . 29
2.3.2.1 Non-Uniqueness of Pseudopotentials . . . . . 30
2.3.2.2 Local and non-local Pseudopotentials . . . . . 32
2.3.2.3 Ultrasoft Pseudopotentials . . . . . 32
2.3.2.4 Norm-conserving Pseudopotentials . . . . . 33
2.3.2.5 Basis Set . . . . . 34
2.4 Momentum Space Formalism of Kohn-Sham Equation . . . . . 35
2.4.1 Energy Cut-off . . . . . 35
2.4.2 k points for Brillouin Zone Summation . . . . . 36
2.4.3 Self Consistency . . . . . 37
2.5 Total Energy and Hellmann-Feynman Forces . . . . . 39
2.6 Geometry Optimisation Scheme . . . . . 40
2.7 Our Computational Code . . . . . 41
2.8 Scanning Tunnelling Microscopy . . . . . 44
2.9 Summary . . . . . 46

**3 Electronic Properties and Interband Optical Transitions of Multilayer Graphene and Graphite 48**

3.1 Introduction . . . . . 48
3.2 Results and Discussion . . . . . 50
3.2.1 Graphene . . . . . 55
3.2.2 Bilayer Graphene . . . . . 61
3.2.3 Trilayer Graphene . . . . . 69

3.2.4 Graphite . . . . . 75
3.2.5 Density of States and Interband Optical Transitions . . . . . 77
3.3 Summary . . . . . 83

**4 The Electronic Structure of ABC-stacked Multilayer Graphene and Trigonal Warping 85**
4.1 Introduction . . . . . 85
4.2 Results . . . . . 87
4.2.1 ABC-Stacked Trilayer Graphene . . . . . 87
4.2.2 ABC-Stacked N-layer Graphene . . . . . 93
4.3 Summary . . . . . 102

**5 Electronic Properties and Interband Optical Transitions of Multilayer Graphene on Hexagonal Boron Nitride 103**
5.1 Introduction . . . . . 103
5.2 Results and Discussion . . . . . 105
5.2.1 Graphene on Mono- and Multi-layer Boron Nitride . . . . . 105
5.2.2 Bilayer Graphene on Monolayer Boron Nitride . . . . . 117
5.2.3 Trilayer Graphene on Monolayer Boron Nitride . . . . . 119
5.3 Density of States and Interband Optical Transitions . . . . . 128
5.4 Summary . . . . . 130

**6 Electronic Properties and Transparency of Graphene on InAs(111) 133**
6.1 Introduction . . . . . 133
6.2 Results . . . . . 134
6.2.1 Clean InAs(111) Surface . . . . . 138
6.2.2 Graphene on InAs(111) surface . . . . . 140
6.3 Summary . . . . . 149

**7 Concluding Remarks** **153**

7.1 Summary of Results . . . . . 153

7.2 Future Work . . . . . 157

**A Crystal Structure and Symmetry** **160**

A.0.1 Lattice and Primitive Unit Cell . . . . . 161

A.0.2 Reciprocal Lattice and Brillouin Zone . . . . . 163

A.0.3 Cubic Crystal Structures . . . . . 166

A.0.4 Bloch's Theorem . . . . . 168

A.0.5 Free Electron Band Structure . . . . . 169

A.0.6 Density of States . . . . . 170

# List of Figures


1.1 (a) An $sp^2$ hybridised in C atom. (b) $\sigma$ and $\pi$ bonding [8]. . . . . 3

1.2 Graphene is a basic building unit for graphitic materials of all other dimensionalities: 0-dimensional fullerene (left side), 1-dimensional carbon nanotube (middle), and 3-dimensional graphite (right side) [12]. . . . . 4

1.3 Crystal structures of (a) AB-stacked and (b) ABC-stacked graphite. (c) The primitive unit cell is the equilateral parallelogram (solid lines) with $\mathbf{a}_1$ and $\mathbf{a}_2$ lattice vectors. (d) The hexagonal Brillouin zone of graphite ($\mathbf{b}_1$, $\mathbf{b}_2$, and $\mathbf{b}_3$ are reciprocal lattice vectors) with the high symmetry points labelled $\mathbf{\Gamma}$, $\mathbf{K}$, and $\mathbf{H}$. . . . . 6

1.4 (a) The honeycomb structure of graphene. The equilateral parallelogram presents an unit cell with the lattice vectors ($\mathbf{a}_1$ and $\mathbf{a}_2$). (b) The Brouillin zone of graphene ($\mathbf{b}_1$ and $\mathbf{b}_2$ are reciprocal lattice vectors) with indication of the high-symmetry points. . . . . 8

1.5 The lattice structure of hexagonal boron nitride. . . . . 9

1.6 Atomic structure of the (001) face of group IV semiconductors. Schematic representation of bulk region, surface region, vacuum region, and dangling bonds. . . . . 11

1.7 A schematic representation of supercell geometry. . . . . 13

1.8 Top views of the (a) InAs(111)A-(2×2) In-vacancy and (b) As trimer model of the InAs(111)B-(2 × 2) reconstructions. (c) Surface Brillouin zone for InAs(111)-2×2. . . . . 15

2.1 Flow chart explaining the iterations of optimising procedure. . . . . 42

2.2 The Tersoff-Hamann model of STM, where the tip is modelled as a locally spherical potential well with radius of curvature $R$ and at a distance $d$ above the surface. . . . . 46

3.1 Total energy of graphene with a lattice constant of 2.46 Å using 36×36×1 **k**-points as a function of the cut-off energy. Filled symbols represent numerically calculated data points and lines are joining to the data points. . . . . 52

3.2 Total energies for graphene with a lattice constant of 2.46 Å and $E_{cut}$=45 Ryd as a function of the parameter $n$ in the choices of the Monkhorst-Pack **k**-points set, $n \times n$×1. Filled symbols represent numerically calculated data points and lines are joining to the data points. . . . . 53

3.3 Total energy of graphene with $E_{cut}$=45 and 36×36×1 **k**-points as a function of the lattice parameter, $a$. The circle filled symbols show numerically calculated data points, while the curve shows the fits of the DFT data. The arrow indicates the equilibrium value of $a$ corresponding to the minimum of the total energy. . . . . 54

3.4 Total energy of graphene as a function of the lattice parameter, $a$. The circle filled symbols show numerically calculated data points. Line is joining to the data points. . . . . 56

3.5 (a) The electronic structure of graphene. (b) Dispersion curve for the $\pi/\pi^*$ bands close to the **K** point. The filled symbols show numerically calculated data points and the line shows a linear fit of the DFT data. The filled triangle symbols represent experimental data read from Ref. [121]. . . . . 58

3.6 Dispersion curve for the $\pi/\pi^*$ bands very close to the **K** point using different cut-off energies. The filled symbols show numerically calculated data points and lines are joining to the data points. . . . 59

3.7 Dispersion curve for the $\pi/\pi^*$ bands very close to the **K** point using different the Monkhorst-Pack **k**-points. The filled and unfilled symbols show numerically calculated data points and lines are joining to the data points. . . . . 60

3.8 The polynomial fit of the $\pi^*$ bands using two ranges of energies (up to 0.192 eV and up to 0.441 eV) above the **K** point for graphene. The symbols show numerically calculated data points and the line shows a linear fit of the DFT data. . . . . 62

3.9 Dispersion curve for the $\pi/\pi^*$ bands in graphene very close to the **K** point using using lattice constants of $a$=2.458 Å, $a$=2.460 Å and $a$=2.466 Å. The filled symbols show numerically calculated data points and lines are joining to the data points. . . . . 63

3.10 Total energy of bilayer graphene as a function of the interlayer distance. The circle filled symbols show numerically calculated data points. Line is joining to the data points. . . . . 64

3.11 (a) Electronic band structure of bilayer graphene. (b) The inner-pair of bands very close to the **K** point. The filled symbols show numerically calculated data points and lines are joining to the data points. . . . . 66

3.12 The inner and outer pair of $\pi/\pi^*$ bands close to the **K** point for bilayer graphene with using lattice constants of $a$=2.458 Å, $a$=2.460 Å and $a$=2.466 Å. The filled symbols show numerically calculated data points and lines are joining to the data points. . . . . 67

3.13 The polynomial fit of the $\pi^*$ bands using two ranges of energies (up to 0.08 eV and up to 0.33 eV) above the **K** point for bilayer graphene. The square filled symbols show numerically calculated data points and the line shows a polynomial fit of the DFT data. . . 70

3.14 Total energy of ABA-stacked trilayer graphene as a function of the interlayer distance. The circle filled symbols show the DFT data the curve shows the fits of the DFT data as described in the text. . . 71

3.15 (a) Electronic band structure of ABA-stacked trilayer graphene. (b) The inner-most pair of bands close to the **K** point. The filled symbols show numerically calculated data points and the curves are joining to the data points. . . . . 73

3.16 The inner pair of $\pi/\pi^*$ bands close to the **K** point for trilayer graphene with using lattice constants of $a$=2.458 Å, $a$=2.460 Å and $a$=2.466 Å. The filled symbols show numerically calculated data points and lines are joining to the data points. . . . . 74

3.17 The polynomial fit of the inner-most $\pi^*$ bands up to 0.0149 eV and up to 0.0462 eV above the **K** point for ABA-stacked trilayer graphene. The symbols show numerically calculated data points and the curve shows a polynomial fit of the DFT data. . . . . 76

3.18 Electronic band structure of graphite along (a) the **ΚΓΜΚΗΓΑ** and (b) the **KH** directions and close to the Fermi level. Solid line represents the Fermi level. The filled symbols show numerically calculated data points. . . . . 78

3.19 The most inner pair of the $\pi/\pi^*$ bands along to the **KH** directions. The filled symbols show numerically calculated data points. . . . . 79

3.20 Density of states for (a) graphene (MLG), (b) bilayer graphene (BLG), (c) ABA-stacked trilayer graphene (TLG), and (d) graphite. These points were obtained by Gaussian broadening of energy bands ($E_n$(k)) by 5 meV for each **k**-point included in DOS calculation. . . . . 80

4.1 (a) Atomic structure of ABC-stacked trilayer graphene containing six basis carbon atoms in the primitive unit cell. (b) Schematic of the unit cell of ABC-stacked trilayer graphene. . . . . 88

4.2 Band structure of the ABC-stacked trilayer graphene close to **K** point (a) along $k_x$, (b) along $-k_x$ (the **K**$\Gamma$ direction), and (c) along the surface normal (the **KH** direction). The Fermi level is set to zero energy. The hexagonal Brillouin zone is also shown. Filled symbols represent numerically calculated data points. . . . . 90

4.3 (a) Band structure of ABC-stacked $N$=3 layer graphene close to **K** point using our equilibrium lattice constant $a$=2.458 Å and (b) different lattice constants around the equilibrium value. Filled symbols represent numerically calculated data points and lines are joining the data points. . . . . 91

4.4 The electronic energy contour plots of ABC-stacked trilayer graphene for (a) the lowest conduction band up to 0.846 eV above the Fermi level and (b) the highest valence band up to 0.72 eV below the Fermi level. The energy values (in eV) are indicated on the right hand side with the minimum value shown in the lighest colour and the highest value with the darkest colour. Electronic charge density contour plots at the **K** point are also given for (c) the lowest conduction band and (d) the highest valence band. . . . . 92

4.5 (a) Band structure of ABC-stacked $N$=4 layer graphene close to **K** point using our equilibrium lattice constant $a$=2.458 Å and (b) different lattice constants ($a$=2.460 Å and $a$=2.462 Å). Filled symbols represent numerically calculated data points and lines are joining the data points. . . . . 94

4.6 The electronic energy contour plots of ABC-stacked $N$=4 layer graphene for (a) the lowest conduction band up to 0.792 eV above the Fermi level and (b) the highest valance band up to 0.648 eV below the Fermi level. The energy values (in eV) are indicated on the right hand side with the minimum value shown in the lighest colour and the highest value with the darkest colour. Electronic charge density contour plots at the **K** point are also given for (c) the lowest conduction band and (d) the highest valence band. . . . . 95

4.7 (a) Band structure of ABC-stacked $N$=5 layer graphene close to **K** point using our equilibrium lattice constant $a$=2.458 Å and (b) different lattice constants ($a$=2.460 Å and $a$=2.462 Å). Filled symbols represent numerically calculated data points and lines are joining the data points. . . . . 97

4.8 The electronic energy contour plots of ABC-stacked $N$=5 layer graphene for (a) the lowest conduction band up to 0.864 eV above the Fermi level and (b) the highest valence band up to 0.612 eV below the Fermi level. The energy values (in eV) are indicated on the right hand side with the minimum value shown in the lighest colour and the highest value with the darkest colour. Electronic charge density contour plots at the **K** point are also given for (c) the lowest conduction band and (d) the highest valence band. . . . . 98

4.9 (a) Band structure of ABC-stacked $N$=5 layer graphene close to **K** point using our equilibrium lattice constant $a$=2.458 Å and (b) different lattice constants ($a$=2.460 Å and $a$=2.462 Å). Filled symbols represent numerically calculated data points and lines are joining the data points. . . . . 99

4.10 The electronic energy contour plots of ABC-stacked $N$=6 layer graphene for (a) the lowest conduction band up to 0.828 eV above the Fermi level and (b) the highest valence band up to 0.612 eV below the Fermi level. The energy values (in eV) are indicated on the right hand side with the minimum value shown in the lighest colour and the highest value with the darkest colour. Electronic charge density contour plots at the **K** point are also given for (c) the lowest conduction band and (d) the highest valence band. . . . . 100

4.11 Panel (a) shows the density of states close to the Fermi level for the ABC-stacked $N$=3 layer graphene. The two peaks closest to the Fermi level are zoomed as an inset. Panel (b) shows the results for the two peaks closest to the Fermi level for the $N$=4, 5, 6 layer graphene systems. The energy zero is set at the Fermi level. Filled symbols represent numerically calculated data points. . . . . 101

5.1 Dependence of (a) band gap and (b) total energy results for MLG deposited on MLBN as a function of the parameter $n$ in the zone-centred Monkhorst-Pack special **k**-points set. Filled symbols represent numerically calculated data points and lines are joining the data points. . . . . 106

5.2 Top: Top view of three inequivalent orientations of the graphene sheet on the monolayer h-BN surface. Bottom: Variation of the total energy $E$ with the vertical distance between the graphene sheet and the BN sheet. The filled symbols show numerically calculated data points, while the curve shows the fits of the DFT data described in Chapter 3. . . . . 107

5.3 Total energies of graphene on MLBN in (a) configuration $\alpha$, (b) $\beta$, and (c) $\gamma$ as a function of the vertical distance $d$ close to our equilibrium values for all three configurations. Filled symbols represent numerically calculated data points and lines are joining the data points. . . . . 109

5.4 (a) The electronic structure for the equilibrium configuration of graphene adsorbed on a monolayer h-BN sheet. (b) Dispersion curves for the $\pi$ and $\pi^*$ bands very close to the **K** point. The curves for graphene are reproduced. Filled symbols represent numerically calculated data points and lines are joining the data points. . . 111

5.5 The polynomial fit of the $\pi^*$ bands using two ranges of energies (up to 0.204 eV and up to 0.463 eV) above the **K** point for MLG/MLBN system. The symbols show numerically calculated data points and the line shows a polynomial fit of the DFT data as described in the text. . . . . 112

5.6 (a) The dispersion of the inner pair of $\pi/\pi^*$ very close to the **K** point for MLG/MLBN interface system using different lattice constants around the equilibrium value of 2.450 Å. Filled symbols represent numerically calculated data points and lines are joining the data points. . . . . 113

5.7 The variation of the electronic charge density difference $\Delta\rho$ across the graphene sheet, due to graphene/BN interface formation, along the interface normal direction for (a) the $\gamma$ and (b) $\alpha$ configurations. Red and black lines indicate the locations of graphene and a monolayer boron nitride planes, respectively. . . . . 116

5.8 The electronic charge density (a) along the B-C and (b) B-N bonds for configuration $\gamma$ and (c) along the B-C bond for configuration $\alpha$. 118

5.9 (a) Lattice structure of BLG on MLBN. (b) The band structure of BLG/MLBN along the symmetry directions. Filled symbols represent numerically calculated data points and lines are joining the data points. . . . . 120

5.10 (a) The dispersion of the inner pair of $\pi/\pi^*$ near the **K** point with the equilibrium lattice constant $a$=2.450 Å and (b) close to the equilibrium value. Filled symbols represent numerically calculated data points and lines are joining the data points. . . . . 121

5.11 The polynomial fit of the $\pi^*$ bandsfor energies up to 0.045 eV and up to 0.081 eV above the minimum for BLG/MLBN. The square filled symbols show numerically calculated data points and the line shows a polynomial fit of the DFT data. . . . . 122

5.12 (a) The atomic structure of ABA-stacked TLG on the MLBN. (b) Band structure along **K**Γ**M** direction. Filled symbols represent numerically calculated data points and lines are joining the data points. 124

5.13 (a) The dispersion curve of the inner pair of $\pi/\pi^*$ in the vicinity of **K** point for TLG/MLBN interface system with the equilibrium lattice constant $a$=2.458 Å and (b) around the equilibrium value. Filled symbols represent numerically calculated data points and lines are joining the data points. . . . . 125

5.14 The polynomial fit of the $\pi^*$ bands for energies up to 0.218 eV and up to 0.464 eV above the **K** point for TLG/MLBN system. The symbols show numerically calculated data points and the line shows a polynomial fit of the DFT data as described in the text. . . . . 126

5.15 The planar-average electronic charge density difference $\Delta\rho$ along the interface normal direction for (a) BLG/MLBN and (b) ABA-TLG/MLBN. Red, green, and blue lines indicate the location of graphene plane and black line indicates the location of a monolayer boron nitride plane. . . . . 127

5.16 Comparison of the density of states for (a) MLG and MLG/MLBN, (b) BLG and BLG/MLBN, and (c) TLG and TLG/MLBN. Filled symbols represent numerically calculated data points and lines are joining the data points. . . . . 129

6.1 Total energy of bulk InAs as a function of the lattice parameter, $a$. The circle filled symbols show numerically calculated data points, while the curve shows the fits of the DFT data. The arrow indicates the equilibrium value of $a$ corresponding to the minimum of the total energy. . . . . 136

6.2 Total energy of bulk InAs as a function of the lattice parameter $a$ close to the equilibrium. The circle filled symbols show numerically calculated data points. Line is joining to the data points . . . . 137

6.3 Surface unit cell and the Brillouin zone used in this work for (a) first model of InAs(111)A-($2 \times 2$) graphene system and (b) second model of InAs(111)A-($2 \times 2$) graphene system. Filled symbols represent numerically calculated data points and lines are joining to the data points. . . . . 139

6.4 (a) Band structure of the InAs(111)-(2×2) surface and (b) the graphene on InAs(111)-(2×2) system, with the Fermi energy set to zero. The centre of the surface Brillouin zone $\bar{\Gamma}$ maps onto the $K$ point of graphene Brillouin zone. The edge of the surface Brillouin zone $\bar{Y}$ maps onto the $M$ point of graphene Brillouin zone. Filled symbols represent numerically calculated data points and lines are joining to the data points. . . . . 141

6.5 Band structure of the InAs(111)A-(2×2) surface using differnt lattice constants around the equilibrium value of 6.018 Å. . . . . 142

6.6 Detailed atomic layer geometry for graphene deposited on InAs(111)A-(2×2). . . . . 144

6.7 In the top panel of the diagram the solid lines represent the band structure of graphene close to the Dirac point calculated using the (2×2) large unitcell used for the graphene/InAs system. The partial charge density plots in panels (b), (c) and (d) clearly indicate that the metallic behaviour of the band structure within the Dirac lines originates from bonding between the graphene and In interface layer [atoms are indicated by filled circles]. Filled symbols in label (a) represent numerically calculated data points. Red lines is reproduced by using large unit cell of graphene. . . . . 145

6.8 (a) Total charge contour plot for graphene/InAs(111) surface in a horizontal plane passing through the graphene. (b) The difference of charge density in a horizontal plane at the graphene level. (c) Simulated STM image with a bias of -2 eV just above graphene. (d) Simulated STM image just above the InAs(111) surface for a bias of -2 eV. . . . . 147

6.9 Plot of the difference of the planar averaged charge density $\delta\rho(z) = \rho(z, \text{graphene/InAs}) - \rho(z, \text{InAs}) - \rho(z, \text{graphene})$. There is a charge re-distribution across the graphene sheet. Black, blue, and orange lines indicate the location of graphene, the first layer and second layer of InAs planes, respectively. . . . . 148

6.10 Electronic density of states for graphene, InAs(111)-(2×2) and the graphene/InAs(111)-(2×2) system. The zero along the energy axis is the Fermi energy. Changes due the interface formation are indicated by arrows. Filled symbols represent numerically calculated data points. and lines are joining to the data points. . . . . 150

6.11 The presented work in this chapter has been selected as a cover page in Journal of Physics: Condensed Matter, Volume: 24, Number: 48, 5 December 2012. . . . . 152

A.1 (a) The zinc-blende structure, (b) the face-centred cubic structure. When all atoms are of identical species in the zinc-blende structure, it turns into the diamond structure. . . . . 162

A.2 Miller indices of important planes for the cubic lattice . . . . . 164

A.3 (a) Construction of a two-dimensional Wigner-Seitz cell, (b) filling of space with WS cells. . . . . 165

A.4 Brillouin zones and special **k** points for (a) fcc lattice and (b) hcp lattice. . . . . 167

A.5 Electronic band structure of bulk InAs, calculated by pseudopotential technique. Occupied and unoccupied states are shown by black and red curves, respectively. The symmetry points in the Brillouin zone are explained in section 1.2. Filled symbols represent the numerically calculated data and lines are joining to the data points. . . . . 171

A.6 Density of states $D(E)$ for bulk InAs. The zero energy in panel (b) presents the Fermi level and filled symbols are our numerically calculated datas. Curves are joining the data points . . . . . 173

# List of Tables


3.1 The energy band gap between the outer pair of the $\pi/\pi^*$ bands in bilayer graphene at the **K** point for different values of the lattice parameter $a$ and interlayer distance $d$ around the equilibrium values. 68

3.2 Effective masses of bilayer graphene for different lattice constans. . 69

3.3 The energy band gap values for the outer pair of the $\pi/\pi^*$ bands of graphite at **K** and **H** point with different lattice constants. . . . . 77

3.4 The interband transitions for MLG, BLG, TLG, and graphite. The results in bold font are for the optimium choice of lattice constant $a$ and **k** sampling. . . . . 82

3.5 Optical transition energies (in eV) between the innermost $\sigma$ and $\sigma^*$ bands at $\Gamma$, and between the innermost $\pi$ and $\pi^*$ at **M** point. . . . . 83

5.1 The interband transitions for MLG/MLBN, BLG/MLBN, and TLG/MLBN systems. The results in bold font are for the optimium choice of lattice constant $a$ and **k** sampling. The error estimations are with reference to the results presented in bold. . . . . 131

5.2 Optical transition energies (in eV) between the innermost $\sigma$ and $\sigma^*$ bands at $\Gamma$, and between the innermost $\pi$ and $\pi^*$ at **M** point. . . . . 132

# Chapter 1

# Introduction

## 1.1 Introduction

Carbon is one of the most intriguing elements in the Periodic Table in Group IV. Due to the amazing flexibility of its bonding structure, it is very active in forming unlimited numbers of molecular compounds and crystalline solids. The electron configuration of a carbon atom is $1s^2 2s^2 2p^2$ and thus there are four valence electrons in the outer shell, two of them occupying 2s state and two of them occupying 2p states. When carbon atoms come together to form a crystal, one of the 2s electrons is excited to the $2p_z$ orbital from energy gained from neighboring nuclei, which has the net effect of lowering the overall energy of the system. Interactions or bonding subsequently follow between the 2s and 2p orbitals of neighboring carbon atoms. These interactions or mixing of atomic orbitals are commonly called hybridisation.

In carbon, there are three possible hybridisations: sp, $sp^2$, and $sp^3$. In the sp hybridisation, the 2s orbital mixes with one of the 2p orbitals resulting in two sp orbitals and two remaining unchanged p orbitals. In the case of $sp^2$ hybridisation the 2s orbital and two 2p orbitals are combined leaving the third p orbital unchanged and form three equivalent hybrids (see Fig. 1.1 (a)). These hybrids are at

120° to each other in a plane. If the hybrids lie in the $x - y$ plane, the unaffected $p_z$ orbital remains normal to the $x - y$ plane. In the $sp^3$ hybridisation, the 2s orbital and all three 2p orbitals are mixed with each other, forming four equivalent hybrids. The hybrids are at 109° to each other in tetrahedral arrangement. The existence of these hybridisations in carbon is what leads to the different bonding geometries. For instance, $sp^3$ hybridisation favours tetrahedral bonding which is found in the diamond cubic and wurtzite structures. On the other hand, $sp^2$ hybridisation favours planar structures such as graphene.

Graphene is the one-atom-thick layer of $sp^2$-bonded carbon atoms arranged in a hexagonal lattice. It can be considered as the mother of the carbon allotropes of other dimensionalities. The wrapping of graphene into a sphere produces buckyballs, rolling of graphene segments with different boundaries produces carbon nanotubes, and stacking several sheets of graphene, stabilized by weak interlayer interactions, leads to three-dimensional graphite. Furthermore, cutting graphene into a small ribbon results in nanoribbons. These crystalline forms are illustrated in Fig. 1.2.

In graphene, the 2s orbital interacts with the $2p_x$ and $2p_y$ orbitals to form three $sp^2$ hybrids. The $sp^2$ interactions result in three bonds called $\sigma$-bonds (see Fig. 1.1 (b)), which are stronger than those $sp^3$ bonds in diamonds. The $\sigma$-bonds have the electrons localized along the plane connecting carbon atoms and are responsible for the great strength and mechanical properties of graphene. The $2p_z$ electrons forms covalent bonds called $\pi$-bonds (see Fig. 1.1 (b)), where the electron cloud is distributed normal to the plane connecting carbon atoms. The $2p_z$ electrons are weakly bound to the nuclei and, hence, are relatively delocalized. These delocalized electrons are the ones responsible for the electronic properties of graphene.

Recently, graphene has become one of the most exciting topics of condensed-matter physics and material science. This is due to its remarkable electronic, mechanical and thermal properties [1, 2, 3, 4, 5, 6, 7], in particular its charge carriers

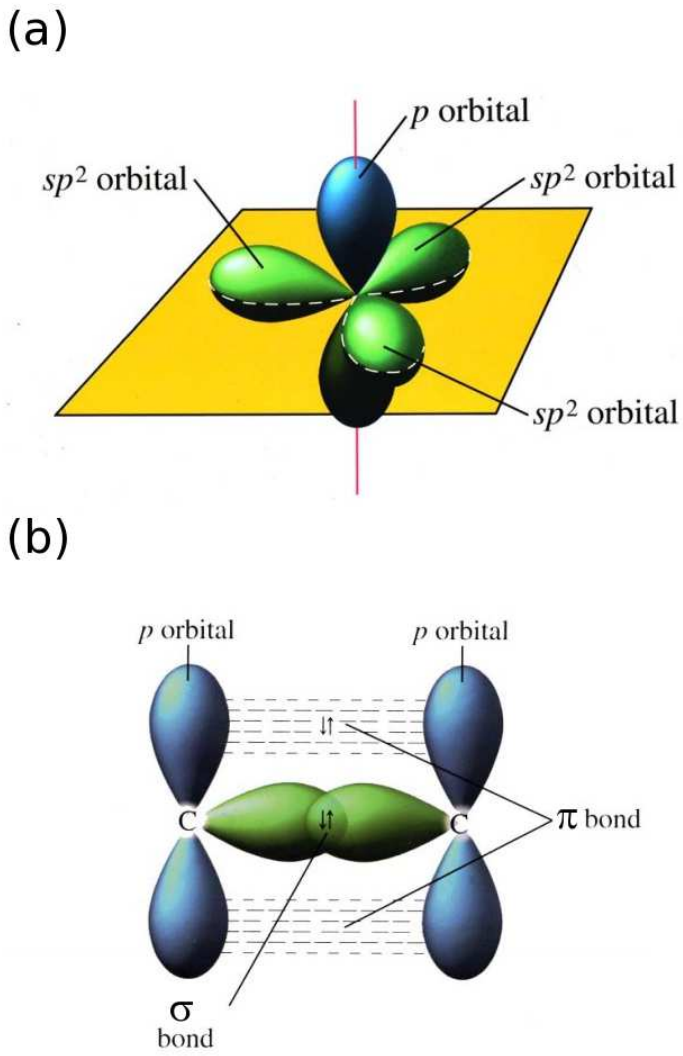


Figure 1.1: (a) An $sp^2$ hybridised in C atom. (b) $\sigma$ and $\pi$ bonding [8].

behave like massless Dirac particles. Until graphene was isolated and observed in its free form in 2004 by Novoselov *et al.* [1], it was assumed that graphene was thermodynamically unstable [9, 10]. In 2010, A. K. Geim and K. S. Novoselov were awarded the Nobel Prize in Physics for groundbreaking experiments regarding the two-dimensional material graphene [11]. The realization of isolated graphene sheets has opened huge possibilities in electronic device fabrication and has also shown much promise in replacing silicon-based electronics. Besides this, most technological applications require graphene to be grown on [13, 14, 15], or

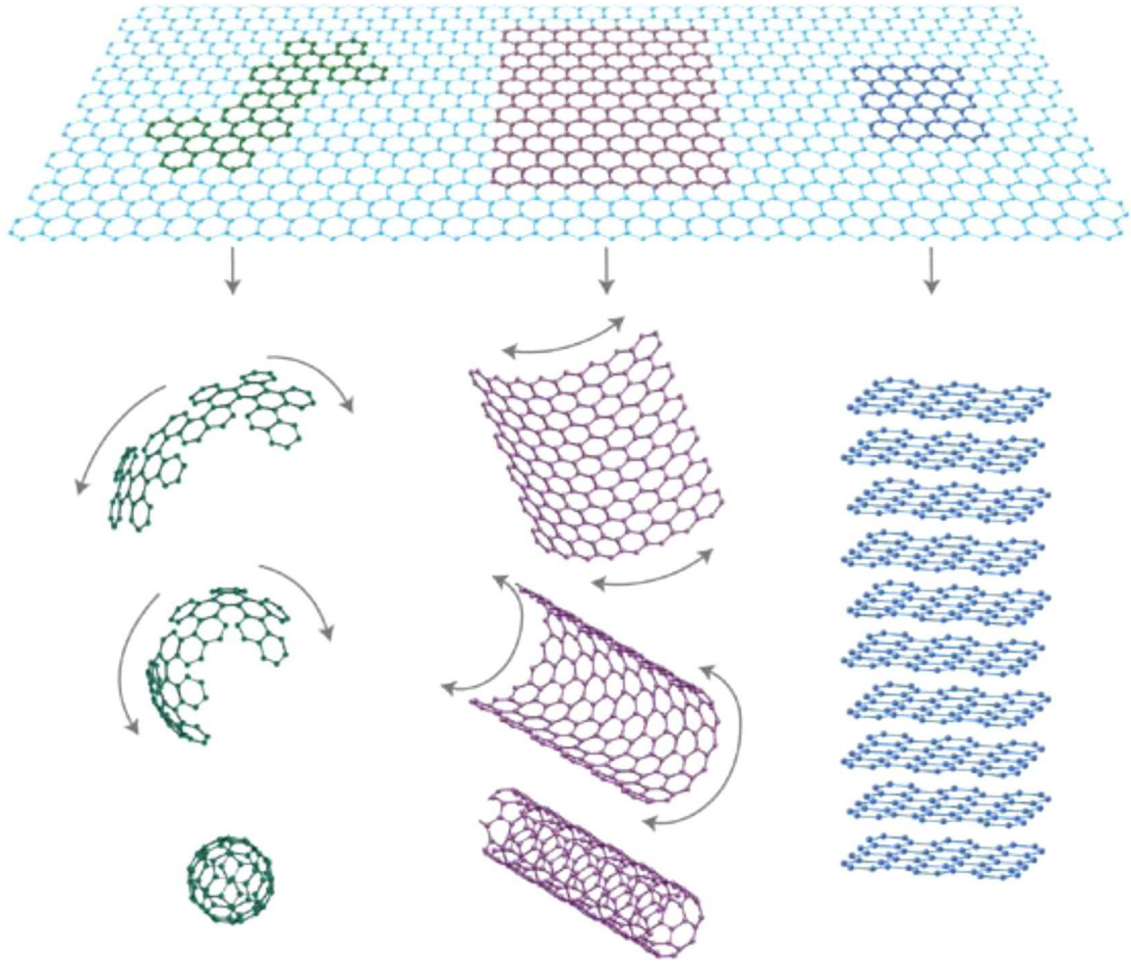

Figure 1.2: Graphene is a basic building unit for graphitic materials of all other dimensionalities: 0-dimensional fullerene (left side), 1-dimensional carbon nanotube (middle), and 3-dimensional graphite (right side) [12].

transferred to [16, 17], a supporting three-dimensional substrate. Additionally, the energy band gap tuning in the zero-band gap graphene plays a critical role in nanoelectronic devices [1, 18]. There are several reports of band gap opening in graphene with hydrogenation [19], graphene-substrate interaction [20, 21], by absorption of molecules [22], and by depositing it on a latticed-matched substrate such as $SiO_2$ or hexagonal boron nitride (h-BN) [23, 24].

In this chapter, I will give an introductory description of the physical structure of graphene-based systems. I will continue introducing the basic concepts of

semiconductor surfaces. The reason why the relaxation and reconstruction of these surfaces will be described in three basic principles. I will only consider the InAs(111) semiconductor surface which will be interfaced with graphene in Chapter 6. Furthermore, the concept of periodic boundary condition to theoretically study the surfaces will be explained.

### 1.1.1 Graphite

In nature graphite is the most frequent form of graphene. It consists of stacked sheets of graphene held together by Van der Waals interactions. It is one of the most stable crystalline solids. C atoms form a honeycomb structure placed on top of each other to form a three-dimensional solid, but the interaction between planes is rather weak. There are two known forms of graphite. In the most common hexagonal crystal form of graphite the layers are stacked in an ABAB... sequence which is called Bernal stacking as shown in Fig 1.3 (a). The other one is the rhombohedral form of graphite in which the graphene (single layer of crystalline graphite) layers are stacked in the ABCABC... sequence as shown in Fig. 1.3 (b). The unit cell of graphite is shown Fig. 1.3 (c). There are four C atoms in its unit cell. The primitive lattice vectors are given by:

$$\begin{aligned} \mathbf{a}_1 &= a(1,0,0) \\ \mathbf{a}_2 &= a\Big(-\frac{1}{2},\frac{\sqrt{3}}{2},0\Big) \\ \mathbf{a}_3 &= a\Big(0,0,\frac{c}{a}\Big), \end{aligned} \tag{1.1}$$

where $a$ = 2.461 Å is the lattice constant. The in-plane nearest neighbour distance between C atoms is 1.421 Å and $\mathbf{a}_3$ is perpendicular to the layers (the c-axis) where the $c$ is 6.708 Å and the interplanar distance $c/2$. This indicates a weak bonding between planes compared to the in-plane bonds is that the distance between nearest neighbor atoms on a plane is a factor of 2.36 larger than the distance between successive planes.

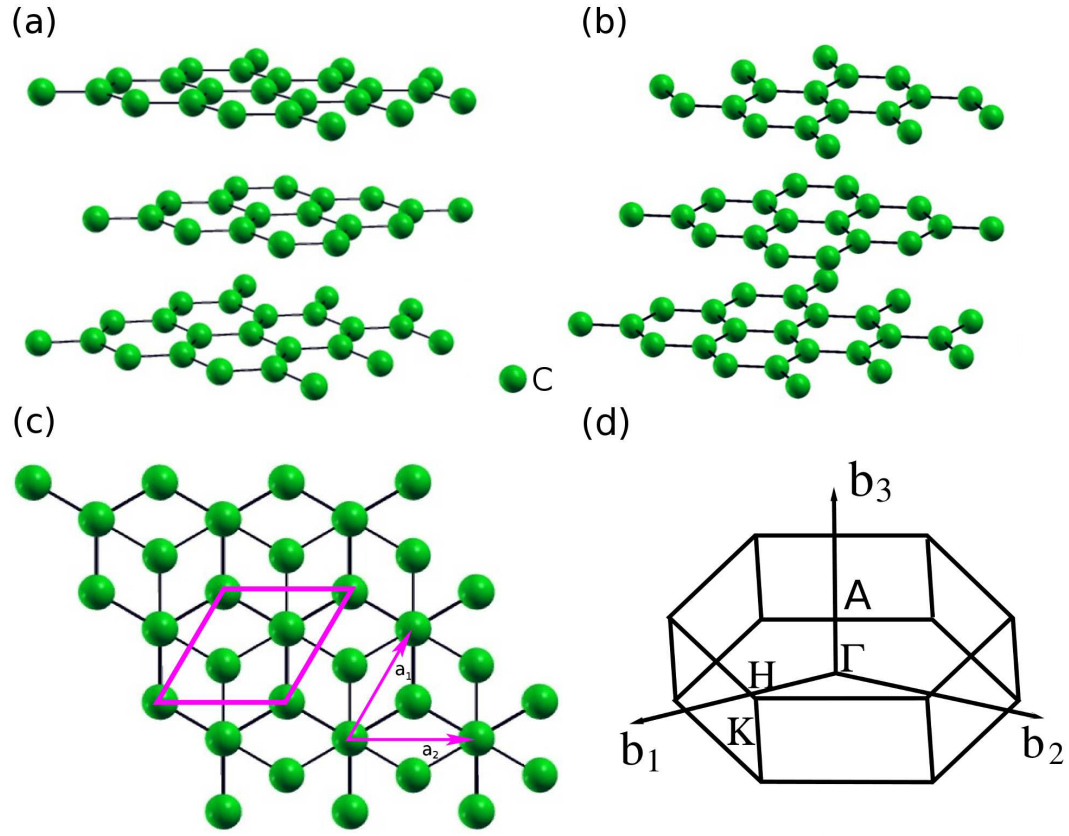


Figure 1.3: Crystal structures of (a) AB-stacked and (b) ABC-stacked graphite. (c) The primitive unit cell is the equilateral parallelogram (solid lines) with $\mathbf{a}_1$ and $\mathbf{a}_2$ lattice vectors. (d) The hexagonal Brillouin zone of graphite ($\mathbf{b}_1$, $\mathbf{b}_2$, and $\mathbf{b}_3$ are reciprocal lattice vectors) with the high symmetry points labelled $\mathbf{\Gamma}$, $\mathbf{K}$, and $\mathbf{H}$.

The primitive translation vectors of the reciprocal lattice of graphite can be computed from Eq. A.3 and 1.1:

$$\begin{aligned} \mathbf{b}_1 &= \frac{2\pi}{a}\left(1, \frac{1}{\sqrt{3}}, 0\right) \\ \mathbf{b}_2 &= \frac{2\pi}{a}\left(0, \frac{2}{\sqrt{3}}, 0\right) \\ \mathbf{b}_3 &= \frac{2\pi}{c}(0, 0, 1). \end{aligned} \tag{1.2}$$

Therefore, the reciprocal lattice is hexagonal. The first Brillouin zone is shown in

1.3 (d). The high symmetry points are

$$\begin{aligned}\mathbf{\Gamma} &= \{0,0,0\}\\ \mathbf{K} &= \left\{\frac{1}{3},\frac{1}{3},0\right\}\\ \mathbf{M} &= \left\{0,\frac{1}{2},0\right\}\\ \mathbf{H} &= \left\{\frac{1}{3},\frac{1}{3},\frac{1}{2}\right\}\\ \mathbf{A} &= \left\{0,0,\frac{1}{2}\right\}.\end{aligned}$$

### 1.1.2 Graphene

Graphene is a single layer of graphite which forms a honeycomb structure with a hexagonal lattice and two basis C atoms per primitive cell, as shown in Fig. 1.4 (a). The primitive lattice vectors are given by:

$$\begin{aligned}\mathbf{a}_1 &= a(1,0)\\ \mathbf{a}_2 &= a\Big(-\frac{1}{2},\frac{\sqrt{3}}{2}\Big),\end{aligned} \tag{1.3}$$

where $a$ = 2.4561 Å lattice constant. The nearest neighbor distance is $a/\sqrt{3}$. The primitive lattice vectors of the reciprocal lattice can be found by using Eq. A.3 and 1.3:

$$\begin{aligned}\mathbf{b}_1 &= \frac{2\pi}{a}\Big(1,\frac{1}{\sqrt{3}}\Big)\\ \mathbf{b}_2 &= \frac{2\pi}{a}\Big(0,\frac{2}{\sqrt{3}}\Big).\end{aligned} \tag{1.4}$$

The irreducible part of graphene Brillouin zone is shown in Fig. 1.4 (b), where the three high symmetry points are

$$\begin{aligned}\mathbf{\Gamma} &= \{0,0\}\\ \mathbf{K} &= \left\{\frac{1}{3},\frac{1}{3}\right\}\\ \mathbf{M} &= \left\{0,\frac{1}{2}\right\}.\end{aligned}$$

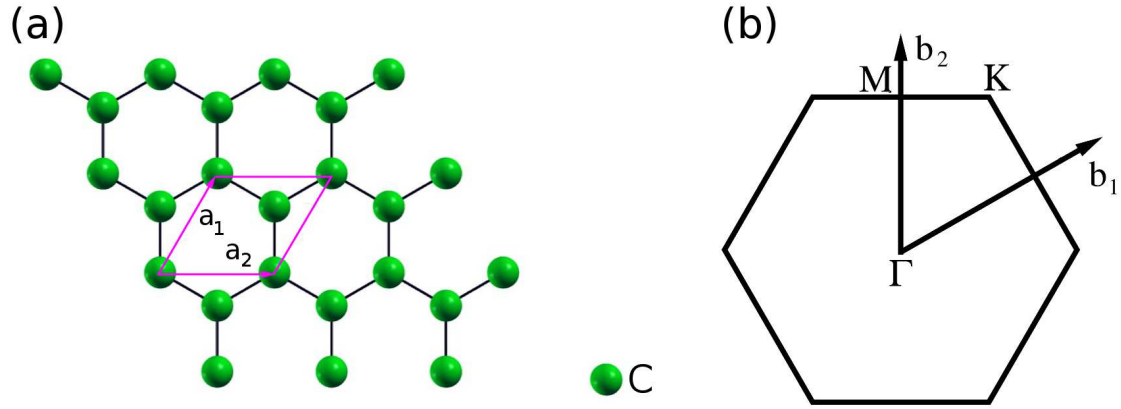


Figure 1.4: (a) The honeycomb structure of graphene. The equilateral parallelogram presents an unit cell with the lattice vectors ($\mathbf{a}_1$ and $\mathbf{a}_2$). (b) The Brouillin zone of graphene ($\mathbf{b}_1$ and $\mathbf{b}_2$ are reciprocal lattice vectors) with indication of the high-symmetry points.

### 1.1.3 Hexagonal Boron Nitride

The hexagonal boron nitride (h-BN) structure is similar to the graphite structure. It is constructed from layers of hexagonal BN networks. These h-BN layers are arranged on top of each other in an AAAAAA... sequence, such that B atoms in one layer are bonded to N atoms in the adjacent layer, as shown in Fig. 1.5. The primitive lattice vectors are given by graphite vectors given in Eq.1.1 with $a$ = 2.504 Å. The in-plane distance between B-N atoms is 1.45 Å which is quite close to given C-C distance in graphite. The lattice constant $c$ is 6.661 Å (out-of-plane distance between two alternative graphene sheets). These h-BN sheets are separated by the interlayer spacing of $c/2$ = 3.333 Å. These values are comparable to those of graphite. The first Brillouin zone of h-BN is shown in Fig. 1.3 (d) with the high symmetry points.

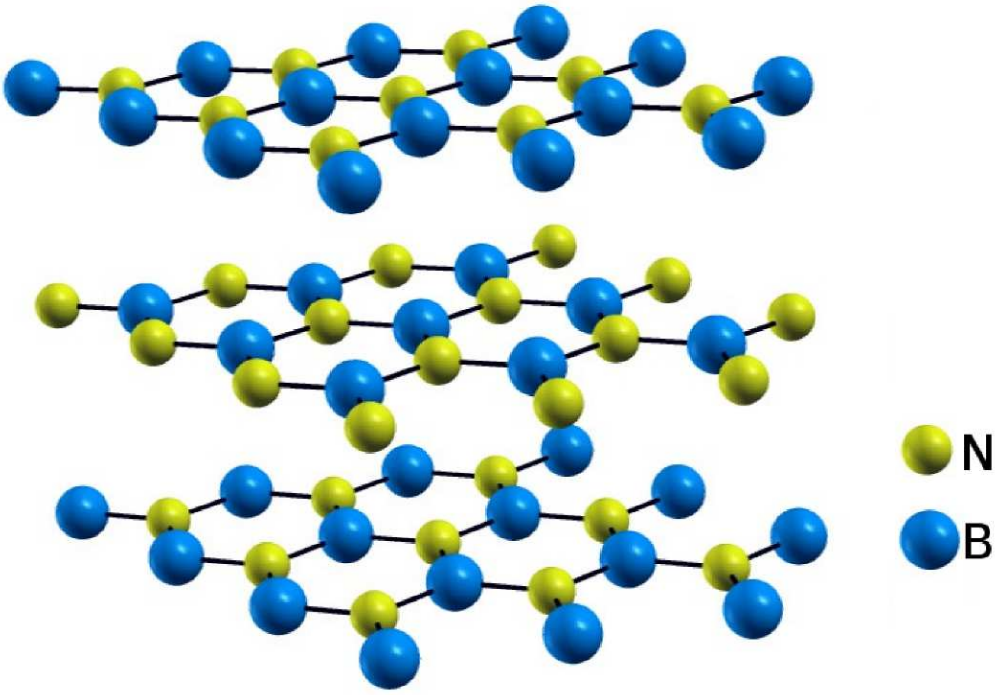


Figure 1.5: The lattice structure of hexagonal boron nitride.

## 1.2 Structure of Clean Semiconductor Surfaces

In nature, real solids do not extend to infinity so that they are terminated on surfaces. Semiconductor surfaces have played a crucial role, due to their very intriguing physical properties and the wide range of their technological applications. In order to generate these surfaces, several methods have been developed. In the second half of the twentieth century the standard method for generating semiconductor surface was to cleave a single crystal in an ultra high vacuum. This technique was used to produce the natural cleavage planes such as Si(111) and Ge(111) and the (110) surface of III-V and II-VI semiconductors with zincblende structure. Since 1970s a number of epitaxial growth techniques have been used to grow good quality semiconductor surfaces. With these exciting developments and applications of fascinating surface-sensitive experimental techniques , the field of atomic and electronic structure theory of the semiconductor

surface has been improved within the last decade.

Therefore, the theory of semiconductor surfaces has been extensively studied for decades and it is nowadays possible to theoretically determine optimal surface structures with a good level of confidence by employing total energy minimisation techniques [25]. Additionally, these calculations easily allow one to reveal trends in the relaxation or reconstruction behavior of semiconductor surfaces and to identify the origin and physical nature of particular surface states. A very good review about these techniques was published by Duke [26] in which the structural properties of semiconductor surfaces were discussed in conjunction with a number of principles that seem to govern semiconductor surface relaxation and reconstruction. In consequence, such calculations have proven extremely useful for suggesting new structural models [27, 28, 29]. Here, I will briefly discuss the reason for surface relaxation and reconstruction and explain periodic boundary conditions and slab models for theoretical calculation of surfaces. As an example of clean semiconductor surfaces, I will only consider the InAs(111) surface which will be interfaced with graphene in Chapter 6.

### 1.2.1 The Surface Relaxiaton and Reconstruction

When cutting a bulk crystal along different crystallographic directions, the generated surface is a different structure from the bulk. In general bonds are broken and dangling bonds contain less than two electrons as shown schematically in Fig. 1.6. These dangling orbitals are unstable and surface atoms try to find new atomic positions to minimise the free energy of the system. These changes of atomic position generally lead the surface to *relax* and it may *reconstruct*. This can be explained by three fundamental principles [30, 31, 32, 33].

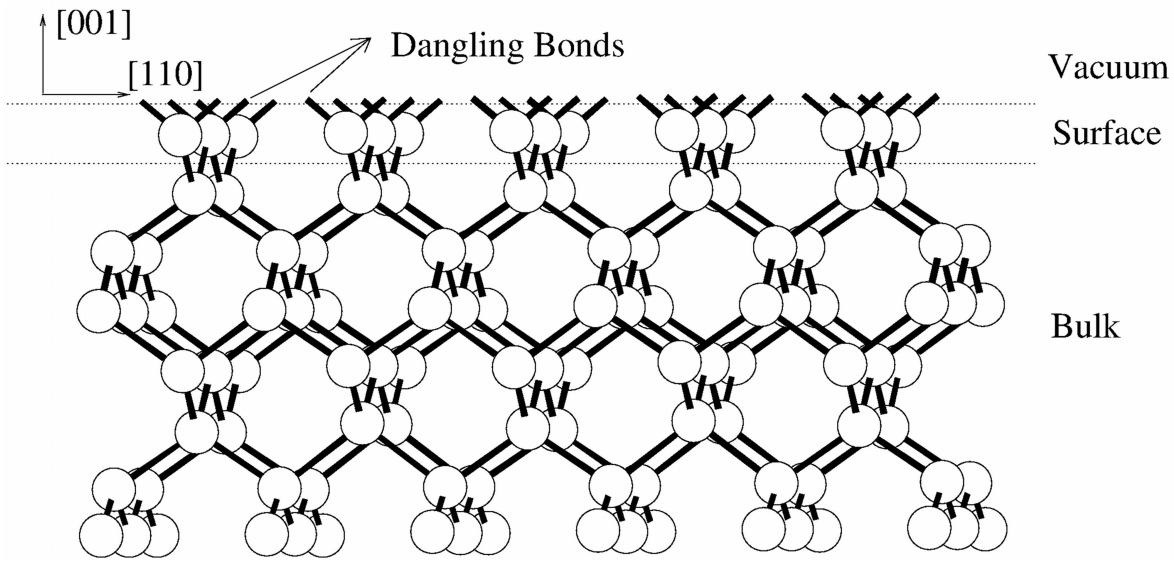


Figure 1.6: Atomic structure of the (001) face of group IV semiconductors. Schematic representation of bulk region, surface region, vacuum region, and dangling bonds.

**Principle 1:** *Surface energy can be reduced by atomic relaxation leading to the semiconducting nature of the system*

The situation of unpaired electrons in dangling bonds in favour of fully paired or fully empty dangling bonds can be changed by the process of atomic relaxation. When the atomic relaxation occurs the surface atoms are displaced from their bulk positions, but the surface periodicity does not change. In addition to this, the surface atoms donate the electronic charge in their dangling bond to fully pair the dangling bond of a neighbouring atom.

**Principle 2:** *Surface reconstruction can reduce the energy by formation of new bonds leading to a semiconducting nature of the system*

When the relaxation of surface atoms leads to a change of surface periodicity, this is called surface reconstruction. In the surface reconstruction, the dangling bonds from neighbouring surface atoms are coupled to create new bonds, thus leading

to fully occupied or fully unoccupied energy states. As a result of this, the surface periodicity is very different from that in bulk.

**Principle 3:** *Surface relaxation or reconstruction obeys the electron counting rule.*
This principle is very helpful for surface relaxation/reconstruction of compound semiconductors which are characterised by the presence of cations and anions. According to the electron counting rule (ECR), the electronic energy of compound semiconductor surfaces is lowered when electronic charge is transferred from less electronegative cations, whose dangling bonds become fully empty, to more electronegative anions, whose dangling bonds become fully occupied.

### 1.2.2 Periodic Boundary conditions and slab models for surfaces

The surface is a slice of material that is infinite in two dimensions, but finite along the surface normal. The periodic boundary condition is used for calculations of the surface properties, such as electronic band structure and density of states. There are two kinds of boundary conditions which are fixed plane boundary condition and Born-von Krman, or periodic, or cyclic, boundary condition. Our approach to study surfaces applies periodic boundary conditions in all three dimensions. The simple idea is shown in Fig. 1.7, where the supercell contains atoms along only a fraction of the vertical direction. The atoms in the lower portion of the supercell fill the entire supercell in the x and y directions, but empty space has been left above the atoms in the top portion of the supercell. This model is called a slab model since, when the supercell is repeated in all three dimensions, it defines a series of stacked slabs of solid material separated by empty spaces. The empty space separating periodic images of the slab along the z direction is called the vacuum space. It is important when using such a model that there is enough vacuum space so that the electron density of the material tails off to zero

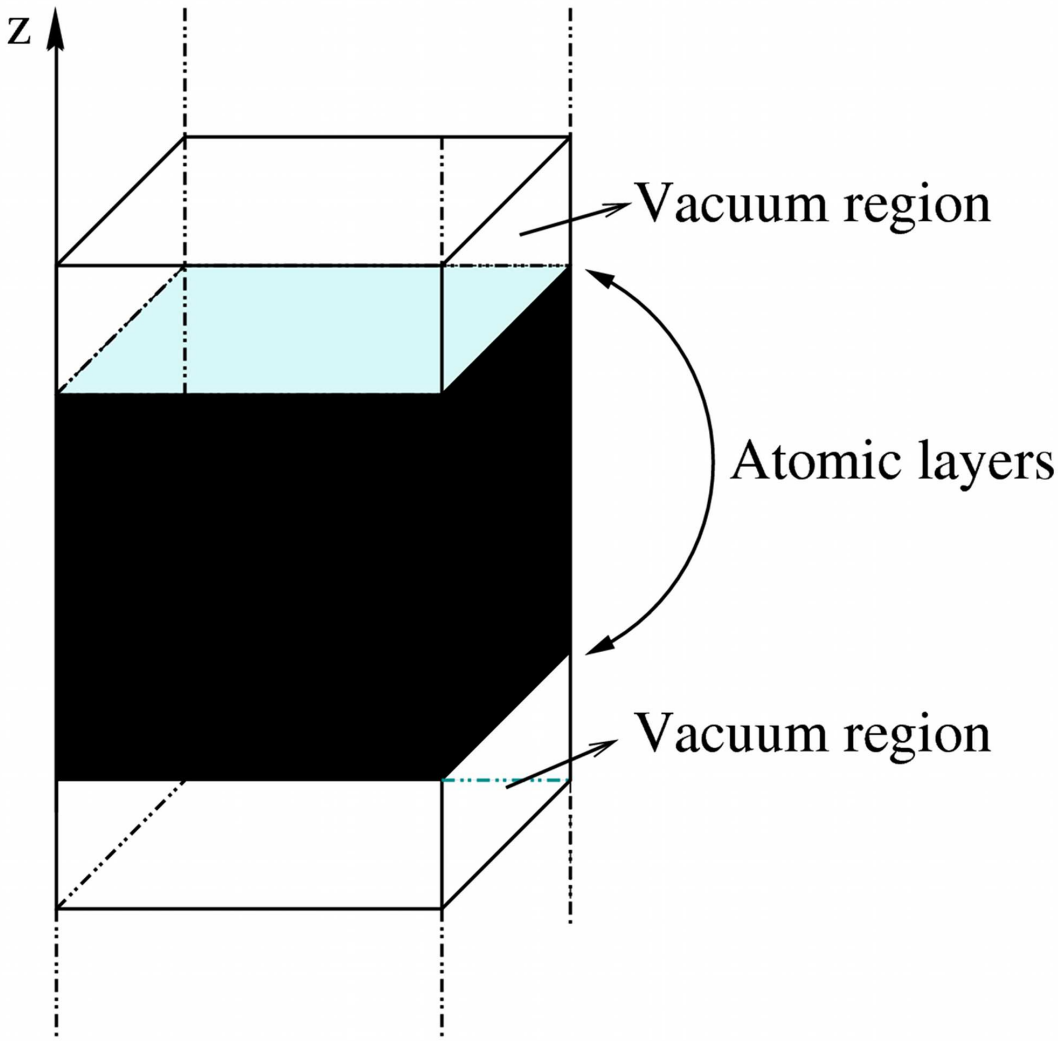


Figure 1.7: A schematic representation of supercell geometry.

in the vacuum and the top of one slab has essentially no effect on the bottom of the next. In this thesis, a repeated slab geometry is employed with the vacuum region of 14 Å for graphene based systems. The dipole potential generated in the middle of the vacuum region due to the asymmetry of the slab is quenched by introducing the scheme given in Ref. [34].

### 1.2.3 InAs(111) Surface

The InAs(111) surface is an electrostatically unstable surface. It reconstructs differently, depending on termination and composition. Therefore, it is common to refer indium terminated surface as InAs(111)A and arsenic terminated surface as InAs(111)B. The InAs(111)A surface has been found to exhibit only a $2 \times 2$ reconstruction with missing indium atom, as shown in Fig. 1.8 (a). The InAs(111)B surface, on the other hand, exhibits $2 \times 2$ reconstruction with As-trimer, as shown in Fig. 1.8 (b). Both the In missing and As-trimer models satisfy the electron counting rule: all the dangling bonds on the electropositive surface atoms (III) are unoccupied and all those on the electronegative atoms (V) are doubly occupied.

The primitive lattice vectors in real-space for the reconstructed InAs(111)A $2 \times 2$ surface are

$$\begin{aligned} \mathbf{a}_1 &= a(\frac{\sqrt{2}}{2}, \sqrt{\frac{3}{2}}, 0) \\ \mathbf{a}_2 &= a\Big(\sqrt{2}, 0, 0\Big), \end{aligned}$$

where $a$ is the bulk cubic-lattice constant. The corresponding primitive reciprocal lattice vectors are

$$\begin{aligned} \mathbf{b}_1 &= \frac{2\pi}{a}\Big(0, \sqrt{\frac{2}{3}}, 0\Big) \\ \mathbf{b}_2 &= \frac{2\pi}{a}\Big(\frac{\sqrt{2}}{2}, -\frac{\sqrt{6}}{6}, 0\Big). \end{aligned}$$

In Fig. 1.8 (c) , the Brillouin zones for the InAs(111)A surface is shown. Certain points in the Brillouin zone are labelled with dedicated letters, where

$$\begin{aligned} \bar{\mathbf{\Gamma}} &= \{0, 0\} \\ \bar{\mathbf{K}} &= \Big\{\frac{2}{3}, \frac{1}{3}\Big\} \\ \bar{\mathbf{M}} &= \Big\{\frac{1}{2}, 0\Big\}. \end{aligned}$$

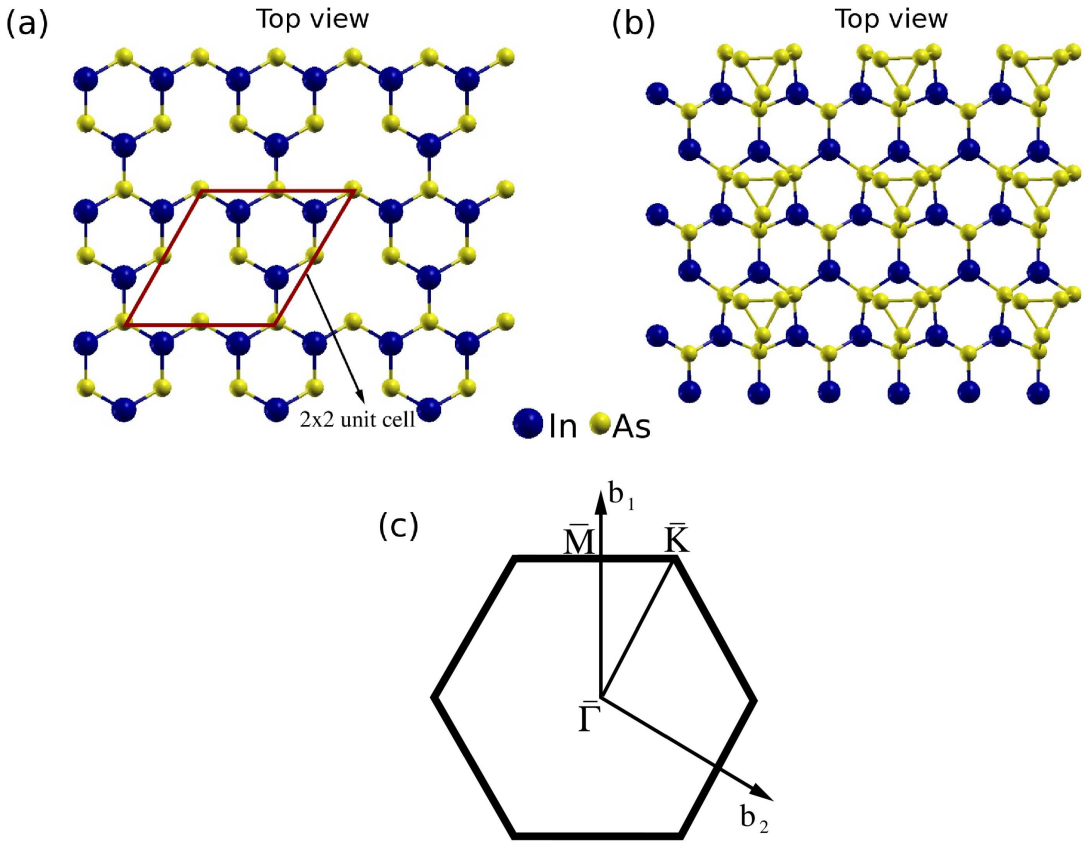


Figure 1.8: Top views of the (a) InAs(111)A-($2 \times 2$) In-vacancy and (b) As trimer model of the InAs(111)B-($2 \times 2$) reconstructions. (c) Surface Brillouin zone for InAs(111)-$2\times2$.

## 1.3 Outline of the Thesis

Density functional theory (DFT) is a successful approach to finding solutions to the Schrödinger equation that describes the quantum behaviour of atoms and molecules. In this thesis, the DFT enables us to understand the electronic structure of graphene based systems and predict some of the not-as-yet experimentally discovered structures related to these systems.

This thesis is organised as follows:

- In the first Chapter, a brief theoretical overview about the structural properties

of graphene based systems is provided. The basic concept of the surfaces such as relaxation and reconstruction of surfaces and modelling of the semiconductor surfaces for the theoretical investigations is briefly discussed to study graphene deposited on InAs(111) semiconductor surface.

- Chapter 2 describes the theoretical background of Density Functional Theory within the Local Density Approximation (LDA) and the plane wave basis set.
- In Chapter 3, electronic properties and interband optical transitions of multi-layer graphene systems have been investigated.
- Chapter 4 provides an explanation of the trigonal warping and the effect of stacking sequences on the electronic properties of ABC stacked multilayer graphene.
- The energy band gap opening in the multilayer graphene using the single layer of h-BN has been studied in Chapter 5. Also, the modification of effective mass and electron velocity are explained for multilayer graphene systems.
- In Chapter 6, the electronic properties and transparency effect of graphene on InAs(111) surface have been investigated.
- Finally, Chapter 7 contains a summary of the thesis and a plan for possible future works.

# Chapter 2

# Theoretical Techniques

## 2.1 Introduction

In this chapter, the theoretical background behind the *ab initio* pseudopotential method used in the present thesis will be discussed and explained in more detail. The main method in this approach is density function theory (DFT) which provides a powerful technique for *ab initio* studies of the electronic and ground states properties of solids. Therefore, the essentials of this method and its implementation are outlined here. Additionally, the theory of scanning tunnelling microscopy (STM) will be discussed.

## 2.2 Many-electron Theory

The describing of ions and interacting electrons in a crystalline system is based on solving a many-body Schrodinger equation

$$\hat{H}\Phi_i(\mathbf{R},\mathbf{r}) = \varepsilon_i\Phi_i(\mathbf{R},\mathbf{r}), \tag{2.1}$$

where $\hat{H}$ represents the Hamiltonian, and $\Phi_i(\mathbf{R},\mathbf{r})$ the wave function, for the collection of all the ions at $\mathbf{R}$ and electrons at $\mathbf{r}$ in the system. This equation can

not be solved without involving several approximations [31, 35, 36]. The Born-Oppenheimer or adiabatic approximation [37] is presented first to simplify the problem.

### 2.2.1 The Adiabatic Approximation

There is a huge difference of mass between atomic nuclei and electrons. This means that the electrons will respond immediately to the movement of the nuclei. For this reason, two seperate eigenvalue equations for the electrons and ions can be written within the adiabatic approximation. Therefore, the Hamiltonian in Eq. 2.1 may be expressed as:

$$H = T_{\mathrm{ion}} + V_{\mathrm{ion-ion}} + T_{\mathrm{el}} + V_{\mathrm{el-el}} + V_{\mathrm{el-ion}}, \tag{2.2}$$

where $T_{\mathrm{ion}}$ and $V_{\mathrm{ion-ion}}$ represent the kinetic and potential energy operators of the ions, $T_{\mathrm{el}}$ represents the kinetic energy operator of the electrons, $V_{\mathrm{el-ion}}$ represents the electron-ion interaction term and $V_{\mathrm{el-el}}$ represents the electron-electron interaction. Within the assumed adiabatic approximation the total wavefunction can be written as a product of the ionic and electronic wavefunctions:

$$\Phi(\mathbf{R}, \mathbf{r}) = \chi(\mathbf{R})\Psi(\mathbf{R}, \mathbf{r}), \tag{2.3}$$

where **R** denotes the positions of all ions ($\mathbf{R}_i$: *i*=1,...,N) and **r** denotes the electron co-ordinates ($\mathbf{r}_i$: *i*=1,...,M). Here $\Psi(\mathbf{R}, \mathbf{r})$ is an ionic wave function depending only on the electronic coordinates **r** and ionic positions, and the electronic wave function $\chi(\mathbf{R})$ depends on the ionic configuration **R**. From the Eq. 2.1 and the Eq. 2.3 one gets two coupled Schrödinger equations [38, 39]:

$$[\hat{H}_{\mathrm{ion}} + \varepsilon_{\mathrm{el}}(\mathbf{R})]\chi(\mathbf{R}) = \varepsilon\chi(\mathbf{R}) \tag{2.4}$$

for the ions, and

$$[\hat{H}_{\mathrm{el}}]\Psi(\mathbf{R}, \mathbf{r}) = \varepsilon_{\mathrm{el}}\Psi(\mathbf{R}, \mathbf{r}) \tag{2.5}$$

for the electrons. The Hamiltonian for the electrons may be written as

$$\hat{H}_{\rm el} = -\frac{\hbar^2}{2m}\sum_i \nabla^2_{\mathbf{r}_i} + \sum_i V_{\rm ext}(\mathbf{r}_i) + \sum_i V_{e-e}(\mathbf{r}_i). \tag{2.6}$$

The potential $\mathrm{V_{ext}}$ consists of the external potential imposed on the electrons by nuclear configuration, $\mathbf{R}_i$, $\mathrm{V}_{e-e}$ is the electron-electron interaction, and $\mathrm{V_{ext}}$ is the electron-ion interaction.

### 2.2.2 Wave-Function Approaches

The many-body eigenvalue problem is still very complicated to solve using the Born-Oppenheimer approximation due to electron-electron interaction. Therefore, further approximations need to be applied in Eq. 2.5. Two distinct approaches, wave-function approach and density functional approach, are presented in this section. They are variational techniques which reduce the many body Schrödinger equations to single particle equations.

#### 2.2.2.1 Hartree Theory

Hartree proposed that the total wave function is the direct product of single-particle wave functions [40]. Therefore, the many-body wave function can be written as:

$$\Phi(\mathbf{r_1}, \mathbf{r_2}, ..., \mathbf{r_N}) = \Phi_1(\mathbf{r_1})\Phi_2(\mathbf{r_2}).....\Phi_N(\mathbf{r_N}), \tag{2.7}$$

from which it follows that the electrons are independent, and interact only via the mean-field Coulomb potential. This yields one-electron Schrödinger equations of the form:

$$\Big(-\frac{\hbar^2}{2m}\nabla^2 + V(\mathbf{r})\Big)\Phi_i(\mathbf{r}) = \varepsilon\Phi_i(\mathbf{r}), \tag{2.8}$$

where $V(\mathbf{r})$ is the potential in which the electron moves, this includes both the nuclear-electron interaction

$$V_{nuc}(\mathbf{r}) = -\frac{Ze^2}{4\pi\epsilon_o}\sum_R \frac{1}{|\mathbf{r}-\mathbf{R}|}, \tag{2.9}$$

and the mean field arising from the $N-1$ other electrons. Similarly the electron potential is given through

$$V_{ele}(\mathbf{r}) = -\frac{e}{4\pi\epsilon_o}\int d\mathbf{r}'\rho(\mathbf{r}')\frac{1}{|\mathbf{r}-\mathbf{r}'|}, \tag{2.10}$$

where

$$\rho(\mathbf{r}) = \sum_i |\Phi_i(\mathbf{r})|^2. \tag{2.11}$$

#### 2.2.2.2 Hartree-Fock Theory

The antisymmetry of the electron wavefunction was not considered in Hartree approximation. Fock improved this problem in Hartree theory by including the particle interchange. According to the Pauli exclusion principle, the many-body wave function is anti-symmetric with respect to interchange of any two electron coordinates as the following:

$$\Phi_1(\mathbf{r_1})\Phi_2(\mathbf{r_2}).....\Phi_N(\mathbf{r_N}) = -\Phi_1(\mathbf{r_2})\Phi_2(\mathbf{r_1}).....\Phi_N(\mathbf{r_N}). \tag{2.12}$$

This modification adds an extra term to the Hamiltonian which is known as exchange. Combining then Hartree-type wavefunctions to form a properly anti-symmetrised wavefunction for the system, we obtain the determinant (first introduced by Slater [41]):

$$\Phi(\mathbf{r_1},\mathbf{r_2},...,\mathbf{r_N}) = \frac{1}{\sqrt{N!}}\begin{vmatrix} \Phi_1(\mathbf{r_1}) & \Phi_2(\mathbf{r_1}) & \dots & \Phi_N(\mathbf{r_1}) \\ \Phi_1(\mathbf{r_2}) & \Phi_2(\mathbf{r_2}) & \dots & \Phi_N(\mathbf{r_2}) \\ \vdots & \vdots & \ddots & \vdots \\ \Phi_1(\mathbf{r_N}) & \Phi_2(\mathbf{r_N}) & \dots & \Phi_N(\mathbf{r_N}) \end{vmatrix}. \tag{2.13}$$

The single particle Hartree-Fock (HF) equation is then written as:

$$\Big\{-\frac{\hbar^2}{2m}\nabla^2 + V_{nuc}(\mathbf{r}) + V_{ele}(\mathbf{r})\Big\}\Phi_i(\mathbf{r}) - \sum_j \int d\mathbf{r}'\frac{\Phi_j^*(\mathbf{r}')\Phi_i^*(\mathbf{r}')\Phi_j(\mathbf{r})}{|\mathbf{r}-\mathbf{r}'|} = \varepsilon_i\Phi_i(\mathbf{r}). \tag{2.14}$$

This equation has one extra term compared with the Hartree equation, the last term of the left-hand side , which is called the exchange term.

The Hartree-Fock calculations have been carried out for the ground state energy of atoms, but for solids these calculations are very complicated. Additionally, the electronic states and total ground state energy of insulators and semiconductors are found to yield unsatisfactory values as this scheme neglects screening of the exchange interaction, generally known as the correlation effect [39].

### 2.2.3 Density Functional Approach

I have discussed the Hartree-Fock method in detail, but, of course, it has its difficulties. For example, HF is very complex and the correlations between electrons due to Coulomb repulsions are not properly treated. Therefore, the idea of density function theory (DFT), providing a different way of treating many-body systems, was proposed. The essential idea behind this theory is that the electron density contains in principle all the information contained in a many-body wave function.

The original DFT of quantum systems is the method of Thomas [42] and Fermi [43] proposed in 1927. Although their approximation is not accurate enough for present-day electronic structure calculations, the approach illustrates the way DFT works. In their method, the kinetic energy is considered to be a functional of the electron density, but in common with the Hartree and HF methods, only incorporated electron-electron interaction via a mean field potential. Both Thomas and Fermi neglected exchange and correlation. Therefore, this was extended by Dirac [44] in 1930, who formulated the local approximation for exchange still in use today. This also failed to significantly improve the method. Thereafter, a modern formulation of DFT is proposed by Hohenberg, Kohn and Sham [45, 46]. This method defines particle density as a fundamental variable for describing any multi-electron system. This conceptual difference leads to a remarkable reduction in difficulty where the density is a function of three variables (cartesian

coordinates) rather than 3N variables as in the full many-body wave function.

#### 2.2.3.1 Thomas Fermi Theory

In the Thomas and Fermi method, they expressed the total electronic energy where the kinetic exchange and correlation contributions were taken from the homogeneous electron gas [35, 36]. They assumed that the electrons move independently in an effective electrostatic potential, and the electron-electron interaction energy arises from the electrostatic energy,

$$E_{est}[n] = \frac{e^2}{8\pi\epsilon_o}\int d\mathbf{r}\int \frac{\rho(\mathbf{r})\rho(\mathbf{r}')}{|\mathbf{r}-\mathbf{r}'|}d\mathbf{r}'. \tag{2.15}$$

Furthermore, the kinetic energy is given by:

$$T[\rho] = \int \rho(\mathbf{r})t[\rho(\mathbf{r})]d\mathbf{r}, \tag{2.16}$$

where $t[\rho]$ is the kinetic energy density for a system of noninteracting electrons with density $\rho$. This is given by

$$t[\rho] = \frac{1}{(2\pi)^3}\int_{|k|\leq k_F}\frac{\hbar^2k^2}{2m}d\mathbf{k}, \tag{2.17}$$

where $k_F$ is the Fermi wave vector and the density function $\rho$ is mathematically defined as:

$$\rho = \frac{4}{3(2\pi)^2k_F^3}. \tag{2.18}$$

This gives

$$T[\rho] = C_k\int\{\rho(\mathbf{r})\}^{5/3}d\mathbf{r}, \tag{2.19}$$

where the coefficient $C_k$ can be given as:

$$C_k = \frac{3\hbar^2(3\pi^2)^{3/2}}{10m}. \tag{2.20}$$

Now the function $E[n]$ is minimised under the condition that the number of electrons ($N$) is kept constant,

$$\int \rho(\mathbf{r})d\mathbf{r} = N. \tag{2.21}$$

Using the method of Lagrange multipliers, it is required that

$$E[\rho] + \lambda N = T[\rho] + E_{est}[\rho] + \int \rho(\mathbf{r})\{V_{ext}(\mathbf{r}) + \lambda\} d\mathbf{r} \tag{2.22}$$

has a minimum. The corresponding Euler equation is the Thomas-Fermi equation

$$\frac{5}{3} C_k \rho(\mathbf{r})^{2/3} + \frac{e^2}{4\pi\epsilon_o} \int \frac{\rho(\mathbf{r}')}{|\mathbf{r} - \mathbf{r}'|} d\mathbf{r}' + V_{ext}(\mathbf{r}) + \lambda = 0. \tag{2.23}$$

The Thomas-Fermi approach is extremely simple, and is qualitatively correct for atoms. However, it has been shown that the Thomas-Fermi theory does not result in atoms binding to form molecules or solids.

#### 2.2.3.2 Hohenberg-Kohn-Sham Theory

The approach of Hohenberg-Kohn-Sham (HKS) is to formulate the DFT [45, 46] as a technique applied in electronic structure theory. The formulation has become the primary tool for condensed matter and quantum chemistry. The HKS theory can be expressed in terms of two simple theorems which are as follows:

**THEOREM 1.** *The density as basic variable*

For a given non-degenerate ground-state many-body wavefunction $\Phi$, there is a unique functional of the ground-state electronic charge density. All other ground-state properties of the system, the kinetic and electron-electron interaction energies, can be expressed in the functionals of $\rho(\mathbf{r})$. Therefore, one may define a unique functional $F[\rho(\mathbf{r})]$ as the following:

$$F[\rho(\mathbf{r})] = < \Phi | (T + V_{el-el}) | \Phi >, \tag{2.24}$$

where $T$ is the kinetic energy operator and $V_{el-el}$ is the electron-electron interaction operator. This functional $F[\rho(\mathbf{r})]$ is a universal functional in the sense that it has the same dependence on the electron density for any system, independent of the external potential concerned. The exact density dependence of this functional

is, however, unknown. Using this functional, one may then define, for a given external potential $\upsilon(\mathbf{r})$, the energy functional

$$E[V_{ext}, \rho(\mathbf{r})] = \int \rho(\mathbf{r})\upsilon(\mathbf{r})d\mathbf{r} + F[\rho(\mathbf{r})], \tag{2.25}$$

where $F[\rho(\mathbf{r})]$ is a universal but unknown functional of the electron density.

**THEOREM 2.** *The energy variational principle*

According to this theorem, the ground state energy may be obtained variationally where the density that minimises the total energy is the exact ground state density. Using these two simple theorems, the total electronic part of the energy corresponding to the true ground state electronic density can be expressed as:

$$E_{el}[V_{ext}, \rho] = T[\rho] + \int V_{ext}(r)\rho(r)d\mathbf{r} + \frac{e^2}{8\pi\epsilon_o}\iint \frac{\rho(r)\rho(r')}{|r-r'|}d\mathbf{r}d\mathbf{r'} + E_{xc}(\rho), \tag{2.26}$$

where $E_{xc}(\rho)$ is the exchange-correlation energy. However, there are three major problems in the solution of the above equation: (i) one needs a suitable method to obtain the self-consistent charge density function $\rho$, (ii) there is no information about $\rho$, evaluating $T[\rho]$ is very difficult, and (iii) $E_{xc}$ remains unknown.

The first problem is completely resolved by following the Kohn-Sham (KS) proposal. Using the Variational principle $(\partial E/\partial\phi = 0)$ with $\phi = \phi_1(\mathbf{r_1})\phi_2(\mathbf{r_2})...\phi_N(\mathbf{r_N})$, Kohn and Sham got a collection of single-particle equations of non-interacting electrons as:

$$\Big(-\frac{\hbar^2}{2m}\nabla^2 + V_{KS}[\rho(r)]\Big)\phi_j(r) = \varepsilon_j\phi_j(r), \tag{2.27}$$

where $\phi_j$ and $\varepsilon_j$ are the KS single-particle wave functions and eigenvalues respectively, and $V_{KS}$ is the KS potential energy which given by:

$$V_{KS}[\rho(r)] = V_{ext}(r) + V_H[\rho(r)] + V_{xc}[\rho(r)]. \tag{2.28}$$

Hence the second problem (the kinetic energy) can be determined from:

$$T[\rho] = \sum_j \langle\phi_j|\varepsilon_j - V_{KS}[\rho]|\phi_j\rangle. \tag{2.29}$$

The third difficulty with the application of the DFT is that the exchange correlation energy is hard to express in terms of the charge density.

### 2.2.4 Exchange Correlation Functional

As I mentioned in the previous section, the third difficulty is that the functional $E_{\rm xc}$ is generally unknown. It is the crucial quantity in the Kohn-Sham approach. In the following section the Local Density Approximation and the Generalised Gradient Approximation are used to express $E_{\rm xc}$.

#### 2.2.4.1 Local Density Approximation

The most common approximation for exchange-correlation energy functional $E_{\rm xc}$, is known as the local density approximation (LDA). This approximation considers that the electronic charge density in the system corresponds to that of a homogeneous electron gas so that $\rho(r)$ is a slowly varying quantity in space. The $E_{\rm xc}$ can then be expressed as:

$$E_{xc}[\rho] = \int \rho(r)\epsilon_{xc}[\rho(r)]d\mathbf{r}, \tag{2.30}$$

where $\epsilon_{xc}[\rho(r)]$ is the exchange-correlation energy per electron of a uniform electron gas of density $\rho$. The exchange-correlation potential is then given by:

$$V_{xc}[\rho(r)] = \frac{d}{d\rho(r)}(\rho(r)\epsilon_{xc}[\rho(r)]), \tag{2.31}$$

while

$$\frac{1}{\rho(r)} = \frac{4\pi}{3}r_s^3, \tag{2.32}$$

where $r_s$ is the mean interelectronic spacing. Therefore one finds

$$V_{xc}[\rho(r)] = \epsilon_{xc} - \frac{r_s}{3}\frac{d\epsilon_{xc}}{dr_s}. \tag{2.33}$$

If the LDA scheme is extended to the unrestricted case (i.e. including the spin orientations), then the obtained scheme is known as the local spin-density approximation (LSDA). There are several analytical fits for $\epsilon_{xc}(r_s)$. In the following

different expressions are presented for both $\epsilon_x(r_s)$ and $\epsilon_c(r_s)$ and similarly an expression for $\epsilon_{xc}(r_s)$.

**1. Kohn-Sham-Gáspár [46, 47] Pure Exchange Energy Expression**

$$\epsilon_x = -\frac{0.4582}{r_s} \qquad \text{(Hartree)}. \tag{2.34}$$

**2. Wigner [48] Correlation Expression**

$$\epsilon_c = -\frac{0.44}{7.8 + r_s} \qquad \text{(Hartree)}. \tag{2.35}$$

**3. Slater [49] Exchange-Correlation Expression**

$$\epsilon_{xc} = -\alpha\frac{0.68725}{r_s} \qquad \text{(Hartree)}, \tag{2.36}$$

where $\alpha$ is the adjusting parameter and its value is in the range of $(\frac{2}{3}, 1)$.

**4. Ceperley-Alder [50] Correlation Expression as parametrised by Perdew and Zunger [51]**

The $\epsilon_{\rm xc}$ is written in two parts:

$$\epsilon_{\rm xc} = \epsilon_{\rm x} + \epsilon_{\rm c} \tag{2.37}$$

with

$$\epsilon_x = -\frac{0.4582}{r_s} \tag{2.38}$$

in Hartrees and

$$\epsilon_c = \begin{cases} -0.1423/(1 + 1.0529\sqrt{r_s} + 0.3334 r_s) & \text{for } r_s \geq 1, \\ -0.0480 + 0.0311 \ln r_s - 0.0116 r_s + 0.0020 r_s \ln r_s & \text{for } r_s < 1, \end{cases}$$

in Hartrees. The parameter $r_s$ is related to the density through the relation $\rho^{-1}=\frac{4\pi}{3}\mathrm{r}_s^3$. The exchange-correlation potential is obtained as

$$V_{\rm xc} = \epsilon_{\rm xc} - \frac{r_s}{3}\frac{d\epsilon_{\rm xc}}{dr_s} \tag{2.39}$$

#### 2.2.4.2 Generalised Gradient Approximation

The best known class of functionals after the LDA uses information about the local electron density and the local gradient in the electron density; this approach defines a generalized gradient approximation (GGA). Perdew *et al.* [52] constructed the concept of the GGA. The exchange part is defined as:

$$E_x^{GGA} = \int \rho \epsilon_x^{unif}(\rho) F_x(s) d\mathbf{r}, \tag{2.40}$$

where

$$\epsilon_x^{unif}(\rho) = -\frac{3k_F}{4\pi}, \tag{2.41}$$

$$k_F = (3\pi^2\rho)^{1/3}, \tag{2.42}$$

$$s = \frac{\nabla\rho}{2k_F\rho}, \tag{2.43}$$

and

$$F_x = 1 + \kappa - \frac{\kappa}{1 + \frac{\eta s^2}{\kappa}}. \tag{2.44}$$

The values of constants are $\kappa = 0.084$ and $\eta = 0.21951$.

Similarly the correlation part of GGA is defined as following:

$$E_c^{GGA} = \int \rho[\epsilon_c^{unif}(r_s) + H(r_s, t)] d\mathbf{r}, \tag{2.45}$$

where

$$H = \gamma ln\Big\{1 + \frac{\beta}{\gamma} t^2 \Big[\frac{1 + At^2}{1 + At^2 + A^2t^4}\Big]\Big\}, \tag{2.46}$$

$$A = \frac{\beta}{\gamma}[exp^{-(\epsilon_c^{unif}/\gamma)} - 1]^{-1}, \tag{2.47}$$

$$t = \frac{|\nabla\rho(r)|}{2k_s}\rho(r), \tag{2.48}$$

and

$$k_s = \frac{4k_F}{\pi}. \tag{2.49}$$

The values of constants are $\gamma = 0.031091$ and $\beta = 0.066725$. When the spin orientation is considered in this scheme, then the method is called the spin generalised gradient approximation ($\sigma$GGA).

*Comparison between LDA and GGA*: In 1992, Garcia *et al.* found that GGA does not provide a consistent and unequivocal improvement over the LDA in the calculated structural properties of crystalline solids [53]. However, the GGA is better than the simple LDA in describing the binding energy of molecules [54], activation energy barriers [55] and magnetic structures [56]. Despite these successes, the GGA sometimes overcorrects the LDA results for solids [57, 58]. Furthermore, the structural and electronic properties of graphite and hexagonal Boron Nitride have been already analysed by using LDA and GGA [59, 60, 61, 62, 63, 64]. It was found that GGA calculations give little or no bonding whereas LDA gives reasonable results for bonding energies and interatomic distances, comparable to experimental values (the relative difference being smaller than $0.1\%$). The reason for the failure of GGA was intuitively clear: the semilocal gradient approximation cannot describe well the inherently non-local interaction.
In this thesis, I mainly worked with the LDA with the Ceperley-Alder [50] correlation expression as parametrised by Perdew and Zunger [51] which is the most common and considered to be provide better results verified by Refs. [65, 66].

## 2.3 Electron-Ion Interaction

In an attempt to solve the KS equation, one has to consider two important issues: (i) how to treat the electron-ion interaction or what is known as the external potential $V_{ext}(r)$, and (ii) finding a new mathematical way to represent the single-particle orbitals. To solve the first issue, I will consider and discuss the electron-ion interaction and then focus on two main theories related to this subject. There

are two common approaches used to treat $V_{\text{ext}}$: all-electron and pseudopotential approaches.

### 2.3.1 All-electron methods

This method deals explicitly with all electrons in the system (valence and core electrons). It is the so called all electron method. In this method, there are different successful schemes which are the Linear Muffin-Tin Orbital approach (LMTO) [67] and the Full Potential Linearised Augmented Plane Wave approach (FLAPW) [68]. In these schemes, the choice of basis function is primarly different to construct single-particle wave function. Skriver [69] has described the LMTO method which has successfully been applied to the study of the electronic and ground-state properties of metals and semiconductors. In this approach (LMTO), the problem is broken up into different constituent parts. The Schrödinger equation is solved for the isolated atoms inside a spherical region around each atom, whereas the free electron Schrödinger equation is solved in the interstitial regions. The other method (FLAPW) is used by Wimmer *et al*. [70]. According to this method, the atomic Schrödinger equation is solved inside a spherical region around each atom and using a plane wave basis in the interstitial regions. The FLAPW method is very well described by Wei *et al*. [71] to calculate energy bands, equilibrium lattice constant, bulk modulus, and cohesive energy of Tungsten.

### 2.3.2 Pseudopotential Method

In the pseudopotential method for a solid, one considers the ion cores as a background in which the valence electrons move. These valence electrons actively participate in determining the chemical and physical properties of molecules and solids. This has led to the idea of the pseudopotential method: the interaction be-

tween the valence electrons and the ion core is treated with the pseudopotential which allows us to understand why the electron-ion core interaction is apparently so weak. The fact that pseudopotentials are not unique allows the freedom to choose forms that simplify the calculations and the interpretation of the resulting electronic structure.

#### 2.3.2.1 Non-Uniqueness of Pseudopotentials

The single-particle Kohn-Sham equation was given in Eq. 2.27. By considering a proper transformation of this equation, the concept of pseudopotential can be devoloped. The Eq. 2.27 can be written as

$$h\phi = \varepsilon\phi \tag{2.50}$$

with

$$\begin{aligned} h &= t_0[\rho] + v_{KS}[\rho] \\ &= t_0[\rho] - \frac{1}{4\pi\varepsilon_0}\frac{Z_{nucl}e^2}{r} + v_H[\rho] + v_{xc}[\rho], \end{aligned} \tag{2.51}$$

where $Z_{nucl}$ is the atomic number and the Hamiltonian is the sum of the single particle kinetic energy operator $t_0$ and the effective Kohn-Sham potential operator $v_{KS}$. The second term in Eq. 2.51 represents the Coulomb potential experienced by an electron positioned at r with respect to the nuclear site and $v_{KS}$ represents an 'all electron' attractive potential which can be denoted as $v_A$.

For the developing of the pseudopotential concept we express the total number of electrons ($Z_{nucl}$) as a sum of core ($Z_{core}$) and valence ($Z$) electrons:

$$Z_{nucl} = Z_{core} + Z. \tag{2.52}$$

We then expand the single-particle wave function $\phi$ as

$$\phi = \psi + \sum_c \alpha_c \psi_c \tag{2.53}$$

where $\psi$ is a smooth part corresponding to valence electron states, $\psi_c$ is a core function corresponding to one of the bound states in the ion core and the $\alpha_c$ are determined by the following condition,

$$< \phi|\psi_c >= 0. \tag{2.54}$$

By using Eqs. 2.53 and 2.54, Eq. 2.50 can be rewritten as

$$h\psi + \sum_c (\varepsilon - E_c)|\psi_c >< \psi_c|\psi = \varepsilon\psi \tag{2.55}$$

with $E_c$ as the eigenvalue of a core state. Eq. 2.55 can be represented as

$$(h + v_R)\psi = \varepsilon\psi \tag{2.56}$$

where $v_R$ is a repulsive potential operator. We can further express Eq. 2.56 as

$$(t_0 + v^{PS})\psi = \varepsilon\psi. \tag{2.57}$$

The operator

$$v^{PS} = v_A + v_R = v_A + \sum_c (\varepsilon - E_c)|\psi_c >< \psi_c| \tag{2.58}$$

represents a weak attractive potential, denoting the balance between the attractive potential $v_A$ and the repulsive potential $v_R$, and is called a pseudopotential, first discussed by Phillips and Kleinman [72] and by Antončik [73].

There is an enormous freedom to define the potential $v_{ps}$, depending on how effective the cancellation is. Although pseudopotentials gained differently and reflecting different degrees of cancellation, they often produces similar results. This reflects the non-uniqueness of pseudopotentials. This feature of pseudopotentials has been utilised extensively in various applications, resulting in the development of different types of pseudopotentials. Here I will discuss local, non-local, norm-conserving, and ultrasoft pseudopotentials.

#### 2.3.2.2 Local and non-local Pseudopotentials

The pseudopotential was expressed in the equation 2.58. This can be rewritten in the following form

$$V^{ps} = \frac{Z_c e}{r}\hat{I} + \sum_c (\varepsilon_v - \varepsilon_c)|\varphi_c\rangle\langle\varphi_c|, \tag{2.59}$$

where $\hat{I}$ is the identity operator. As clearly seen from the above equation, this pseudopotential acts differently on wave functions of different angular momentum. The most general form of a pseudopotential of this kind is given as

$$V^{ps}(\mathbf{r}) = \sum_{l=0}^{\infty}\sum_{m=-l}^{l} v_{ps}^{l}|lm\rangle\langle lm| = \sum_{l=0}^{\infty} v_{ps}^{l}(r)P_l, \tag{2.60}$$

where $v_{ps}^{l}(r)$is the pseudopotential corresponding to the angular component $l$ and the operator

$$P_l = \sum_{m=-l}^{l} |lm\rangle\langle lm| \tag{2.61}$$

is a projection operator onto the $l^{th}$ angular momentum subspace. This equation means that when $V_{ps}$ acts on the electronic wave function, the projection operator $P_l$ selects the $l^{th}$ angular component of the wave function, which is then multiplied by the corresponding pseudopotential $v_{ps}^{l}(r)$. Pseudopotentials of this form are known as non-local because they act differently on the various angular components of the wave function. In practice $v_{ps}^{l}(r)$ is a local operator in the radial coordinate. Therefore, a better name for this type of expression is a semi-local pseudopotential. However, if all the angular components of the pseudopotential are taken to be the same (or if only $l$=0 is considered), then the pseudopotential is said to be a local pseudopotential.

#### 2.3.2.3 Ultrasoft Pseudopotentials

One goal of pseudopotentials is to create pseudo-wavefunctions that are as smooth as possible and accurate. Norm-conserving pseudopotentials achieve the goal of

accuracy, usually at some sacrifice of smoothness. Therefore, a different approach known as ultrasoft (US) pseudopotentials was developed by Vanderbilt [74, 75].

#### 2.3.2.4 Norm-conserving Pseudopotentials

Most modern pseudopotential calculations are based upon a norm-conserving potential. The requirment of norm-conservation is the key step in making accurate, transferable pseudopotentials, which is essential so that a pseudopotential constructed in one enviroment can faithfully describe the valence properties in different environments including atoms, ions, molecules, and condensed matter. The first form of norm-conserving pseudopotential was established by Hamann, Schlüter and Chiang (HSC) [76]. However, there are other forms of this kind of pseudopotential, for example, Bachelet, Hamann, and Schlüter pseudopotential (BHS) [77], Troullier-Martins pseudopotential (TM) [78] and Kleinman-Bylander (KB) pseudopotential [79].

In this thesis, all the DFT calculations are performed using the KB pseudopotentials. Kleinman and Bylander suggested that it is possible to construct a form of non-local (both in angular and radial coordinates) and fully separable pseudopotential. The advantage of this form lies in the computational ease and computer storage saving when evaluating pseudopotential matrix elements in momentum space. For instance, with $N$ plane waves in the basis, the number of matrix elements scales as $N$ in the KB form and as $N^2$ in the semi-local (non-local in angular coordinates but local in the radial coordinate) form. Obviously, therefore, use of the KB form brings a great detail of computational saving for large-scale electronic structure and total energy calculations [80]. A detailed analysis and discussion of the appropriateness of using the KB separable pseudopotentials for large-size system were given in Ref. [81].

The accuracy of the pseudopotential, or its transferability, may be gauged by its ability to reproduce the results for a given element in a wide range of environ-

ments, *e.g.* a pseudopotential for the carbon atom should give accurate results when used in diamond, graphene or graphite. Although ultrasoft pseudopotentials reduce the basis-set size further and achieve convergence faster, they are less transferable compared to the KB pseudopotentials. In the work of Ref. [82] the equilibrium lattice constant, bulk modulus and cohesive energy for face centred cubic (fcc) Cu and diamond has been calculated using norm-conserving and ultrasoft pseudopotentials. They found the cohesive energy for fcc Cu and diamond changes by approximately 0.1 eV. More detail about the theory and applications of pseudopotentials can be also found in Refs. [31, 83].

#### 2.3.2.5 Basis Set

In an attempt to solve Kohn-Sham equations with pseudopotentials for a crystalline material, it is necessary to choose a basis set in which to express the electron wavefunctions. There are basically three different choices to express the wavefunction.

1) Express $\phi$ as a linear combination of plane waves (LCPWs).

2) Express $\phi$ as a linear combination of atomic orbitals (LCAOs).

3) Express $\phi$ as a linear combination of some plane waves and some atomic orbitals.

Due to the simplicity and appropriateness in modern electronic structure calculations, one of the most used choices is the plane-wave basis set [31]. In such a basis we express the single-particle wave function $\Psi_k(\mathbf{r})$ at a point **r** in a crystal as follows

$$\Psi_j(\mathbf{k},\mathbf{r}) = \frac{1}{\sqrt{N_0\Omega}} \sum_G A_j(\mathbf{k}+\mathbf{G}) e^{i(\mathbf{k}+\mathbf{G})\cdot\mathbf{r}}, \tag{2.62}$$

where $N_0$ is the number of unit cells, $\Omega$ is the volume of the chosen unit cell, **k** is the electronic wave vector lying within the first Brillouin zone, **j** denotes the band index, **G** is a reciprocal lattice vector, and $A_j(\mathbf{k}+\mathbf{G})$ are the Fourier coefficients.

## 2.4 Momentum Space Formalism of Kohn-Sham Equation

Using pseudopotential approach within plane-wave basis, the Kohn-Sham equation Eq. 2.57 for a crystal can be expressed in momentum space as follows

$$\sum_{\mathbf{G}'} H_{\mathbf{G},\mathbf{G}'}(\mathbf{k}) A_j(\mathbf{k}+\mathbf{G}') = \varepsilon_j(\mathbf{k}) A_j(\mathbf{k}+\mathbf{G}) \tag{2.63}$$

with

$$H_{\mathbf{G},\mathbf{G}'}(\mathbf{k}) = \frac{\hbar^2}{2m}|\mathbf{k}+\mathbf{G}|^2 \delta_{\mathbf{G},\mathbf{G}'} + V_{\mathrm{ps}}(\mathbf{k}+\mathbf{G}, \mathbf{k}+\mathbf{G}'). \tag{2.64}$$

In the above equation $V_{\mathrm{ps}}$ is the screened pseudopotential. In general it is a non-local potential and a Fourier component of this potential can be expressed as

$$\begin{aligned} V_{\mathrm{ps}}(\mathbf{k}+\mathbf{G}, \mathbf{k}+\mathbf{G}') &= V_{\mathrm{ps}}(\mathbf{k}+\mathbf{G}, \mathbf{k}+\mathbf{G}') + V_{\mathrm{H}}(\mathbf{G}-\mathbf{G}') + V_{\mathrm{xc}}(\mathbf{G}-\mathbf{G}') \\ &= V^{ps}_{ionic}(\mathbf{k}+\mathbf{G}, \mathbf{k}+\mathbf{G}') + V_{screen}(\mathbf{G}-\mathbf{G}'), \end{aligned}$$

where $V_{\mathrm{ps}}$ is the Fourier component of the non-local ionic (i.e. unscreened) crystal pseudopotential, and $V_{\mathrm{H}}(\mathbf{G})$ and $V_{\mathrm{xc}}(\mathbf{G})$ are (local) Fourier components of the Hartree and exchange correlation potentials, respectively. Clearly, in order to calculate various properties of solids we would need to use the non-local, ionic crystal pseudopotential matrix elements $V_{\mathrm{ps}}(\mathbf{G}'-\mathbf{G})$ with respect to the plane-wave basis.

### 2.4.1 Energy Cut-off

In section 2.3.2.5, the KS wave function was expressed in terms of a plane-wave basis set. In order to get more accurate results, an infinite number of plane waves is required which means there is an infinite number of reciprocal lattice vectors G. Therefore, the number of plane waves is considered by imposing an upper cut-off to the kinetic energy defined as

$$\frac{\hbar^2}{2m}|\mathbf{k}+\mathbf{G}|^2 < E_{cut}. \tag{2.65}$$

The plane wave expansion can be truncated to contain the plane waves that consist of the kinetic energy less than the energy cut-off. However the truncation of the plane wave expansion at a small energy cut-off $E_{cut}$ will lead to an error when computing the total energies of system. This error can be decreased with increasing the cut-off energy. In this thesis, different cut-off energies have been tested by calculating total energy of graphene based systems. The cut-off energies of 45 Ryd, 40 Ryd, and 20 Ryd are found to be suitable for Chapters 3 and 5, Chapter 4, and Chapter 6, respectively. In Chapter 3, an example of the convergence of total energy versus cut-off energy calculation will be represented in detail for graphene.

### 2.4.2 k points for Brillouin Zone Summation

Evaluation of many quantities in solids, such as energy and density require integrating periodic functions of a Bloch wave vector over an entire BZ. Several numerical techniques have been adopted for BZ integration such as Baldereschi [84], Chadi and Cohen [85], Cunningham [86], and Monkhorst and Pack [87]. They have presented schemes for generating special **k**-points in the IBZ which would give an excellent approximation to the zone average of an arbitray periodic function. A good description of special k-points for crystals of different symmetries and their use in the calculation of electronic structure and physical properties of solids is presented by Evarestov and Smirnov [88]. All calculations within the present thesis were carried out using the Monkhorst and Pack method. Monkhorst and Pack considered the special points in the form:

$$\mathbf{k}_p = u_{p1}\mathbf{b}_1 + u_{p2}\mathbf{b}_2 + u_{p3}\mathbf{b}_3 + \mathbf{k}_0, \tag{2.66}$$

where $\mathbf{b}_i$ are the reciprocal translational vectors and $\mathbf{k}_0$ is an arbitrary vector. For the cubic system, the coefficients $u_{pi}$ will be determined as follows:

$$u_{pi} = \frac{2p_i - q - 1}{2q}, \tag{2.67}$$

where $p_i$=1, 2, 3,..., q and $i$=1, 2, 3. The integer $q$ evaluates the number of special points in the set. For the hexagonal system, the coefficients $u_{pi}$ with $i$=1, 2 are given as:

$$u_{pi} = \frac{p_i - 1}{q}, \tag{2.68}$$

and $u_{pi}$ for $i$=3 is given as:

$$u_{pi} = \frac{2p_i - q - 1}{2q}, \tag{2.69}$$

where $p_i$=1,2,3,...,q. At this particular stage, another important quantity must be defined. For each special **k** point, there is a factor associated with it which is known as the weight factor. This factor satisfies the following:

$$\overline{f} = \sum_{i=1}^{N} w_i f(\mathbf{k}_i) + remainder, \tag{2.70}$$

where $\overline{f}$ is the average of a periodic function $f(\mathbf{k})$ and $w_i$ is the weight factor ($\sum w_i = 1$). The sum runs over all $N$ chosen **k** points. Computational experiments show that the smaller the $'remainder'$ term, the better the numerical integration technique.

In this thesis, $n \times n \times 1$ or $n \times n \times 2$ Monkhorst–Pack sampling of the BZ is used for graphene based systems. For smaller $n$, however, the total energy varies considerably as $n$ is changed which is a clear indication that the $n$ is insufficient to give a well-converged result. Therefore, the convergence of total energy with respect to $n$ will be obtained for each systems and an example of this calculation will be given in Chapter 3 for graphene.

### 2.4.3 Self Consistency

Considering the trial plane-wave function in Eq. 2.62 and using the pseudoptential approach described in section 2.3.2 we can now begin to solve the KS equation. Although the solutions of KS equations provide the ground state charge density, they can not be taken as the desired results because one can obtain a

more reliable and stable result by using the charge density which is achieved by iterating the solutions of KS equations. This method is called self-consistent field (SCF) approach. The iterative way is outlined in the following algorithm:

(i) Define an initial, trial electron density, $n(\mathbf{r})$.

(ii) Solve the Kohn Sham equations defined using the trial electron density to find the single-particle wave functions, $\phi(\mathbf{r})$.

(iii) Calculate the electron density defined by the Kohn Sham single-particle wave functions from step 2, $n_{KS}(\mathbf{r})$.

(iv) Compare the calculated electron density, $n_{KS}(\mathbf{r})$, with the electron density used in solving the Kohn Sham equations, $n(\mathbf{r})$. If the two densities are the same, then this is the ground-state electron density, and it can be used to compute the total energy. If the two densities are different, then the trial electron density must be updated in some way. Once this is done, the process begins again from step 2. However, this procedure does not usually converge. Because of the long-range nature of the Coulomb interaction, a small change in the input density can lead to a relatively large change in the output density. Therefore, a new charge density needs to be mixed with the input and output density in an appropriate manner to obtain a more stable charge density. There are two main categories of mixing schemes: linear and non-linear schemes. A very good review of these schemes can be found in Ref. [83]. In our calculations we use the Broyden's Jacobian update scheme: one of the most appealing non-linear mixing approaches for self consistent field convergence acceleration. This scheme has been discussed by several groups such as Bendt and Zunger [89], Srivastava [90], Singh *et. al.* [91], and Eyert [92]. In our computational code the method presented by Srivastava [90] is used.

## 2.5 Total Energy and Hellmann-Feynman Forces

Once the solution of KS equations is achieved self-consistently by using the plane-wave pseudopotential scheme, the total energy of the system and Hellmann-Feynman forces [93] on atoms can be evaluated. The total energy of system can be expressed in momentum space as

$$\begin{aligned} E_{tot} &= E_{ion-ion} + E_{ele} \\ &= \frac{e^2}{8\pi\epsilon_0}\sum_{\mathbf{p},b,b'}\frac{Z_b Z_{b'}}{|\mathbf{p}+\tau_b-\tau_{b'}|} \\ &\quad +\frac{\hbar^2}{2m}\sum_{k}^{sp}\sum_{j}^{occ} w(\mathbf{k},j)\sum_{\mathbf{G}}|A_j(\mathbf{k}+\mathbf{G})|^2|\mathbf{k}+\mathbf{G}|^2 \\ &\quad +\frac{1}{M}\sum_{k}^{sp}\sum_{j}^{occ} w(\mathbf{k},j)\sum_{\mathbf{G},\mathbf{G}'}\sum_{b} A_j^*(\mathbf{k}+\mathbf{G}')A_j(\mathbf{k}+\mathbf{G}) \\ &\quad \times\exp[i(\mathbf{G}-\mathbf{G}'.\tau_b)]\sum_{l} v_{b,l}(\mathbf{k}+\mathbf{G},\mathbf{k}+\mathbf{G}') \\ &\quad +\frac{e^2}{8\pi\epsilon_0}\sum_{\mathbf{G}}\frac{|\rho(\mathbf{G})|^2}{|\mathbf{G}|^2}+\sum_{\mathbf{G}}\rho^*(\mathbf{G})\epsilon_{xc}(\mathbf{G}), \end{aligned} \tag{2.71}$$

where $v_b$ is the pseudopotential due to the $b^{th}$ atom at site $\tau_b$ in the unit cell and $\rho(\mathbf{G})$ is the Fourier coefficient of the valence charge density which can be evaluated by using a special $\mathbf{k}$-points scheme

$$\rho(\mathbf{G}) = \sum_{\mathbf{k}}^{sp}\sum_{j}^{occ} w(\mathbf{k},j)\rho_{\mathbf{k}j}(\mathbf{G}). \tag{2.72}$$

Equation 2.71 can be rewritten:

$$E_{tot} = \sum_{\mathbf{k}}^{sp}\sum_{j}^{occ}\epsilon_j - E'_H + \Delta E_{xc} + \gamma_E + E_0, \tag{2.73}$$

where

$$\begin{aligned} E'_H &= \frac{e^2}{8\pi\epsilon_0}\sum_{\mathbf{G}\neq\mathbf{0}}|\rho(\mathbf{G})|^2 \\ \Delta E_{xc} &= \frac{1}{4\pi\epsilon_0}\sum_{\mathbf{G}}\rho^*(\mathbf{G})[\epsilon_{xc}(\mathbf{G})-V_{xc}(\mathbf{G})] \\ \gamma_E &= E_{ion-ion} - \frac{1}{8\pi\epsilon_0}\frac{1}{\Omega_{at}}\sum_{b}\int d\mathbf{r}\,\frac{Z_b^2 e^2}{r} \end{aligned}$$

$$E_0 = \frac{1}{M}\frac{1}{\Omega_{at}}\sum_b Z_b e \sum_b \int d\mathbf{r}\ (v_b(\mathbf{r}) + \frac{1}{4\pi\epsilon_0}\frac{Z_b e^2}{r}). \quad (2.74)$$

In the above the Ewald energy $\gamma_E$ is obtained by removing the divergence from the ion-ion Coulomb interaction energy $E_{ion-ion}$ and adding it to have the finite term $E_0$.

The derivative of the total energy with respect to the space element gives force acting on a system. Therefore, the Hellmann-Feynman force ($F_b = F_b^{ele} + F_b^{ion}$) acting on the $b^{th}$ atom in the unit cell is simply obtained by differentiating the total energy (Eq. 2.71) with respect to $\tau_b$

$$F_b = -\frac{\partial E_{tot}}{\partial \tau_b}. \quad (2.75)$$

The electronic part of the Hellmann-Feynman force can be expressed as:

$$F_b^{ele} = -\frac{1}{4\pi\epsilon_0}\mathrm{Re}\Bigg\{\frac{i}{M}\sum_k^{sp}\sum_j^{occ} w(\mathbf{k},j)\sum_{\mathbf{G},\mathbf{G}'} A_j^*(\mathbf{k}+\mathbf{G}')A_j(\mathbf{k}+\mathbf{G}) + (\mathbf{G}-\mathbf{G}')\exp[i(\mathbf{G}-\mathbf{G}')\cdot\tau_\mathbf{b}]\sum_l v_{b,l}(\mathbf{k}+\mathbf{G},\mathbf{k}+\mathbf{G}')\Bigg\}, \quad (2.76)$$

whereas the ionic part is obtained as:

$$F_b^{ion} = \frac{e^2 Z_b}{4\pi\epsilon_0}\sum_{b'\neq b} Z_{b'}\Bigg\{\frac{4\pi}{\Omega}\sum_{\mathbf{G}}{}' \left[\frac{\mathbf{G}}{|\mathbf{G}|^2}\sin[\mathbf{G}\cdot(\tau_b-\tau_{b'})]\exp(-\frac{|\mathbf{G}|^2}{4\eta^2})\right] + \sum_{\mathbf{p}}\left[\frac{\mathbf{x}\ \mathrm{erfc}(\eta x)}{x^2} + \frac{2\eta\mathbf{x}}{\sqrt{\pi}x^2}\exp(-|\eta|x^2)\right]_{\mathbf{x}=\mathbf{p}-\tau_b-\tau_{b'}}\Bigg\}, \quad (2.77)$$

where $\eta$ is a control parameter which yields the convergence of the summations.

## 2.6 Geometry Optimisation Scheme

We have so far only described DFT calculations in which the position of every atom in the supercell is fixed. This is fine for a regular periodic structure where each atom has the same surroundings and thus there is no force. However, a slight departure from the regularity in atomic positions would lead to

finite forces on atoms within each unit cell. Due to these forces, the geometry of the unit cell needs to be optimised, as all atoms in the supercell would like to settle down to zero force configuration, inducing to a configuration with a minimum in total energy. This optimisation can be done by using total energy and Hellmann-Feynman forces techniques. There are two main iterative adjustments to determine the optimised geometry of any studied system. In the first iterative adjustment, the KS equations are solved to achieve a reasonably good level of self-consistency through adjustment of charge density. In the second iterative adjustment, the optimised geometry is determined by altering the atomic positions in response to the resulting force. These iterations are repeated until the fully relaxed atomic geometry is obtained. The geometry optimisation procedure is shown in Fig. 2.1. Although there are different approaches to geometry optimisation, Bendt-Zunger's conjugate gradient scheme [94] and Car-Parrinello's molecular dynamics approach [95, 96] are the most extensively.

## 2.7 Our Computational Code

Our calculations have been done using a sophisticated LDA computer code which was originated by Prof. G. P. Srivastava, has undergone over fifteen years of development and is continually being refined to extend its accuracy and range of applicability. Essentially, this code performs the hugely successful density functional theory (DFT) of Kohn-Sham. The code has been used to successfully predict properties of various materials such as the energies, forces, band structures, densities of states, and charge densities. In order to compute these properties, the code solves the Kohn-Sham equation self-consistently using plane-waves and Kleinman-Bylander pseudopotential as explained in detail previously [30]. Self-consistency simply means that the charge density generated by an external potential is the same as the charge density that generated that potential, to within

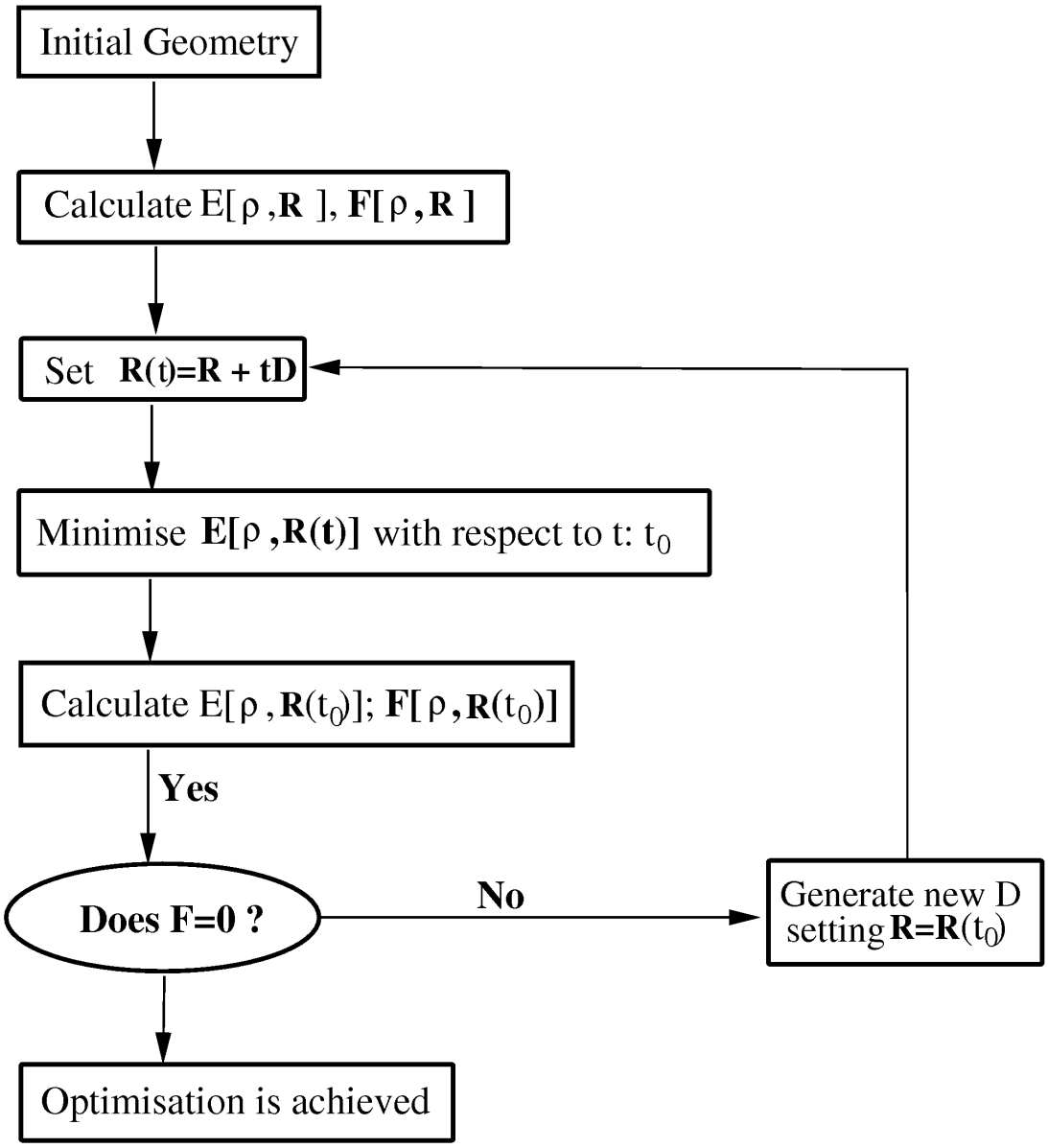


Figure 2.1: Flow chart explaining the iterations of optimising procedure.

some tolerance.

Our method uses the KB pseudopotentials and a model for the crystal structure as the starting point of the calculation. After the wave functions have been obtained the contribution of the valence electrons to the potential is calculated. It is then used to evaluate the total one-electron potential, which is compared with the starting potential. Self-consistency is achieved when the calculated one-electron potential agrees with the sarting potential.

After the solutions of the Kohn-Sham equation are obtained for a given ionic configuration self-consistently, the forces on the ions are calculated using the Hellmann-Feynman theorem. Using these forces as a guide the code then performs geometry optimisation which was described in section 2.6. In the optimisation, atoms are allowed to move until the residual forces between any atoms are smaller than the convergence in eV/Å. In this thesis, relaxed atomic positions for all systems are obtained within a force convergence criterion of 50 meV/Å.

For graphene related systems, the interaction between layers and substrates is expected to be better described by the van der Waals (vdW) interaction. This interaction is weak compared with the covalent interaction and relatively long ranged. Due to the complexity of the vdW interaction, its quantum nature, and its nonlocal characteristics, it remains a real challenge to determine such interaction in the DFT. Therefore, various techniques have been proposed to overcome this problem, but there is no real satisfactory solution until now. For instance, the parametrised form proposed by Grimme [97], with further improvement by Scheffler et al. [98, 99], has been employed by several groups. Dion et al. [100], on the other hand, proposed a new approach to accurately describe the vdW forces within the density functional theory (vdW-DFT). In this scheme, the non-local (long ranged) interactions have been expressed in terms of a density-density interaction formula, with further development of the formulation presented in Ref. [101]. The vdW-DFT scheme has been applied to graphite and a large number of

graphene/metal systems [102, 103, 104, 105]. However, systematic improvement of results from the vdW-DFT theory has not yet been evidenced for all systems. For example, agreement between theory and experiment for interlayer spacing in graphite is less favourable from the vdW-DFT theory than from the LDA-DFT theory [105]. For graphene/metal systems that LDA finds to be weakly bonded, both LDA-DFT and vdW-DFT methods are reported to result in very similar interlayer spacings and band structures, despite the LDA-DFT calculations underestimating the adhesion energy [106, 107]. On the other hand, some previous studies have advocated the suitability of DFT-LDA approach to describe the energetic and structural properties of graphitic systems where the long range interactions are ruled by $\pi - \pi$ stacking interactions [60, 108]. Thus, with the above considerations in mind we have performed calculations using the LDA-DFT scheme in our computational code.

## 2.8 Scanning Tunnelling Microscopy

The scanning tunnelling microscope (STM) was invented by Binnig and Rohrer in 1982 [109]. This technique was the first to generate real-space images of surface with atomic resolution. This is achieved by exploiting the quantum-mechanical electron tunnelling effect of electrons between two states. For STM, electrons tunnel between states on two separate surfaces between which a potential difference is applied - one of these surfaces is the STM tip and the other is the sample under investigation. The tip is rastered across an area of the surface whilst the tunnelling current is measured to produce a topographic image. For images of sample surfaces, the STM oparetes in two regimes: constant height and constant current. In the constant height mode, the tip's vertical height above the surface is kept fixed, and the tip is then rastered across the surface, measuring the current due to the electron density. In the constant current regime, the STM is pro-

grammed to adjust the vertical height of the tip such that it registers a selected current. The tip is slowly rastered across the surface, always allowing the tip to move vertically to the correct height. This type of method yields excellent structural information, with an excellent profile of the surface and information about the bonding between atoms. In our simulated STM images, the constant-height mode and Tersoff and Hamann theory are considered.

In 1983, Tersoff and Hamann developed a theory of STM which is still widely used in models for the STM [110, 111]. The Tersoff-Hamann model is shown in Figure 2.2. This model defines an STM tip centred on $r_0$ with a radius of curvature of $R$ and at a distance $d$ above the surface. The full expression of the tunnelling current is given as:

$$I = \frac{2\pi e}{\hbar} \sum_{\mu,v} f(E_\mu)[1 - f(E_v + eV)]|M_{\mu,v}|^2 \delta(E_\mu - E_v), \tag{2.78}$$

where $f(E)$ is the Fermi function, $V$ is the bias voltage, $|M_{\mu,v}|$ is the tunnelling matrix element between the probe $\varphi_\mu$ and surface $\varphi_v$ states, and $E_\mu$ and $E_v$ are the energy levels of the probe and surface states in the isolated systems, respectively. At low temperature, the above expression (Eq. 2.78) can be rewritten as:

$$I = \frac{2\pi}{\hbar} e^2 V \sum_{\mu,v} |M_{\mu,v}|^2 \delta(E_v - E_F)\delta(E_\mu - E_F), \tag{2.79}$$

where the Fermi level $E_F$ is adjusted by the voltage bias $V$. When the tip wave functions are localised, then the matrix element is proportional to the local density of states (LDOS, the amplitude of $\varphi_v$) at the Fermi level. Therefore, Eq. 2.79 can be expressed as:

$$I = 32\pi^3 \hbar^{-1} e^2 V \phi^2 D_t(E_F) R^2 \kappa^{-4} e^{2\kappa R} \times \sum_v |\varphi_v(\mathbf{r}_0)|^2 \delta(E_v - E_F), \tag{2.80}$$

where $D_t$ is the density of states per unit volume of the probe tip, $R$ is the radius of the tip atom, $\mathbf{r}_0$ is the tip atom centre, and $\kappa = \hbar^{-1}(2m\phi)^{1/2}$ represents the minimum inverse decay length for the wave function in vacuum, expressed in

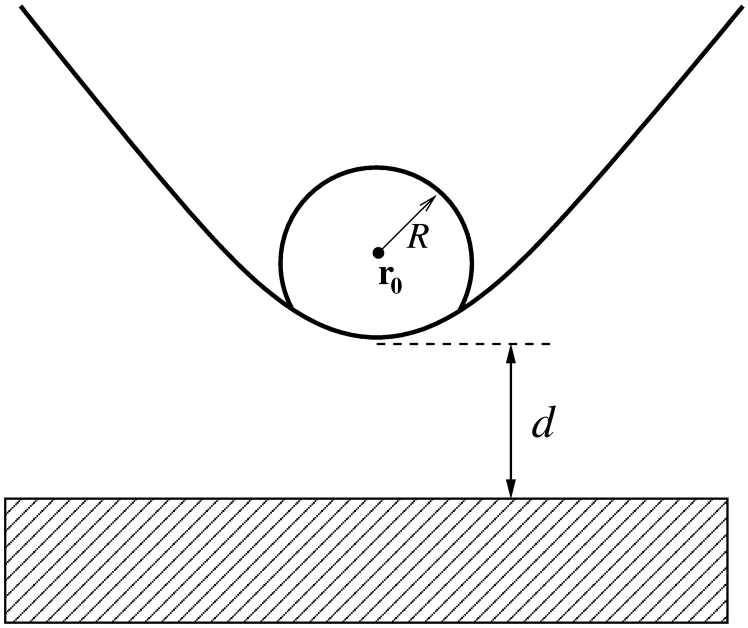


Figure 2.2: The Tersoff-Hamann model of STM, where the tip is modelled as a locally spherical potential well with radius of curvature $R$ and at a distance $d$ above the surface.

terms of $\phi$, the work function between tip and sample's surface. This equation can be rewritten as:

$$I \propto \sum_v \rho_v \delta(E_v - E_F), \tag{2.81}$$

or

$$I \propto LDOS. \tag{2.82}$$

## 2.9 Summary

In this Chapter, the theoretical background for the methods used in this research is presented. Mainly, the density functional theory (DFT) and its essential ingredients are outlined. Furthermore, the self-consistent solution of Kohn-Sham (KS) equations, the total energy, the Hellmann-Feynman forces acting on atoms, and the geometry optimisation scheme within the planewave pseudopotential

framework are explained. Lastly, the theory of STM which gives very detailed information about geometrical structures and electronic states of surfaces is described.

# Chapter 3

# Electronic Properties and Interband Optical Transitions of Multilayer Graphene and Graphite

## 3.1 Introduction

One of the most remarkable properties of monolayer graphene (MLG) is its linear dispersion of the electron and hole states close to the **K** point (the so-called Dirac point) of its Brillouin zone, originating from $\pi$ and $\pi^*$ bondings between the two carbon basis atoms within the hexagonal primitive unit cell. This results in the valence electrons behaving as massless Dirac particles with very large Fermi velocity [112].

More recently, the attention has been given to electronic properties of graphene multilayers such as bilayer and trilayer [113]. The AB-stacked bilayer graphene (BLG) and ABA-stacked trilayer graphene (TLG) show some unusual electronic properties which are quite different from those of MLG. In the BLG, there is no band gap between its conduction and valence bands but they show quadratic and linear behaviour at the **K** point. In the TLG, there is more complex interlayer

interactions that supply a richer electronic structure than those for MLG and TLG systems.

As we have described in section 1.1.1, graphite can be obtained by simply stacking graphene layers in a periodic manner. The electronic properties of graphite have been studied extensively for a long time. The first theoretical study was done by Wallace in 1947 [114]. After a few years, the Slonczewski-Weiss-McClure (SWM) model was introduced to describe the band structure of graphite [115, 116], but, the assignment of the electron and hole states within this model was opposite to what is agreed today. In 1968, Schroeder et al. established the currently accepted locations of electron and hole pockets [117]. Furthermore, the SWM model was not able to describe the van der Waals interactions between graphene sheets. Thus, recently, this model has been revisited by Rydberg *et al.* [118]. They recommended the replacement of GGA as a standard method in total-energy calculations with vdW-DF for descriptions of layered systems.

Predictions of observable properties by density-functional theory calculations are used increasingly often in experimental condensed-matter physics and materials engineering as reliable data. In condensed-matter physics, the DFT is not only used to understand the observed behavior of solids, but increasingly more to predict characteristics of compounds that have not yet been determined experimentally. In both cases DFT results provide a point of reference, either to analyze data from measurements or to plan future experiments. Increasingly more experimental scientists in these fields therefore face the natural question: what is the expected error for DFT predictions? Information and experience about this question is scattered over two decades of literature but in DFT applications this is much less common practice. The DFT as such is an exact reformulation of quantum physics. From a purely theoretical point of view, it should lead to exact predictions, with no need for an error estimate. It is therefore essential to have a quantitative idea of the expected deviation between a DFT prediction of a cer-

tain property and the corresponding experimental value. This leads to a practical protocol that allows any scientist - experimental or theoretical - to determine justifiable error estimates for many basic property predictions, without having to perform additional DFT calculations. For several properties of each crystal, the difference between DFT results and experimental values is assessed [119, 120].
The atomic and electronic structures of monolayer, bilayer, trilayer graphene and graphite are studied extensively using our computational code as explained in Chapter 2. From these theoretical studies, electron effective masses and velocities have been estimated. These results are compared with experimental data recently measured for one to four monolayers of graphene by using angle-resolved photoemission spectroscopy (ARPES) [121]. While the experimental interband optical transition values are available for monolayer graphene [122] there is no experimental study focussing on these values for other multilayer graphene systems. Therefore, for the first time in literature, the interband optical transitions have been investigated theoretically for bilayer, trilayer graphene and graphite systems in this Chapter.
In this Chapter, I will also present an estimate of *computational errors* in the DFT with local density approximation for multilayer graphene systems. Here the errors mean benchmark studies, examining different parameters used to obtained presented results for the multilayer graphene systems. These studies were already done during my PhD research and an example of these calculations is presented in this Chapter.

## 3.2 Results and Discussion

Before presenting any results, it is important to ensure that the system is in equilibrium. One way to do this is to minimise the energy and calculate the equilibrium parameters of the system that corresponds to the minimum energy. There-

fore, the convergence of the system is checked by calculating total energy versus kinetic energy cut-off and total energy versus the size of the Monkhorst-Pack **k**-points set.

Figure 3.1 shows computed total energy of graphene with respect to the convergence of cut-off energy. Higher cut-off energies give marginally lower energies with 65 Ryd giving lower energies than 45 Ryd. However the differences become very small (less than $3.8\times10^{-3}$ Ryd) and do not effect the accuracy of the results. Therefore, I choose 45 Ryd cut-off energy to reduce computational cost.

The convergence of the computed total energy of graphene as a function of the parameter $n$ in the choices of the Monkhorst-Pack **k**-points set is shown in Fig. 3.2. When $n \geq 24$, the total energy of graphene seems to be (almost) independent of the number of **k** points. More specifically the variation in the energy as $n$ varies in the range of 24≤n≤54 is less than $10^{-4}$ Ryd. For smaller numbers of **k**-points, however, the energy varies considerably as the number of **k**-point is changed. I used a uniform mesh of 36×36×1 of **k**-points for the monolayer graphene since it gives good convergence at a reasonable computational cost. Because of the quasi two-dimensional structure of multilayer graphene, we use the 36×36×2 grid instead of the 36×36×1. We found that the 36×36×2 grid provides a slightly better sampling for calculations of charge density results for multilayer graphene. This grid also results in differences of 2 meV and 3.4 meV in the energy band gap (at **K**) and dispersion (along **K-H**), respectively for ABC-stacked multilayer graphene.

For $E_{cut}$=45 Ryd and the **k**-mesh 36×36×1 the variation of total energy with a few values of the lattice constant $a$ is shown in Fig. 3.3. Following standard practice [65] we fitted the results to the cubic spline curve and thus determined the equilibrium lattice constant at 2.460 Å corresponding to the lowest energy value. To verify that this determined value $a$ is accurate, we made total energy calculations for a large number of $a$ values in the range 2.443 - 2.467 Å. The results are shown

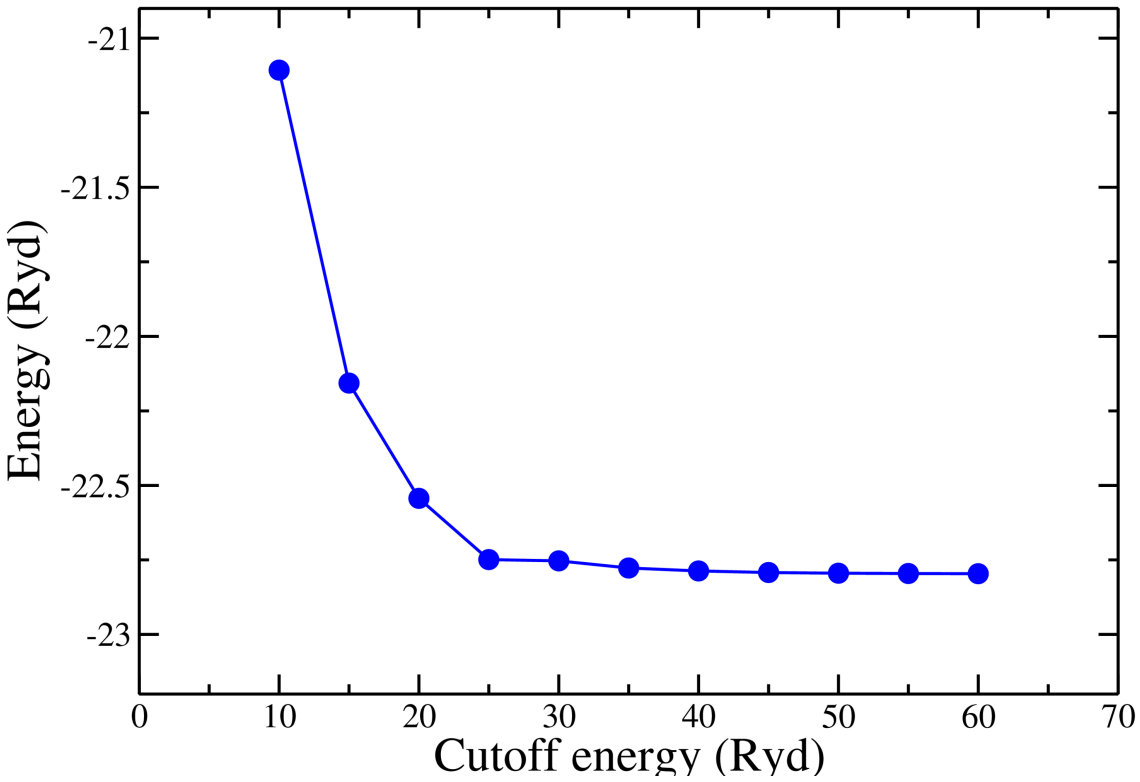


Figure 3.1: Total energy of graphene with a lattice constant of 2.46 Å using 36×36×1 **k**-points as a function of the cut-off energy. Filled symbols represent numerically calculated data points and lines are joining to the data points.

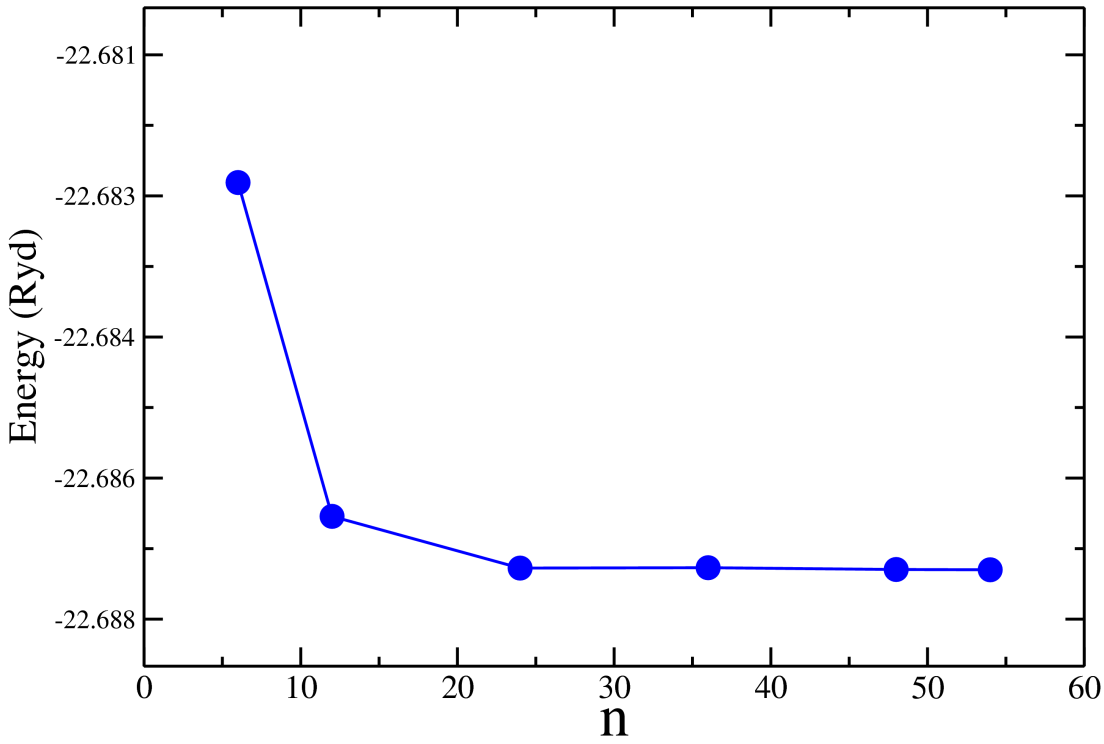


Figure 3.2: Total energies for graphene with a lattice constant of 2.46 Å and $E_{cut}$=45 Ryd as a function of the parameter $n$ in the choices of the Monkhorst-Pack **k**-points set, $n \times n \times 1$. Filled symbols represent numerically calculated data points and lines are joining to the data points.

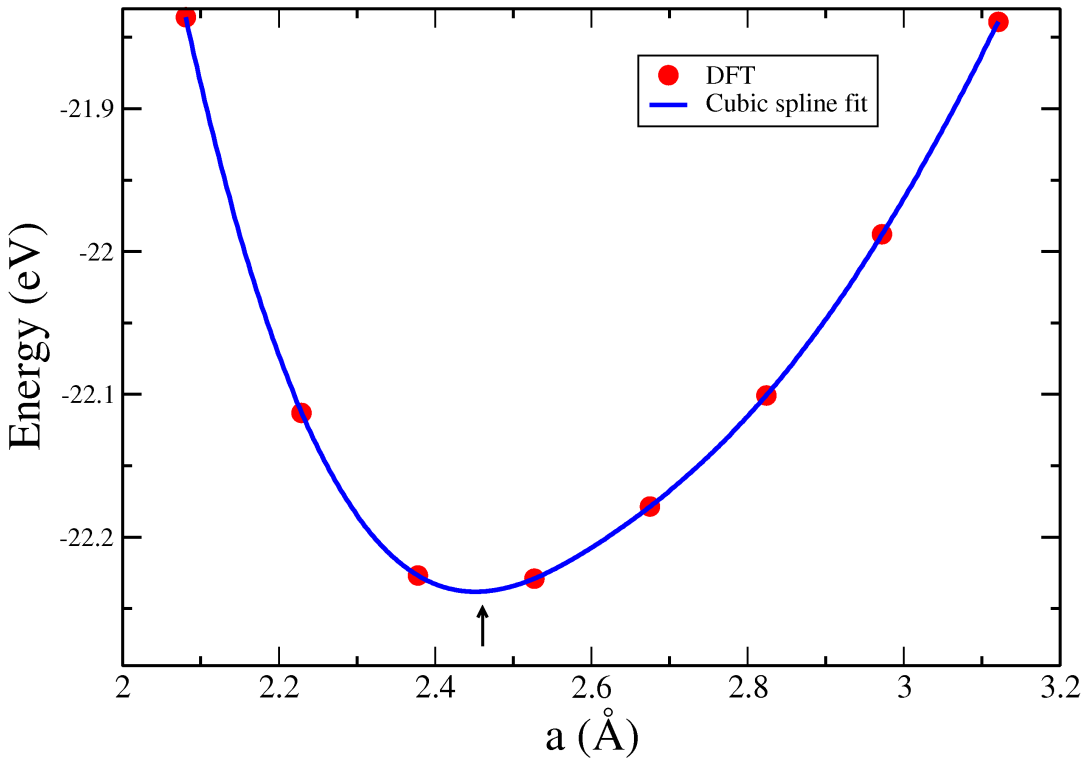


Figure 3.3: Total energy of graphene with $E_{cut}$=45 and 36×36×1 **k**-points as a function of the lattice parameter, $a$. The circle filled symbols show numerically calculated data points, while the curve shows the fits of the DFT data. The arrow indicates the equilibrium value of $a$ corresponding to the minimum of the total energy.

in Fig. 3.4. Within the numerical noise of calculated values we note that energy minimum occurs for $a$=2.458 Å. Thus, we establish that the error margin in our numerical estimate is 0.002 Å. Therefore, we quote our numerical estimate of $a$ as $a$=(2.460$\pm$0.002) Å.

In terms of **k**-integration, insulators and semiconductors are well-behaved in the sense that the density of states goes to zero smoothly before the gap and the integration of a smooth function usually does not cause problems. For metals on the other hand, resolution of functions to be integrated in planewaves can be very hard and the functions need first to be multiplied by a sharp Fermi occupation. In our work eigenvalues at the special **k**-points are thermally smeared by 3 meV for Brillouin zone integration.

### 3.2.1 Graphene

The electron dispersion curves are shown in Fig. 3.5. The $\pi$ and $\pi^*$ bands, formed by the combination of the $p_z$ orbitals of the two basis C atoms per primitive hexagonal unit cell, are degenerate at the **K** point of the Brillouin zone and Fermi level. The dispersion around the **K** point is linear for both electron and hole bands. The error analysis of the band structure of graphene given in Fig. 3.5 (a) very close to **K** point is represented in Figs. 3.6 and 3.7. The results in Fig. 3.6 clearly indicate that almost identical results for the relative positions of $\pi/\pi^*$ bands can be obtained for any values of $E_{cut}$ at 30 Ryd or larger. However, when the small cut-off of 20 Ryd is considered, some small differences in the dispersion of $\pi^*$ is noted. We estimate that the $\pi^*$ band with 20 Ryd cut-off is 0.087 eV higher than the result obtained from 45 Ryd at **k**=**K**+2 $nm^{-1}$. It is however conforting to note that the important physics of the $\pi/\pi^*$ bands close to **K** point can be equally well studied even for $E_{cut}$=20 Ryd. Moreover, there is no significant difference in the calculated energy band when different sets of the Monkhorst-Pack **k**-points are

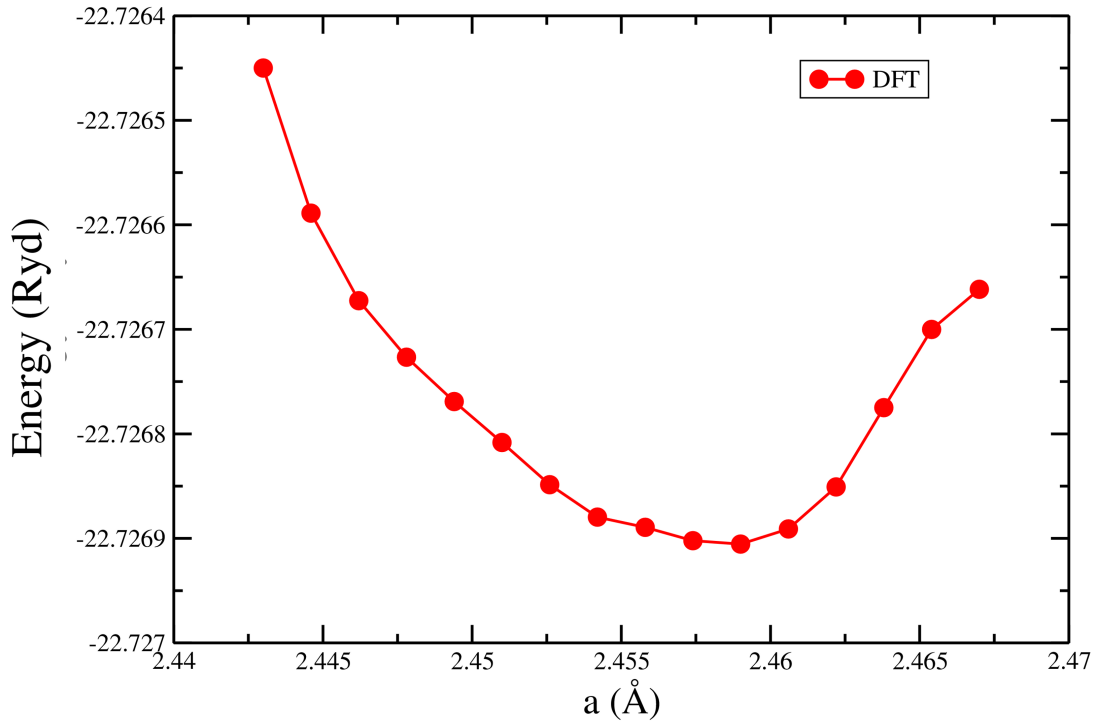


Figure 3.4: Total energy of graphene as a function of the lattice parameter, $a$. The circle filled symbols show numerically calculated data points. Line is joining to the data points.

used, as shown in Fig. 3.7. The linear dispersion for electron band is in good agreement with theoretical results obtained by Latil and Henrard [123] and the ARPES measurements [121] as presented in Fig. 3.5.

In order to estimate the Fermi velocity, I have made a fit of my numerical data using the linear equation

$$E = A_0 k, \tag{3.1}$$

where $k$ is measured from the **K** point using the numerical data for our theoretical lattice constant (a=2.460 Å) in Fig. 3.8 for two different ranges of energy above the Dirac point, explicitly up to 0.441 eV and up to 0.192 eV. Using the XMGRACE plotting software available on our computer system, I estimated $A_0$=0.612 eV nm within the RMS error of 0.5% for the first range and $A_0$=0.566 eV nm within the RMS error of 0.44% for the second range. Note that XMGRACE uses the simple least squares fit procedure to produce RMS errors. Therefore the errors quoted where this procedure has been used neglect any error bars in the original data points. With Eq. 3.1 the Fermi velocity can be found as

$$\begin{aligned} v_F &= \frac{1}{\hbar}\frac{\partial E}{\partial k} \\ &= \frac{A_0}{\hbar}. \end{aligned} \tag{3.2}$$

The numerical estimate for velocity is, thus, $0.93(\pm 0.07)\times 10^6$ m/s. The estimate for velocity, following the above mentioned steps, changes to $0.87(\pm 0.02)\times 10^6$ m/s when we use the slightly different lattice constant of $a$=2.462 Å (0.1% larger). When we use $a$=2.458 Å (0.1% smaller) the same procedure gives me velocity as $0.89(\pm 0.08)\times 10^6$ m/s. Therefore, we estimate that 0.1% error in the lattice constant results in 5% error in the estimate of the velocity. We, thus, notice that an error margin of 7% can occur due to sampling of the numerical data up to different energy range above the Dirac point and only 5% error due to 0.1% error in the lattice constant. Based upon this it is clear that a maximum of 12% error can be expected in our theoretical estimate of velocity. It is interesting to

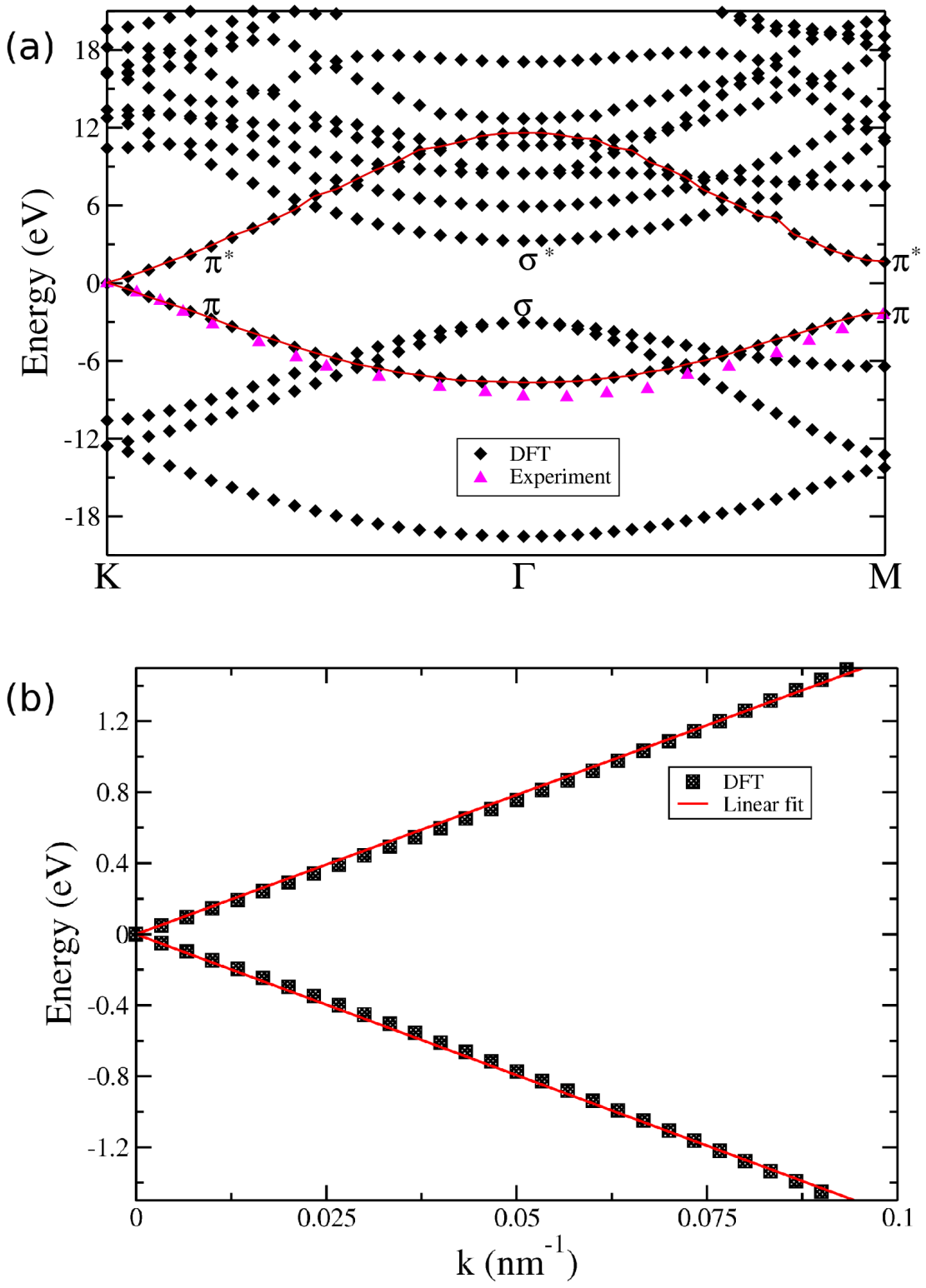


Figure 3.5: (a) The electronic structure of graphene. (b) Dispersion curve for the $\pi/\pi^*$ bands close to the **K** point. The filled symbols show numerically calculated data points and the line shows a linear fit of the DFT data. The filled triangle symbols represent experimental data read from Ref. [121].

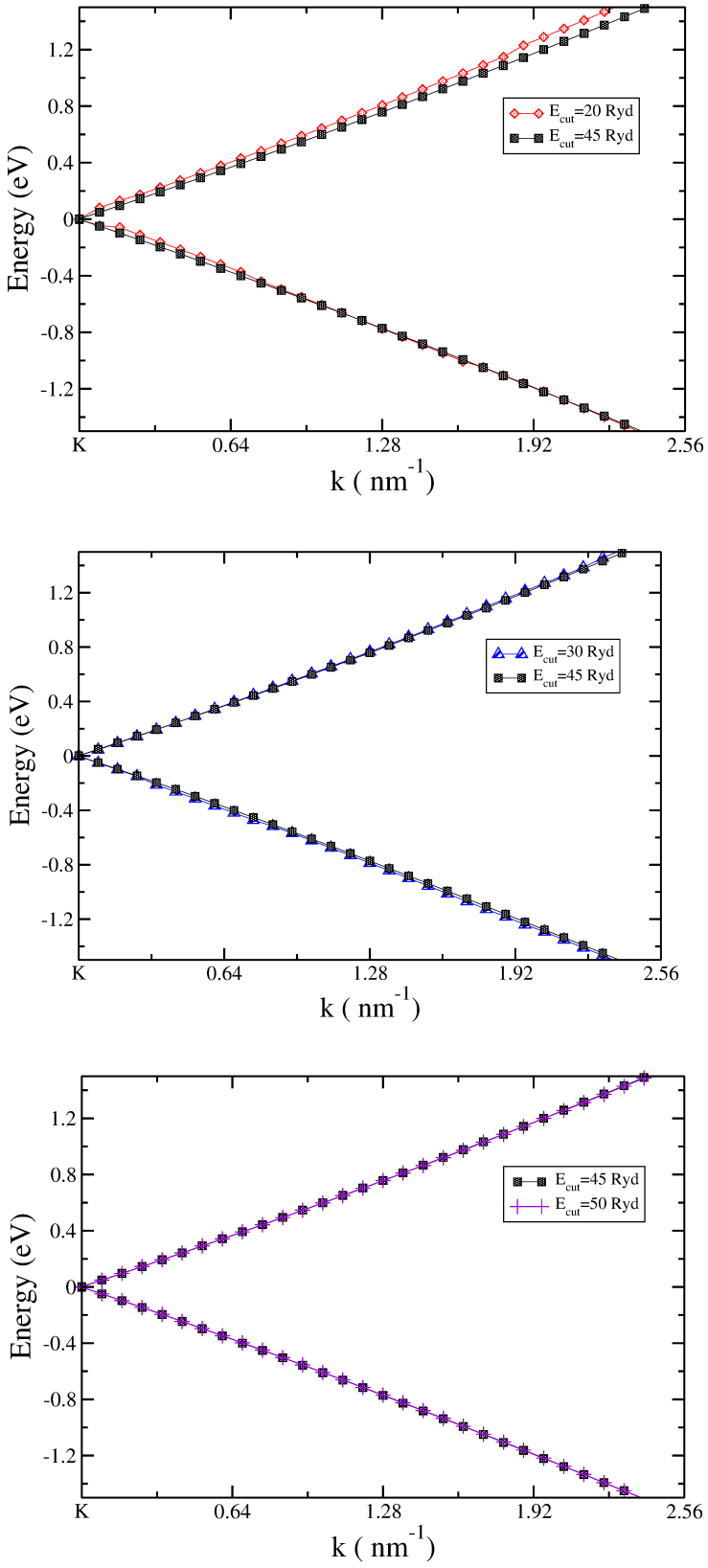


Figure 3.6: Dispersion curve for the $\pi/\pi^*$ bands very close to the **K** point using different cut-off energies. The filled symbols show numerically calculated data points and lines are joining to the data points.

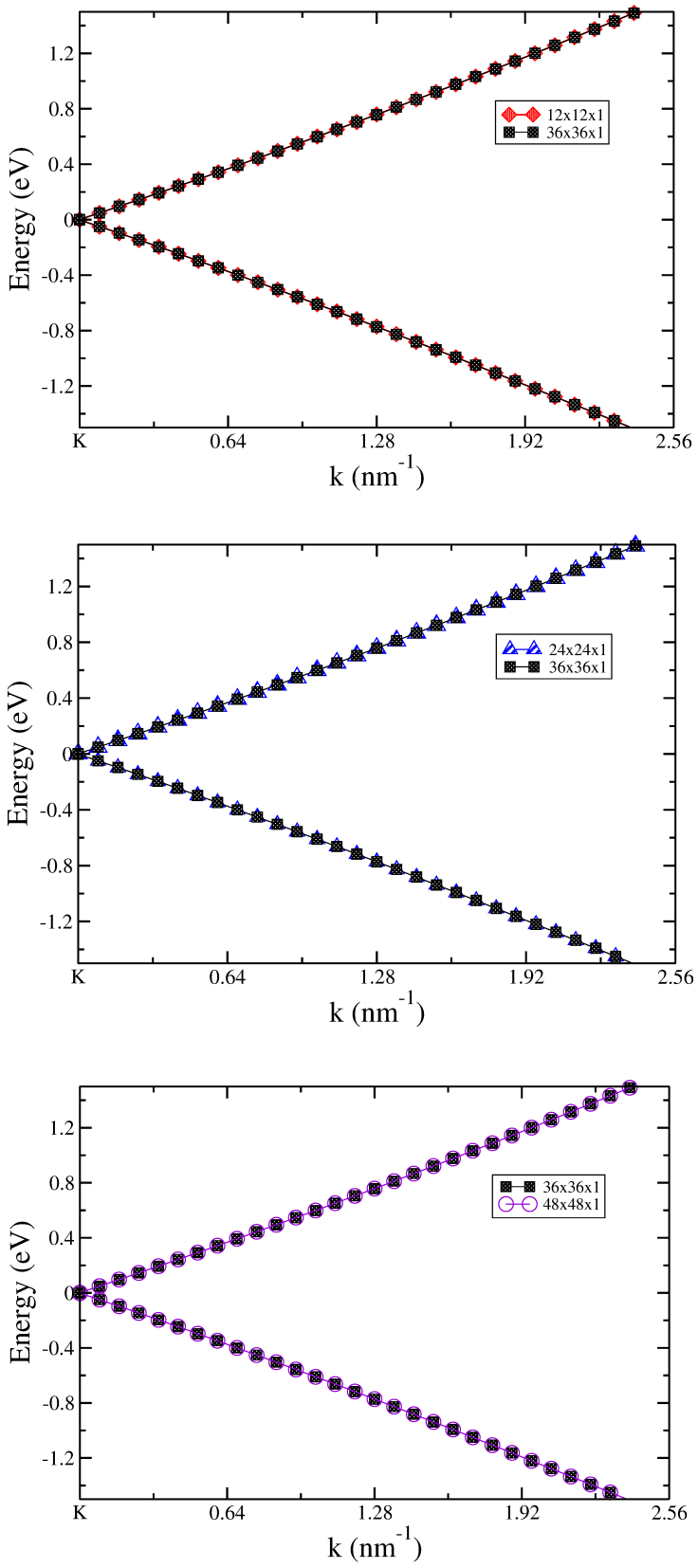


Figure 3.7: Dispersion curve for the $\pi/\pi^*$ bands very close to the **K** point using different the Monkhorst-Pack **k**-points. The filled and unfilled symbols show numerically calculated data points and lines are joining to the data points.

note that there is a 10% spread in reported experimental values of the velocity [14, 112, 124, 125, 126, 127]. Our results compare very well with other LDA works using different computer codes based on similar (plane wave pseudopotential) method [128, 129]. Our results as well as other theoretical results are slightly below the range of experimental values ($1.0\times10^6$ m/s and $1.1\times10^6$ m/s obtained from various different techniques) available [14, 112, 124, 125, 126, 127]. The agreement between theory and experiment has been reported to improve by adapting a theory beyond the DFT [128, 129]. However, that theory is beyond the scope of this thesis.

By changing lattice constant around the theoretical equilibrium lattice constant ($a$=2.460 Å), we find that the zero band gap at the **K** point splits. Figure 3.9 shows under the homogeneous compression of 0.1% ($a$=2.458 Å) and streching of 0.24% ($a$=2.466 Å) band gaps of 24 meV and 38 meV, respectively, are obtained. The band gap opening under homogeneous compression is supported by another theoretical work, using a similar theoretical method, for bilayer graphene [130].

### 3.2.2 Bilayer Graphene

We considered bilayer graphene using the AB stacking model. Following the same procedure in finding the equilibrium lattice constant of graphene in section 3.2.1 we determined the inter-layer distance ($d$) between adjacent layers in BLG as a value of 3.330 Å with our theoretical lattice constant of 2.460 Å for graphene. To verify the accurancy of this determined value, we made total energy calculations for a large number of $d$ values in the range 3.270 - 3.386 Å. As shown in Fig. 3.10, within the numerical noise of calculated values we found that energy minimum occurs for 3.344 Å. Therefore, the error margin in our numerical estimate of inter-layer distance is 0.014 Å. This value is in agreement with several previous ab initio calculations [131, 132].

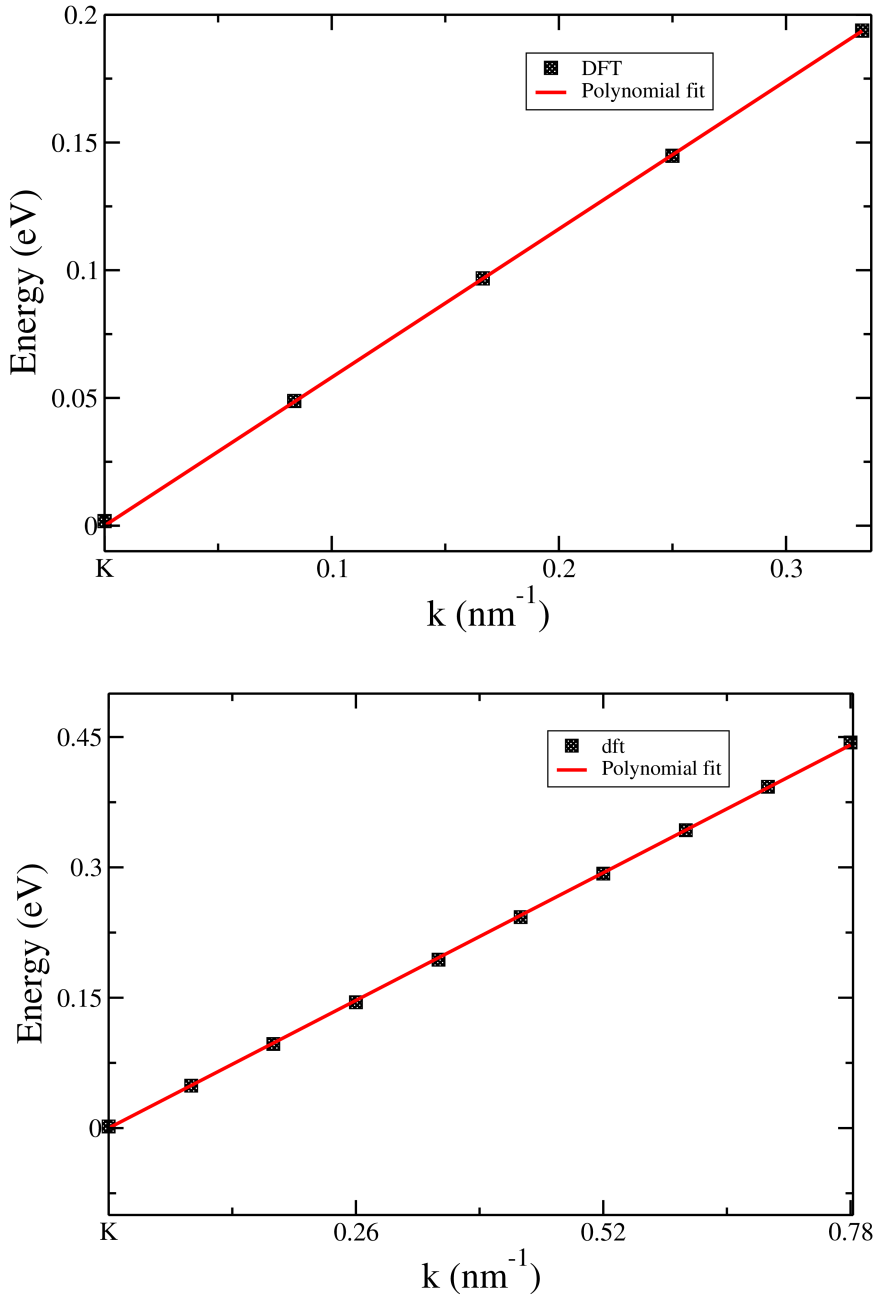


Figure 3.8: The polynomial fit of the $\pi^*$ bands using two ranges of energies (up to 0.192 eV and up to 0.441 eV) above the **K** point for graphene. The symbols show numerically calculated data points and the line shows a linear fit of the DFT data.

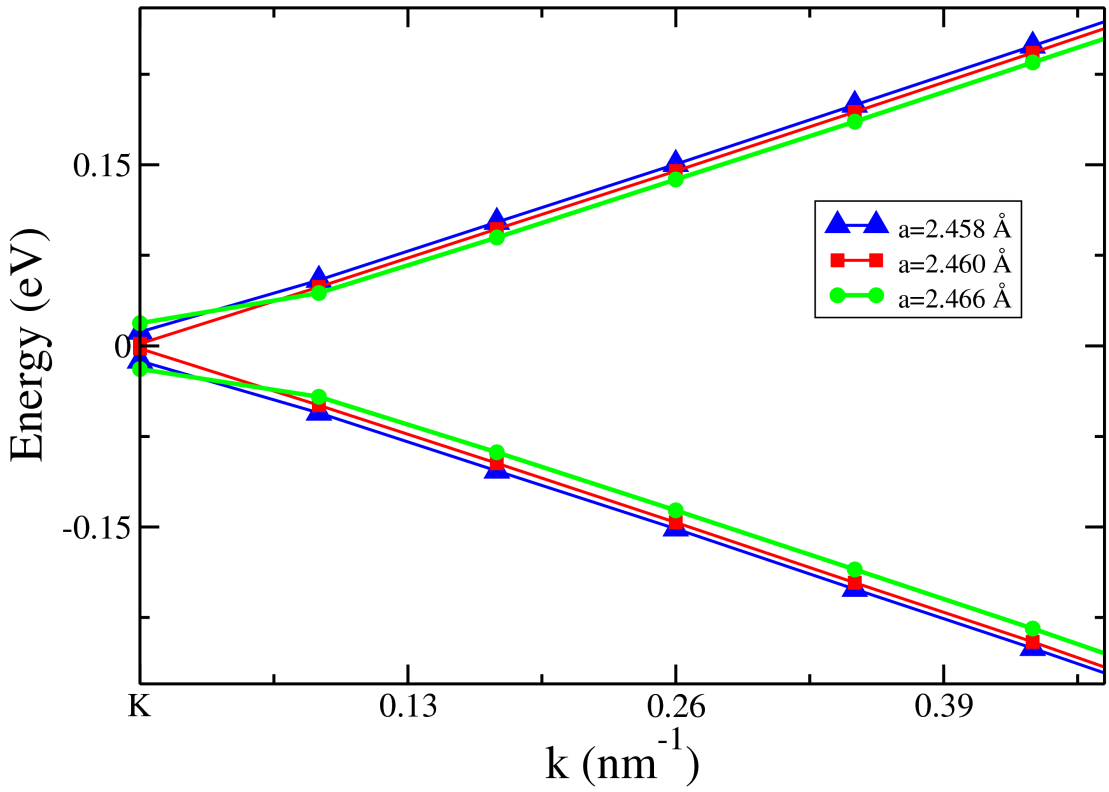


Figure 3.9: Dispersion curve for the $\pi/\pi^*$ bands in graphene very close to the **K** point using using lattice constants of $a$=2.458 Å, $a$=2.460 Å and $a$=2.466 Å. The filled symbols show numerically calculated data points and lines are joining to the data points.

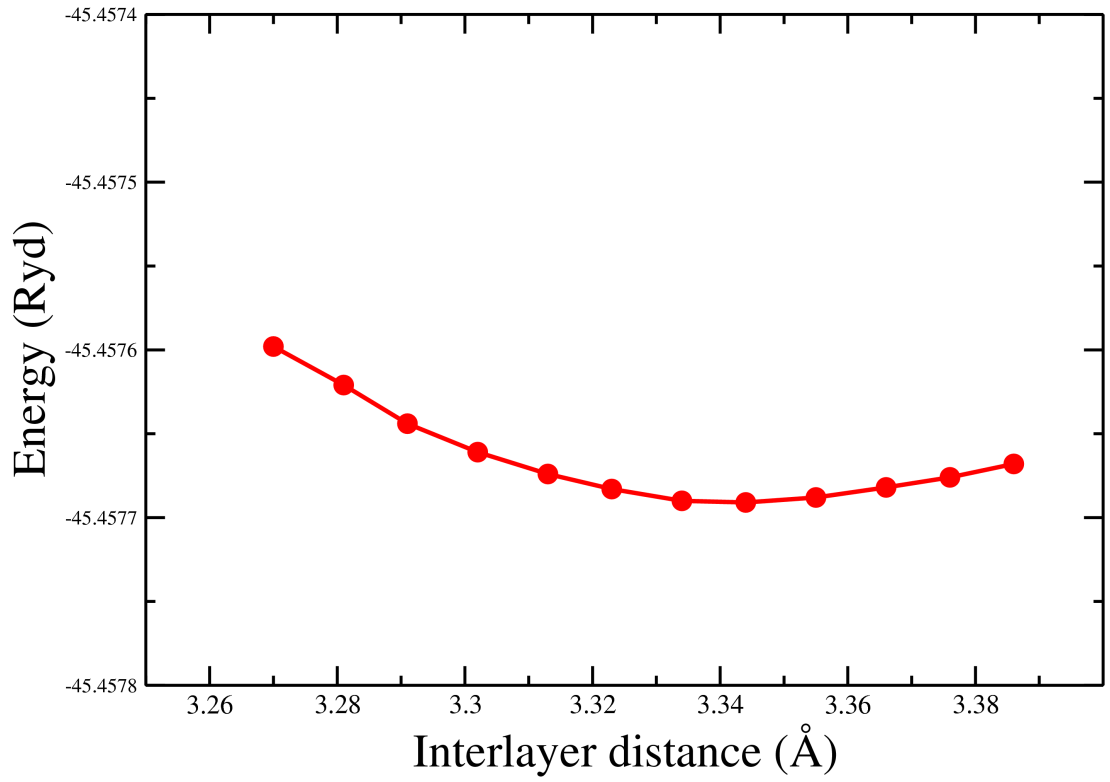


Figure 3.10: Total energy of bilayer graphene as a function of the interlayer distance. The circle filled symbols show numerically calculated data points. Line is joining to the data points.

Due to four basis atoms in its unit cell, there are two pairs of $\pi/\pi^*$ bands, as shown in Fig. 3.11 (a). We find that the inner pair of the $\pi/\pi^*$ bands is degenerate at the **K** point. From our theoretical calculations, with $d$=3.330 Å, we note that homogeneous compression or stretching of bilayer graphene by 0.1% ($a$=2.458) and 0.24% ($a$=2.466), respectively, the degeneracy of the bands is not changed. For the outer pair of the $\pi/\pi^*$ bands at the **K** point the band gap of 0.716 eV is obtained for $a$=2.460 Å. This band gap is increased by 2.1 % with the homogeneous compression of 0.1% ($a$=2.458 Å) and by 1 % with streching of 0.24% ($a$=2.466 Å), as shown in Fig. 3.12. In addition using different values of the lattice parameter $a$ and interlayer distance $d$ close to our equilibrium values, the variation of the band gap between the outer pair of $\pi/\pi^*$ bands is examined. As the results are listed in Tab. 3.1, we judged that the maximum error in our estimate of the gap is 26 meV.

To explain the behaviour of the $\pi/\pi^*$ bands very close to the **K** point, the numerical data for our theoretical lattice constant (a=2.460 Å) for energies up to 0.07 eV using the data in top panel of Fig. 3.13 and up to 0.34 eV using the data in bottom panel of Fig. 3.13 above the **K** point is fitted by following equation

$$E = A_0 k + A_1 k^2. \tag{3.3}$$

Using the same method as described in section 3.2.1, I estimated $A_0$=0.296 eV nm within the RMS error of 0.43% and $A_1$=3.36 eV nm$^2$ within the RMS error of 0.49% for the energies up to 0.07 eV above the **K** point. For the other energy, $A_0$=0.63 eV nm within the RMS error of 0.41% and $A_1$=2.56 eV nm$^2$ within the RMS error of 0.47% is estimated. Therefore, the in-plane dispersion relation of the inner $\pi^*$ band close to the **K** point has a mixture of quadratic and linear behaviour. Using

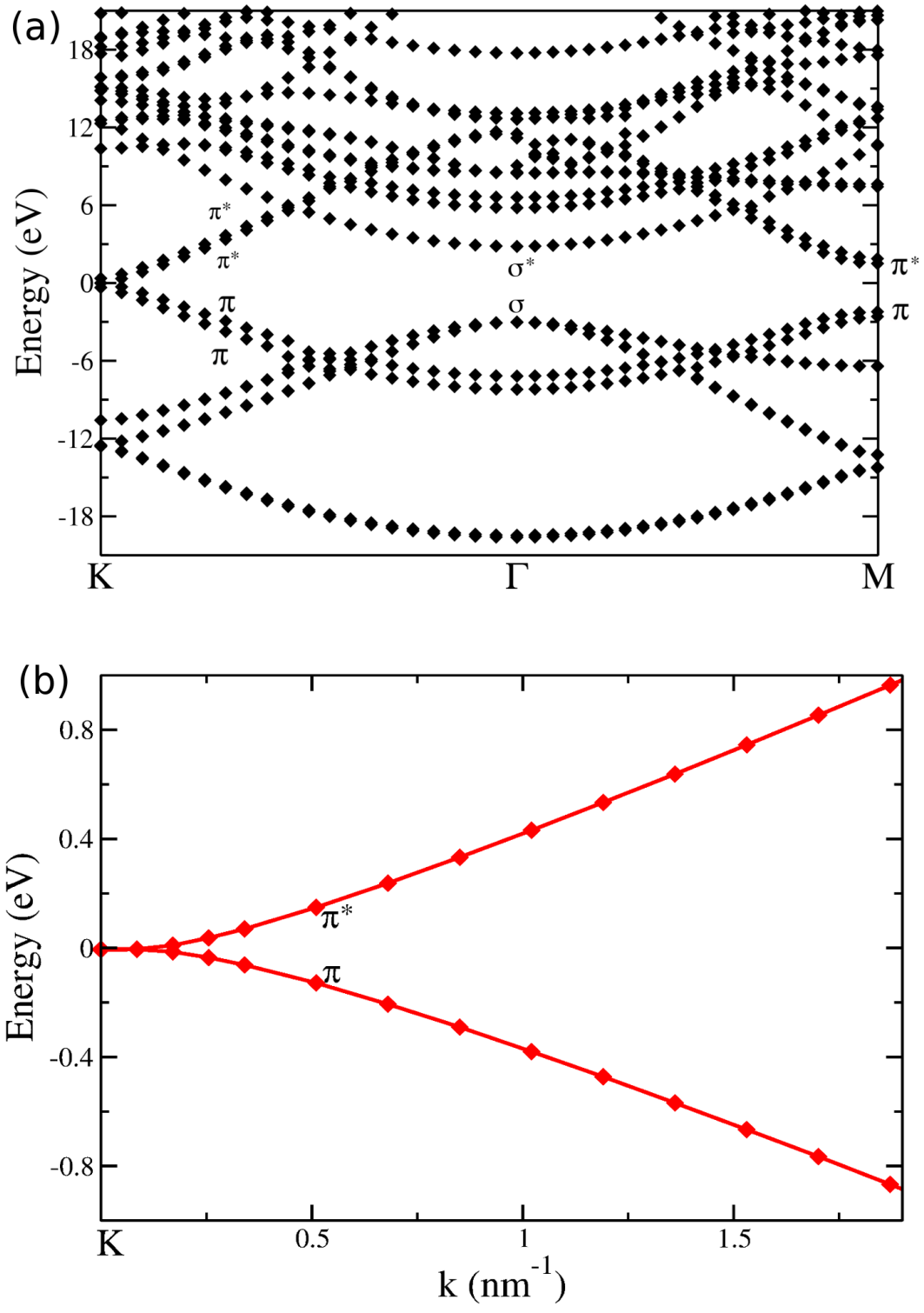


Figure 3.11: (a) Electronic band structure of bilayer graphene. (b) The inner-pair of bands very close to the **K** point. The filled symbols show numerically calculated data points and lines are joining to the data points.

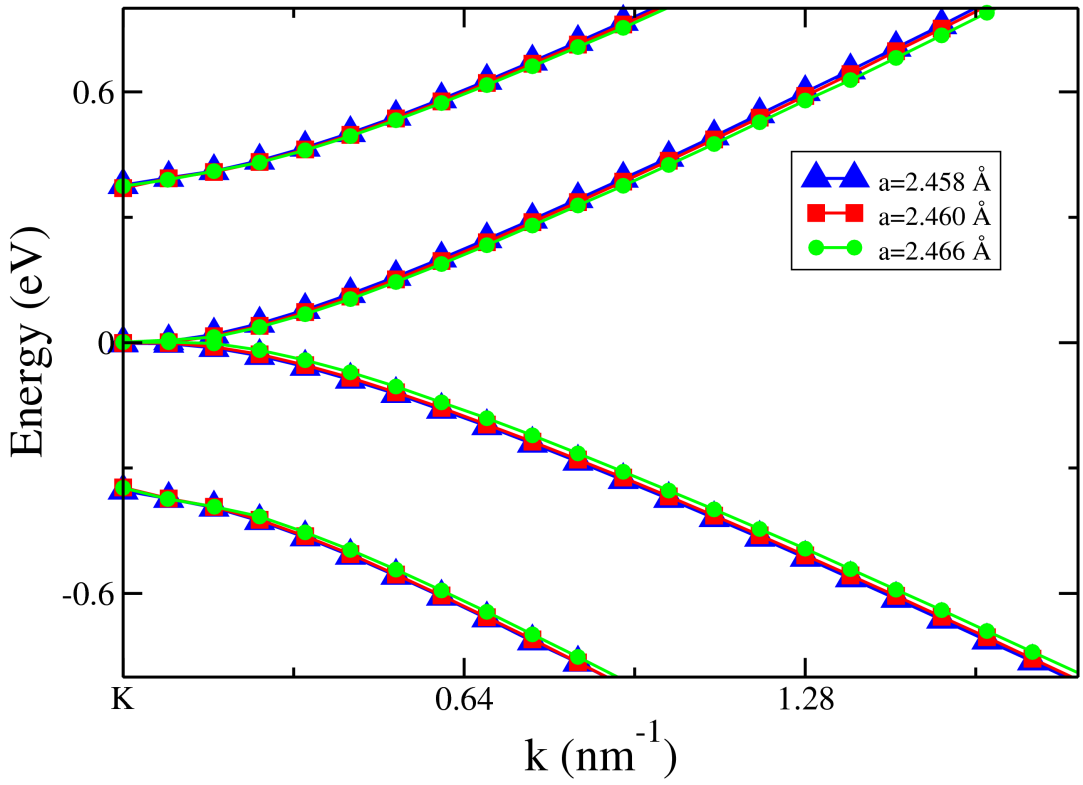


Figure 3.12: The inner and outer pair of $\pi/\pi^*$ bands close to the **K** point for bilayer graphene with using lattice constants of $a$=2.458 Å, $a$=2.460 Å and $a$=2.466 Å. The filled symbols show numerically calculated data points and lines are joining to the data points.

Table 3.1: The energy band gap between the outer pair of the $\pi/\pi^*$ bands in bilayer graphene at the **K** point for different values of the lattice parameter $a$ and interlayer distance $d$ around the equilibrium values.

| $a$ (Å) | $d$ (Å) | $E_g$ (eV) |
|---|---|---|
| 2.458 | 3.320 | 0.7334 |
| | 3.330 | 0.7310 |
| | 3.340 | 0.7120 |
| | 3.344 | 0.7085 |
| 2.460 | 3.320 | 0.7340 |
| | 3.330 | 0.7160 |
| | 3.340 | 0.7130 |
| | 3.344 | 0.7086 |
| 2.462 | 3.320 | 0.7337 |
| | 3.330 | 0.7232 |
| | 3.340 | 0.7127 |
| | 3.344 | 0.7088 |

Eq. 3.3, the effective mass can be found as

$$m^* = \frac{\hbar^2}{\frac{\partial^2 E}{\partial^2 k}} \tag{3.4}$$

$$= \frac{1}{2}\frac{\hbar^2}{A_1}. \tag{3.5}$$

I made calculations for three different lattice constants. Following the procedure with the data in the top and bottom panels of Fig. 3.13, the obtained results are listed in the Tab. 3.2. From these results it is obvious that estimate of the effective mass is robust against to choices of $a$, provided that the same range of energy values are considered in the calculations. However, there is a clear difference in m$^*$ when the energy range is changed (in the top or bottom panel of

Table 3.2: Effective masses of bilayer graphene for different lattice constans.

| $a$ (Å) | Number of data points | $m^*$ |
|---|---|---|
| 2.458 | 5 | $0.0245m_e$ |
| | 8 | $0.0354m_e$ |
| 2.460 | 5 | $0.0230m_e$ |
| | 8 | $0.0300m_e$ |
| 2.466 | 5 | $0.0268m_e$ |
| | 8 | $0.0341m_e$ |

Fig. 3.13). From the data presented in the Tab. 3.2 our estimate of the effective mass is $m^*=0.029(\pm0.006)m_e$. This value is close to the estimate of $m^*=0.037m_e$ made by Koshino *et al.* [133, 134], who used an inter-layer distance of 3.34 Å, which is larger than what we used in our works. Our effective mass also has good agreement with the estimate made by McCann *et al.* [135] by using a tight binding approach.

### 3.2.3 Trilayer Graphene

There are two possible atomic-layer stackings for trilayer graphene: ABA and ABC. It is thought that during the mechanical exfoliation process both stackings are produced, though the ABA stacking is much more prevalent [136, 137, 138]. Indeed, theoretical calculations reveal that the total energies of both stackings are quite similar with the ABA stacking being slightly more energetically stable [139]. We, thus, modelled the ABA-stacked trilayer graphene with our theoretical inter-layer distance of 3.33 Å in agreement with Refs. [133, 137]. This distance is determined by following the same procedure for interlayer distance of bilayer graphene in section 3.2.2. Figure 3.14 shows the convergence of the total energy versus interlayer distance of ABA-stacked trilayer.

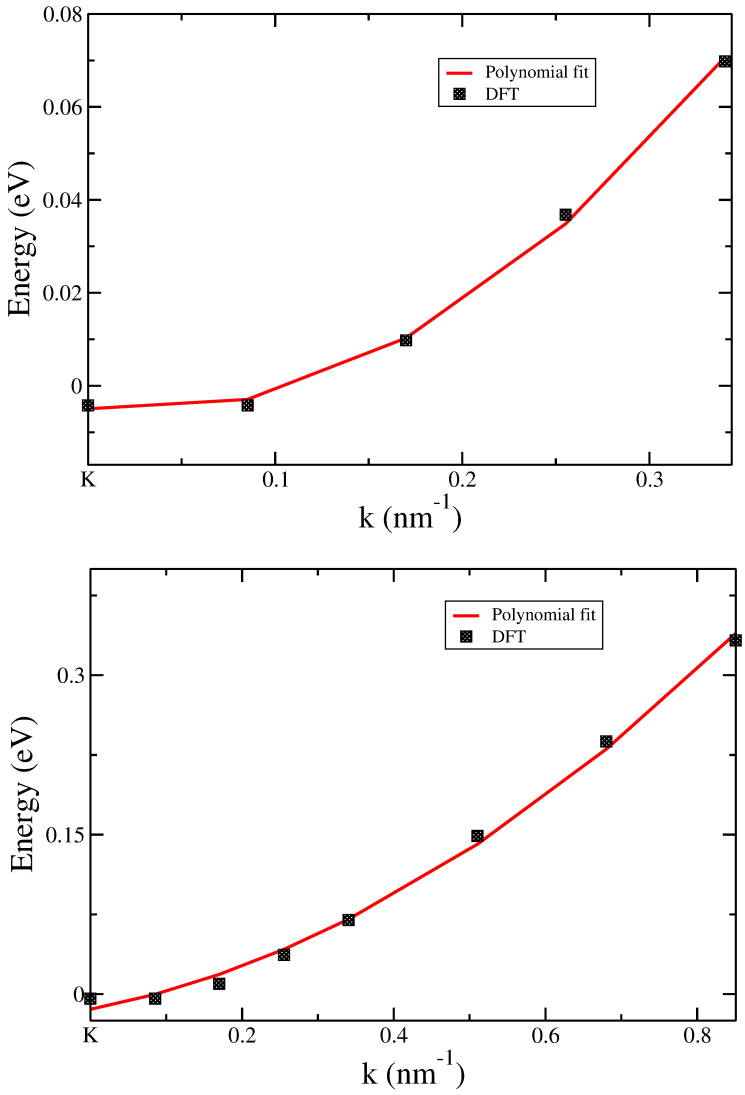


Figure 3.13: The polynomial fit of the $\pi^*$ bands using two ranges of energies (up to 0.08 eV and up to 0.33 eV) above the **K** point for bilayer graphene. The square filled symbols show numerically calculated data points and the line shows a polynomial fit of the DFT data.

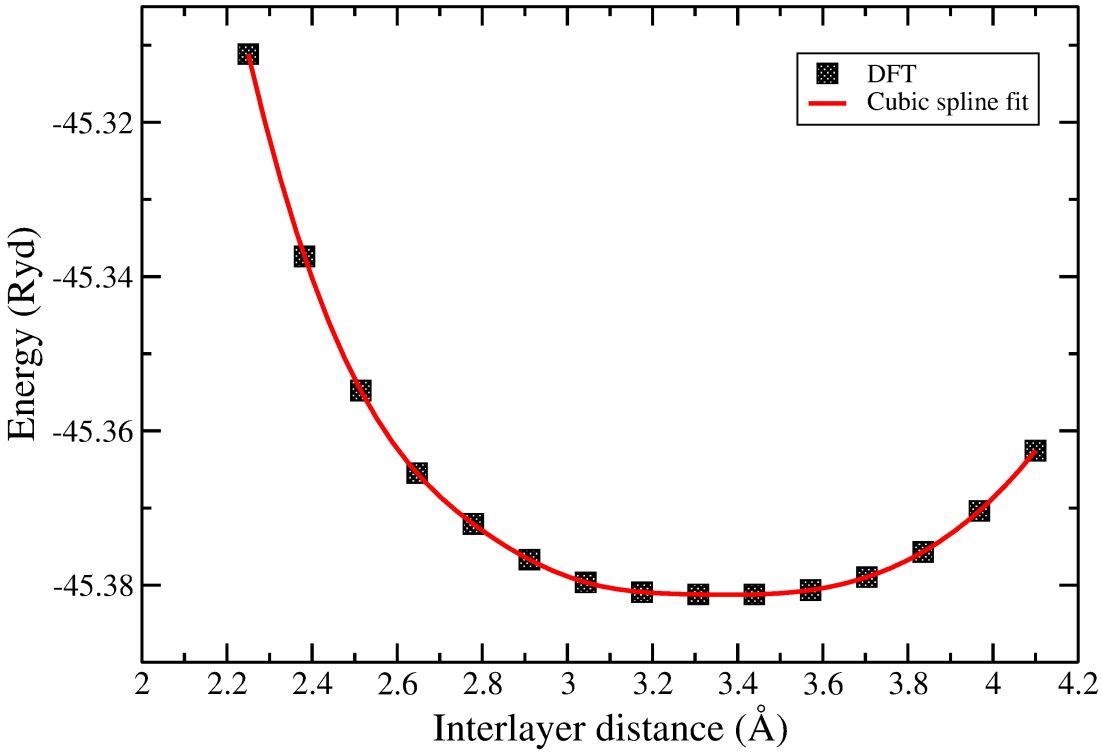


Figure 3.14: Total energy of ABA-stacked trilayer graphene as a function of the interlayer distance. The circle filled symbols show the DFT data the curve shows the fits of the DFT data as described in the text.

The electronic properties of trilayer graphene differ from monolayer graphene and bilayer graphene. The electronic property strongly depends on the interlayer stacking sequence [133, 137]. Due to six C atoms in its unit cell , there are three pairs of $\pi/\pi^*$ bands around the Fermi level at the **K** point, as presented in Fig. 3.15 (a). The inner-most pair of such bands are split at the **K** point by 19 meV, with lattice constant $a$=2.460 Å, around the Fermi energy and cross each other as the in-plane wavevector moves slightly away from the **K** point towards the zone centre. As shown in Fig. 3.15 (b), we find that for the values of the wavenumber in the range 0.06 - 0.25 $nm^{-1}$ from the **K** point, there is a co-existence of electron and hole states. This mixed state occupies a maximum energy range of 14 meV at 0.15 $nm^{-1}$ away from the **K** point. Therefore, the trilayer graphene is semimetallic. The splitting of the bands at the **K** point increases very slightly (by less than 3 meV) for values of $a$ slightly smaller or larger than our equilibrium $a$=2.460 Å. Also, the crossing point between the two bands shifts very slightly away from the **K** point (by less than 0.007 $nm^{-1}$) for values of $a$ slightly away from the equilibrium. The results are shown in Fig. 3.16.

To estimate the effective mass of electron in trilayer graphene, I follow the same method as described for bilayer graphene in section 3.2.2. I make a polynomial fit of the numerical data for the $\pi^*$ band using two energy ranges (up to 0.0149 eV and up to 0.0462 eV above the **K** point), as represented in Fig.3.17, using the following equation,

$$E = A_0 k + A_1 k^2 + A_2 k^3 + A_3, \tag{3.6}$$

$A_2$=-8.37$\times10^{-8}$ eV $nm^3$ for the energies up to 0.0149 eV above the **K** point are estimated within the RMS error of 2.7$\times10^{-7}\%$ by following the same procedure as described in section 3.2.1. For the range of energies up to 0.0462 eV above the **K** point, I estimated $A_0$=-0.205 eV nm, $A_1$=0.695 eV $nm^2$, and $A_2$=-5.51$\times10^{-7}$ eV $nm^3$ within the RMS error of 4.29$\times10^{-7}\%$. From these results, it is found that the innermost pair of $\pi/\pi^*$ bands show a mixture of linear and quadratic be-

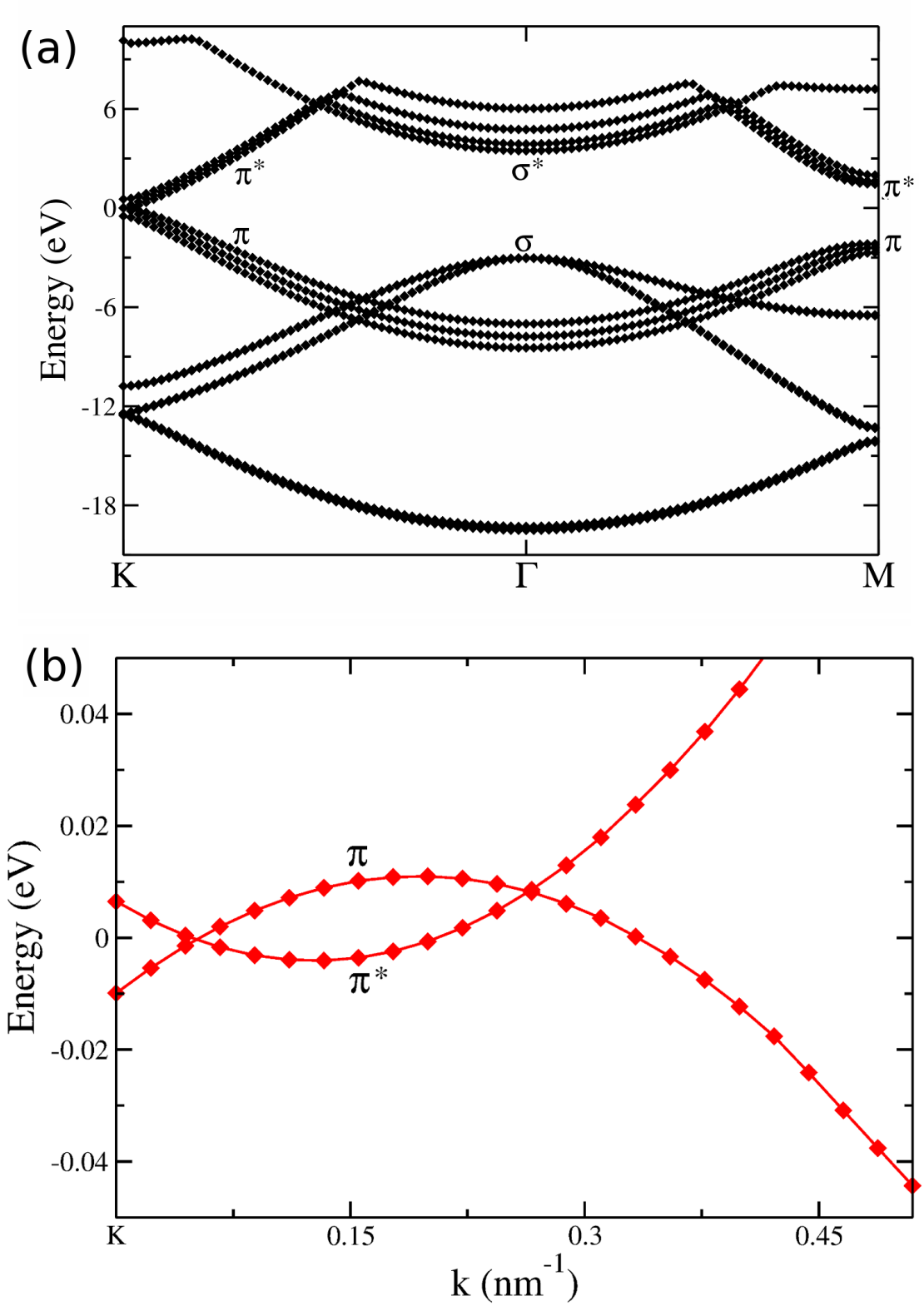


Figure 3.15: (a) Electronic band structure of ABA-stacked trilayer graphene. (b) The inner-most pair of bands close to the **K** point. The filled symbols show numerically calculated data points and the curves are joining to the data points.

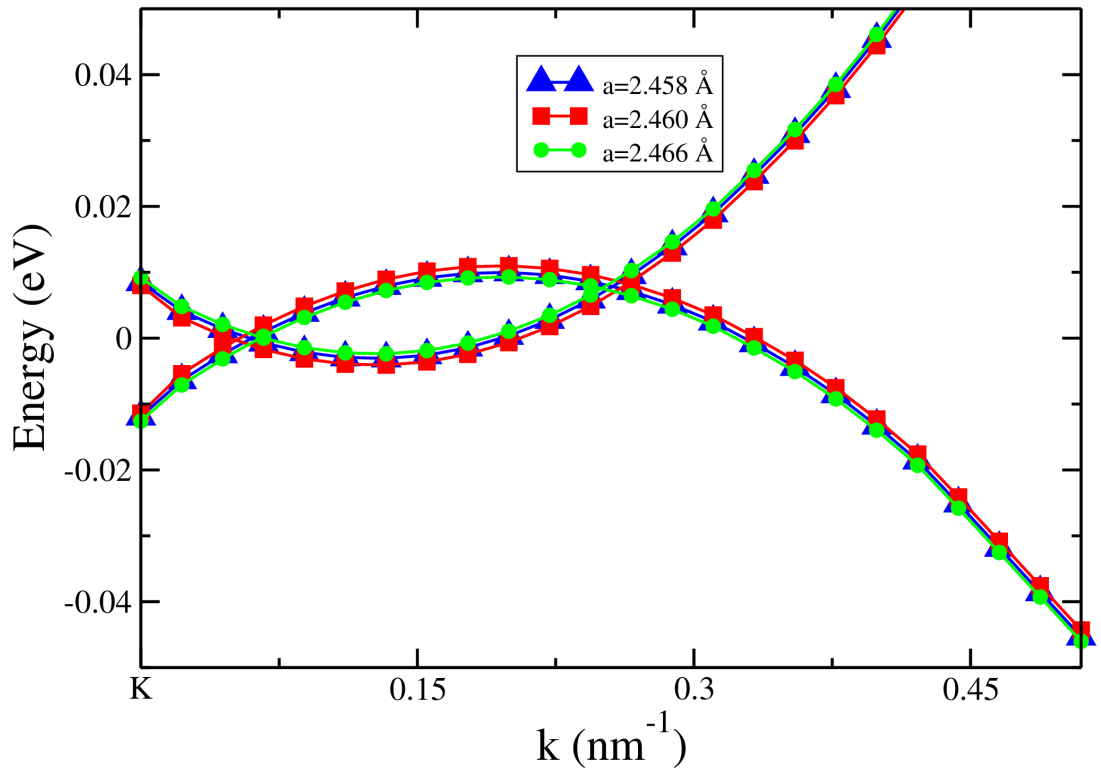


Figure 3.16: The inner pair of $\pi/\pi^*$ bands close to the **K** point for trilayer graphene with using lattice constants of $a$=2.458 Å, $a$=2.460 Å and $a$=2.466 Å. The filled symbols show numerically calculated data points and lines are joining to the data points.

haviour. By using the quadratic term $A_1$ and neglecting the term $A_2$, for our equilibrium lattice constant of $a$=2.460 Å the effective electron mass is estimated as (0.054$\pm$0.011)$m_e$. A similar result has been obtained by Koshino and McCann [133] with a tight binding approach. Following the above steps, we obtained effective mass as (0.052$\pm$0.012)$m_e$ for slightly smaller lattice constant $a$=2.458 Å and (0.048$\pm$0.014)$m_e$ for slightly large lattice constant $a$=2.462 Å. Clearly, the error margin in the lattice constant generates much smaller error bar in the effective mass calculations. Overall, therefore, expressed our theoretical estimate of the effective mass as 0.054m$_e$ with the maximum error of 0.014m$_e$. It is interesting to note that the effective mass for trilayer graphene is larger than that for bilayer graphene. This is in agreement with the work of Thompson *et al.* [140] who obtained increment in the effective mass for different layers ($N$=2-6).

### 3.2.4 Graphite

Graphite consists of graphene layers stacked in an ABA configuration as shown in Fig. 1.3. Using the in-plane lattice constant $a$=2.460 Å, the distance between two graphene layers is found to be 3.33 Å by using the method as described in section 3.2.2. The unit cell of graphite contains four carbon atoms. Therefore, there are two pairs of $\pi/\pi^*$ bands around the Fermi level at the **K** point. Figure 3.18 (a) shows the electronic structure of graphite along the **ΚΓΜΚΗΓΑ**. The inner pair of the $\pi/\pi^*$ bands is degenerate at the **K** point and shows quadratic behaviour around the Fermi level close to the **K** point. This behaviour, thus, suggests that the carriers are normal (massive) electrons. Following the procedure for determinig the effective mass of trilayer graphene in section 3.2.3 our estimation of the effective electron mass value in graphite is m$^*$=(0.043$\pm$0.009)m$_e$ using our equilibrium lattice constant of 2.460 Å. This value has good agreement with the reported theoretical value of 0.045m$_e$ [141, 142] and the experimental result

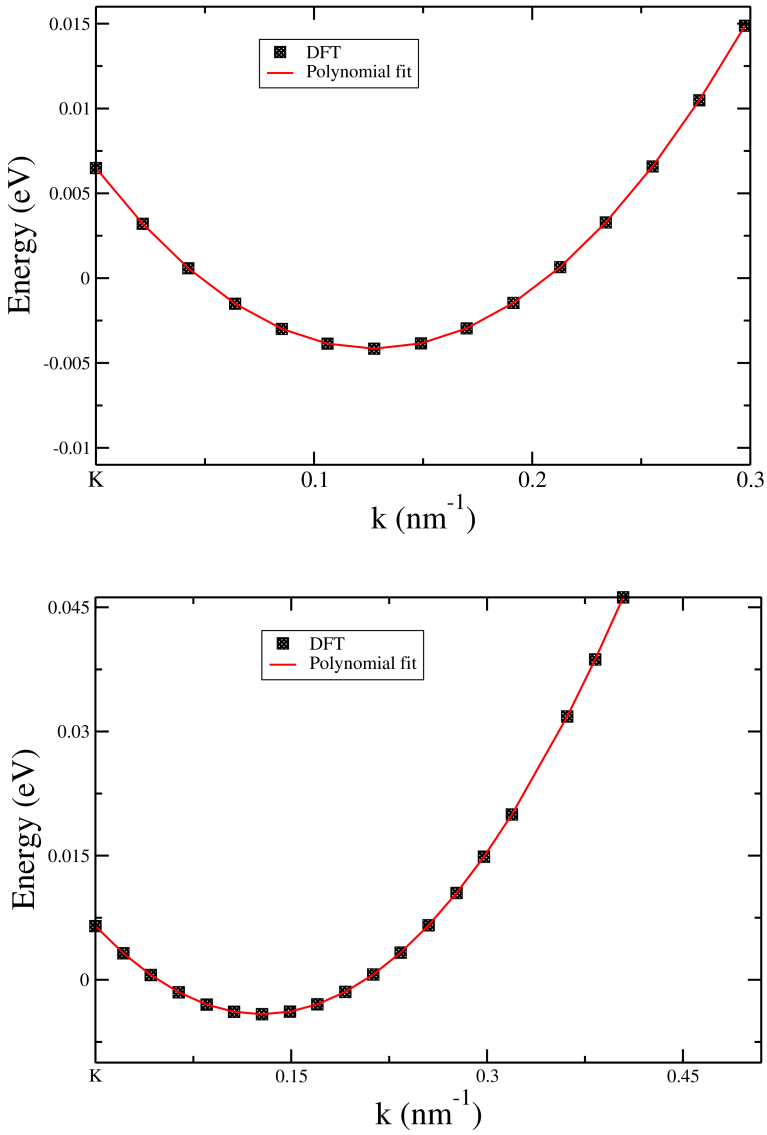


Figure 3.17: The polynomial fit of the inner-most $\pi^*$ bands up to 0.0149 eV and up to 0.0462 eV above the **K** point for ABA-stacked trilayer graphene. The symbols show numerically calculated data points and the curve shows a polynomial fit of the DFT data.

of 0.06$m_e$ [143]. The error in the estimation of the lattice constant increases the effective mass to (0.054±0.007)$m_e$ and (0.052±0.006)$m_e$ for the lattice constants of 2.458 Å and 2.462 Å, respectively. Therefore, our theoretical estimate of 0.043$m_e$ with a possible maximum error of 0.01$m_e$. In Fig. 3.18 (b) we also plot the band structure of graphite along the **KH** direction in the Brillouin zone. The inner pair of the $\pi/\pi^*$ bands is degenerate but shows very little dispersion. Moreover, this band crosses the Fermi level at nearly **KH/3**, as shown in Fig. 3.19. This behaviour suggests that the hole state is more lengthened than the electron state. These results are in agreement with previous first-principles work [141]. For the outer pair of the $\pi/\pi^*$ bands, we found energy gap of 0.02 eV at the **H** point and 1.43 eV at the **K** point. Furthermore, the $\pi$ and $\pi^*$ bands move upward and downward along the **KH** direction, respectively.

The small changes in the lattice constant from the theoretical value of 2.460 Å increases the band gap both at the **K** and **H** point. These changes are given in Tab. 3.3. It is clear that the gap value is robust within 10 meV with respect to reasonable errors in the lattice constant.

Table 3.3: The energy band gap values for the outer pair of the $\pi/\pi^*$ bands of graphite at **K** and **H** point with different lattice constants.

| $a$ (Å) | Band gap at **K** | Band gap at **H** |
|---|---|---|
| 2.458 | 1.436 eV | 0.024 eV |
| 2.460 | 1.430 eV | 0.020 eV |
| 2.466 | 1.438 eV | 0.034 eV |

### 3.2.5 Density of States and Interband Optical Transitions

The density of states (DOS) for graphene, BLG, TLG, and graphite are shown in Fig. 3.20. From our calculations we found a peak at $E_F$-2.286 eV in occu-

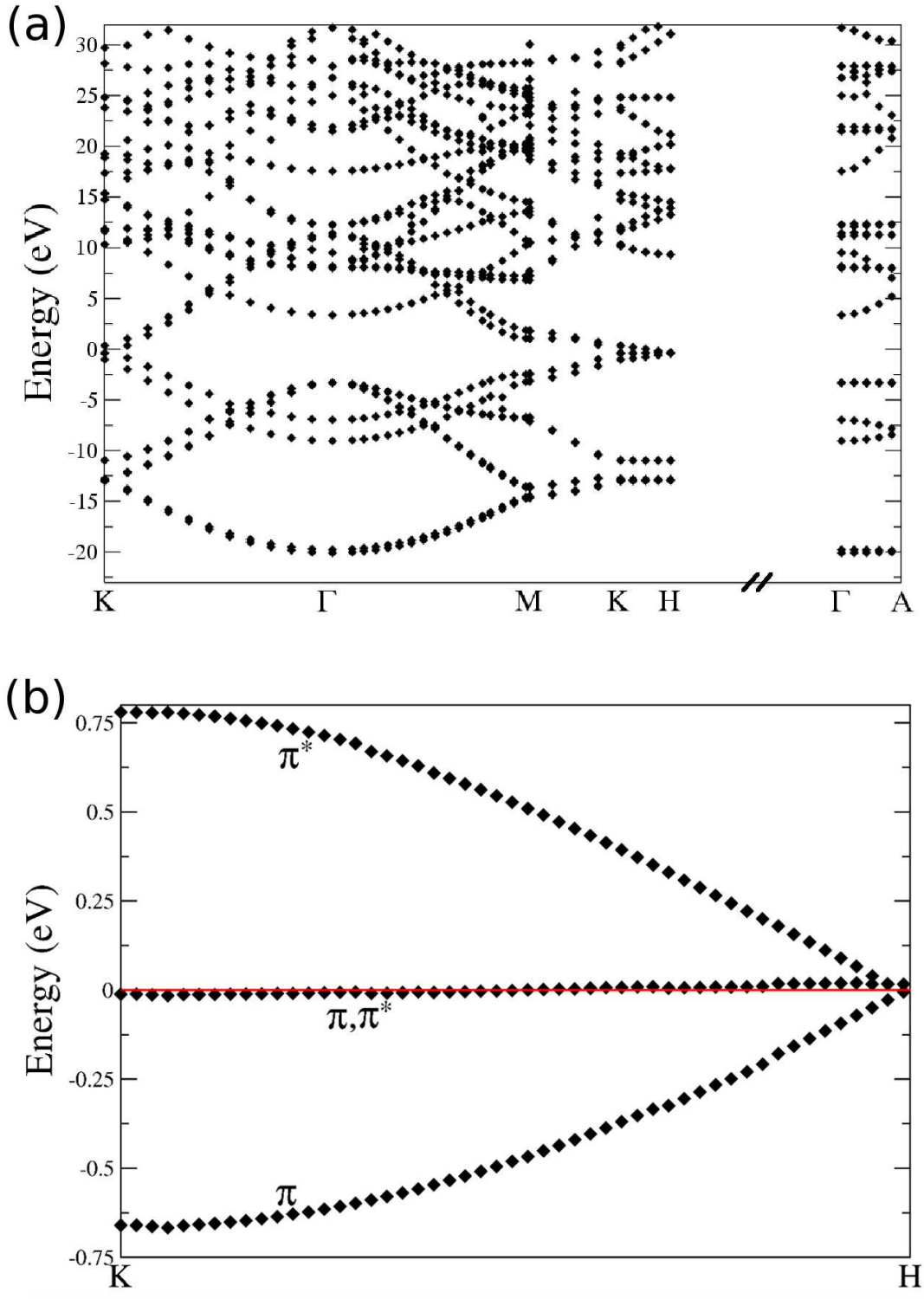


Figure 3.18: Electronic band structure of graphite along (a) the **ΚΓΜΚΗΓΑ** and (b) the **KH** directions and close to the Fermi level. Solid line represents the Fermi level. The filled symbols show numerically calculated data points.

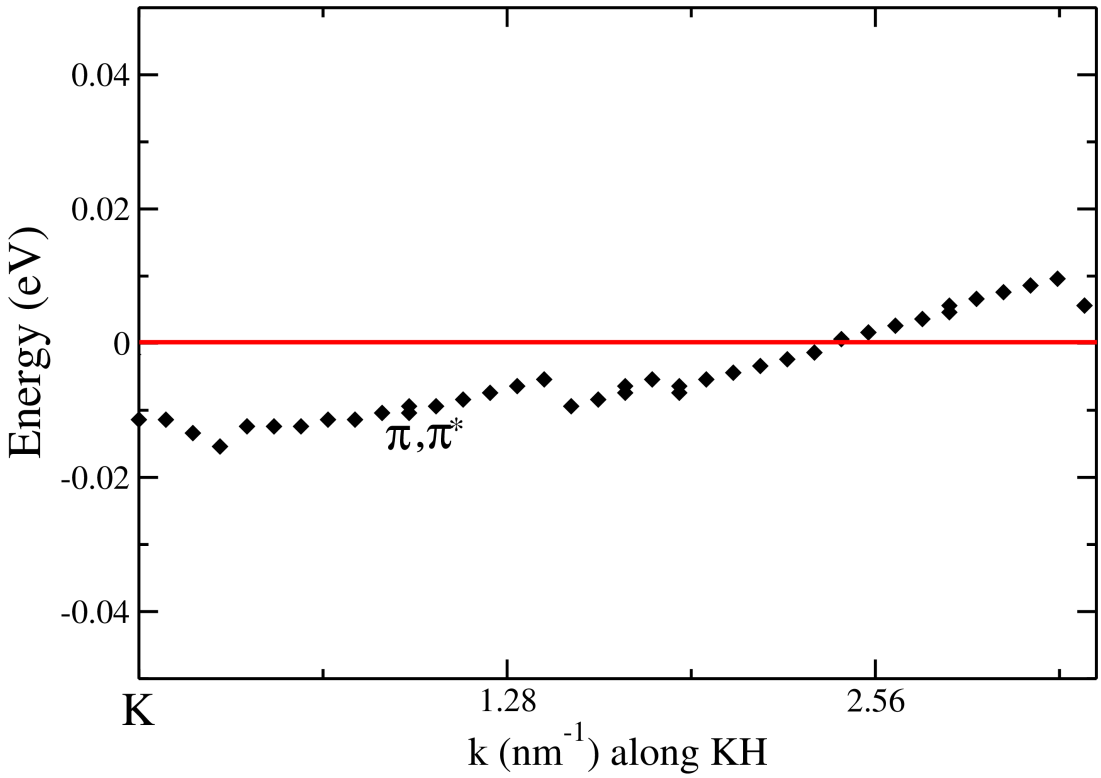


Figure 3.19: The most inner pair of the $\pi/\pi^*$ bands along to the **KH** directions. The filled symbols show numerically calculated data points.

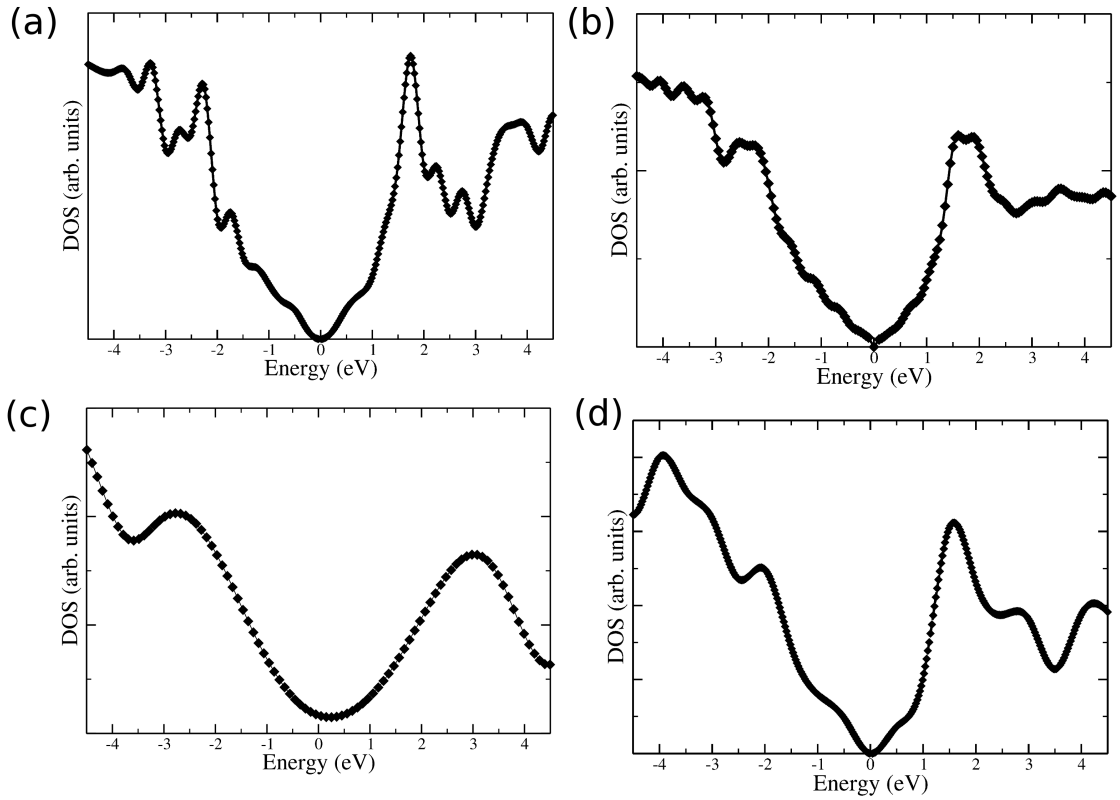


Figure 3.20: Density of states for (a) graphene (MLG), (b) bilayer graphene (BLG), (c) ABA-stacked trilayer graphene (TLG), and (d) graphite. These points were obtained by Gaussian broadening of energy bands ($E_n$(k)) by 5 meV for each **k**-point included in DOS calculation.

pied region for graphene. For bilayer graphene, ABA-stacked trilayer graphene, and graphite shoulders around $E_F$-2.397 eV, $E_F$-2.868 e,V and $E_F$-2.064 eV are obtained respectively. In the unoccupied region, the peak at $E_F$+1.763 eV in graphene moves to $E_F$+3.01 eV for TLG. This peak shifted to $E_F$+1.611 eV in graphite. The energy difference between the two peaks around $E_F$ for graphene increases when the layer thickness increases but it is almost identical in graphite. The location of the peaks in DOS for all graphene systems are in good agreement with experimental and theoretical studies [144, 145]. These changes provide a clear evidence that optical properties of graphene will change with the layer thickness. Furthermore, we found that the energy separation between the highest occupied ($\sigma$) and the lowest unoccupied ($\sigma^*$) states at the zone centre is 6.3 and the energy separation between the $\pi$ and $\pi^*$ bands at the **M** symmetry point is 4.03 eV as can be seen in Fig. 3.5. These LDA results for the transition energies should be taken as lower bounds, because of the undersetimation of band gaps using DFT. Indeed, experimental results for $\pi \rightarrow \pi^*$ transition in isolated graphene is reported to be 4.6 eV [122]. Our calculations suggest that the interband transitions ($\sigma \rightarrow \sigma^*$ and $\pi \rightarrow \pi^*$) show small changes in BLG, TLG, and graphite with respect to the MLG.

Table 3.4 presents the computed results for the transition energies $\sigma \rightarrow \sigma^*$ (at $\Gamma$) and $\pi \rightarrow \pi^*$(at **M**) obtained for different **k**-sampling and lattice constants. As seen in Tab. 3.5, the error margin for these transition energies for each of these sytems (MLG, BLG, TLG, and Graphite) is very small. From these error estimates, we note that the results presented in this thesis for the equilibrium lattice $a$=2.460 Å and the choice of the **k**-sampling are robust against reasonable variations in the choice of lattice constant and **k**-sampling.

Table 3.4: The interband transitions for MLG, BLG, TLG, and graphite. The results in bold font are for the optimium choice of lattice constant $a$ and **k** sampling.

| System | Sampling Method | Transition Energies (eV) | |
|---|---|---|---|
| | | $\sigma \rightarrow \sigma^*$ (at $\Gamma$) | $\pi \rightarrow \pi^*$ (at **M**) |
| MLG | **k**-sampling using a=2.46Å | | |
| | **36×36×1** | **6.300** | **4.030** |
| | 48×48×1 | 6.362 | 4.036 |
| | $a$-sampling using **k**: 36×36×1 | | |
| | 2.458 Å | 6.330 | 4.080 |
| | **2.460 Å** | **6.300** | **4.030** |
| | 2.462 Å | 6.363 | 4.022 |
| BLG | **k**-sampling using a=2.46Å | | |
| | 36×36×1 | 5.823 | 3.690 |
| | 48×48×1 | 5.823 | 3.690 |
| | **36×36×2** | **5.820** | **3.690** |
| | $a$-sampling using **k**: 36×36×2 | | |
| | 2.458 Å | 5.789 | 3.707 |
| | **2.460** Å | **5.820** | **3.690** |
| | 2.462 Å | 5.812 | 3.685 |
| TLG | **k**-sampling using a=2.46Å | | |
| | 36×36×1 | 6.013 | 3.624 |
| | 48×48×1 | 6.014 | 3.624 |
| | **36×36×2** | **6.000** | **3.630** |
| | $a$-sampling using **k**: 36×36×2 | | |
| | 2.458 Å | 5.980 | 3.640 |
| | **2.460 Å** | **6.000** | **3.630** |
| | 2.462 Å | 6.010 | 3.620 |
| Graphite | **k**-sampling using a=2.46Å | | |
| | 36×36×1 | 6.754 | 3.560 |
| | 48×48×1 | 6.754 | 3.560 |
| | **36×36×2** | **6.690** | **3.520** |
| | $a$-sampling using **k**: 36×36×2 | | |
| | 2.458 Å | 6.770 | 3.570 |
| | **2.460 Å** | **6.690** | **3.520** |
| | 2.462 Å | 6.790 | 3.560 |

Table 3.5: Optical transition energies (in eV) between the innermost $\sigma$ and $\sigma^*$ bands at $\Gamma$, and between the innermost $\pi$ and $\pi^*$ at **M** point.

| System | $\sigma \rightarrow \sigma^*$[1] | $\pi \rightarrow \pi^*$[1] |
|---|---|---|
| MLG | 6.30 (0.06) | 4.03 (0.05) |
| BLG | 5.82 (0.03) | 3.69 (0.02) |
| TLG | 6.00 (0.02) | 3.63 (0.02) |
| Graphite | 6.69 (0.08) | 3.52 (0.05) |

[1]The values in the parenthesis represent the maximum error estimated from the results presented in Tab. 3.4 using different sampling schemes.

## 3.3 Summary

We have presented *ab initio* calculations to investigate the electronic structure of graphene, BLG, ABA-stacked TLG, and graphite using the density functional theory within the local approximation with plane wave pseudopotentials and periodic boundary conditions. The in-plane electronic band dispersion around the Fermi level at the **K** point is linear (Dirac-like) for graphene, and a mixture of quadratic and linear for BLG, TLG, and quadratic for graphite. The computed electron effective masses for BLG, TLG, and graphite are $0.029(\pm 0.006)\mathrm{m}_e$, $0.054(\pm 0.011)\mathrm{m}_e$, and $0.043(\pm 0.009)\mathrm{m}_e$, respectively. The electron velocity in monolayer graphene is $\mathbf{0.93(\pm 0.07)\times 10^6}$ **m/s**. Our theoretically found values for these systems are in agreement with experimental results. The modifications in the electronic properties due to increasing the number of graphene layer is very little. Our results also suggest that the electronic properties of a graphene sample after 7 atomic layers would approach that of bulk graphite. We showed the changes in interband optical transitions of BLG, ABA-stacked TLG, and graphite as com-

pared to MLG.

# Chapter 4

# The Electronic Structure of ABC-stacked Multilayer Graphene and Trigonal Warping

## 4.1 Introduction

Experiments reveal that the single layer graphene and stacks of graphene layers can be used in the design of new electronic devices [113, 146, 147]. In addition to the fascinating development in research on properties of mono- and few-layer graphene (FLG) has also gained recent attention [148, 149, 150, 151]. The ability of creating stacks of the individual graphene sheets in FLG provides an extra degree of freedom on electronic properties [152, 153, 154, 155]. It has been predicted and suggested that different stacking orders, with distinct lattice symmetries, have a substatial effect on the electronic band structure of FLG [152, 153, 154, 155, 156, 157]. Experimentally, the strong influence of stacking order on the low-energy electronic structure of FLG was recently demonstrated by infrared (IR) spectroscopy [152]. The band structures of graphene from one to four layers were also measured using angle-resolved photoemission spectroscopy [158].

Although the FLG and graphite are mostly Bernal-stacked (AB), trilayer graphene has two different stacking orders: ABA (Bernal) and ABC (rhombohedral). These stackings are expected to be metal-like [159] and predicted as two stable configurations in Refs. [151, 153, 160]. Even though there are small cohesive energy differences between these two types of trilayer graphene, recent studies indicate that they exhibit very different electronic properties that are of interest for technological applications [153, 154, 161]. Koshino and McCann have made a detailed study of the electronic structure, within an effective mass approximation and an empirical tight-binding model, of the ABA-stacked graphene [162, 163] and ABC-stacked multilayer graphene [164, 165]. The work in Ref. [164] shows that the type of interlayer coupling present in ABC-stacked multilayer with $N$ layers graphene gives rise to trigonal warping of the energy bands near the Fermi surface that is both qualitatively and quantitatively different from that in bilayer graphene. The work in Ref. [164] further suggests that the trigonal warping in ABC-stacked multilayer graphene is most prominent for the trilayer (i.e. with $N$=3).

In this chapter, we examine the band structure of ABC-stacked $N$-layer graphene by employing the plane wave pseudopotential method within the density functional scheme. The orbital natures of the highest occupied molecular orbital (HOMO) and lowest unoccupied molecular orbital (LUMO) states are investigated using partial charge density plots which can be very useful for researchers to understand the effect of stacking sequences on the multilayer graphene systems. We show that the dispersion curve of the highest valence and lowest conduction bands for the ABC stacked trilayer graphene are a mixture of cubic, quadratic, and linear behaviours. Moreover, in a unique way, we examine the nature of the trigonal warping of energy bands slightly above the Fermi level for different layer thicknesses by using first principles calculations. This is achieved through an examination of the orbital origins of the highest occupied and lowest

unoccupied bands at the Dirac (**K**) point.

## 4.2 Results

### 4.2.1 ABC-Stacked Trilayer Graphene

In ABC-stacked trilayer graphene (the $N = 3$ trilayer case) there are six basis carbon atoms in its unit cell with two basis carbon atoms in each layer. As illustrated in Fig. 4.1, while the bottom and middle layers of the ABC-stacked trilayer graphene are arranged in Bernal (AB), the basis $C_{31}$ in the top layer lies exactly above the basis $C_{22}$ in the middle layer and the second basis $C_{32}$ on the top layer is at the centre of the hexagon formed by the carbon atoms in the bottom layer. The interlayer separation is found to be 3.33 Å by using our theoretical lattice constant of 2.458 Å after several total energy calculations. This interlayer distance is in good agreement with experimentally measured interlayer distance of graphite [166]. These structural parameters are also in very good agreement, within our numerical accurancy as discussed before, with the ABA-stacked trilayer graphene in the previous chapter.

The electronic band structure was examined close to the Dirac point (the **K** point in the Brillouin zone) for wavevectors lying both in the graphene plane as well as along the surface normal. As represented in Figs. 4.2, along $k_x$ two bands lying close to the Fermi energy cross each other, thus indicating metallic behaviour of the system. These bands, however, do not cross each other for $-k_x$ values, indicating semiconducting behaviour along the $\mathbf{K} - \mathbf{\Gamma}$ direction. A similar behaviour of these bands are also found in the work of Latil and Henrard [153]. Along the surface normal direction (the **K-H** direction in the Brillouin zone for the supercell geometry adopted in our calculations) these two bands cross each other much closer to the **K** point, a feature somewhat similar to what is found for graphite in

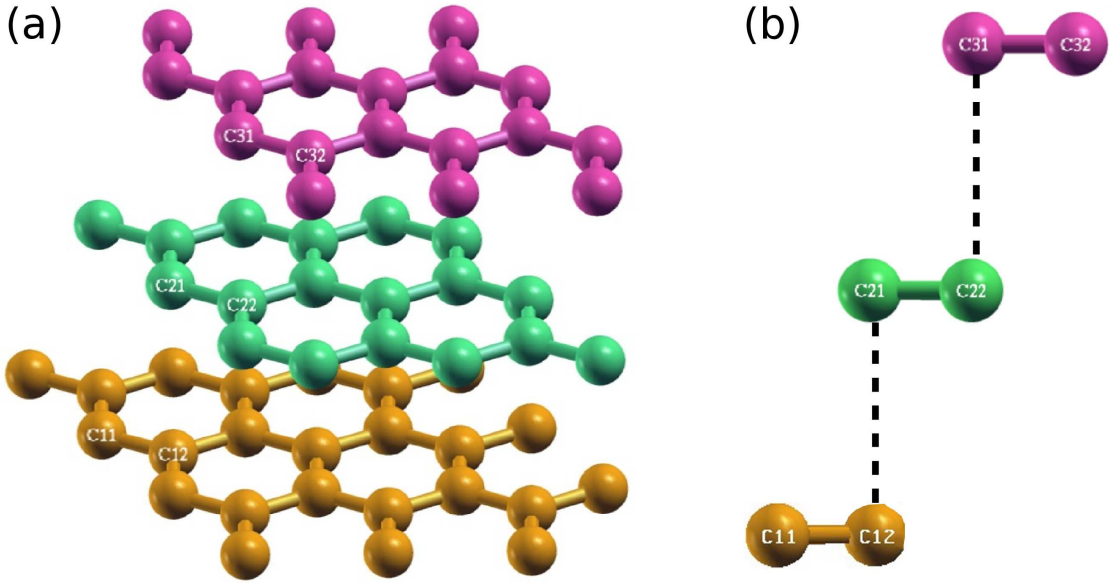


Figure 4.1: (a) Atomic structure of ABC-stacked trilayer graphene containing six basis carbon atoms in the primitive unit cell. (b) Schematic of the unit cell of ABC-stacked trilayer graphene.

Chapter 3. A polynomial fit of the part of the curve in Fig. 4.3 (a) shows a mixture of linear, quadratic and cubic terms:

$$E = a_0 + a_1 k_x + a_2 k_x^2 + a_3 k_x^3, \tag{4.1}$$

where $k_x$ is expressed in nm$^{-1}$ from the **K** point, $E$ in eV, and $a_0$=-0.004 eV, $a_1$=0.0027 eV nm, $a_2$=0.91 eV nm$^2$, $a_3$=4.524 eV nm$^3$ within the RMS error of 0.54%.

As we discussed in Chapter 3, when comparing the result for $a$=2.458 Å and $a$=2.460 Å for the ABA-stacked trilayer graphene we noted small differences in the band gap at the **K** point and the crossing point away from the **K** point between the two bands around the Fermi energy. Using the same lattice constant as well as a slightly larger lattice constant $a$=2.462 Å for ABC-stacked trilayer graphene, we do not observe any significant change at the band gap at the **K** point or the crossing point away from the **K** point, as shown in Fig. 4.3 (b). There is, however, a slightly larger band gap for $a$=2.458 Å for **k**$>$ 0.18 nm$^{-1}$. Generally, the changes in the results for the ABA- and ABC-stacked trilayer graphene follow the same trend for **k**$>$0.18 nm$^{-1}$. For **k**$<$0.18 nm$^{-1}$ while there is a slight variation in the gap for ABA-stacked trilayer graphene, there are insignificant changes for ABC-stacked trilayer graphene.

We calculated the energy contours using 50$\times$50 division around the **K** point, which results in consideration of 2500 **k**-points. For the ABC-stacked trilayer graphene energy contour plots up to the energy values 0.846 eV above and 0.72 eV below the Fermi level and close to the **K** point are shown in Fig. 4.4 (a) and (b), respectively. In this figure, the lowest energy contour appears to be located at 0.2555 nm$^{-1}$ from the **K** point and 45 meV above the Fermi level. These energy contour plots clearly indicate prominent trigonal warping – stretching of equienergy lines along directions at 120$^o$ from each other. Our first-principles results have good agreement with the tight-binding results [167].

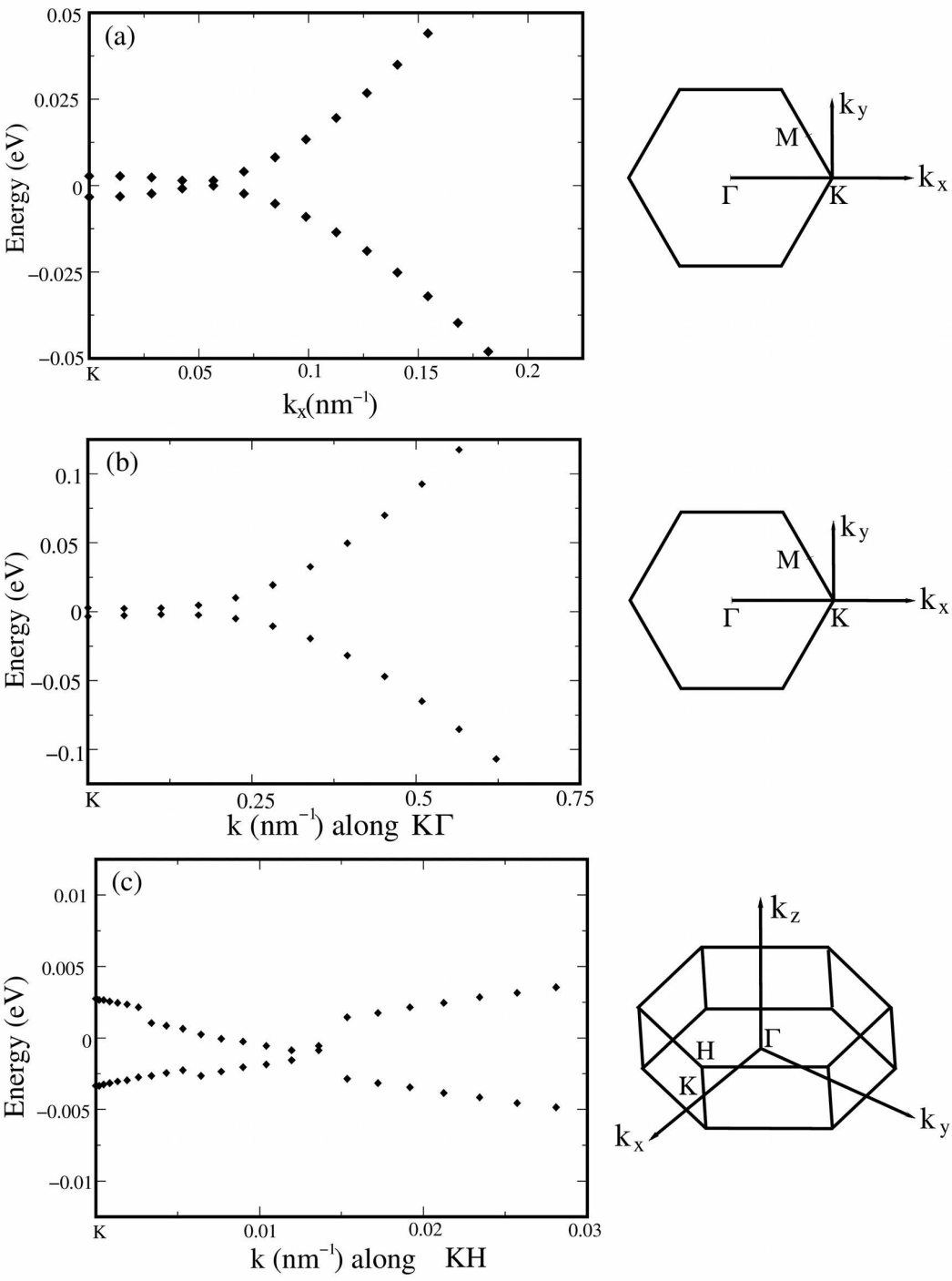


Figure 4.2: Band structure of the ABC-stacked trilayer graphene close to **K** point (a) along $k_x$, (b) along $-k_x$ (the **K**Γ direction), and (c) along the surface normal (the **KH** direction). The Fermi level is set to zero energy. The hexagonal Brillouin zone is also shown. Filled symbols represent numerically calculated data points.

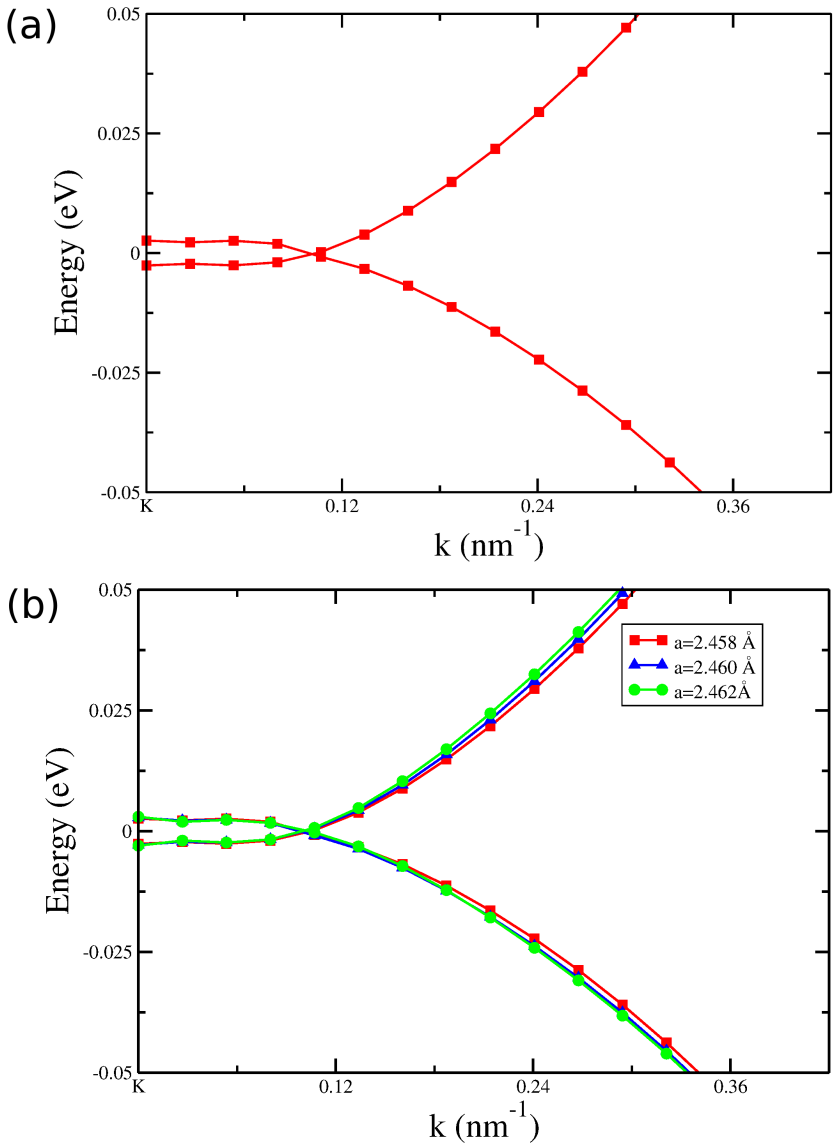


Figure 4.3: (a) Band structure of ABC-stacked $N$=3 layer graphene close to **K** point using our equilibrium lattice constant $a$=2.458 Å and (b) different lattice constants around the equilibrium value. Filled symbols represent numerically calculated data points and lines are joining the data points.

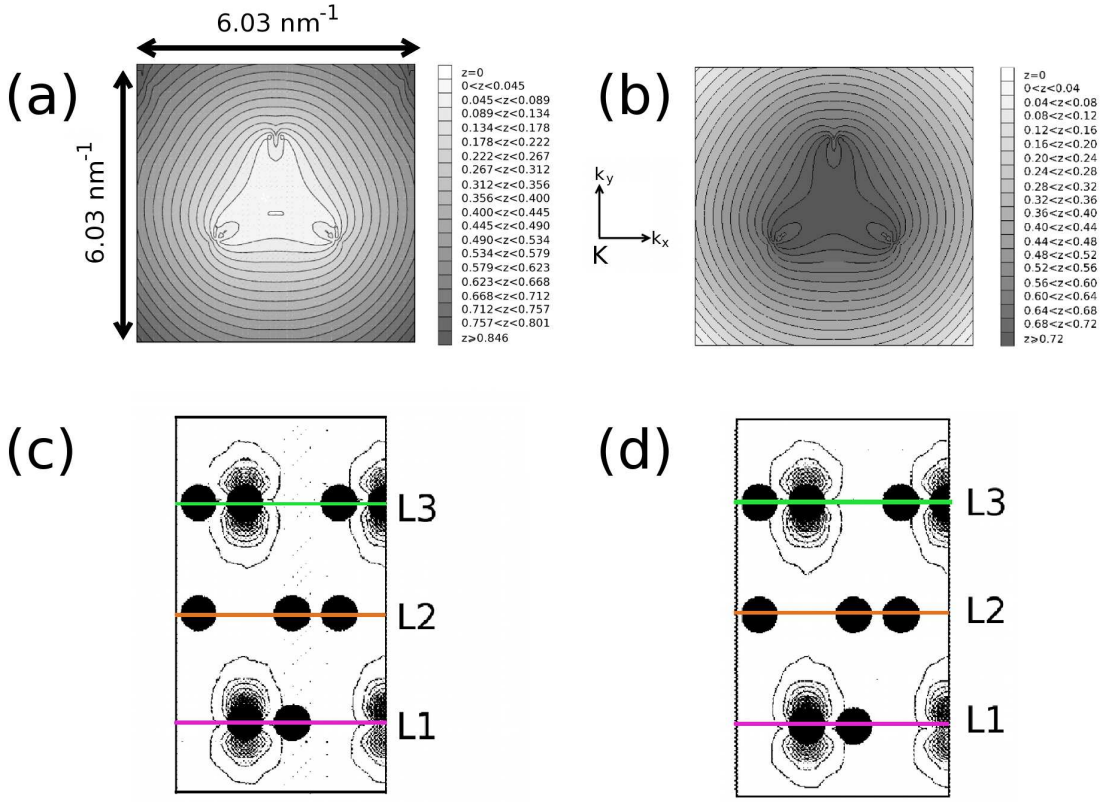


Figure 4.4: The electronic energy contour plots of ABC-stacked trilayer graphene for (a) the lowest conduction band up to 0.846 eV above the Fermi level and (b) the highest valence band up to 0.72 eV below the Fermi level. The energy values (in eV) are indicated on the right hand side with the minimum value shown in the lighest colour and the highest value with the darkest colour. Electronic charge density contour plots at the **K** point are also given for (c) the lowest conduction band and (d) the highest valence band.

### 4.2.2 ABC-Stacked N-layer Graphene

We now model ABC-stacked multilayer graphene. In particular, we consider the $N$-layer stacking sequences ABCA, ABCAB, and ABCABC with $N$=4, $N$=5 and $N$=6, respectively. For the $N$=4 multilayer the top layer graphene sheet is exactly above the bottom layer of the ABC-stacked trilayer. In general, for $N$ >3 the top layer graphene sheet lies exactly above the ($N$-3)$^{\mathrm{rd}}$ layer(s).

The inner-most pair of bands for $N$=4 are shown in Fig. 4.5 (a). The two bands are degenerate at the **K** point at which the Fermi level lies. These bands split by a maximum of 2.5 meV slightly away from **K** along $k_x$ and then cross each other at a slightly larger value of the wavevector. This result is also in good agreement with the work in Ref. [153]. The inaccuracy in the band results can be discussed by comparing the result for $a$=2.458 Å, $a$=2.460 Å, and $a$=2.462 Å. As presented in Fig. 4.5 (b), while the degeneracy at the **K** point is maintained and the position of crossing between the two bands remains unchanged at other **k**-points, the band gap changes by the maximum value of 5.6 meV for the wavevector nearly half way between the **K** and the crossing point. The pronounced trigonal warping seen for $N$=3 system has been reduced for the $N$=4 case. Figure 4.6 (a) and (b) show the energy contour plots up to 0.792 eV above and 0.648 eV below the Fermi level.

As shown in Fig. 4.7 (a), when the graphene thickness is increased to $N$=5 layers, the inner-most pair of bands become quite flat around the Fermi level very close to the **K** point. With the increase in the wavevector along $k_x$, these bands cross each other twice in the close vicinity of the **K** point. Between the two crossings there is a maximum splitting of approximately 10 meV between these bands. The amount of this splitting is larger than that for the $N$=3 and $N$=4 cases. We examined possible inaccurancies in the splitting and the crossing point by using $a$=2.460 Å and $a$=2.462 Å. The first crossing point remains unshifted but only

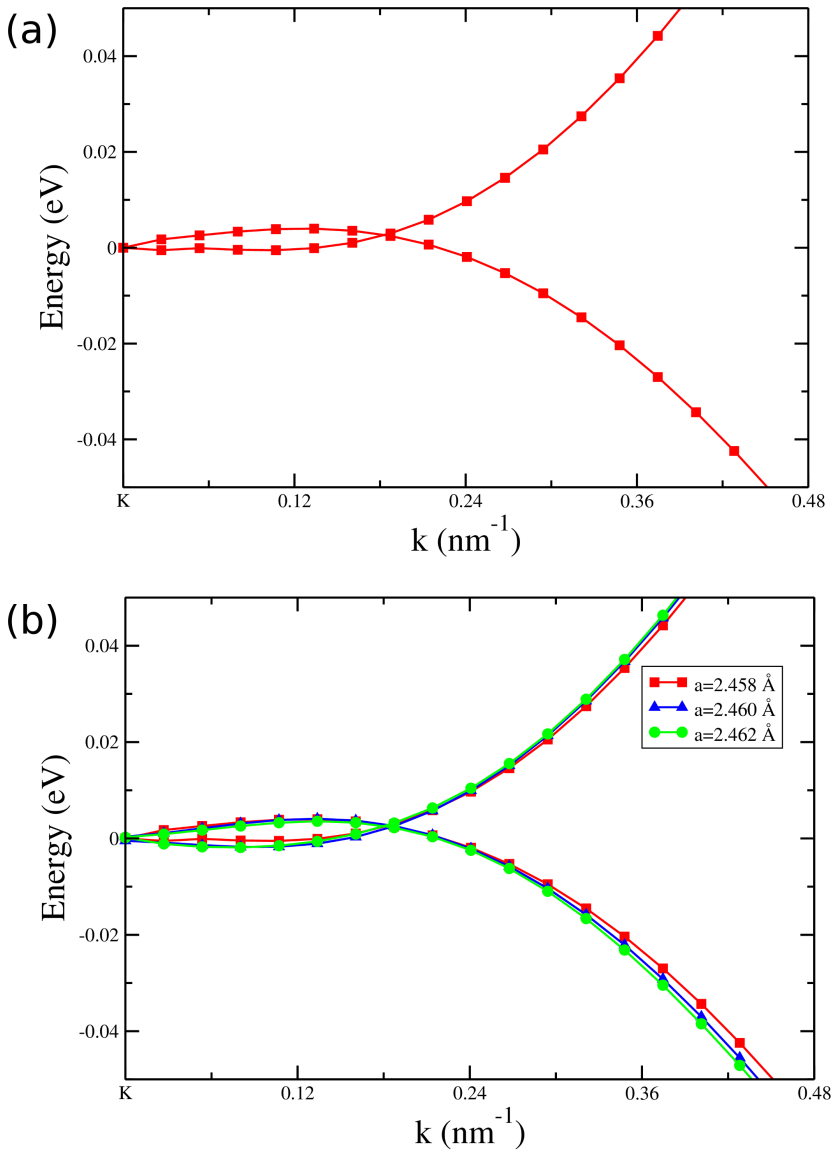


Figure 4.5: (a) Band structure of ABC-stacked $N$=4 layer graphene close to **K** point using our equilibrium lattice constant $a$=2.458 Å and (b) different lattice constants ($a$=2.460 Å and $a$=2.462 Å). Filled symbols represent numerically calculated data points and lines are joining the data points.

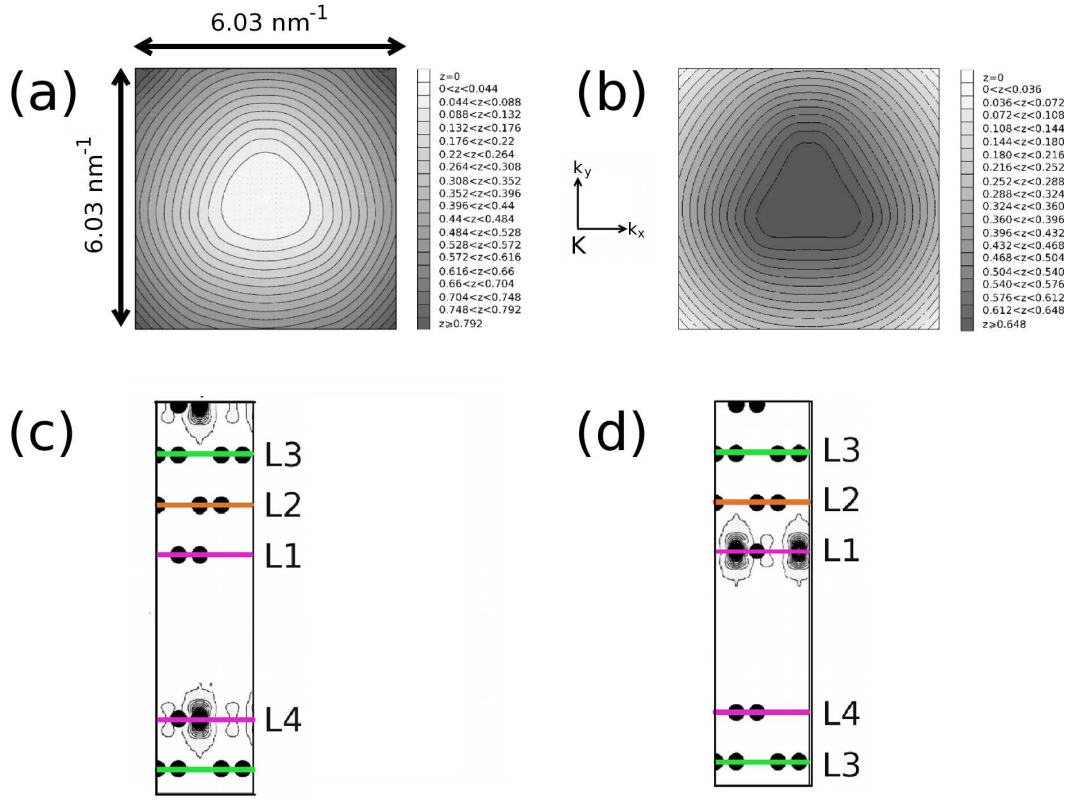


Figure 4.6: The electronic energy contour plots of ABC-stacked $N$=4 layer graphene for (a) the lowest conduction band up to 0.792 eV above the Fermi level and (b) the highest valance band up to 0.648 eV below the Fermi level. The energy values (in eV) are indicated on the right hand side with the minimum value shown in the lighest colour and the highest value with the darkest colour. Electronic charge density contour plots at the **K** point are also given for (c) the lowest conduction band and (d) the highest valence band.

the second crossing point slightly changed for $a$=2.462 Å, as seen in Fig. 4.7 (b). The splitting of 3.8 meV at the **K** point is almost unchanged but the maximum splitting of 10 meV at **k**=**K**+0.19 nm$^{-1}$ is decreased by 3 meV for $a$=2.462 and increased by almost 1 meV for $a$=2.460 Å. The energy contour plots in Fig. 4.8 (a) and (b) reveal that the trigonal warping present for $N$=3 is almost lost for the $N$=5 system.

The electronic band structure of the ABC-stacked 6-layer graphene is presented in Fig. 4.9 (a). There is a small amount of separation between the two bands around the Fermi level at the **K** point. These bands become degenerate slightly away from **K** point and remain so for some distance along $k_x$, in contrast with the $N$=3, 4, 5 cases. When there is an error in the estimation of the lattice constant $a$ the changes in the band is very small, as shown in 4.9 (b). The trigonal warping is found to be quite weak for this system, as seen in Fig. 4.10 (a) and (b).

Figure 4.11 shows the electronic densities of states for the $N$-layer ABC-stacked multilayer graphene systems very close to the Dirac point. As illustrated in panel (a), for the $N$=3 multilayer we observe two peaks in the occupied region at energies $\mathrm{E_F} - 3.5$ meV and $\mathrm{E_F} - 360$ meV. In the unoccupied region two peaks are obtained at energies $\mathrm{E_F} + 2.5$ meV and $\mathrm{E_F} - 340$ meV. The gap of 6 meV between the two peaks closest to the Fermi level is clarified in the inset of panel (a). There are also two peaks in the density of states very close to the Dirac point for the $N = 4, 5, 6$ systems, as shown in panel (b). For $N = 4, 5, 6$, respectively, there are sharp peaks at $\mathrm{E_F} - 0.5$ meV, $\mathrm{E_F} - 1$ meV and $\mathrm{E_F} - 2$ meV in the occupied region and at $\mathrm{E_F} + 0.5$ meV, $\mathrm{E_F} + 1$ meV and $\mathrm{E_F} + 0.2$ meV in the unoccupied region.

In order to examine the origin of the HOMO and LUMO energy states at the **K** point, we made partial charge density plots in a vertical plane for ABC-stacked $N$-layer graphene. It is found that for $N$=3 and $N$=6 both HOMO and LUMO states are derived from the appropriate combinations of the $\mathrm{p}_z$ orbitals on the first basis atom ($\mathrm{C}_{11}$) on the bottommost layer and the second basis atom ($\mathrm{C}_{32}$

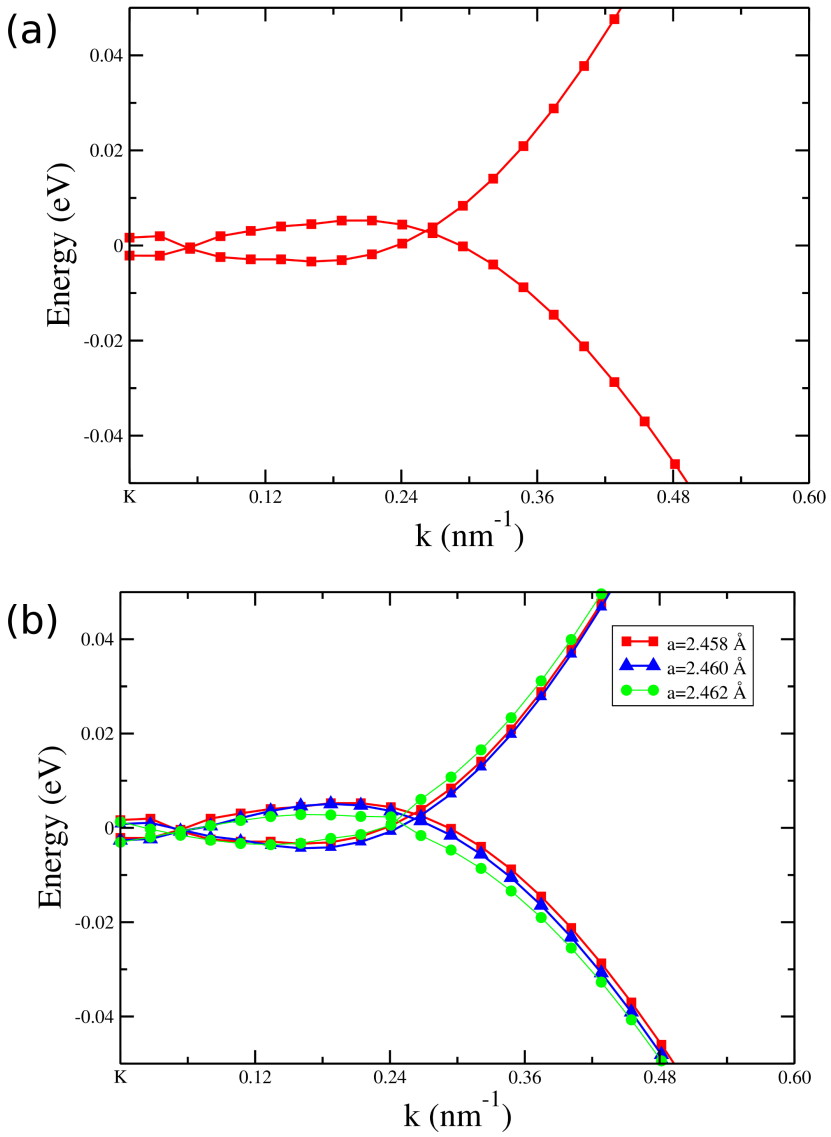


Figure 4.7: (a) Band structure of ABC-stacked $N$=5 layer graphene close to **K** point using our equilibrium lattice constant $a$=2.458 Å and (b) different lattice constants ($a$=2.460 Å and $a$=2.462 Å). Filled symbols represent numerically calculated data points and lines are joining the data points.

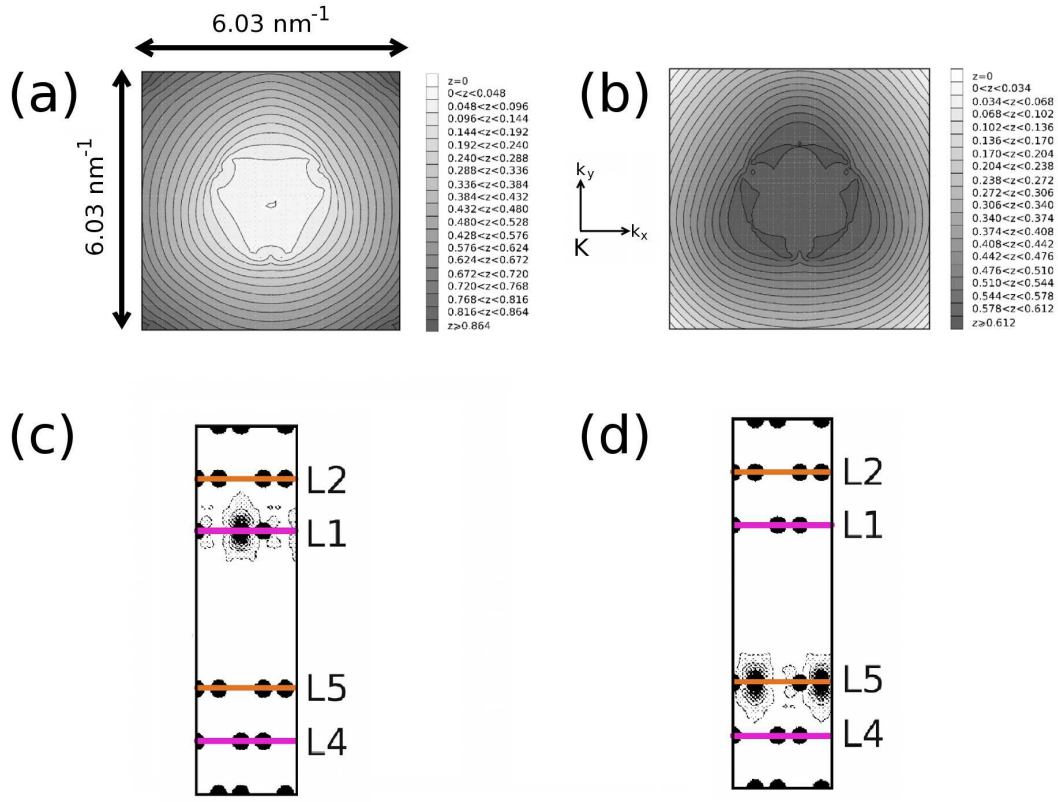


Figure 4.8: The electronic energy contour plots of ABC-stacked $N$=5 layer graphene for (a) the lowest conduction band up to 0.864 eV above the Fermi level and (b) the highest valence band up to 0.612 eV below the Fermi level. The energy values (in eV) are indicated on the right hand side with the minimum value shown in the lighest colour and the highest value with the darkest colour. Electronic charge density contour plots at the **K** point are also given for (c) the lowest conduction band and (d) the highest valence band.

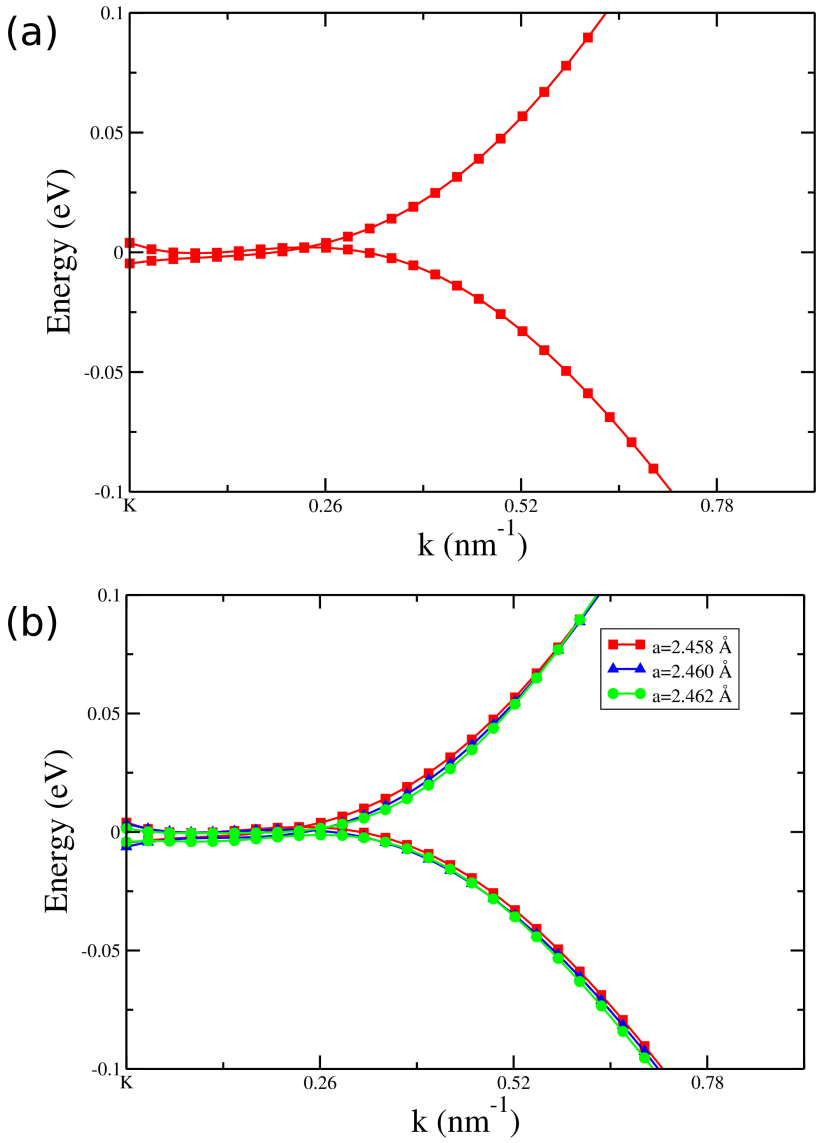


Figure 4.9: (a) Band structure of ABC-stacked $N$=5 layer graphene close to **K** point using our equilibrium lattice constant $a$=2.458 Å and (b) different lattice constants ($a$=2.460 Å and $a$=2.462 Å). Filled symbols represent numerically calculated data points and lines are joining the data points.

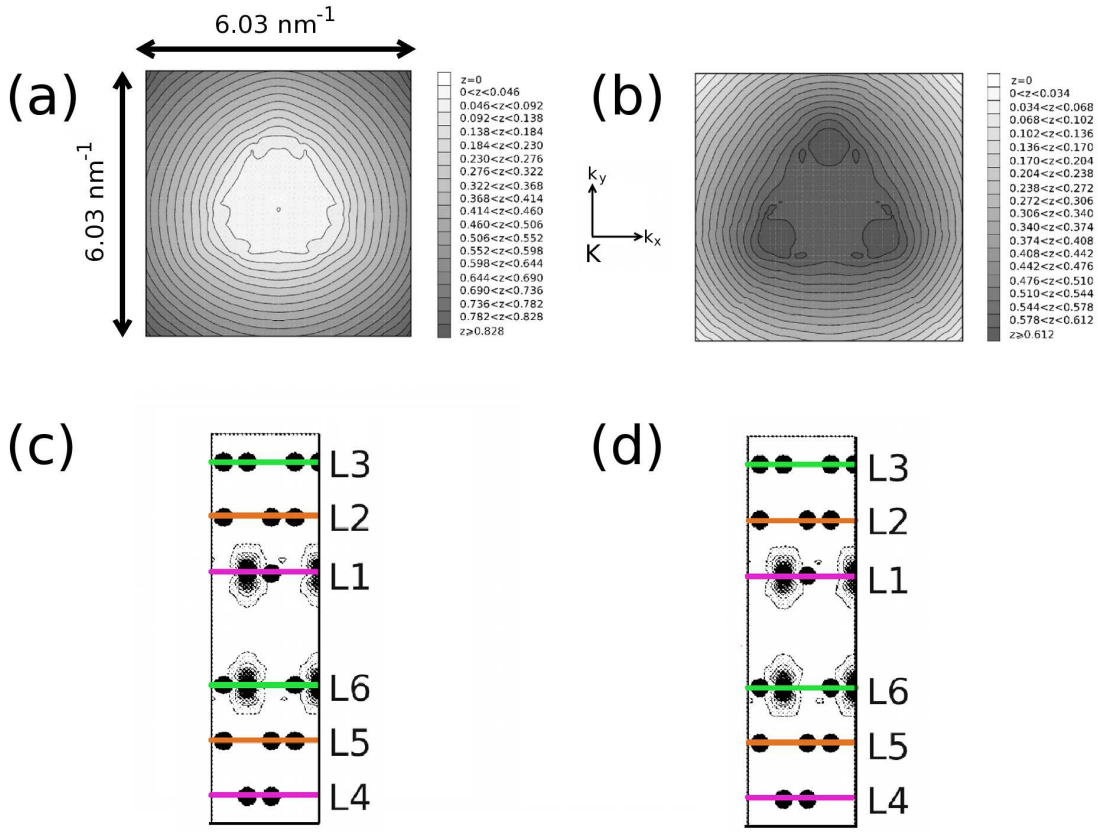


Figure 4.10: The electronic energy contour plots of ABC-stacked $N$=6 layer graphene for (a) the lowest conduction band up to 0.828 eV above the Fermi level and (b) the highest valence band up to 0.612 eV below the Fermi level. The energy values (in eV) are indicated on the right hand side with the minimum value shown in the lighest colour and the highest value with the darkest colour. Electronic charge density contour plots at the **K** point are also given for (c) the lowest conduction band and (d) the highest valence band.

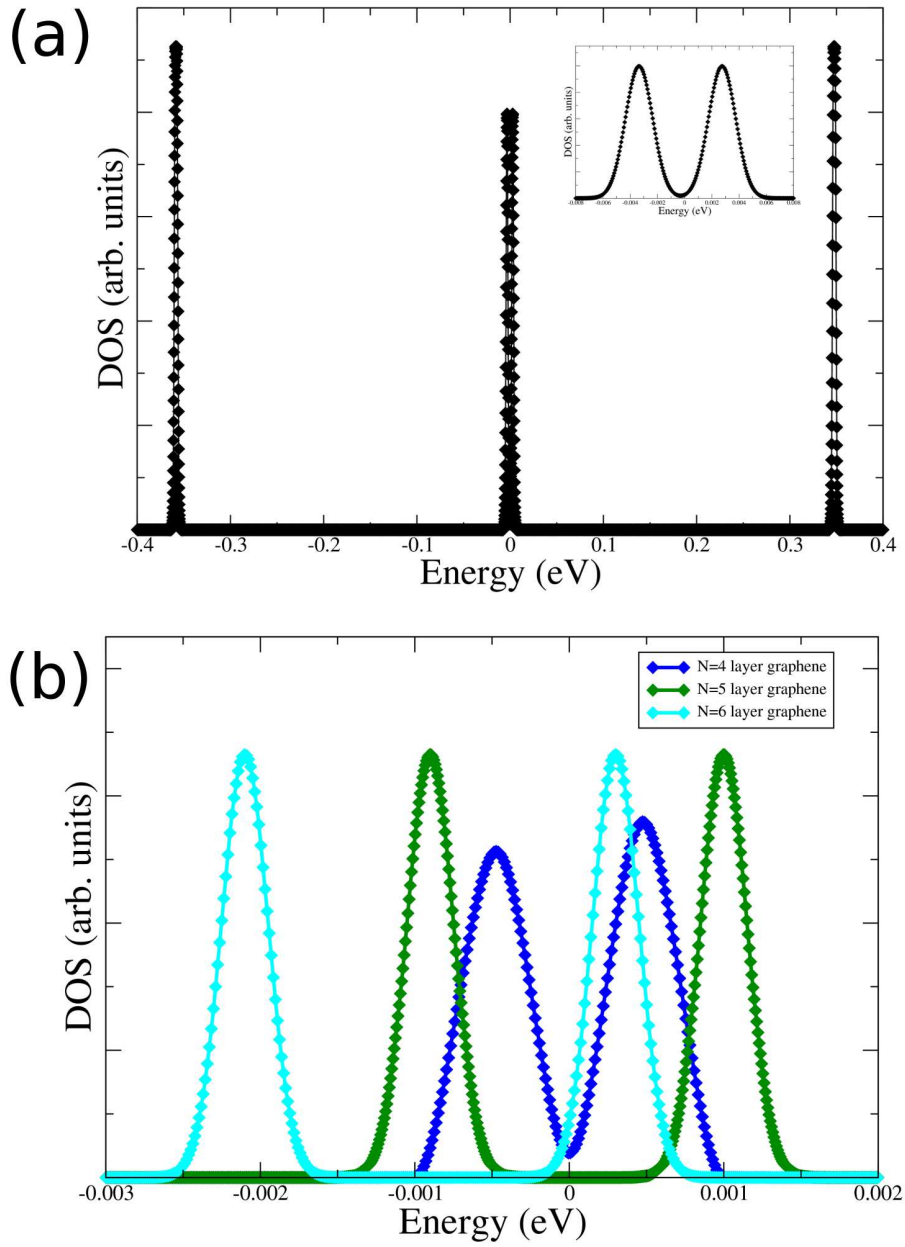


Figure 4.11: Panel (a) shows the density of states close to the Fermi level for the ABC-stacked $N$=3 layer graphene. The two peaks closest to the Fermi level are zoomed as an inset. Panel (b) shows the results for the two peaks closest to the Fermi level for the $N$=4, 5, 6 layer graphene systems. The energy zero is set at the Fermi level. Filled symbols represent numerically calculated data points.

or $C_{62}$) on the topmost layer. In contrast, for $N$=4 and $N$=5, both HOMO and LUMO have maximum contribution from the $p_z$ orbital of only one basis atom, either on the bottommost or the uppermost layer. The largest contribution for HOMO comes from $C_{11}$ for $N$=4 and from $C_{52}$ for $N$=5. The largest contribution for LUMO comes from $C_{42}$ for $N$=4 and from $C_{11}$ for $N$=5. These features can be seen in the contour plots presented in the Figs. 4.4-4.10 (c) and (d). Besides our calculations, the underlying physics behind these locations needs to be studied in future in more detail.

## 4.3 Summary

In summary, we have studied the ABC-stacked $N$-layer graphene by using the density functional theory within the local approximation and the plane wave pseudopotential method. The dispersion of $\pi/\pi^*$ bands close to Dirac point is established to show a mixture of cubic, quadratic, and linear behaviours for the ABC-stacked trilayer graphene. Equienergy contour plots clearly indicate prominent trigonal warping in the ABC-stacked system– stretching of equienergy lines along directions at $120^o$ from each other. ABC-stacked systems with layer numbers $N > 3$ are characterised by much reduced level of trigonal warping. Our first-principles results for the warping of equienergy contours confirm the tight-binding results presented by Koshino and McCann [164]. Density of states calculations reveal two sharp peaks close to the Fermi level for the systems with $N = 4, 5, 6$. From an analysis of partial charge density plots, we have established that the highest occupied state and the lowest unoccupied state at the **K** point originate from the $p_z$ orbitals of carbon atoms in the bottom and uppermost layers of the $N$=3 and $N$=6 systems, but only from one of the layers for the $N$=4 and $N$=5 systems.

# Chapter 5

# Electronic Properties and Interband Optical Transitions of Multilayer Graphene on Hexagonal Boron Nitride

## 5.1 Introduction

Using a chemical-solution-derived method, starting from single-crystalline h-BN, Han and co-workers have successfully synthesised BN mono-atomic layer [168]. Alem *et al.* have also achieved a successful ex-situ isolation of suspended single h-BN using a combination of mechanical exfoliation and reactive ion etching [169]. The h-BN monolayer (MLBN) has a two-dimensional honeycomb structure similar to graphene but contains two chemically inequivalent atomic species per unit cell, making it an insulator with a large band gap. It has been theoretically demonstrated that by depositing graphene on the single or multilayer h-BN a small band gap can be induced [21, 170, 171]. Furthermore, the successful fabrication of gated graphene layers on h-BN substrates has been demonstrated by re-

searchers [172, 173, 174]. Graphene/BN heterobilayers have also been grown on Ru(0001) substrate by chemical vapor deposition technique [175]. More recently, theoretical investigations of disorder-limited electrical conductivity of monolayer and bilayer graphene on h-BN substrate have been presented [176]. It is, therefore, timely and important to investigate modifications of the electronic properties of multilayer graphene/h-BN systems.

In this chapter, the equilibrium atomic geometry and electronic structure of multilayer graphene adsorbed on a monolayer h-BN substrate has been investigated. When we first started to work on this systems it was not that popular and was very hard to find any experimental study about it. After a while, single layer h-BN produced experimentally and started to gain researchers attention. However, our work was one of the first theoretical study in which the multilayer graphene interfaced with monolayer h-BN and a detail investigation to describe the interaction between these layers provided. Additionally, we concluded that the monolayer graphene (MLG) sheets are weakly adsorbed on the MLBN. Furthermore, it has been shown that it is possible to open a range of band gaps in such a system. There is no significant difference in the band gap by increasing the number of h-BN layers. The origin of such gap opening is explained by analysing the planar-average electronic charge density difference for the multilayer graphene/MLBN interface along the interface normal. The importance of the interlayer interaction and stacking patterns of graphene/BN is clearly explained. It has been also shown that the electronic band gap and effective mass of bilayer (BLG) and trilayer graphene (TLG) can be modified and tuned by using MLBN as a substrate. Finally, optical interband transitions for the multilayer graphene on MLBN system have been reported.

## 5.2 Results and Discussion

Before presenting results, I made several total energy calculation to determine equilibrium parameters of graphene on h-BN system. As discussed in Chapter 3, from the calculation of total energy versus cut-off energy it is found that the choice of $E_{cut}$= 45 Ryd is totally satisfactory for graphene on h-BN system. Following the procedure described in Chapter 3, using pseudopotentials for C, B, and N the lattice constant for the joint system is obtained as 2.450$\pm$0.003 Å. This amounts to 1.2% compression of the graphene sheet compared to the equilibrium in-plane lattice constant for the graphene/BN system.

In Figs. 5.1 (a) and (b) we show the dependence, of the band gap and total energy for the graphene/h-BN system the parameter $n$ in the choice of the zone-centred Monkhorst-Pack **k**-points set. We found that a set $n \times n \times 2$, with $n \geq 20$ is required to obtain acceptably converged values of the total energy and band gap. Same calculation is repated for the set of $n \times n \times 1$ which changes total energy less than 3 meV. The reason of using $n \times n \times 2$ sets has been discussed in Chapters 3 and 4.

### 5.2.1 Graphene on Mono- and Multi-layer Boron Nitride

We first modelled the graphene/BN system using three inequivalent orientations of the graphene sheet with respect to the h-BN are considered which is shown in Figure 5.2. In configuration $\alpha$, one carbon basis atom is over B, and the other carbon basis atom is over N. In configuration $\beta$, one carbon is over N and the other is centred above the BN hexagon. In configuration $\gamma$, one carbon is over B and the other is centred above the BN hexagon. For these configurations, calculations were made with the $36 \times 36 \times 2$ grid of special **k** points and the BN layer was held fixed, and the C atoms were allowed to relax vertically along the substrate normal direction. The variation of the total energy with the vertical distance between

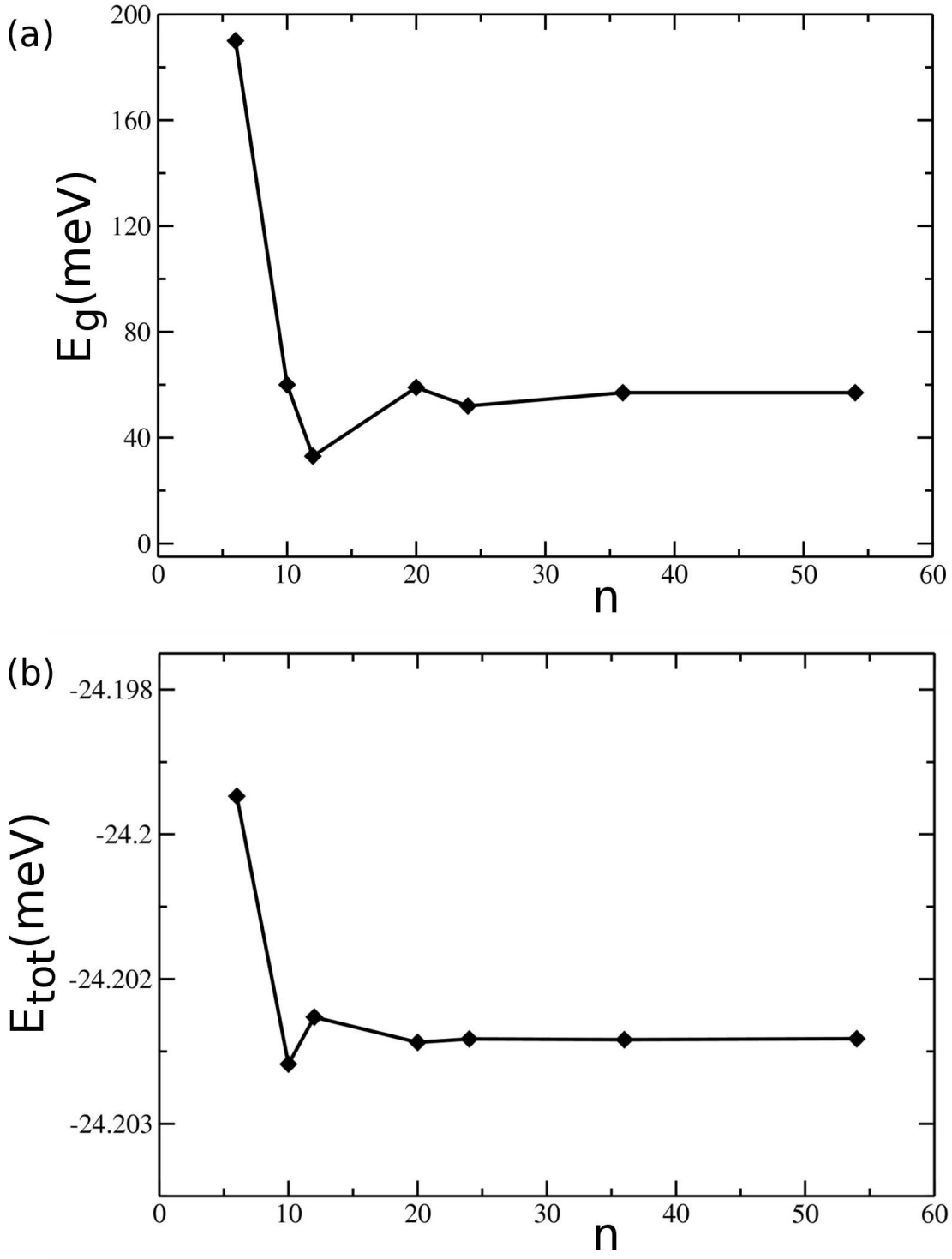


Figure 5.1: Dependence of (a) band gap and (b) total energy results for MLG deposited on MLBN as a function of the parameter $n$ in the zone-centred Monkhorst-Pack special **k**-points set. Filled symbols represent numerically calculated data points and lines are joining the data points.

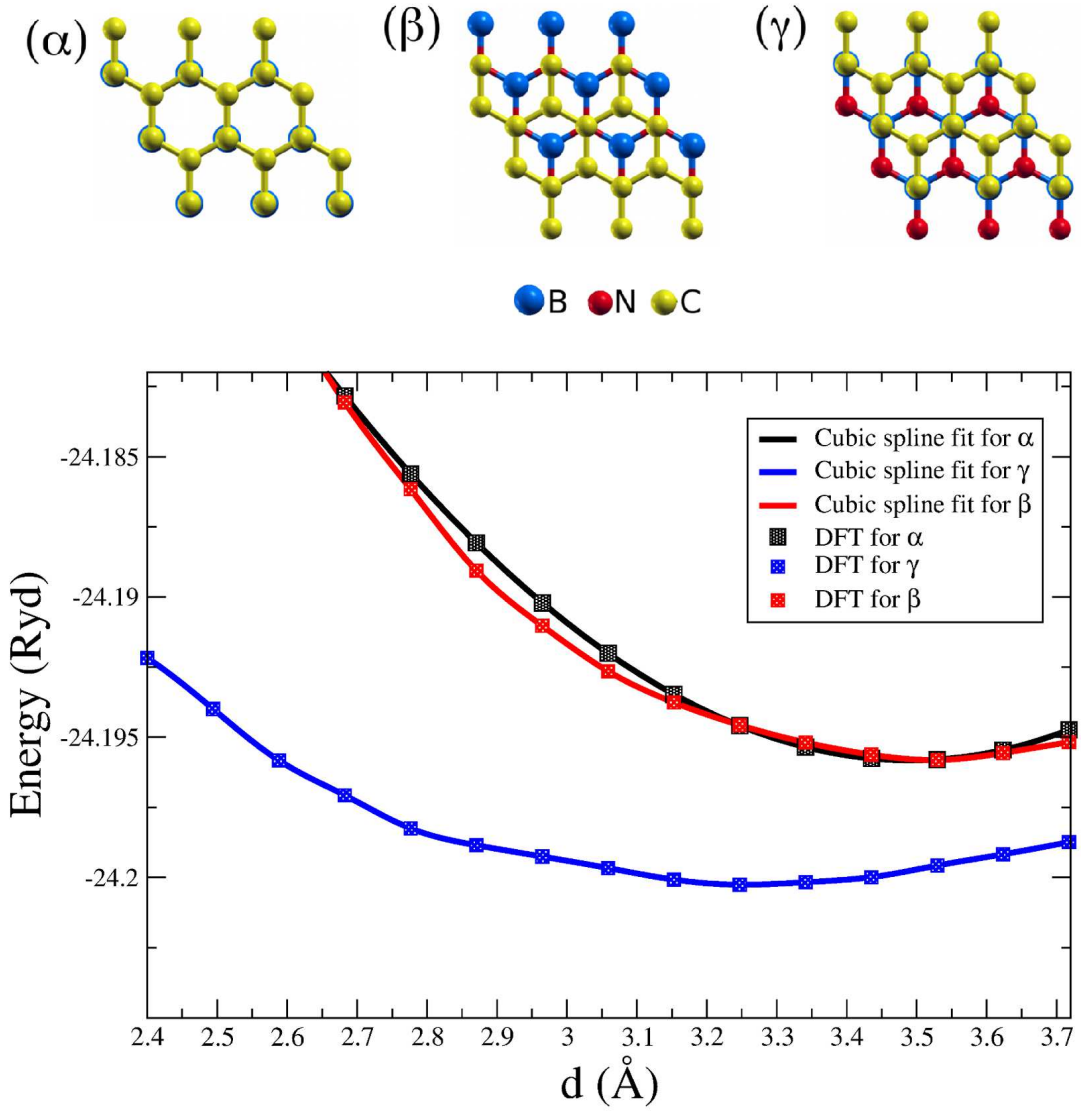


Figure 5.2: Top: Top view of three inequivalent orientations of the graphene sheet on the monolayer h-BN surface. Bottom: Variation of the total energy $E$ with the vertical distance between the graphene sheet and the BN sheet. The filled symbols show numerically calculated data points, while the curve shows the fits of the DFT data described in Chapter 3.

the graphene sheet and the BN sheet is shown in Fig. 5.2. For all distances, the lowest-energy configuration is $\gamma$. For all three configurations, the energy landscape is seen to be flat around the energy minimum. Our theoretical equilibrium separation ($d$) is found to be 3.50 Å, 3.40 Å, and 3.22 Å for configurations $\alpha$, $\beta$, and $\gamma$, respectively. The accurancy of these results is examined by making total energy calculations with a large number of $d$ values around the equilibrium separations. As the results are represented in Fig. 5.3, within the numerical noise of calculated values we found the energy minimums at $d$ values of 3.48 Å for configuration $\alpha$, 3.43 Å for configuration $\beta$, and 3.23 Å for configuration $\gamma$. We, thus, determine the error margin in estimating the numerical $d$ values as 0.02 Å, 0.03 Å, and 0.01 Å for configurations $\alpha$, $\beta$, and $\gamma$, respectively.

The adsorption energy $E_{ads}$ of the configuration $\gamma$ is obtained by using the following equation

$$E_{\mathrm{ads}} = E_{\mathrm{MLG/MLBN}} - E_{\mathrm{MLBN}} - E_{\mathrm{MLG}},$$

where $E_{\mathrm{MLG/MLBN}}$ is the total energy of the MLG/MLBN system, $E_{\mathrm{MLBN}}$ is the total energy of the MLBN, and $E_{\mathrm{MLG}}$ is the total energy of the MLG. Our calculations reveal that the estimated binding energy is 43 meV/C for this configuration. It is more stable than either of configurations $\alpha$ and $\beta$. The large C-BN distance of 3.22 Å is consistent with this low binding energy. The various total energy components (per C atom) are: (pseudo) kinetic energy (-10 meV), electrostatic energy (-11 meV), pseudopotential energy (62 meV), exchange-correlation energy (-84 meV), where the positive and negative signs indicate unfavourable and favourable components for binding. Thus, a major part of binding comes from the exchange-correlation component of the total energy.

Present work calculates atomic buckling within each unitcell. There are four atoms per unit cell for MLG/MLBN. In our calculation the two basis B and N atoms are fixed in their equilibrium position and the other two basis carbon atoms

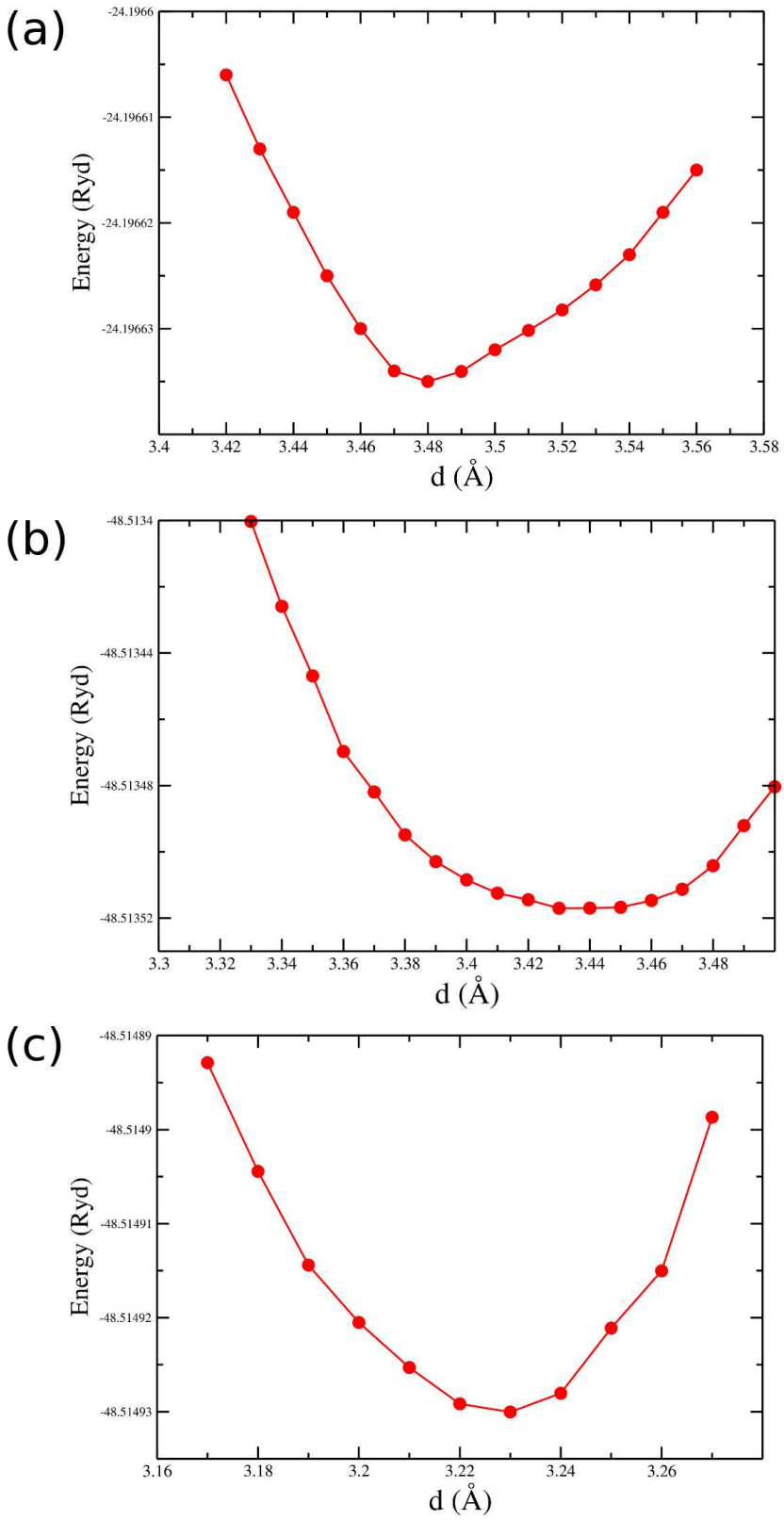


Figure 5.3: Total energies of graphene on MLBN in (a) configuration $\alpha$, (b) $\beta$, and (c) $\gamma$ as a function of the vertical distance $d$ close to our equilibrium values for all three configurations. Filled symbols represent numerically calculated data points and lines are joining the data points.

are allowed to move. After optimisation calculation, one of two basis carbon atoms in the unit cell went up and the other one went down. The changes along the $z$ direction for these basis atoms is almost zero thereby there is no buckling on graphene.

The band structure for the equilibrium geometry of graphene on MLBN, in configuration $\gamma$, is shown in Fig. 5.4. As expected, it is a mixture of the band structure of graphene and two-dimensional h-BN. The adsorption of graphene on the BN sheet has changed the nature of the electron dispersion curve at and near the **K** point in the Brillouin zone (the Dirac point for pristine graphene). There is now a tiny band gap of 57 meV at the **K** point. The band structure shows a slightly flat behaviour in the close vicinity of the **K** point, and thereafter a linear behaviour for a reasonable portion of the distance towards the zone centre. This is clarified in Figure 5.4 (b). This shows that the band structure of the MLG/MLBN is qualitatively identical to graphene. To estimate the electron velocity, I follow the same method for graphene as described in Chapter 3. The numerical band data presented in Fig. 5.5 is fitted using following equation

$$E = A_0 k + A_1. \tag{5.1}$$

where $k$ is measured from the **K** point. I estimated $A_0$=0.592 eV nm and $A_1$=0.018 eV within the RMS error of $2.9\times10^{-8}\%$ for the energy range up to 0.204 eV above the **K** point. For the energy range up to 0.463 eV above the **K** point $A_0$=0.530 eV nm and $A_1$=0.021 eV are estimated within the RMS error of $0.1\%$. Using Eq. 3.2, our estimation of the electron velocity is $0.90(\pm0.09)\times10^6$ m/s for the equilibrium lattice constant of 2.450 Å, which is similar to graphene. The 0.12 $\%$ error in the estimation of the equilibrium lattice constant decreases the velocity by 2.2 $\%$. The robustness of the band gap at the **K** point is shown in Fig. 5.6 by choosing the lattice constants within the estimated error margin ($a$=2.450$\pm$0.003 Å). The band gap at the **K** point is evaluated 57 meV with the maximum error of 4 meV.

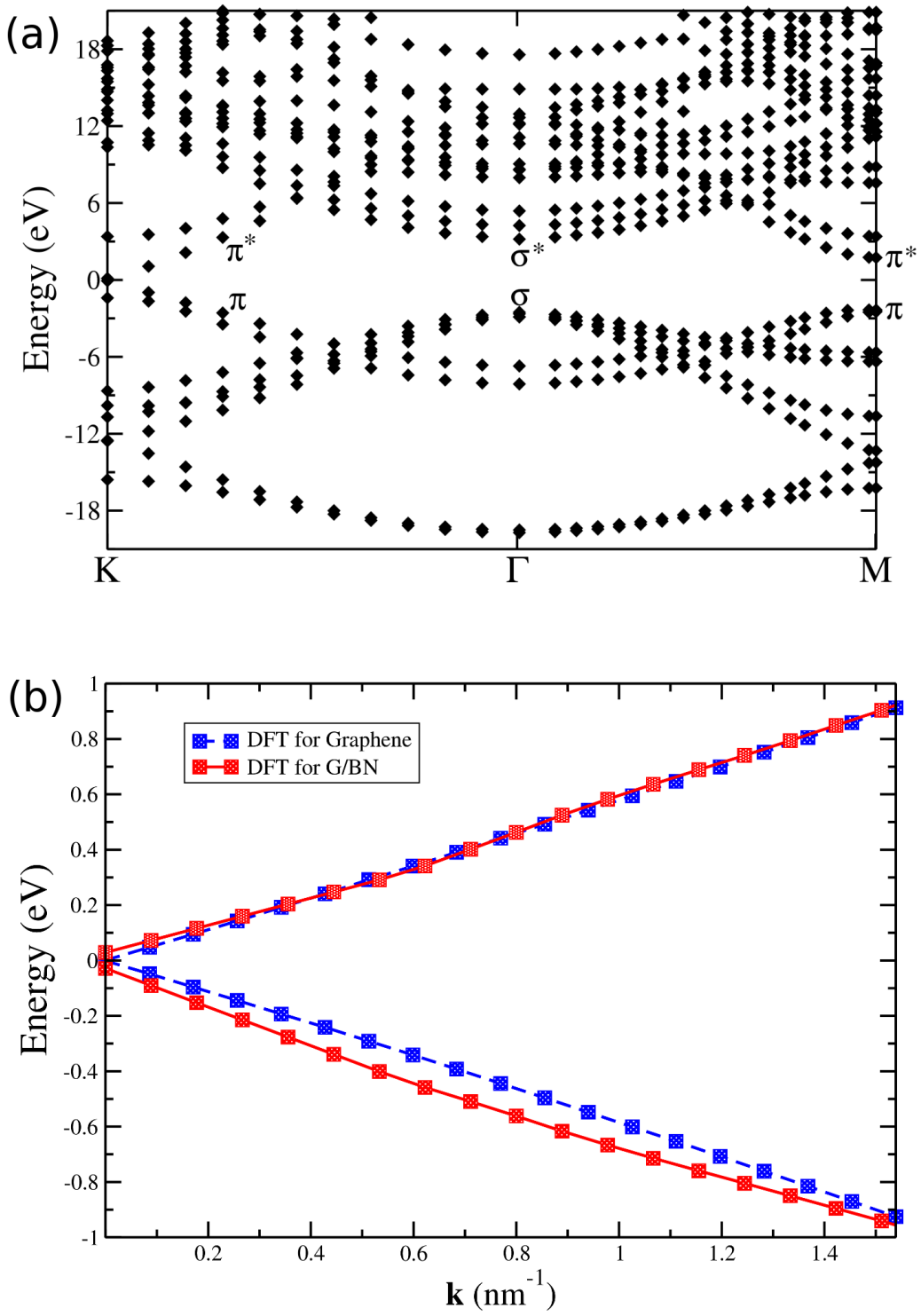


Figure 5.4: (a) The electronic structure for the equilibrium configuration of graphene adsorbed on a monolayer h-BN sheet. (b) Dispersion curves for the $\pi$ and $\pi^*$ bands very close to the **K** point. The curves for graphene are reproduced. Filled symbols represent numerically calculated data points and lines are joining the data points.

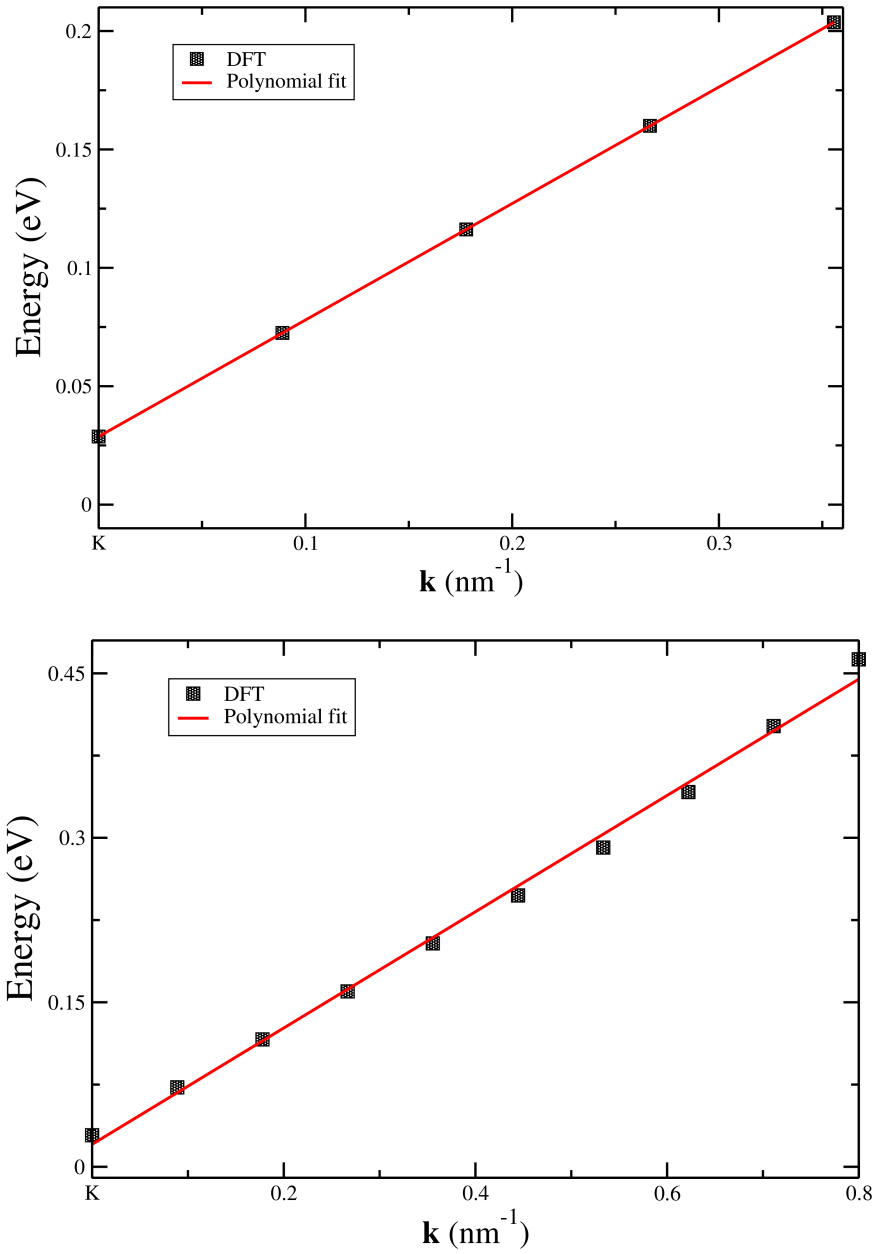


Figure 5.5: The polynomial fit of the $\pi^*$ bands using two ranges of energies (up to 0.204 eV and up to 0.463 eV) above the **K** point for MLG/MLBN system. The symbols show numerically calculated data points and the line shows a polynomial fit of the DFT data as described in the text.

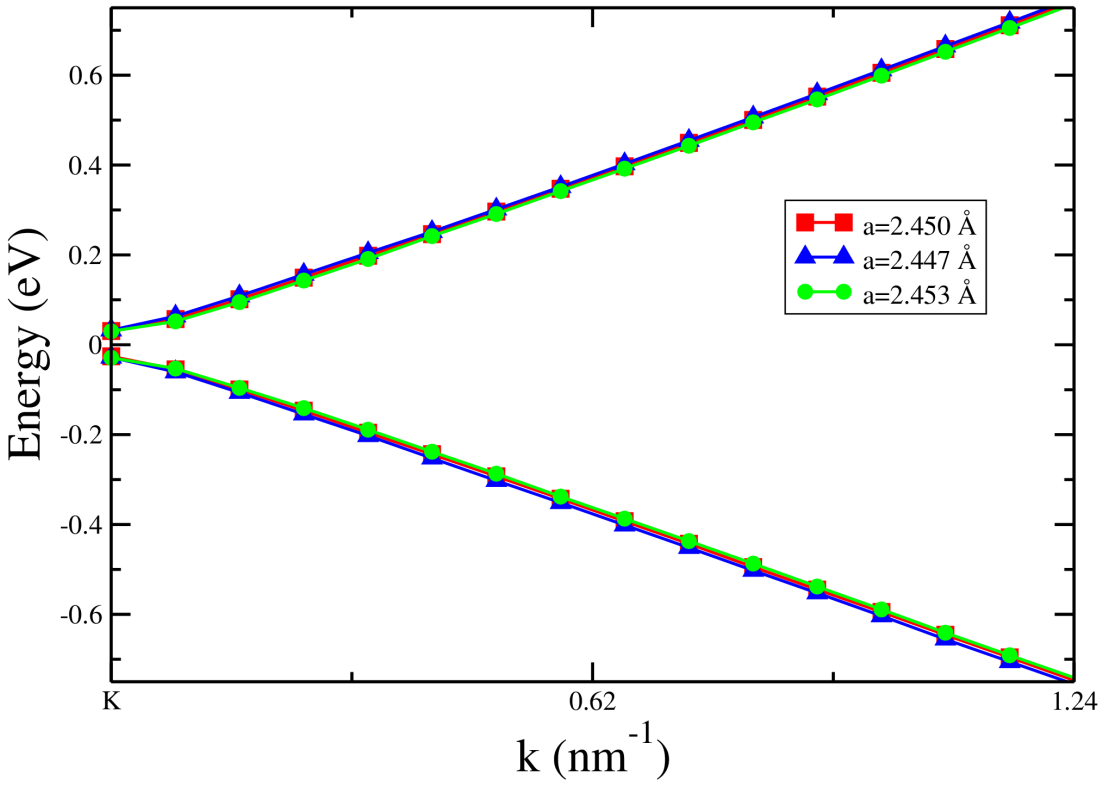


Figure 5.6: (a) The dispersion of the inner pair of $\pi/\pi^*$ very close to the **K** point for MLG/MLBN interface system using different lattice constants around the equilibrium value of 2.450 Å. Filled symbols represent numerically calculated data points and lines are joining the data points.

In reality there exists a lattice mismatch between graphene and h-BN. Such a lattice mismatch is reported to lead to a Moiré superstructure [177, 178], with a periodicity much larger than we can afford to make first-principles calculations for. We have, however, estimated the range of band gap change of our systems by using the primitive unit cell, viz. the (1×1) cell, but using three lattice constants: 2.45, 2.485, and 2.503 Å which correspond to the equilibrium values for graphene, graphene/BN and h-BN systems, respectively. The maximum difference in the band gap values for these lattice constants is found to be 6 meV. Thus we expect the effect of a realistic lattice mismatch not to alter the band gap result reported in this work.

Further calculations were made for the interface between monolayer graphene and thicker layers of h-BN. It was found that the band gap at the **K** point changes little. Using the equilibrium lattice constant ($a$=2.450 Å) we found energy gaps of 62 meV, 42 meV and 56 meV with the h-BN layer thickness changing to two, three and four layers, respectively. We do not observe any significant changes in these band gap when the slightly smaller ($a$=2.447 Å) or larger ($a$=2.453 Å) than the equilibrium lattice constant of $a$=2.450 Å is used in these interface systems. We also estimated an effective mass for electron of $m^*$=0.0047($\pm$0.0008)$m_e$ for graphene on four layers of h-BN following the same prodecure for estimating effective mass of bilayer graphene in Chapter 3. This result is in good agreement with the value reported by Giovannetti *et al.* [21]. It is interesting to note that this value of the effective mass is smaller than bilayer and trilayer graphene [179]. Such a decrease in effective mass could prove significant for an enhancement of carrier mobility.

In order to understand the origin of the development of the tiny-gap semiconducting nature of the graphene/BN interface, we examined the planar-average electronic charge density difference for the configurations $\alpha$ and $\gamma$ along the in-

terface normal, defined as follows

$$\Delta\rho = \rho[\mathrm{MLG/MLBN}] - \rho[\mathrm{MLG}] - \rho[\mathrm{MLBN}], \tag{5.2}$$

where $\rho[\mathrm{MLG/BN}]$, $\rho[\mathrm{MLG}]$ and $\rho[\mathrm{MLBN}]$ represent the charge density of the MLG/BN, MLG, and MLBN systems, respectively. As shown in Figure 5.7, there is a redistribution of the charge density around the graphene sheet: with an increase (decrease) towards (away from) the MLBN sheet. This leads to the development of a dipole across the graphene sheet. The magnitude of the dipole moment per unit cell in the $z$ direction can be computed as follows:

$$p = -\int \rho(z) z \mathrm{d}z + \sum_i Z_i e z_i, \tag{5.3}$$

where $\rho(z)$ is the valence electron density integrated over the *x-y* plane [$\rho(z) \geq 0$ by definition], $Z_i e$ is valence charge on the $i^{\mathrm{th}}$ atom in the unit cell, $-e$ is the electronic charge ($e > 0$), and $z_i$ is the *z*-coordinate of the $i^{\mathrm{th}}$ atom. We estimated the electric dipole moment of magnitude 0.019 Debye for configuration ($\gamma$). The corresponding development of the electrostatic potential across the graphene sheet was numerically calculated using the expression

$$\Delta V = -4\pi e p. \tag{5.4}$$

Our estimated magnitude of the dipole potential is 0.102 eV nm$^{-1}$. It is the development of this internal electrostatic potential that produces the band gap of 57 meV for the MLG/MLBN system. This may be interpreted as internal Stark effect.

There is insignificant difference in the band gap and dipole moment with increasing layer thickness of h-BN. However, for the four-layer BN substrate, the behaviour of bands at the **K** point becomes quadratic. We also considered superlattice (with interlayer spacing 3.22 Å) and nanoribbon formations with MLG and MLBN using the configuration $\gamma$. While the superlattice becomes metallic, the

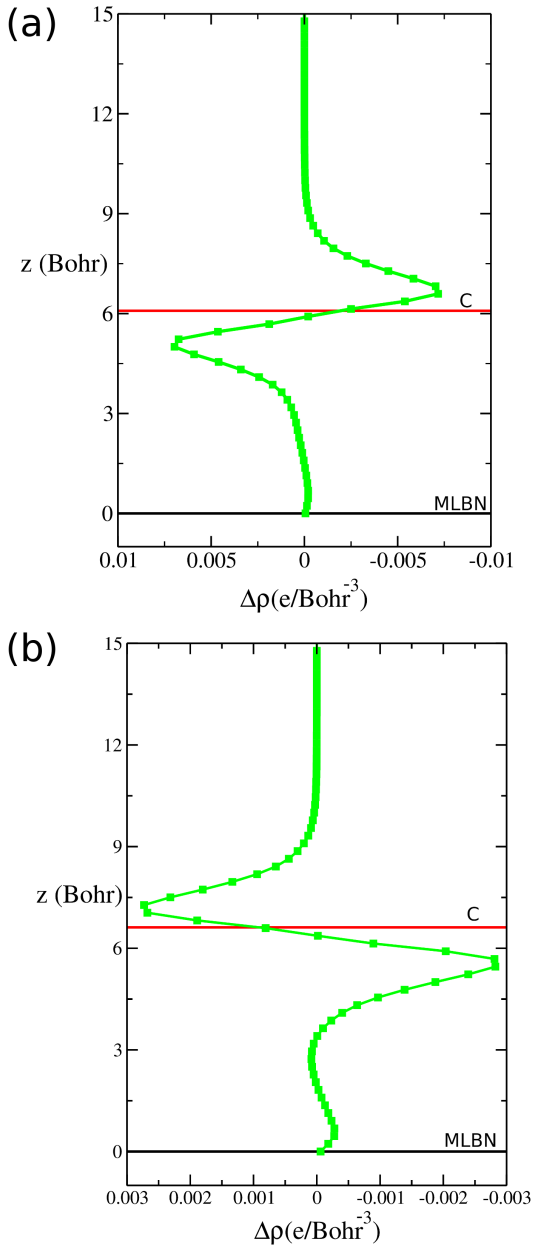


Figure 5.7: The variation of the electronic charge density difference $\Delta\rho$ across the graphene sheet, due to graphene/BN interface formation, along the interface normal direction for (a) the $\gamma$ and (b) $\alpha$ configurations. Red and black lines indicate the locations of graphene and a monolayer boron nitride planes, respectively.

ultrathin armchair nanoribbon (of width 2.45 Å) exhibits a band gap of 1.84 eV at the zone centre. The band gap of the MLG-MLBN nanoribbon is larger than the band gap (1.48 eV) of the MLG nanoribbon. While the band gap for the graphene nanoribbon is produced by the confinement effect, the gap for the MLG-MLBN nanoribbon is a joint result of confinement and the internal (dipolar) field.
To investigate the development of the electrostatic potential across the graphene sheet, we calculated the charge density along the B-C bond for the configurations $\alpha$ and $\gamma$. As shown in Figure 5.8, while there is a weak bonding between the B and C atoms in configuration $\gamma$ (panel (a)), there is practically no bonding between them in configuration $\alpha$ (panel (b)). This is consistent with the larger interlayer separation for configuration $\alpha$. Thus, we may conclude that the difference in the symmetry between the two layers affects the electronic asymmetry and leads to changes in interlayer spacing, total energy, and dipole moment.

### 5.2.2 Bilayer Graphene on Monolayer Boron Nitride

The atomic structure of the BLG/MLBN system is shown in Fig. 5.9 (a). In this system, AB-stacked BLG with the interlayer distance of 3.33 Å is deposited on MLBN by using the most stable configuration of the MLG/MLBN as presented previously. The distance of 3.22 Å was used between the MLBN and the BLG. To optimise the structure, the BN layer was held fixed, and the BLG was allowed to relax. After the optimisation, the bottom and top layers of the BLG are buckled by 0.01 Å and 0.02 Å, respectively. The binding energy of 27 meV/C is estimated for the BLG/MLBN system. There is a band gap of 278 meV at the **K** point for the lattice constant of $a$=2.450 Å and inter atomic layer distances mentioned earlier. The dispersion curves for $\pi/\pi^*$ show a quadratic behaviour near the **K** point as presented in Fig. 5.10 (a). The robustness of the band gap at the **K** point with the lattice constant $a$ is shown in Fig. 5.10 (b). We establish the maximum error of 21

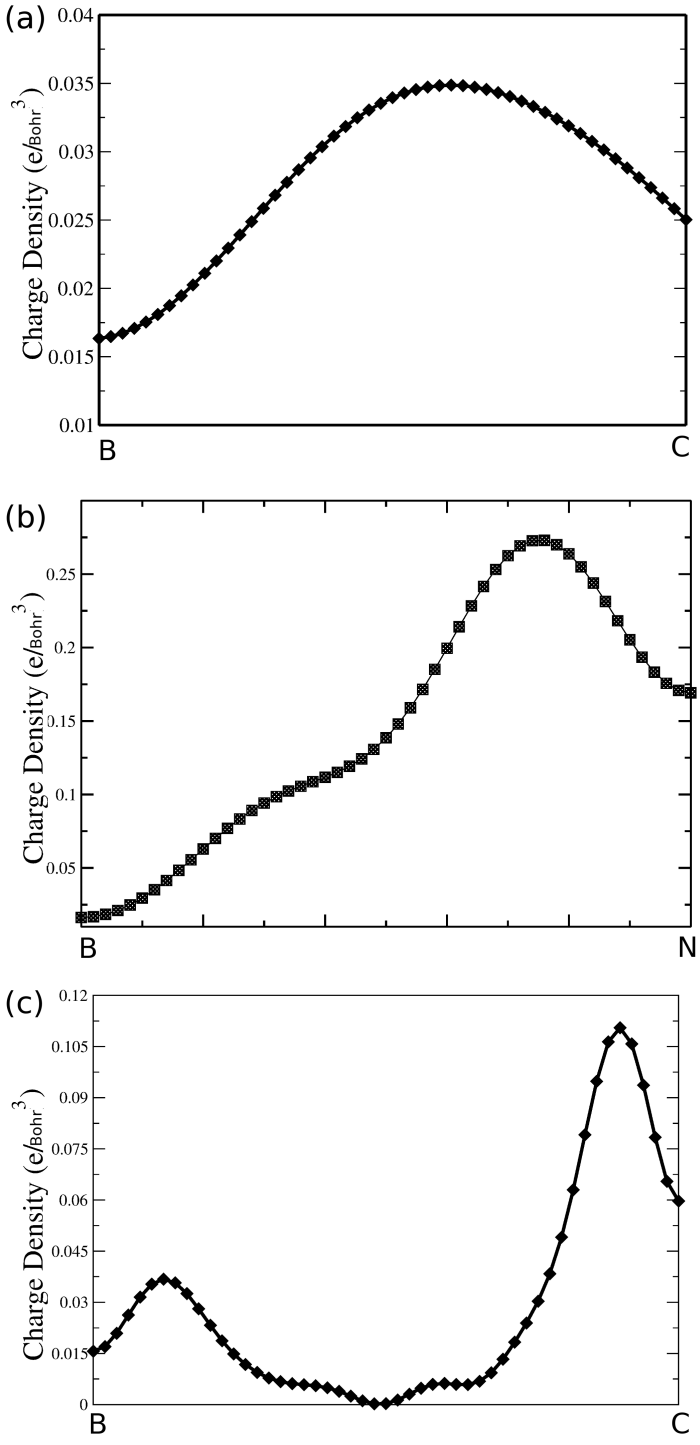


Figure 5.8: The electronic charge density (a) along the B-C and (b) B-N bonds for configuration $\gamma$ and (c) along the B-C bond for configuration $\alpha$.

meV in the band gap due to a possible error margin in the estimate of $a$.
The results are presented here suggest that the minimum of the lowest conduction band has shifted from the **K** point to **k**=**K**+0.48 nm$^{-1}$. By considering data points up to 0.045 eV and up to 0.081 eV above the minimum as represented in Fig. 5.11 and following the procedure adopted for bilayer graphene in Chapter 3 we estimated an effective mass for electron of 0.0021($\pm$0.0003)$m_e$ for the BLG/MLBN system using the equilibrium lattice constant of 2.450 Å. This value of the effective mass is almost ten times smaller than the value of effective mass for the BLG. These results suggest that the electronic properties of the BLG can be altered using the MLBN substrate. Using different lattice constant around the equilibrium value we noted that the effective mass increased to 0.0025($\pm$0.0002)$m_e$ and 0.0024($\pm$0.0003)$m_e$ for the lattice constants $a$=2.447 Å and $a$=2.453 Å, respectively.

As I explained the origin of the tiny-gap for the MLG/MLBN system, we similarly found that there is a charge re-distribution around the bottom and top layer of the BLG (see Fig. 5.7 (b)) and leads to a band gap of 278 meV with the calculated magnitude of the electrostatic potential of 0.083 eV nm$^{-1}$. There are both theoretical and experimental calculations that the application of an external electric field perpendicular the layers can induce a band gap for BLG [180, 181]. Our result suggests that a band gap can also be opened without the application of an external field, but by generating an *internal field* achieved by synthesising a monolayer graphene on a binary semiconducting or insulating substrate, such as a monolayer h-BN.

### 5.2.3 Trilayer Graphene on Monolayer Boron Nitride

As presented in Fig. 5.12 (a), we modelled TLG/MLBN system. The ABA-stacked TLG is adsorbed on the MLBN using the configuration of the MLG/MLBN sys-

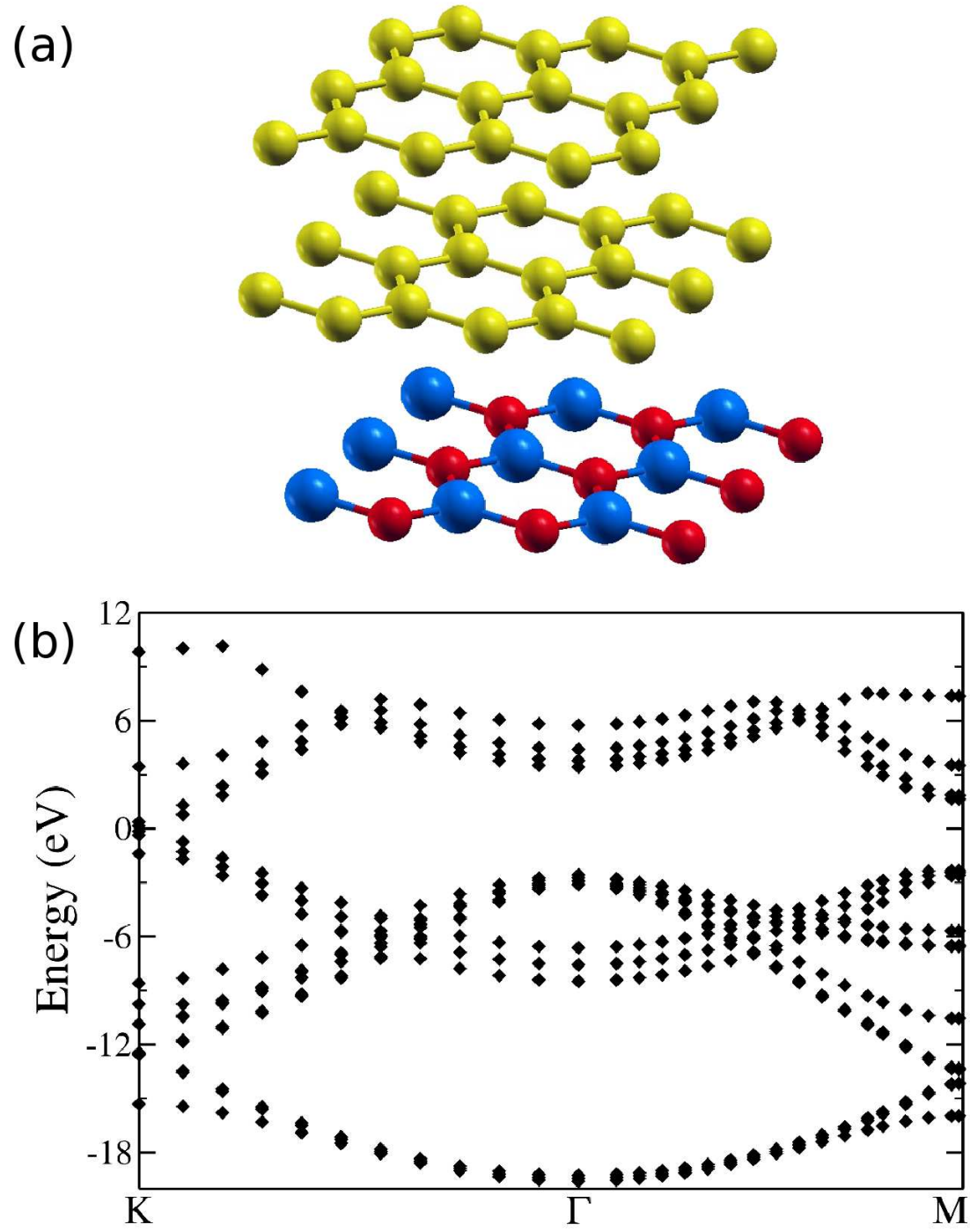


Figure 5.9: (a) Lattice structure of BLG on MLBN. (b) The band structure of BLG/MLBN along the symmetry directions. Filled symbols represent numerically calculated data points and lines are joining the data points.

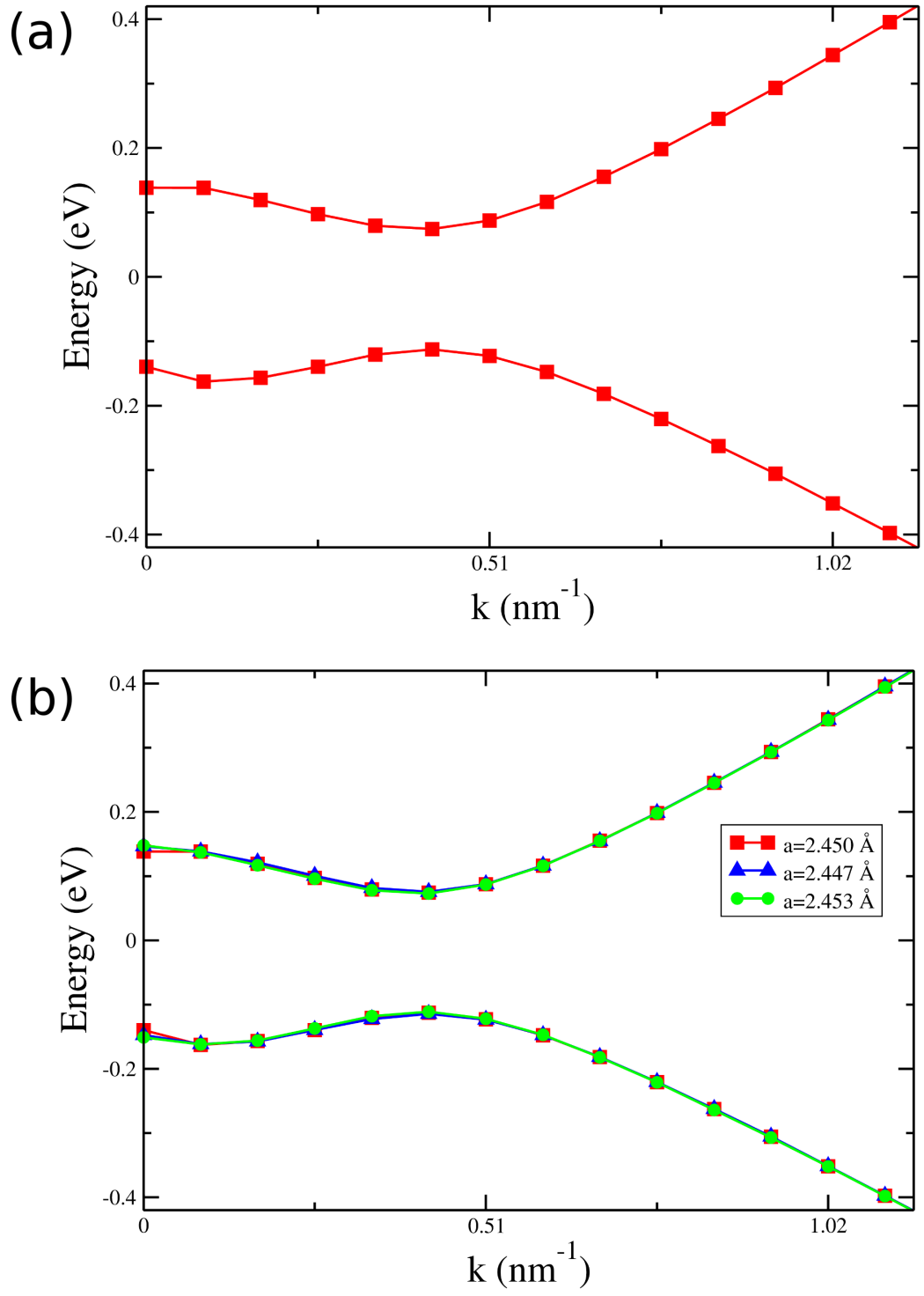


Figure 5.10: (a) The dispersion of the inner pair of $\pi/\pi^*$ near the **K** point with the equilibrium lattice constant $a$=2.450 Å and (b) close to the equilibrium value. Filled symbols represent numerically calculated data points and lines are joining the data points.

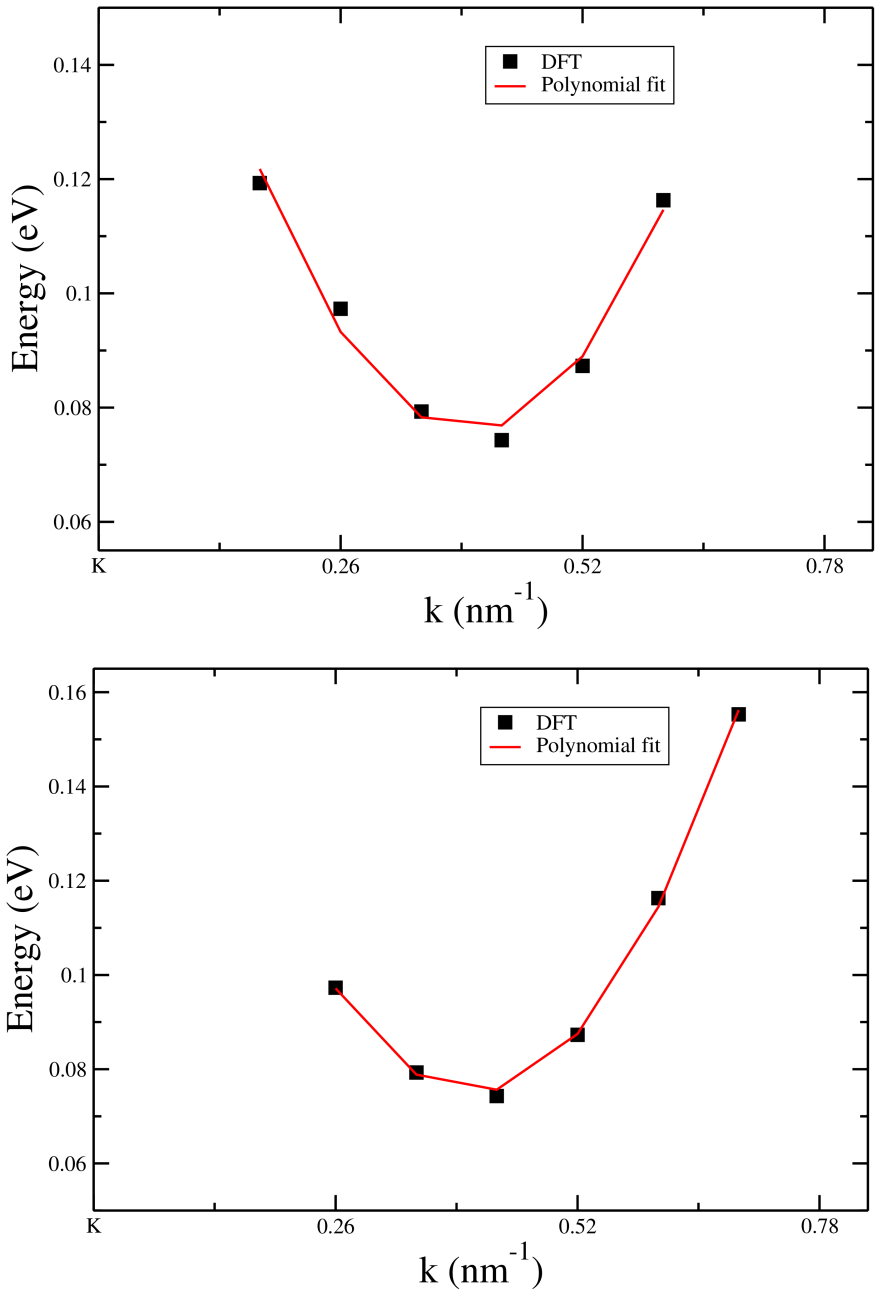


Figure 5.11: The polynomial fit of the $\pi^*$ bandsfor energies up to 0.045 eV and up to 0.081 eV above the minimum for BLG/MLBN. The square filled symbols show numerically calculated data points and the line shows a polynomial fit of the DFT data.

tem and the distance of 3.22 Å between the substrate and the TLG. For the interlayer distance in the TLG, our theoretical value of 3.33 Å is used. Our relaxation calculations reveal that only the C atoms on the MLBN buckled by 0.001 Å. We found the binding energy of 10 meV/C for TLG/MLBN. Figure 5.12 (b) shows the band structure of TLG/MLBN. We obtained the band gap at the **K** point of 41 meV with for the lattice constant of $a$=2.450 Å and interlayer separation mentioned earlier. As shown in Fig. 5.13 (a), the behaviour of the highest and the lowest band slightly away from the **K** point is mostly linear. Our partial charge density calculation suggests that these bands at the **K** point derived from the B atom on the bottom layer and C atom on the bottom layer of TLG lying above the B atom. The electron velocity is estimated by following the same procedure as used for the MLG/MLBN system. We make a polynomial fit using Eq. 5.1 for our numerical band data for energies up to 0.218 eV and up to 0.464 eV above the **K** point, as represented in Fig. 5.14. We, thus, estimate the electron velocity as $0.93(\pm0.04)\times10^6$ m/s using our equilibrium lattice constant of 2.450 Å. Following the above step, this electron velocity decreased to $0.89(\pm0.06)\times10^6$ m/s and $0.90(\pm0.07)\times10^6$ m/s using the slightly different lattice constants of 2.447 Å and 2.453 Å, respectively. It is interesting to note that our theoretical value of the electron velocity for TLG/MLBN almost matches coincidently with graphene. We also found that the Dirac point is located at **K** point but is split. Figure 5.13 (b) shows the robustness of the band gap at the **K** point against the possible error in the estimation of in plane lattice constant $a$. We establsih the maxium error margin of 28 meV in the band gap at the **K** point.

For TLG/MLBN system, we calculated the energy band gap tuning of 41 meV is traced to arise from a charge accumulation between the MLBN and the layer of TLG closest to MLBN, as seen in Fig. 5.7 (c). We found the dipole moment of magnitude 0.03 Debye for this system and estimated the electrostatic potential of 0.104 eV $nm^{-1}$.

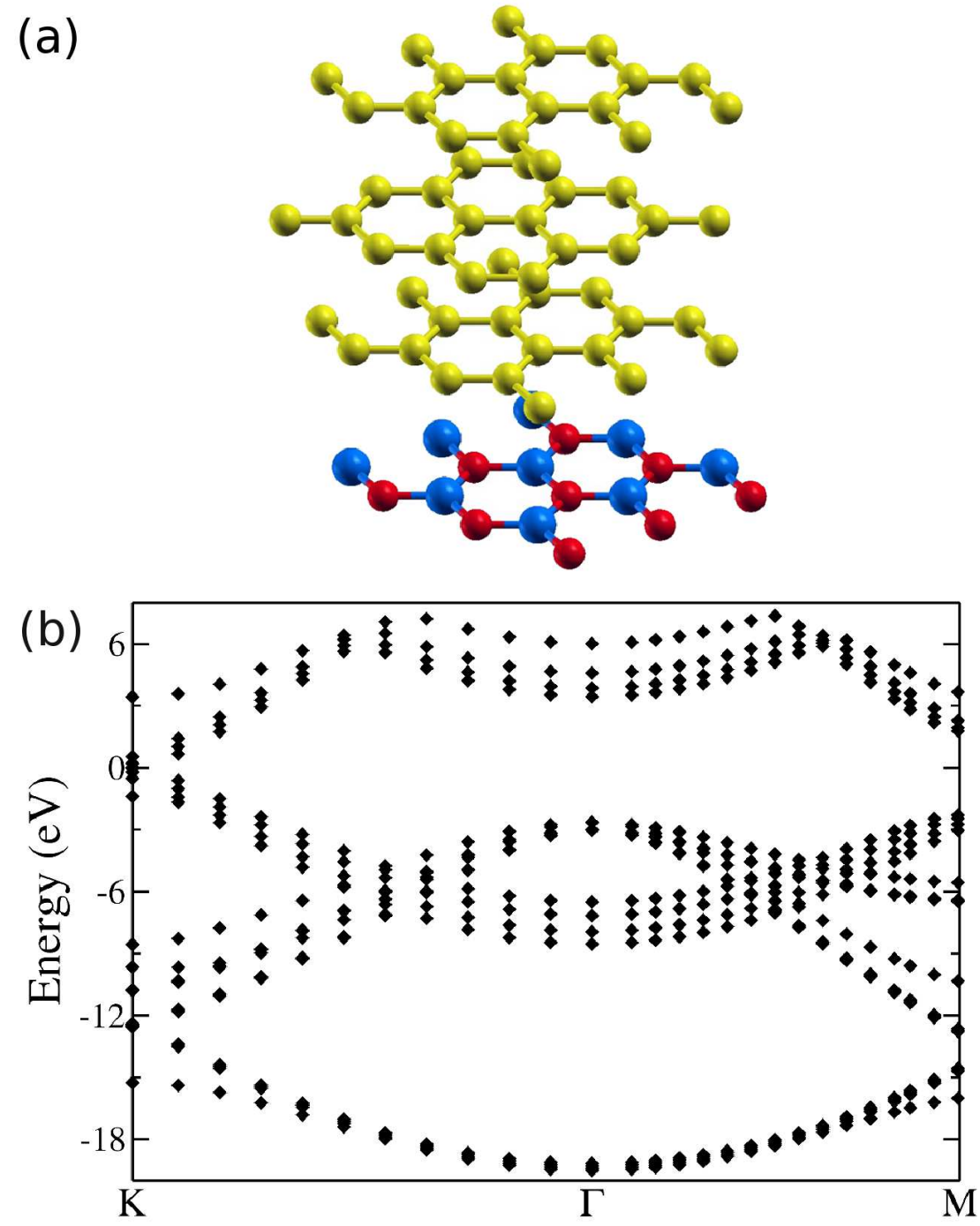


Figure 5.12: (a) The atomic structure of ABA-stacked TLG on the MLBN. (b) Band structure along **K**Γ**M** direction. Filled symbols represent numerically calculated data points and lines are joining the data points.

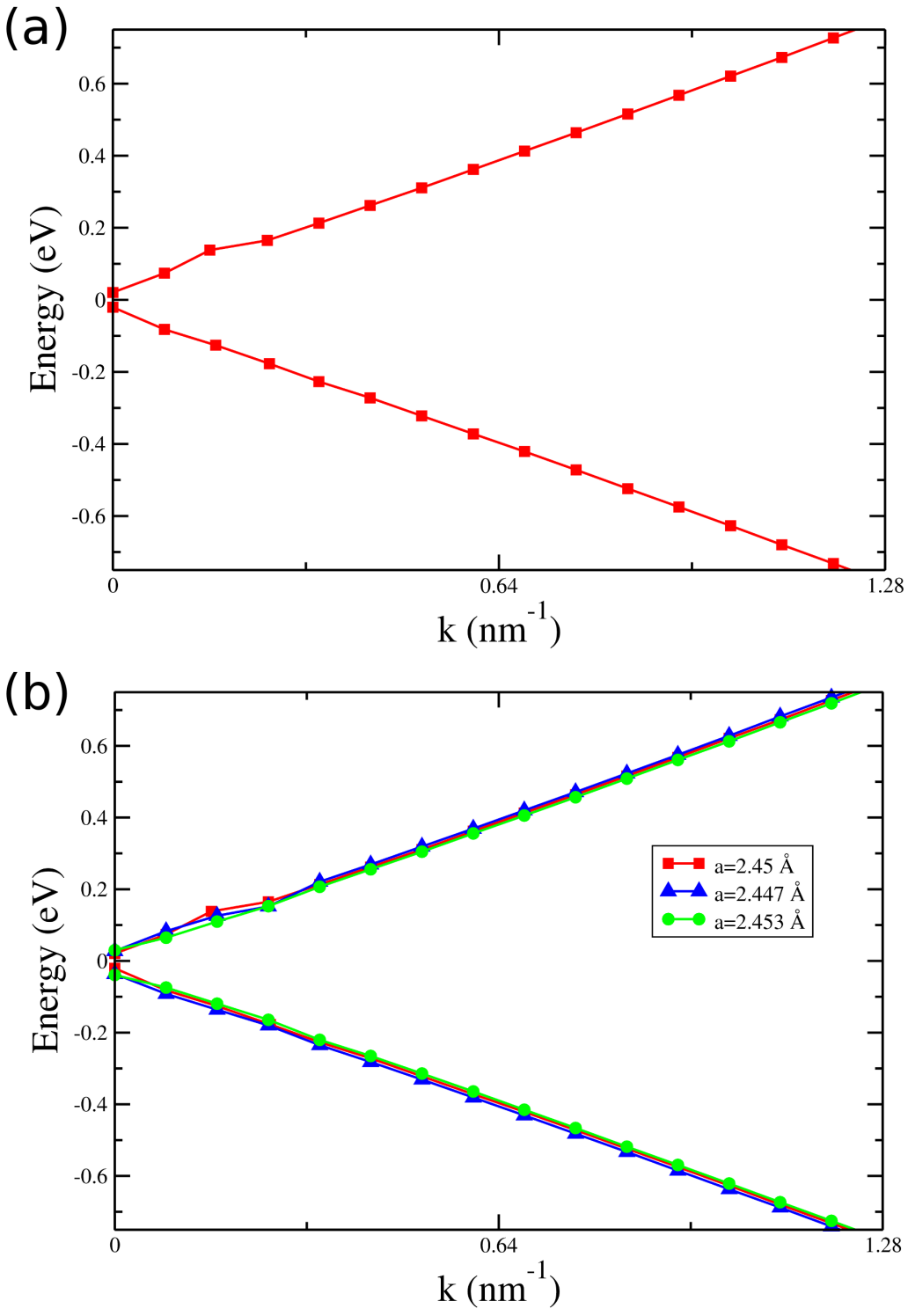


Figure 5.13: (a) The dispersion curve of the inner pair of $\pi/\pi^*$ in the vicinity of **K** point for TLG/MLBN interface system with the equilibrium lattice constant $a$=2.458 Å and (b) around the equilibrium value. Filled symbols represent numerically calculated data points and lines are joining the data points.

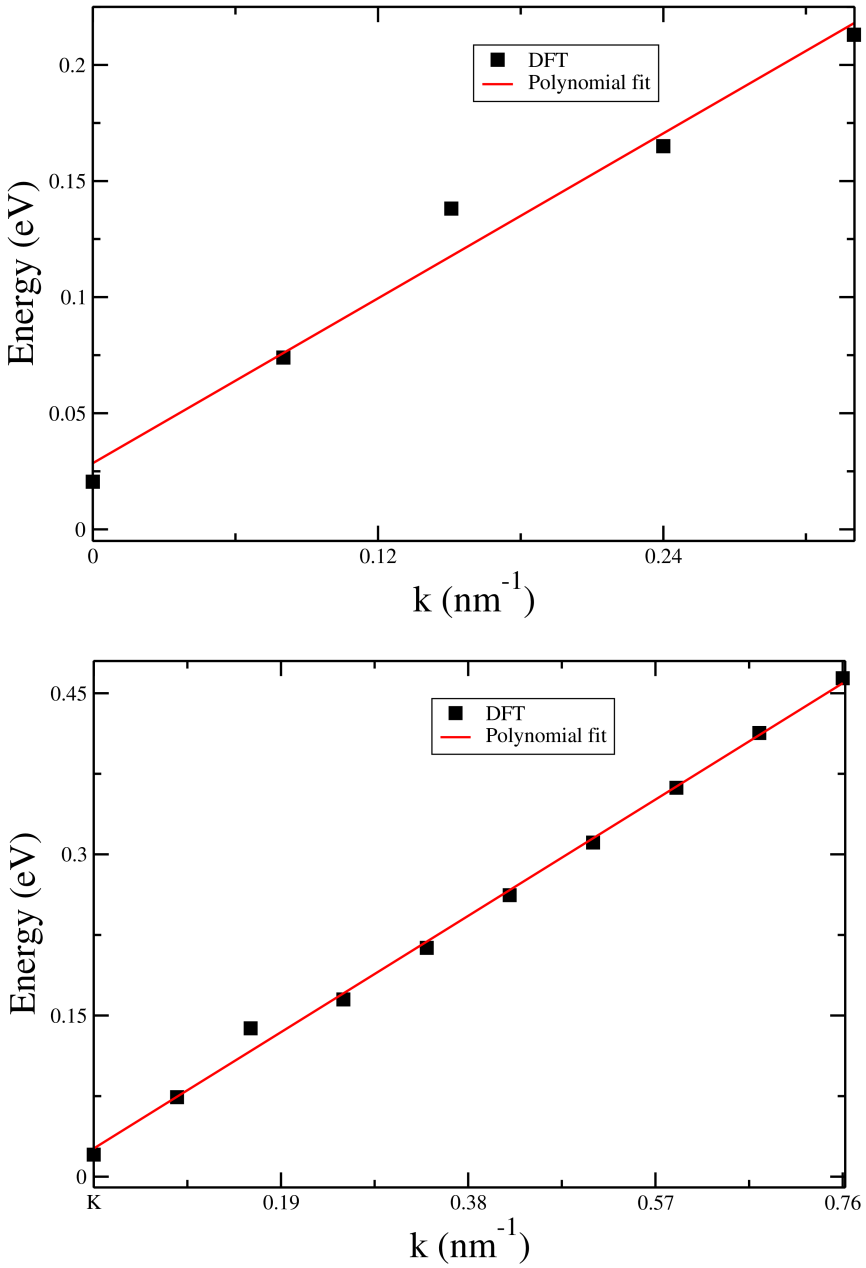


Figure 5.14: The polynomial fit of the $\pi^*$ bands for energies up to 0.218 eV and up to 0.464 eV above the **K** point for TLG/MLBN system. The symbols show numerically calculated data points and the line shows a polynomial fit of the DFT data as described in the text.

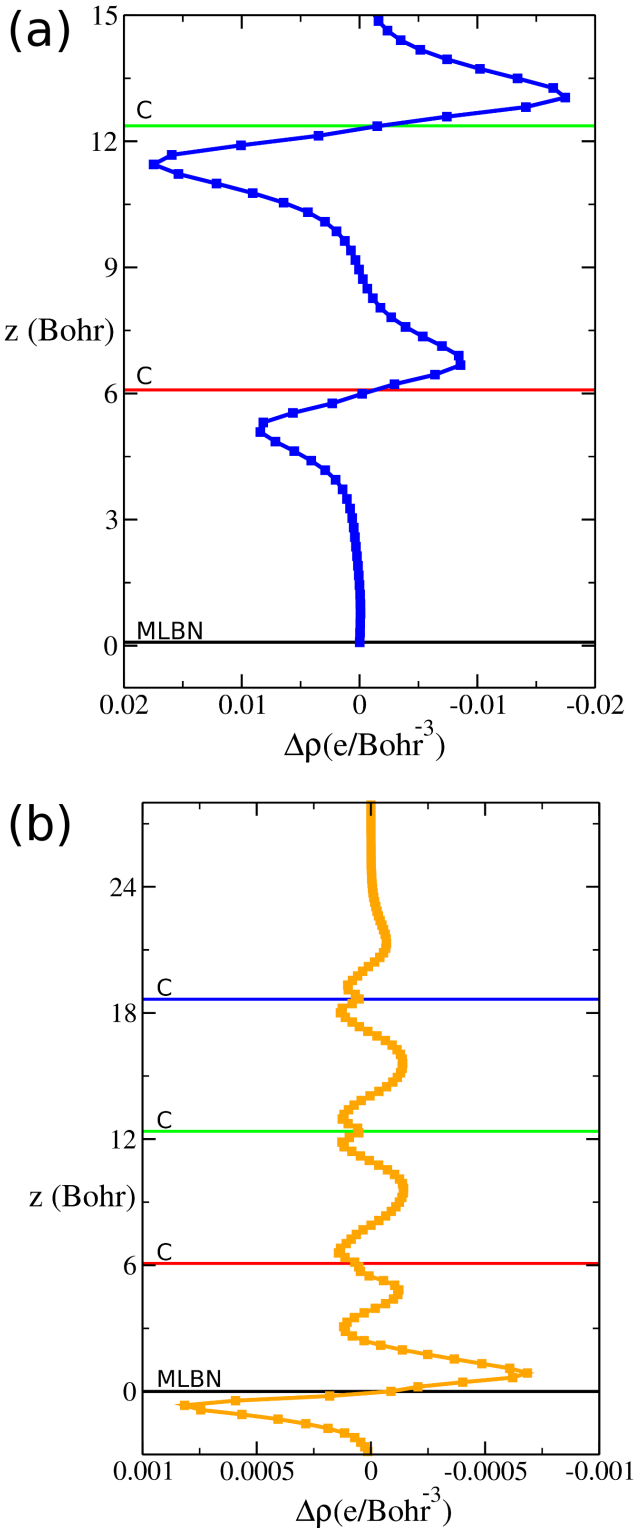


Figure 5.15: The planar-average electronic charge density difference $\Delta\rho$ along the interface normal direction for (a) BLG/MLBN and (b) ABA-TLG/MLBN. Red, green, and blue lines indicate the location of graphene plane and black line indicates the location of a monolayer boron nitride plane.

## 5.3 Density of States and Interband Optical Transitions

The density of states for the MLG/MLBN system, shown in Fig. 5.16 (a), starts to show deviation from that for isolated graphene for energies larger than 1 eV from the Fermi level. For the MLG/MLBN system there is a shoulder at $E_F$-0.655 eV and at $E_F$-4.762 eV and significantly large peaks at $E_F$-3.162 eV and at $E_F$+3.587 eV, $E_F$+6.162 eV, and $E_F$+7.598 eV. Fig. 5.16 (b) shows the density of states for the BLG/MLBN sytem. By depositing the BLG on the MLBN two new peaks are generated at $E_F$+3.122 eV and $E_F$+3.904 eV in the unoccupied region and the shoulder for the BLG at $E_F$-2.385 eV is shifted to around $E_F$-3.523 eV. The density of states for the TLG/MLBN system is shown in Fig. 5.16 (c). We found two shoulders around $E_F$-3.157 eV and $E_F$-3.919 eV in the occupied region and two shoulders are obtained around $E_F$+2.247 eV and $E_F$+3.883 eV. These changes indicate that there is an interaction between multilayer graphene and the MLBN which has also an influence on the optical properties of the MLG, BLG, and TLG. To investigate this effect we further calculate the interband transitions ($\sigma \rightarrow \sigma^*$ at $\Gamma$ and $\pi \rightarrow \pi^*$ at and **M**) for the MLG/MLBN, the BLG/MLBN, and the TLG/MLBN. Using different **k**-sampling and lattice constants around the equilibrium value of 2.45 Å the numerically calculated interband transition energies are listed in Tab. 5.1 for each system. The error margin due to different samplings are also presented in Tab. 5.2. The results presented in Tab. 5.1 indicate that the transition energy results are very well convergenced with respect to **k**-point sampling. There is a maximum difference of only 1 meV from the results obtained using samplings 36×36×1, 48×48×1, and 36×36×2. Consideration of lattice constant variation of 0.003 Å around the equilibrium value 2.450 Å leads to the maximum error in $\sigma \rightarrow \sigma^*$ transition energy of 23 meV for MLG/MLBN, 31 meV for BLG/MLBN, and 35 meV for TLG/MLBN systems. The corresponding

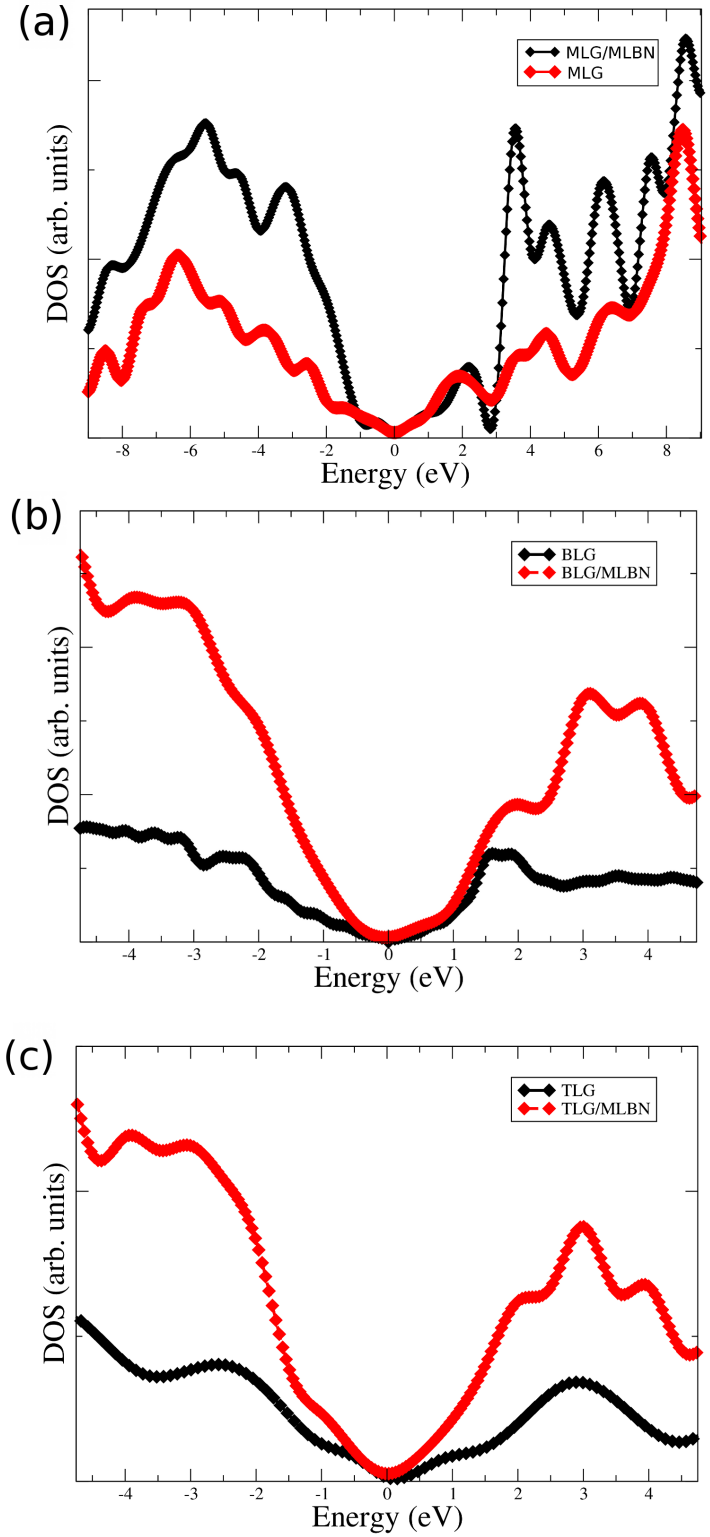


Figure 5.16: Comparison of the density of states for (a) MLG and MLG/MLBN, (b) BLG and BLG/MLBN, and (c) TLG and TLG/MLBN. Filled symbols represent numerically calculated data points and lines are joining the data points.

errors for the $\pi \rightarrow \pi^*$ transition energy are 38 meV for MLG/MLBN, 6 meV for BLG/MLBN, and 10 meV for TLG/MLBN systems.

Comparing our computed transition energies for the MLG, BLG, and TLG systems as previously given in Chapter 3 in Tab. 3.4, it can be concluded that the effect of substrate leaves these interband transition energies to remain unchanged within 0.2 eV.

## 5.4 Summary

In summary, our detailed *ab initio* calculations show that the band gap and effective mass of graphene/h-BN can be tuned by changing interlayer distance, structural symmetry, and width (*e.g.* by making nanoribbons). The binding energy per C atom is found to gradually decrease as the number of graphene layers increases. The zero band-gap graphene turns into a semiconductor when deposited on a monolayer BN sheet, *albeit* with a tiny band-gap of 57 meV with the maximum error of 4 meV. This has been explained by examining the chemical bonding between B and C atoms, the relative symmetry of the graphene and BN sheets, and the interlayer separation. No significant changes in the band gap value is noted when the monolayer graphene is interfaced with h-BN of thicknesses, bilayer, trilayer, and four layers. The effect of the BN sheet is to generate an electric dipole, of moment magnitude 0.019 Debye, across the graphene sheet, leading to the development of an electrostatic potential of magnitude 137 meV. For the bilayer graphene interfaced with a monolayer BN, the band gap increases to 278 meV with the maximum error of 21 meV but reduces to 41 meV with the maximum error of 28 meV for TLG/MLBN. The opening of the band gap in multilayer graphene is due to the interaction between graphene and its substrate. The dispersions of the highest valence and the lowest conduction bands are linear for the MLG/MLBN and the TLG/MLBN, but show significant quadratic behaviour for

Table 5.1: The interband transitions for MLG/MLBN, BLG/MLBN, and TLG/MLBN systems. The results in bold font are for the optimium choice of lattice constant $a$ and **k** sampling. The error estimations are with reference to the results presented in bold.

| System | Sampling Method | Transition Energies (eV) | |
|---|---|---|---|
| | | $\sigma \rightarrow \sigma^*$ (at $\Gamma$) | $\pi \rightarrow \pi^*$ (at **M**) |
| MLG/MLBN | **k**-sampling using a=2.450 Å | | |
| | 36×36×1 | 5.700 | 4.080 |
| | 48×48×1 | 5.700 | 4.080 |
| | **36×36×2** | **5.700** | **4.080** |
| | $a$-sampling using **k**: 36×36×2 | | |
| | 2.447 Å | 5.667 | 4.118 |
| | **2.450 Å** | **5.700** | **4.080** |
| | 2.453 Å | 5.693 | 4.045 |
| BLG/MLBN | **k**-sampling using a=2.450 Å | | |
| | 36×36×1 | 5.840 | 3.620 |
| | 48×48×1 | 5.841 | 3.621 |
| | **36×36×2** | **5.840** | **3.620** |
| | $a$-sampling using **k**: 36×36×2 | | |
| | 2.447 Å | 5.810 | 3.626 |
| | **2.450 Å** | **5.840** | **3.620** |
| | 2.453 Å | 5.871 | 3.617 |
| TLG/MLBN | **k**-sampling using a=2.450 Å | | |
| | 36×36×1 | 5.930 | 3.800 |
| | 48×48×1 | 5.929 | 3.799 |
| | **36×36×2** | **5.930** | **3.800** |
| | $a$-sampling using **k**: 36×36×2 | | |
| | 2.447 Å | 5.895 | 3.810 |
| | **2.450 Å** | **5.930** | **3.800** |
| | 2.453 Å | 5.960 | 3.794 |

Table 5.2: Optical transition energies (in eV) between the innermost $\sigma$ and $\sigma^*$ bands at $\Gamma$, and between the innermost $\pi$ and $\pi^*$ at **M** point.

| System | $\sigma \rightarrow \sigma^{*1}$ | $\pi \rightarrow \pi^{*1}$ |
|---|---|---|
| MLG/MLBN | 5.700 (0.033) | 4.080 (0.038) |
| BLG/MLBN | 5.840 (0.031) | 3.620 (0.006) |
| TLG/MLBN | 5.930 (0.035) | 3.800 (0.010) |

[1]The values in the parenthesis represent the maximum error estimated from the results presented in Tab. 5.1 using different sampling schemes.

the BLG/MLBN. Furthermore, the linear dispersion for the MLG/MLBN starts to acquire quadratic behaviour as the thickness of the BN layer increases. We estimate an electron effective mass of $0.0047(\pm 0.0008)m_e$ for graphene interfaced with the four-layer thick h-BN and $0.0021(\pm 0.0003)m_e$ for BLG/MLBN. Additionally, the electron velocity of $0.090(\pm 0.09)\times 10^6$ m/s and $0.093(\pm 0.04)\times 10^6$ m/s are found for MLG/MLBN and TLG/MLBN systems, respectively. We showed the changes in interband transition energies of the MLG, BLG, and TLG when they are deposited on the MLBN substrate.

# Chapter 6

# Electronic Properties and Transparency of Graphene on InAs(111)

## 6.1 Introduction

A survey by Kim *et al.* [182] suggests that InAs and CdSe provide two examples of lattice-matched substrates for zigzag carbon nanotubes in the [110] direction. It is thus reasonable to consider deposition of a graphene monoloyer on a surface of InAs or CdSe.

The atomic and electronic structure of graphene can be significantly altered due to its interface formation with another solid material. There are reports of successful deposition of graphene on many semiconducting and insulating substrates, including silicon carbide [13, 15, 183], silicon dioxide [184] and hydrogen-passivated silicon [16]. In most cases, the features investigated are large graphene sheets obtained via solution deposition [185]. In a detailed theoretical work, Khomyakov *et al.* also studied the electronic charge transfer for graphene sheets adsorbed on metal surfaces [186]. The interface between graphene and SiC(0001) shows

large-scale atomic reconstruction due to large lattice mismatch, leading to huge alteration in its electronic property [15, 187]. He *et al.* [188] deposited pristine, nanometer-sized graphene pieces in situ onto atomically flat UHV-cleaved GaAs(110) and InAs(110) substrates with low amounts of extraneous contamination. In contrast to charge transfer at the graphene/metal interface, experimental investigations do not find any evidence of doping process for graphene/III-V(110) semiconductor systems [189]. However, first-principles calculations suggest that graphene can be doped if it is deposited on n- or p-type III-V(110) substrates [190]. Recently, from *ab initio* studies we have concluded that graphene is weakly attached to, and is transparent on the InAs(110) surface [191]. Following these attempts, it would be both important and useful to investigate the stability and electronic properties of graphene on other lattice-matched semiconductor surfaces with different orientations and termination. For example, it would be interesting to examine the interface between graphene and InAs(111) for In as well as As termination.

In this chapter, we investigate the equilibrium atomic geometry and electronic structure of the graphene/InAs(111)A interface. The effect of the substrate on electronic charge redistribution around the graphene sheet is examined in some detail. For the first time, the transparency effect of graphene has been investigated theoretically by simulating scanning tunnelling microscopy (STM) images. By analysing the results for graphene/InAs(110) and graphene/InAs(111)A we deduce the possible orientational dependence of a substrate on the change in the electronic property of graphene.

## 6.2 Results

As explained in Section 1.2.2, a repeated slab geometry was employed in the calculations. The slab contained three bi-layers of the In-terminated $(2 \times 2)$ re-

constructed InAs(111), the graphene sheet on the top, and a fractionally charged hydrogen layer at the back. The graphene layer experiences a minimal amount of lattice mismatch with InAs(110) and InAs(111) surfaces as discussed in Refs [191, 182]. Using the total energy minimisation method as we used for graphene systems in Chapter 3, the energy minimum is found to be at the lattice constant of 6.018 Å for bulk InAs, as shown in Fig. 6.1. To verify the accurancy of this lattice constant, I made another total energy calculations for a large number of $a$ values in the range 5.82 - 6.19 Å. The results are shown in Fig. 6.2. Within the numerical noise of calculated values we note that energy minimum occurs for $a$=5.995 Å. As a result, the error margin in our numerical estimate is 0.023 Å. With our theoretical lattice constant of 6.018 Å for bulk InAs and 2.458 Å for graphene, the lattice mismatch between the graphene overlayer and the InAs(111)-$(2 \times 2)$ substrate is 0.16 $\%$. The As dangling bonds on the other side of the InAs(111) slab were saturated with pseudo-hydrogen atoms fractionally charged with 0.75e.

For Brillouin zone integration the eigenvalues at the special **k**-points were thermally smeared by using a broadening factor of 3 meV in Chapter 3 for graphene systems which are characterised by small or zero band gap materials. For obtaining numerically stable solutions to Khon-Sham equations and related quantities (such as total energy, energy eigen values and density of states) for metallic systems a larger broadening factor becomes almost a necessity. In our work we found that a broadening factor of 15 meV produces stable solutions when 10 Monkhorst-Pack special **k**-points with the unshifted 4×4×1 divisions of the supercell Brillouin zone are employed. We have also examined the adequacy of the **k**-mesh. For example, the binding energy changed very little, from 38 meV/(C atom) to 37.8 meV/(C atom) when the sampling grid was changed from 4×4×1 to 8×8×1. The DOS calculations were made with the 8×8×1 grid. However, the band calculations were performed for k-points which correspond to a region very close to the K point in graphene's Brillouin zone.

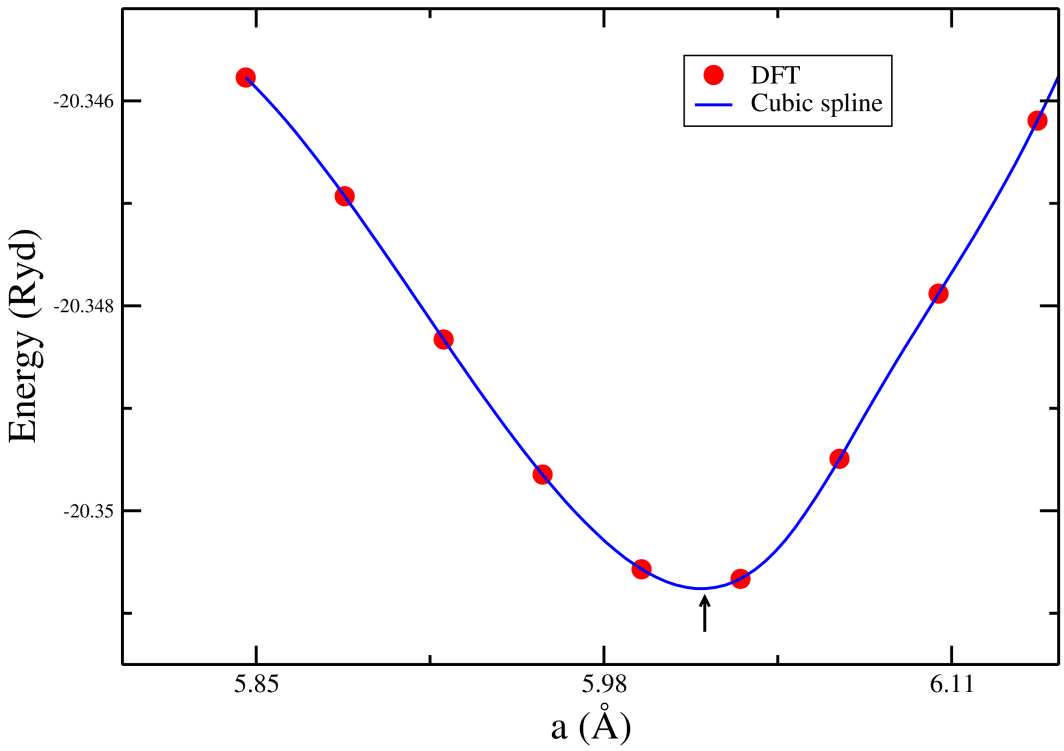


Figure 6.1: Total energy of bulk InAs as a function of the lattice parameter, $a$. The circle filled symbols show numerically calculated data points, while the curve shows the fits of the DFT data. The arrow indicates the equilibrium value of $a$ corresponding to the minimum of the total energy.

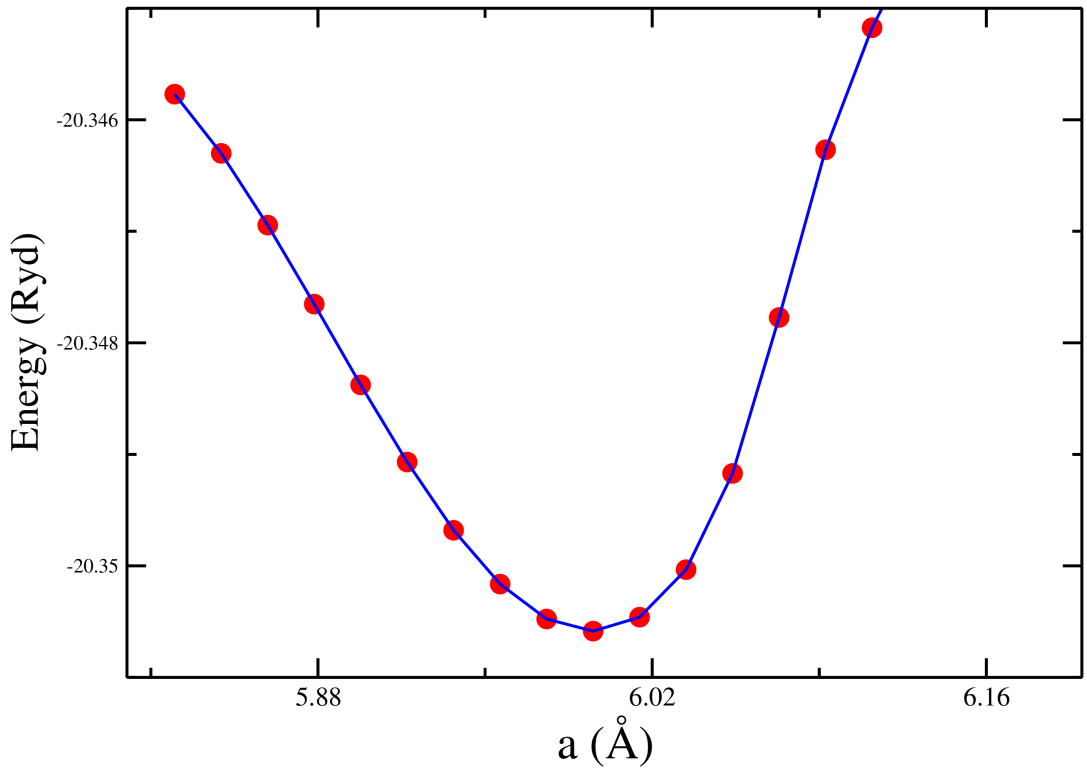


Figure 6.2: Total energy of bulk InAs as a function of the lattice parameter $a$ close to the equilibrium. The circle filled symbols show numerically calculated data points. Line is joining to the data points

There are two choices for the surface unit cell. One of them is already shown in Fig. 1.8 but we use the rectangular unit cell for simplicity as shown in the Fig. 6.3 (a), which can be described with primitive unit vectors

$$\begin{aligned} \mathbf{A}_1 &= a(\sqrt{2}, 0, 0) \\ \mathbf{A}_2 &= a(0, \sqrt{\frac{3}{2}}, 0) \\ \mathbf{A}_3 &= a(0, 0, \eta), \end{aligned}$$

where $a = 6.018$ Å and $\eta$ is an appropriate number. Accordingly, the surface Brillouin zone is a square, with $\bar{\Gamma}$ as its centre and $\bar{Y}$ = $\frac{2\pi}{a}$(0, $\sqrt{\frac{1}{6}}$, 0) as the edge of surface Brillouin zone. With the primitive translation vectors for graphene given in chapter 1.1.2, we note that the centre of the surface Brillouin zone corresponding to the graphene $K$ point (the so-called Dirac point) and the $\bar{\Gamma} - \bar{Y}$ direction is the $K - M$ direction for the graphene Brillouin zone.

### 6.2.1 Clean InAs(111) Surface

Our computed LDA band gap of bulk InAs at our equilibrium lattice constant of 6.018 Å is 0.2 eV, which is approximately half of the reported experimental value of 0.43 eV at 0 K [192]. **The error in estimation of the lattice constant results in the maximum error of 6 meV in the LDA band gap of bulk InAs.** The cleaned InAs(111)A surface is known, both experimentally and theoretically, to be $(2 \times 2)$ reconstructed, with an In vacancy in the In-terminated surface layer [193, 194, 195]. To start with, we investigated the relaxed atomic coordinates and the electronic structure of the InAs(111)A-$(2\times2)$ system. The presently calculated band structure in Fig. 6.4 shows the semiconductor behaviour with a band gap of 0.41 eV, which happens to be much larger than our theoretical band gap of 0.2 eV for bulk InAs. The band gap of the InAs(111)A surface is examined using different lattice constants ($a$=5.995 Å and $a$=6.041 Å) around the equilibrium value, as shown in Fig. 6.5. There is no significant change in the band gap (the maximum

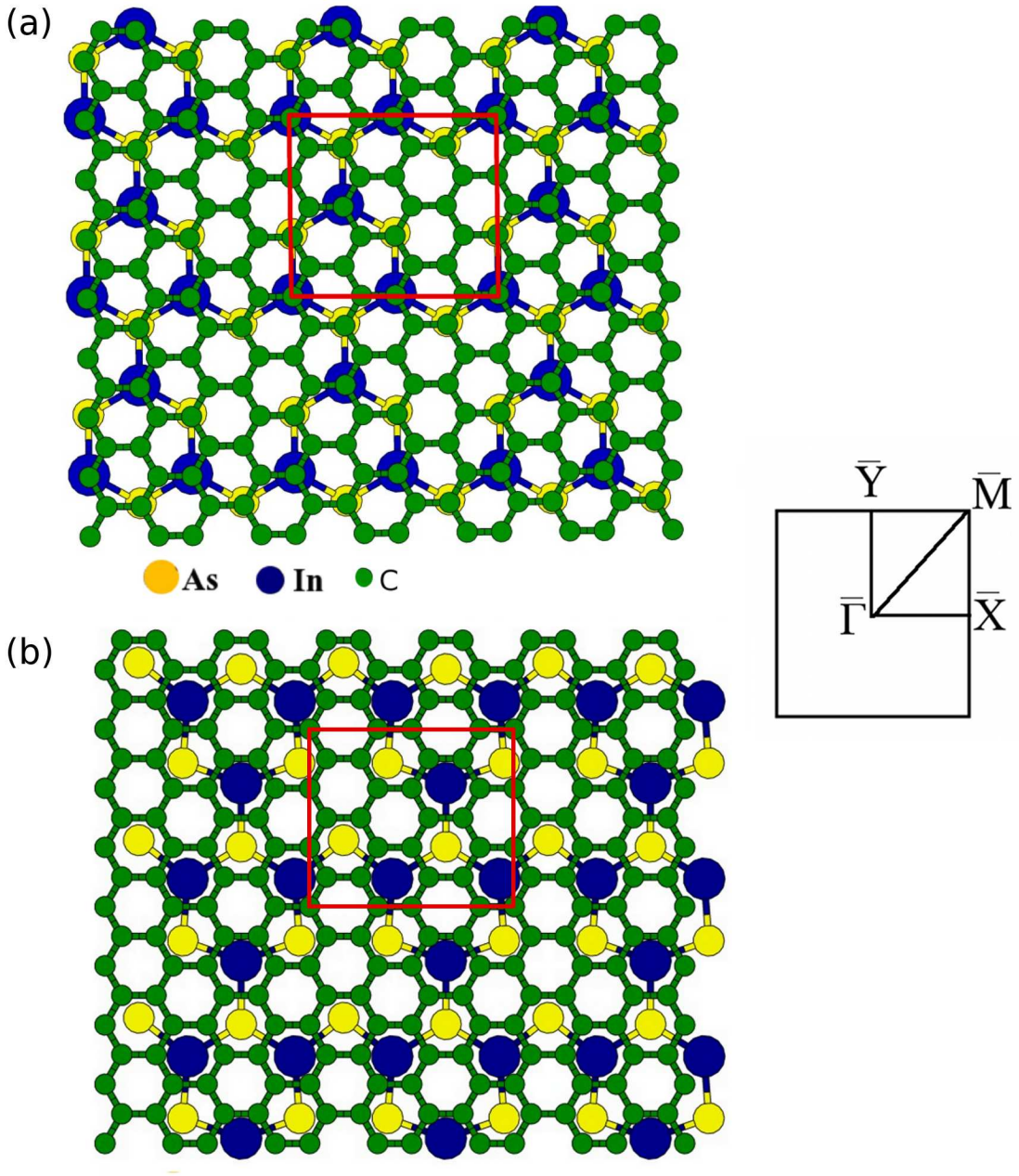


Figure 6.3: Surface unit cell and the Brillouin zone used in this work for (a) first model of InAs(111)A-($2 \times 2$) graphene system and (b) second model of InAs(111)A-($2 \times 2$) graphene system. Filled symbols represent numerically calculated data points and lines are joining to the data points.

error is 11 meV) at the $\bar{\Gamma}$ point. However, we observe small changes in the gap for $\mathbf{k}$>1.56 nm$^{-1}$. Calculated band gap for the InAs(110) surface has also been found to be larger than the bulk band gap of InAs [182, 191]. The increase in the band gap for the repeated slab geometry can be attributed to the electronic confinement effect. The numerical value of the planar average total charge density along surface normal was found to be extremely small, indicating that there is virtually no interaction between neighbouring slabs.

### 6.2.2 Graphene on InAs(111) surface

For placing graphene on the InAs(111)A surface, two possible models are considered as shown in Fig. 6.3 (a) and (b). In Fig. 6.3 (a) the In and As atoms can be seen to lie almost directly below carbon hexagon sites, while in Fig. 6.3 (b) the postions of the In and As atoms correspond to the centre of the graphene hexagon. The adsorption energy $E_{ads}$ of the graphene on the InAs(111) surface models [referred to further in this chapter as graphene/InAs(111)] is obtained by using the following equation

$$E_{ads} = E_{\text{graphene/InAs(111)}} - E_{\text{InAs(111)}} - E_{\text{Graphene}},$$

where $E_{\text{graphene/InAs(111)}}$ is the total energy of the combined system, $E_{\text{InAs(111)}}$ is the total energy of the clean surface, and $E_{\text{Graphene}}$ is the total energy of isolated graphene. Theoretical calculations reveal that the total energies of the geometrical models in Fig. 6.3 (a) and (b) are quite similar, with the first model being slightly more energetically stable. We find that deposition of graphene on InAs(111)A is exothermic for both models. We have estimated the binding energies of 38 meV per C atom and 29 meV per C atom for the first and second models, respectively. These estimates are much smaller than the adsorption energy of 400 meV/(C atom) for the (6,0) carbon nanotube on InAs(111) [182]. However, the present estimate of the graphene/InAs(111)A binding energy is comparable to 24 meV/(C

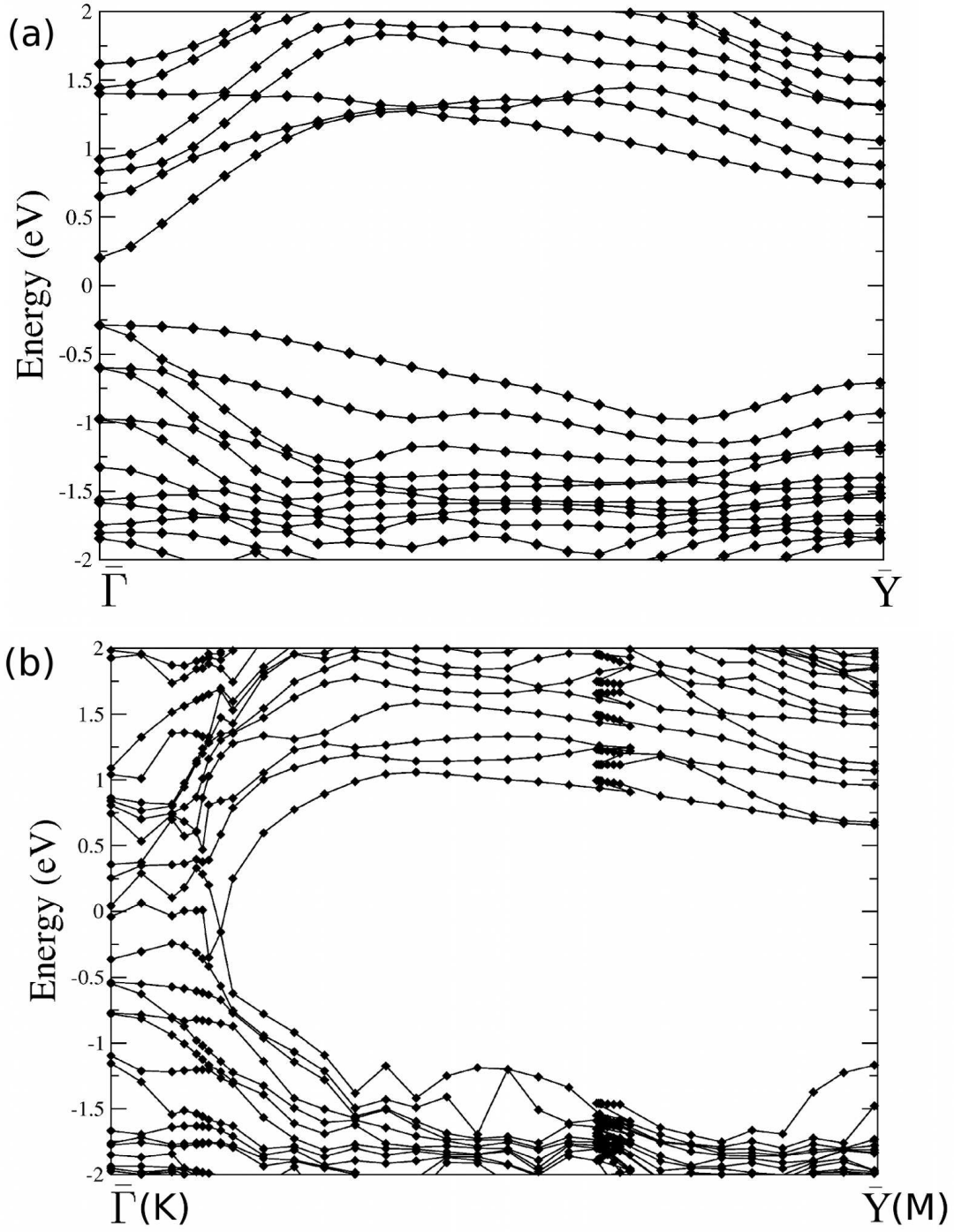


Figure 6.4: (a) Band structure of the InAs(111)-(2×2) surface and (b) the graphene on InAs(111)-(2×2) system, with the Fermi energy set to zero. The centre of the surface Brillouin zone $\bar{\Gamma}$ maps onto the $K$ point of graphene Brillouin zone. The edge of the surface Brillouin zone $\bar{Y}$ maps onto the $M$ point of graphene Brillouin zone. Filled symbols represent numerically calculated data points and lines are joining to the data points.

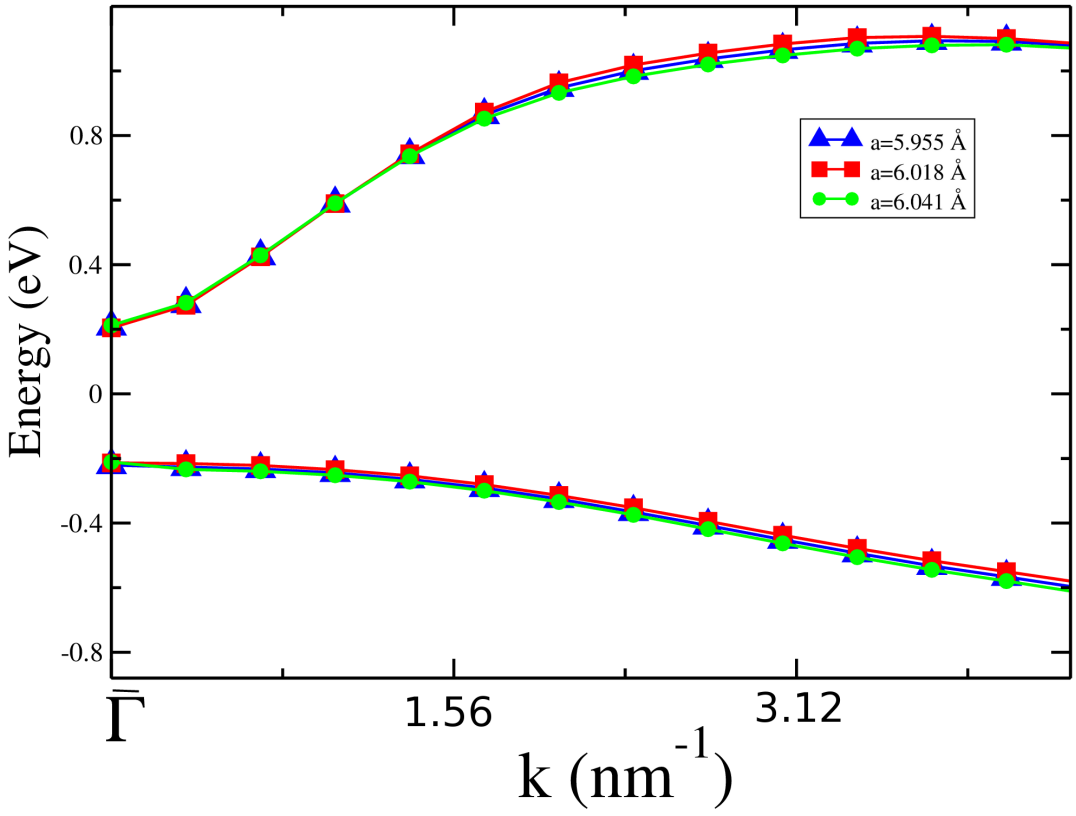


Figure 6.5: Band structure of the InAs(111)A-(2×2) surface using differnt lattice constants around the equilibrium value of 6.018 Å.

atom) obtained in our earlier work for graphene/InAs(110) [191]. These energy differences are with in the confidence level of our calculation indicates different binding strength between overlayer and substrate.

We extended our calculations of the adsorption energy for graphene deposited on InAs(111)B, the As terminated surface. For this we considered the same supercell geometry based on the $(2\times2)$ surface unit cell, but with 1.75 monolayer coverage of As termination of the top-end of the slab [196], and the In dangling bonds at the back end saturated with pseudo-hydrogen atoms fractionally charged with 1.25e. It was found that this process is endothermic, with an adsorption energy of 60 meV/(C atom).

For the graphene/InAs(111)A system, the adsorbed graphene sheet is buckled by 0.053 Å and the average vertical C-In distance is 3.077 Å as represented in Fig. 6.6. Typical error margin in surface atomic geometry calculations using the theory and computational method adopted in this work is in the range of 0.005 Å-0.01 Å [194, 197]. We have determined this range of error margin by examining atomic postions in the last three iterations of the 'atomic relaxation' cycle. We estimate similar error margin in our calculations of interlayer separation and buckling. The average C-In interlayer distance is significantly larger than the sum of the covalent radii of 2.21 Å but smaller than the sum of the van der Waals radii of 3.6 Å for C and In atoms. This result indicates that there is a weak chemical bonding between the graphene and the InAs(111)A surface. Figure 6.7 shows the electronic band structure results for the graphene/InAs(111) system along the $\bar{\Gamma}-\bar{Y}$ symmetry direction. A comparison of Fig. 6.4 with Fig. 6.7 clearly suggests that several electronic states are generated within the InAs band gap close to the surface Brillouin zone centre $\bar{\Gamma}$, rendering the graphene/InAs(111) metallic. This metallic behaviour has not been experimentally observed. The metallic nature of the band structure for graphene/InAs(111) arises from the interaction between the graphene layer and the InAs(111) surface. This is clearly seen from the partial

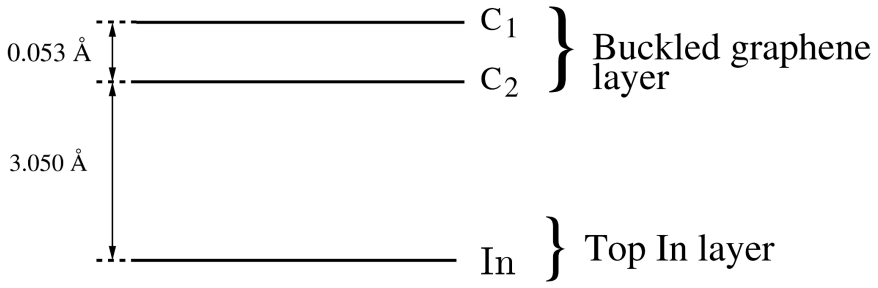


Figure 6.6: Detailed atomic layer geometry for graphene deposited on InAs(111)A-(2×2).

charge density plots in panels (b), (c) and (d) of Fig. 6.7 for the states indicated v1, v2 and c1 lying within the graphene $\pi$ and $\pi^*$ bands. These states are localised in the interface region between the graphene and the highest lying In layers, as indicated in the diagram. The metallic behaviour of electronic structure is also found for the (6,0) carbon nanotube deposited on the InAs(111) surface [182], for the graphene/InAs(110) surface [191], and for graphene deposited on $SiO_2$ [198, 199, 200, 201, 202].

In the work of He *et al.* [188], monolayer graphene has been interfaced in situ onto UHV-cleaved GaAs(110) and InAs(110) surfaces. They observed a bias-dependent semi-transparency effect, in that the substrate atomic structure was clearly visible through the graphene. The apparent height of the nontransparent graphene above the substrate averaged 3.40 Å and 3.63 Å for GaAs(110) and InAs(110), respectively. In comparison, for the semi-transparent graphene case, the apparent height averaged 2.86 Å for GaAs(110) and 2.93 Å for InAs(110). From their investigations it can be concluded that the height of a semi-transparent graphene layer is on average 0.5-0.7 Å smaller compared to a nontransparent graphene layer. These results suggest a stronger tip-graphene-substrate interaction for the semi-transparent case. He *et al.* [188] also noted that the average semi-transparent height 3.03 Å of graphene above III-V semiconductor surfaces is

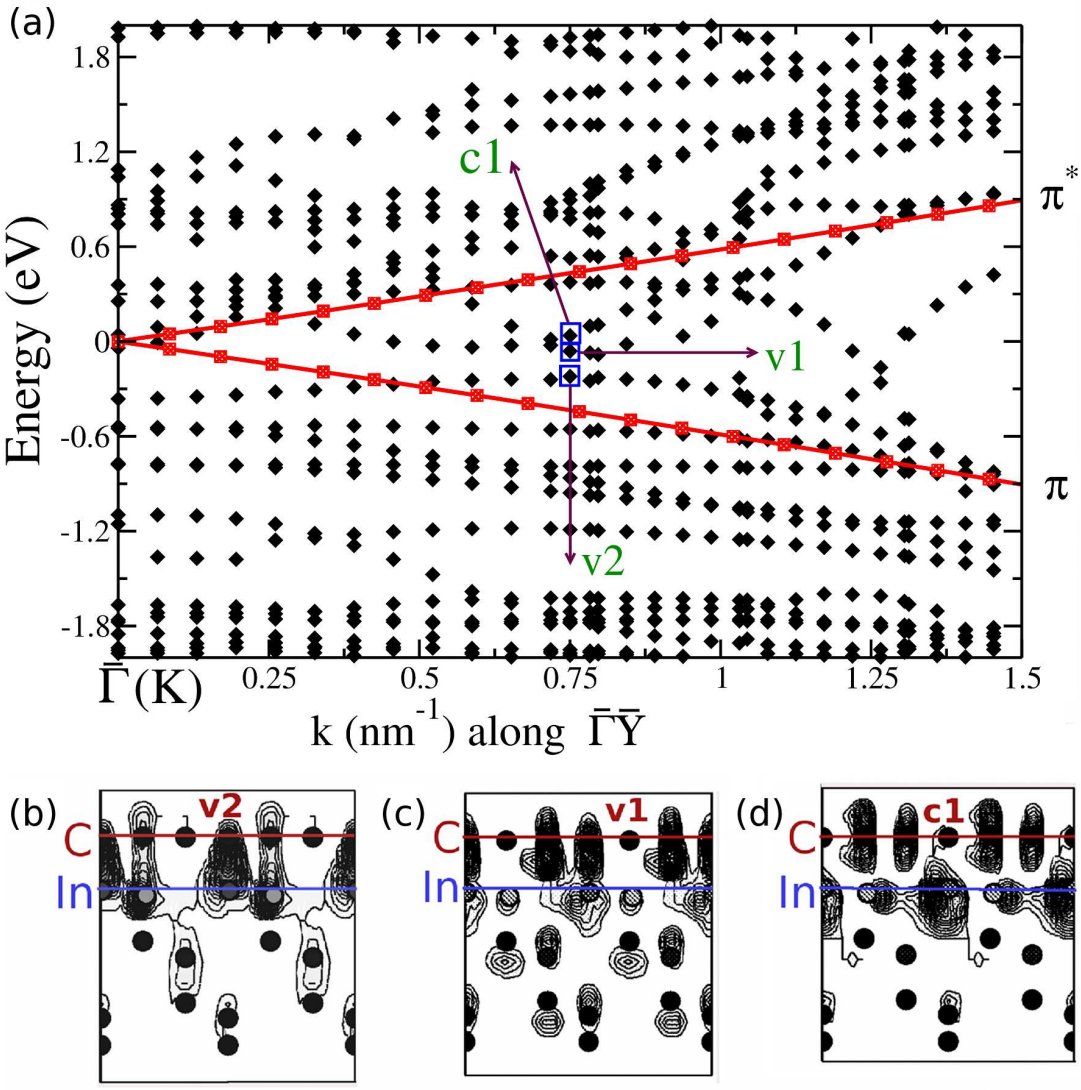


Figure 6.7: In the top panel of the diagram the solid lines represent the band structure of graphene close to the Dirac point calculated using the (2×2) large unitcell used for the graphene/InAs system. The partial charge density plots in panels (b), (c) and (d) clearly indicate that the metallic behaviour of the band structure within the Dirac lines originates from bonding between the graphene and In interface layer [atoms are indicated by filled circles]. Filled symbols in label (a) represent numerically calculated data points. Red lines is reproduced by using large unit cell of graphene.

smaller than 3.3 Å obtained for hydrogen-passivated Si(100) [203] and SiC(0001) [204] surfaces.

As mentioned earlier, the estimated equilibrium distance between the graphene and InAs(111)A surface is 3.077 Å. Based upon the analysis presented in the paper by He *et al.*, it is tempting to suggest that the InAs(111)A substrate should be visible through the graphene monolayer. We examined a tip-sample bias-dependent transparency effect for graphene monolayer features on InAs(111) where the atomic structure of the substrate beneath the graphene is clearly resolved through the graphene monolayer feature by theoretically simulating STM image at a fixed height and for an energy internal of 2 eV below the calculated Fermi energy just above the graphene layer. As shown in Fig. 6.8, the occupied STM image shows that graphene is transparent and the individual As atoms of the top bi-layer of the InAs(111) slab are clearly visible through the graphene sheet. A similar conclusion regarding the transparency of graphene was also established for the graphene/InAs(110) system in a recent work [191].

We also notice that there is charge redistribution around the graphene layer. This is due to charge transfer from InAs(111) to graphene layer. This contributes to bright and dark to hexagonal pattern of carbon atoms in the simulated STM image. This charge re-distribution also leads to the development of a dipole moment along the surface normal. The total charge displacement has also been noted across a carbon (6,0) nanotube on the InAs(111) surface [182], G/a-$SiO_2$ systems [205], and InAs(110) surface [191]. The planar averaged charge density between graphene sheet and InAs(111) surface is calculated and the charge re-distribution across the graphene sheet is presented in Fig. 6.9. To investigate this in detail, we also calculated the difference in total charge density $\delta\rho(x, y)$ due to the interface

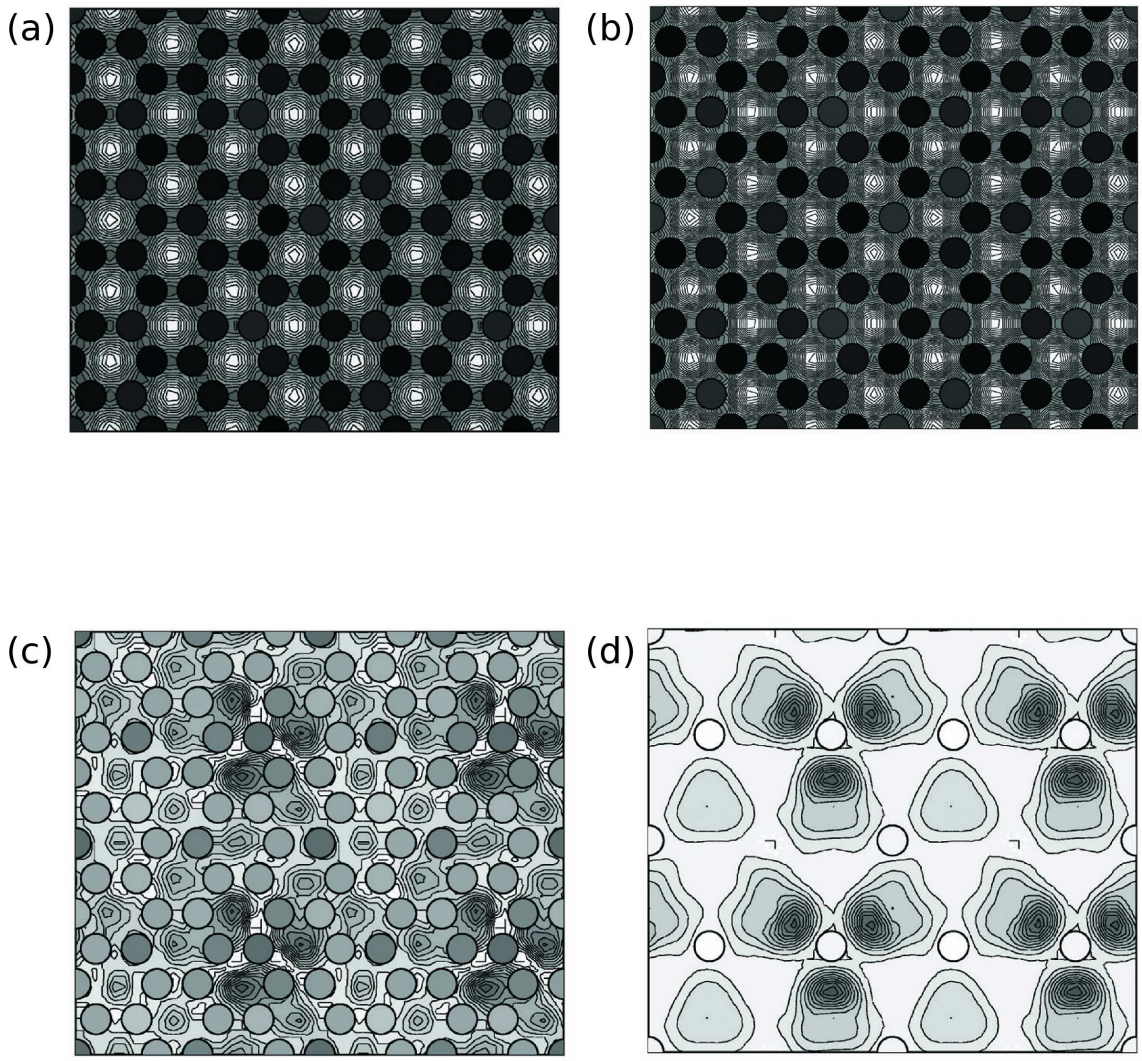


Figure 6.8: (a) Total charge contour plot for graphene/InAs(111) surface in a horizontal plane passing through the graphene. (b) The difference of charge density in a horizontal plane at the graphene level. (c) Simulated STM image with a bias of -2 eV just above graphene. (d) Simulated STM image just above the InAs(111) surface for a bias of -2 eV.

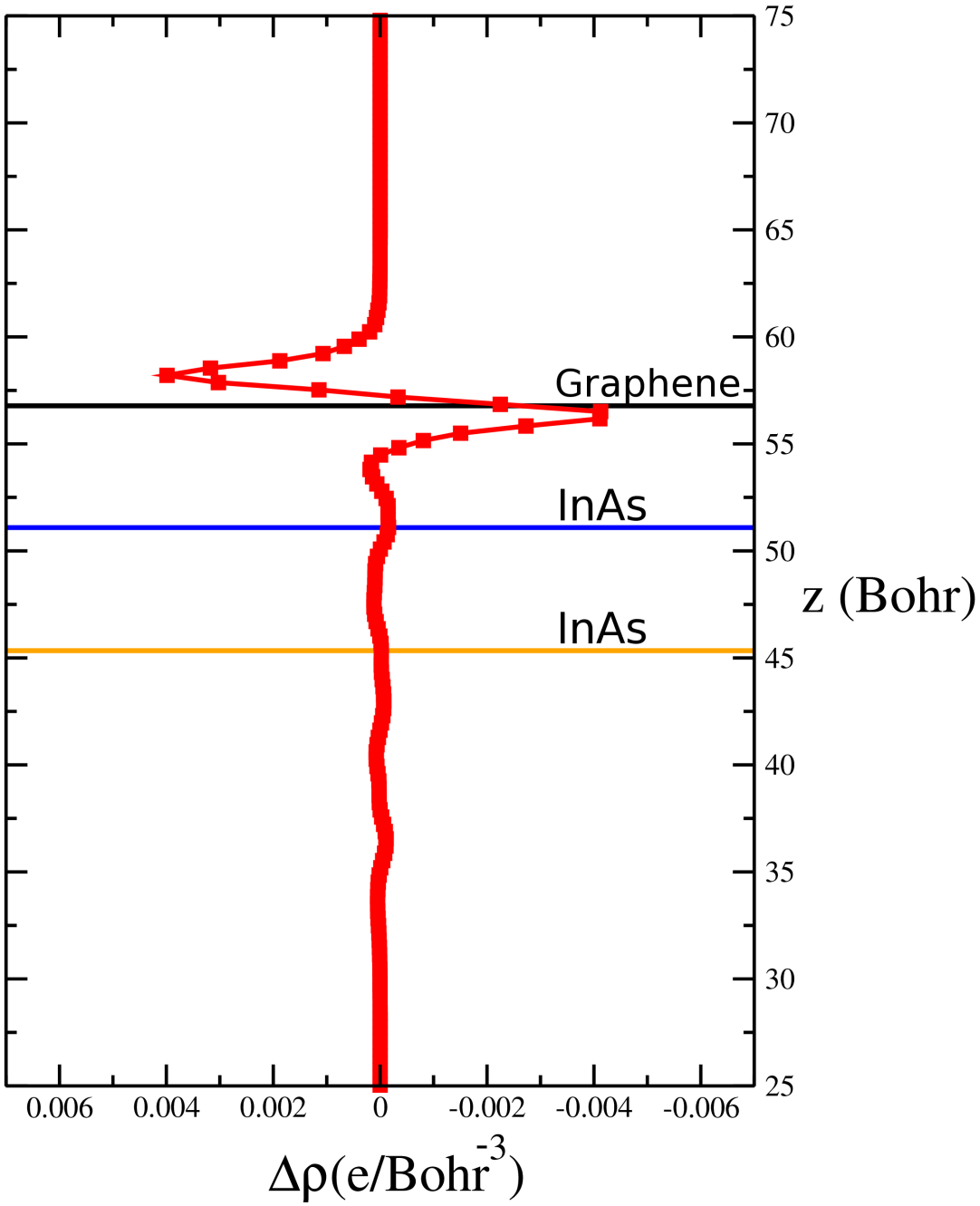


Figure 6.9: Plot of the difference of the planar averaged charge density $\delta\rho(z) = \rho(z, \text{graphene/InAs}) - \rho(z, \text{InAs}) - \rho(z, \text{graphene})$. There is a charge re-distribution across the graphene sheet. Black, blue, and orange lines indicate the location of graphene, the first layer and second layer of InAs planes, respectively.

formation, using the relation

$$\begin{aligned}\delta\rho(x,y) &= \rho((x,y),\text{graphene/InAs}) - \rho((x,y),\text{InAs}) \\ &\quad -\rho((x,y),\text{graphene}),\end{aligned}$$

where $\rho((x,y),\text{graphene/InAs}), \rho((x,y),\text{InAs}), \rho((x,y),\text{graphene})$ are total charge density for graphene/InAs, InAs, and graphene, respectively. As we have discussed earlier for $\delta\rho(z)$, there is a charge transfer towards graphene from the InAs surface. There is more charge around graphene upon the interface formation, seen in the simulated STM image in Fig. 6.8. It is important to note that there is a small difference between the total charge density plots for graphene/InAs and $\delta\rho(x,y)$ supporting the transparency effect for graphene.

Based upon our band calculations, the graphene/InAs(111) system is found to be metallic, with no band gap around the Fermi level at $\bar{\Gamma}$ as shown in Fig. 6.7. The reason for the metallic character is clearly the interaction between the graphene and the InAs(111) surface. Similar metallic behaviour is also found for the (6,0) carbon nanotube on the InAs(111) surface [182], the graphene/InAs(110) surface [191], and graphene on $SiO_2$ [198, 199]. In Fig. 6.10, the numerically calculated density of states for graphene/InAs(111) is presented. In the occupied region around the $E_F$ - 3.718 eV, a new peak is generated due to the interaction between graphene and InAs(111) surfaces in combined system. The shoulder obtained for InAs(111) in the unoccupied region around $E_F$ + 1.051 eV is shifted to around $E_F$ + 2.066 eV. This change also indicates that there is some interaction between the InAs(111) surface and the graphene sheet.

## 6.3 Summary

To summarise, we examined the deposition of graphene on InAs(111) with both In termination (A face) and As termination (B face). The graphene/InAs(111)B

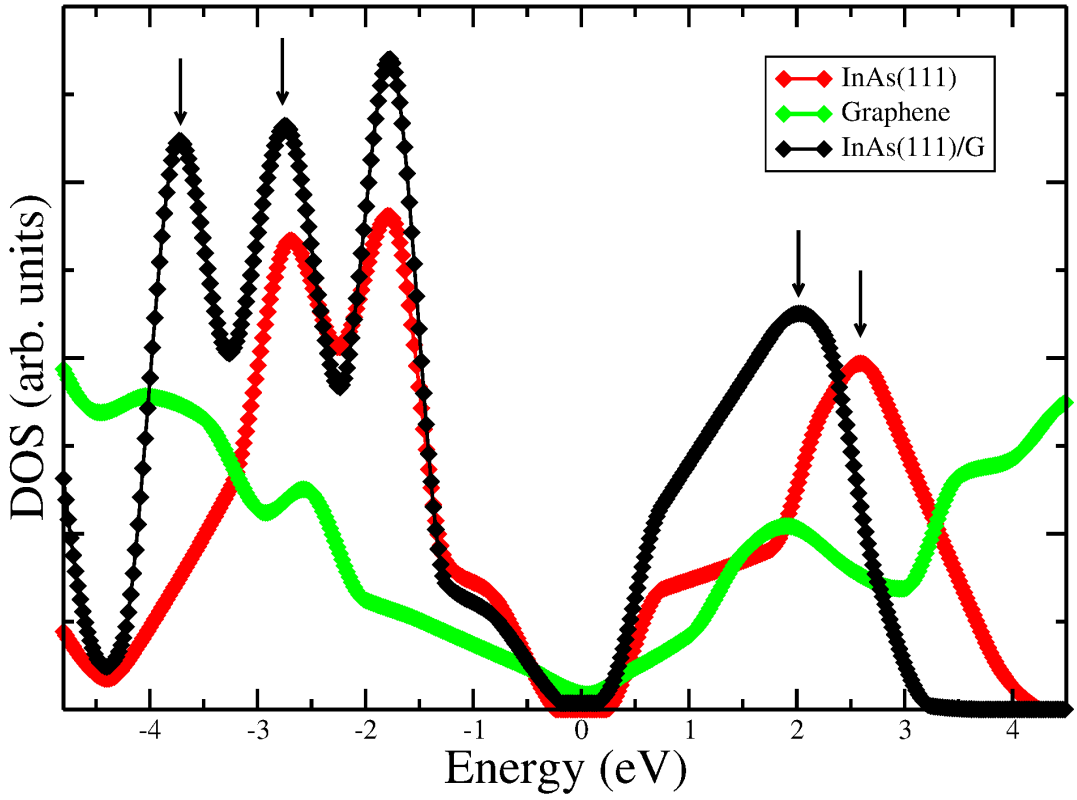


Figure 6.10: Electronic density of states for graphene, InAs(111)-(2×2) and the graphene/InAs(111)-(2×2) system. The zero along the energy axis is the Fermi energy. Changes due the interface formation are indicated by arrows. Filled symbols represent numerically calculated data points. and lines are joining to the data points.

system was found to be endothermic. An LDA band gap of 410 meV with the maximum error of 11 meV is calculated for the InAs(111)A-(2×2) surface. For the graphene/InAs(111)A system, the graphene sheet lies 3.077 Å above the (111) surface. The graphene sheet is weakly adsorbed to InAs(111) with the binding energy of around 38 meV per C atom. Moreover, our band structure shows that this system is metallic. Due to charge re-distribution between the graphene sheet and the (111) surface, a dipole moment is generated across the graphene sheet. The density of states for the graphene/InAs(111) system exhibits new peaks in both occupied and unoccupied regions within a few eV around the Fermi level, indicating some interaction between the InAs(111) surface and the graphene sheet. STM simulations suggest that the graphene sheet is transparent for a bias voltage of 2 eV below the Fermi level.

By comparing the adsorption results presented in this work and in a previous work [191] we conclude that graphene can be favourably deposited both on the non-polar surface InAs(110) and the In-terminated polar surface InAs(111)A.

Figure 6.11: The presented work in this chapter has been selected as a cover page in Journal of Physics: Condensed Matter, Volume: 24, Number: 48, 5 December 2012.

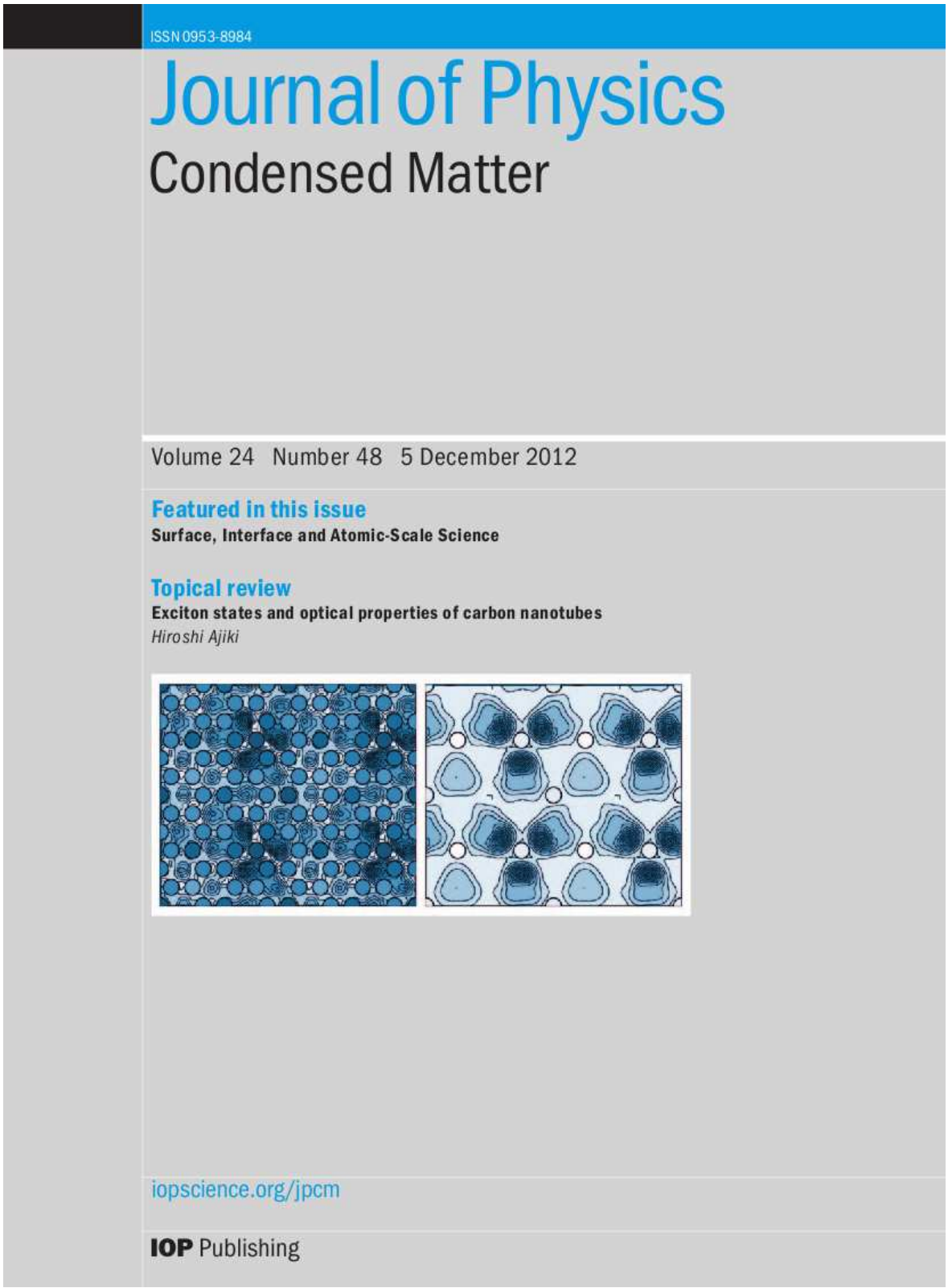

# Chapter 7

# Concluding Remarks

In this thesis I employed the plane wave pseudopotential method within the density functional scheme and local density approximation to investigate the equilibrium atomic geometry, electronic properties, and optical properties of graphene and graphene based systems.

## 7.1 Summary of Results

The first chapter of this thesis provides a brief theoretical overview about the structural properties of graphene based systems. The main principles of the surface relaxation and reconstruction surfaces and modelling of the semiconductor surfaces for study of graphene on surfaces have been briefly discussed. In Chapter 2, *ab initio* calculations based on pseudopotentials and the density functional theory have been described. The geometry optimisation scheme within the plane-wave pseudopotential framework has explained. Additionally, the theory of scanning tunnelling microscope (STM) has been given which gives very detailed information about geometrical structures and electronic states of surfaces. In Chapter 3, *ab initio* calculations to investigate the electronic and optical properties of monolayer (MLG), bilayer (BLG), trilayer (TLG) graphene and graphite

have been presented. The in-plane electronic band dispersion around the Fermi level at the **K** point is linear (Dirac-like) for graphene, and a mixture of quadratic and linear for BLG, TLG, and quadratic for graphite. The computed electron effective masses for BLG, TLG, and graphite are $0.029\pm0.006\mathrm{m}_e$, $0.054\pm0.011\mathrm{m}_e$, and $0.043\pm0.009\mathrm{m}_e$, respectively. The electron velocity in the MLG are $0.93(\pm0.07)\times10^6$ m/s. Our theoretically found values for these systems are in agreement with experimental results. The modifications in the electronic properties due to increasing the number of graphene layer is very little. Our results also suggested that the electronic properties of a graphene sample having more than 7 atomic layers would approach that of bulk graphite. Furthermore, for the first time in literature, the interband optical transitions have been investigated theoretically for bilayer, trilayer graphene and graphite systems and compared to previously studied monolayer graphene.

In Chapter 4, the ABC-stacked $N$-layer graphene systems have been studied by using the density functional theory within the local approximation and the plane wave pseudopotential method. The dispersion of $\pi/\pi^*$ bands close to the Dirac point has been established to show a mixture of cubic, quadratic, and linear behaviours for the ABC-stacked trilayer graphene. Being primarily in the graphene research area, the examination of the trigonal warping of energy bands of ABC-stacked multilayer graphene have been presented by using first principles calculations. Equienergy contour plots clearly indicate prominent trigonal warping in the ABC-stacked system– stretching of equienergy lines along directions at $120^o$ from each other. ABC-stacked systems with layer numbers $N > 3$ are characterised by much reduced level of trigonal warping. Density of states calculations revealed two sharp peaks close to the Fermi level for the systems with $N = 4, 5, 6$. From an analysis of partial charge density plots, we have established that the highest occupied state and the lowest unoccupied state at the **K** point originate from the $\mathrm{p}_z$ orbitals of carbon atoms in the bottom and uppermost layers of the

$N$=3 and $N$=6 systems, but only from one of the layers for the $N$=4 and $N$=5 systems.

In Chapter 5, the multilayer graphene interfaced with monolayer hexagonal boron nitride (h-BN) system has been studied, which is actually one of the first theoretical studies in the literature, and a detail investigation of the interaction between these layers is described. Our detailed *ab initio* calculations showed that the band gap and effective mass of graphene on h-BN can be tuned by changing interlayer distance, structural symmetry, and width (*e.g.* by making nanoribbons). The binding energy per C atom is found to gradually decrease as the number of graphene layers increases. The zero band-gap graphene turns into a semiconductor when deposited on a monolayer h-BN (MLBN) sheet, *albeit* with a tiny band-gap of 57 meV with the maximum error of 4 meV. This has been explained by examining the chemical bonding between B and C atoms, the relative symmetry of the graphene and h-BN sheets, and the interlayer separation. No significant changes in the band gap value is noted when the monolayer graphene is interfaced with h-BN of thicknesses, bilayer, trilayer, and four layers. The effect of the h-BN sheet is to generate an electric dipole, of moment magnitude 0.019 Debye, across the graphene sheet, leading to the development of an electrostatic potential of magnitude 137 meV. For the BLG interfaced with a MLBN , the band gap increases to 278 meV with the maximum error of 21 meV but reduces to 41 meV with the maximum error of 28 meV for TLG/MLBN. The opening of the band gap in multilayer graphene is due to the interaction between graphene and its substrate. The dispersions of the highest valence and the lowest conduction bands are linear for the MLG/MLBN and the TLG/MLBN, but show significant quadratic behaviour for the BLG/MLBN. The dispersion starts for the MLG/MLBN to acquire quadratic behaviour as the thickness of the BN layer increases. We estimate an electron effective mass of $0.0047(\pm 0.0008)\mathrm{m}_e$ for graphene interfaced with the four-layer thick h-BN and $0.0021(\pm 0.0003)\mathrm{m}_e$ for

BLG/MLBN. Additionally, the electron velocity of $0.090(\pm 0.09)\times 10^6$ m/s and $0.093(\pm 0.04)\times 10^6$ m/s are found for MLG/MLBN and TLG/MLBN systems, respectively. We showed the changes in interband transition energies of the MLG, BLG, and TLG when they deposited on the MLBN substrate.

In Chapter 6, the equilibrium atomic geometry, electronic structure, and transparency of the graphene/InAs(111) interface have been investigated. An LDA band gap of 410 meV with the maximum error of 11 meV is calculated for the InAs(111)A-(2×2) surface. For the graphene on InAs(111)A surface, the graphene sheet lies 3.077 Å above the (111) surface. It is found that the graphene sheet is weakly adsorbed to InAs(111) with the binding energy of around 38 meV per C atom. Our band structure shows that this system is metallic. Due to charge re-distribution between the graphene sheet and the (111) surface, a dipole moment is generated across the graphene sheet. The density of states for the graphene/InAs(111) system exhibits new peaks in both occupied and unoccupied regions within a few eV around the Fermi level, indicating some interaction between the InAs(111) surface and the graphene sheet. For the first time, the transparency effect of graphene has been investigated by simulating scanning tunnelling microscopy (STM) images. STM simulations suggest that the graphene sheet is transparent for a bias voltage of 2 eV below the Fermi level. We concluded that graphene can be favourably deposited both on the non-polar surface InAs(110) and the In-terminated polar surface InAs(111)A. The termination of a polar semiconductor surface for graphene becomes evident from our calculations which suggest that the adsorption of graphene on the As-terminated InAs(111)B surface is endothermic.

## 7.2 Future Work

A natural extension of this research can be done by including the van der Waals (vdW) interactions in the density functional theory calculations performed in the thesis. Additionally, the theoretical investigation of optical properties studied in this thesis can be extended. Other possible future works can be listed as:

***Multilayer Graphene Sandwiched Between Hexagonal Boron Nitride: van der Waals study***

In recent years graphene has been used as a transparent conductive electrode in light-emitting diodes [206], as a Hall bar device in a gas sensor device [207] and as a field effect transistor for radio-frequency applications [208]. To design graphene based devices graphene must be deposited on a suitable substrate such as $Si0_2$ [209] and hexagonal boron nitride (h-BN) [210]. It has been experimentally shown that using a mechanical transfer process high quality exfoliated mono- and bilayer graphene (MLG and BLG) devices on single crystal h-BN substrates have been fabricated and characterised [210]. Also these devices have enhanced mobility, reduced carrier inhomogeneity, and reduced intrinsic doping with respect to $SiO_2$-supported devices. Therefore, it is theoretically worth studying the equiblibrium geometry and electronic properties of multilayer graphene sandwiched between h-BN layers. The interaction between graphene and h-BN layers is primarly explained by the van der Waals forces. However, until last few year most theoretical calculations have relied on the local density approximation (LDA) of density functional theory (DFT) without considering the van der Waals forces [211, 212]. Although the DFT-LDA results find a good agreement with experimental findings in graphene interfaced with h-BN systems, it is of great interest to investigate the atomic and electronic structure of these systems including the

van der Waals interaction in the DFT calculations and compare previous the DFT-LDA estimates.

*Adsorption of Hydrogen Atoms on Graphene*

There are several schemes for tuning a band gap in graphene. For example depositing graphene on suitable substrates might induce a band gap but experimentally substrate-induced gaps is still being argued [213]. Another example is creating a finite size nanoribbons out of graphene to open a band gap but it is technologically difficult to control the size of nanoribbons [214]. Because of these drawbacks hydrogenation of graphene might be an alternative way for opening a band gap. Experimental studies have shown that disordered hydrogen adsorption on free graphene [215] and supported graphene layers induces a band gap [216]. It would therefore be interesting and worthwhile to study the atomic and electronic properties of disordered hydrogen adsorption on graphene and supported graphene using density functional theory and plane wave pseudopotential method.

*Adsorption of metal atoms on Few-layer Graphene*

It is crucial to open a band gap in graphene while keeping its high carrier mobility for many potential device applications [217]. Two approaches have been proposed to achieve this goal. One of them is the applicaton of an external electric field perpendicular to the plane of bilayer graphene. It is experimentally obtained that a band gap up to 0.25 eV can be opened in bilayer graphene [218]. This scheme requires two individual gates to control the band gaps but it is technologically desirable to control a transistor's conductance by only one gate. Another scheme is single-side adsorption of BLG. It is found that single-side adsorption of metal atoms such as potassium and aluminium on BLG leads to open a band gap in BLG [219, 220]. This band gap is also tunable with different coverage of

BLG. Furthermore, using the surface adsorption scheme single-gate BLG-based FETS have been fabricated. Because of this progress in BLG recent attention has turned into few-layer graphene. Theoretical and experimental works showed that a band gap can be opened in ABC-stacked FLG by applying a vertical electric field [221, 222]. However the electrically tunable band gap is not found in ABA-stacked FLG. Therefore it would be useful to explore the possiblity of band gap opening in ABA-stacked and ABC-stacked FLG using single-side adsorption of metal.

# Appendix A

# Crystal Structure and Symmetry

One of the most fundamental issues in understanding of the structure of solids is the arrangement of the atoms that make them up. Based upon the atomic arrangement in the solids, solids can be classified in two classes. In one class, atoms in the solid are set in an irregular manner, without any long-range order (and to same extent short range order) in their atomic arrangement. This class of solids is commonly known as noncrystalline or amorphous materials. In another class, atoms or group of atoms in a solid are arranged in a regular order. These solids are referred to as crystalline solids and I will focus on them for the following sections.

Crystalline solids form in one of fourteen basic structural arrangements, known as Bravais lattices: three cubic forms (simple, face-centered or body centered), two tetragonal forms (simple or body-centered), four orthorhombics (simple, body-, base-, or face-centered), rhombohedral, hexagonal, two monoclinic (simple or base-centered), and triclinic. All crystal structures can be explained using one of these basic lattices. For instance, the majority of simple metals form in hexagonal, body-centered or face-centered cubic lattices. Additionally, semiconductors can be found in many different crystal structures with the most important ones as face-centered cubic (fcc) and hexagonal [223, 224, 225, 226]. Among the varieties

of semiconductors, IV and III-V groups are the most important ones for many applications. In IV group, C, Si, and Ge can all occur in the diamond-structure with the face-centered cubic lattice and two atoms per lattice site. For the III-V groups, known as compound semiconductors, the most common crystal structure is zincblende which is described by a face-centred cubic (fcc) lattice with two different atoms per lattice site as presented in Fig. A.1.

In this section, I will give a brief discussion of crystal structure and symmetry using the consept of lattice in both real and reciprocal spaces to study theoretical modelling of atomic structure and electronic properties of graphene and graphene based systems. For understanding of the behavior of electrons in solids, the solution of Schrödinger equation with a suitable potential, which was firstly done by Bloch, and free electron band structure will be explained.

### A.0.1 Lattice and Primitive Unit Cell

A physical crystal can be described as a periodic arrangement of atoms/molecules in an orderly repeating pattern [223, 224, 227, 228]. For any materials, the crystal structure is defined by two different components which are lattice and basis. The lattice is a regular arrangment of points in space, while the basis is a group of repeating atoms at every point in the lattice to form the crystal structure. The lattice can be generated by three fundamental vectors $\mathbf{a}_1$ , $\mathbf{a}_2$ and $\mathbf{a}_3$ which are called pirimitive lattice translation vectors. Any two lattice points can be connected by a vector so called the translational vector and can be written by following form,

$$\mathbf{T} = n_1\mathbf{a}_1 + n_2\mathbf{a}_2 + n_3\mathbf{a}_3, \tag{A.1}$$

where $n_i$ is any integer value.

In the modern theory of solids, the most required obvious symmetry is translational symmmetry which means that in crystals there is a small basic fundamental unit that is repeated over and over in three dimensions and makes up a crystal.

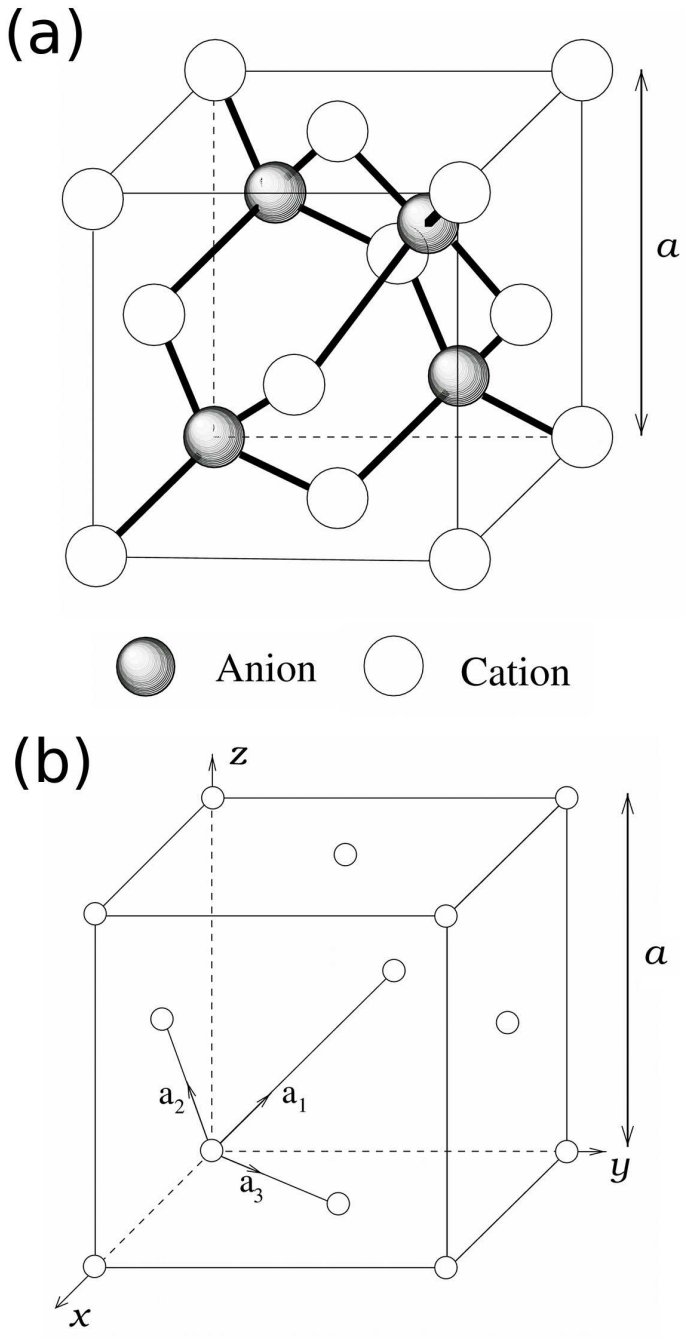


Figure A.1: (a) The zinc-blende structure, (b) the face-centred cubic structure. When all atoms are of identical species in the zinc-blende structure, it turns into the diamond structure.

This basic fundamental unit is called unit cell. If the unit cell is a minimum-volume of lattice, it is defined the primitive unit cell. We define the term unit cell as a cell which will fill all space when translated by multiples of the translational vectors. The difference is that while a primitive unit cell contains one lattice point, a unit cell may contain more. Additionally, the geometry of the lattice can be defined by describing repetition of the unit cell according to axial lengths and interaxial angles. This consideration provides fourteen Bravais lattices in three dimensions.

In a real three-dimensional crystal, planes are usually defined in terms of Miller indices which are expressed as a set of three integers between brackets, (*hkl*). The Miller indices are determined by taking the reciprocal of the intercepts and then reduce to the smallest three integers. In the Miller notation, a bar over the top of an integer is used to show that the plane cuts the axis on the negative side. If a plane is parallel to one of the crystal axes with no interception,then the corresponding Miller index for that axis is zero. For example, a plane set parallel to the y-z plane and intercepted at the x-axis is called the (100) plane. For the cubic lattice, miller indices of some important planes are shown in Fig. A.2. Furthermore, a set of equivalent planes is denoted with curly brackets as *hkl*. For example, in the simple cubic lattice (100), (010), (001), ($\bar{1}$00), (0 $\bar{1}$0) are (00$\bar{1}$) equivalent and are denoted by $\{100\}$.

### A.0.2 Reciprocal Lattice and Brillouin Zone

The reciprocal lattice has the most importance to describe and investigate the periodic structures, in particular for X-ray diffraction, surface electron diffraction, phonons and the band structure. It is the quasi-Fourier transformation of the crystal lattice which is also called direct lattice. As we expressed **T** vector in previous section, we define a general translation vector **G** between any two

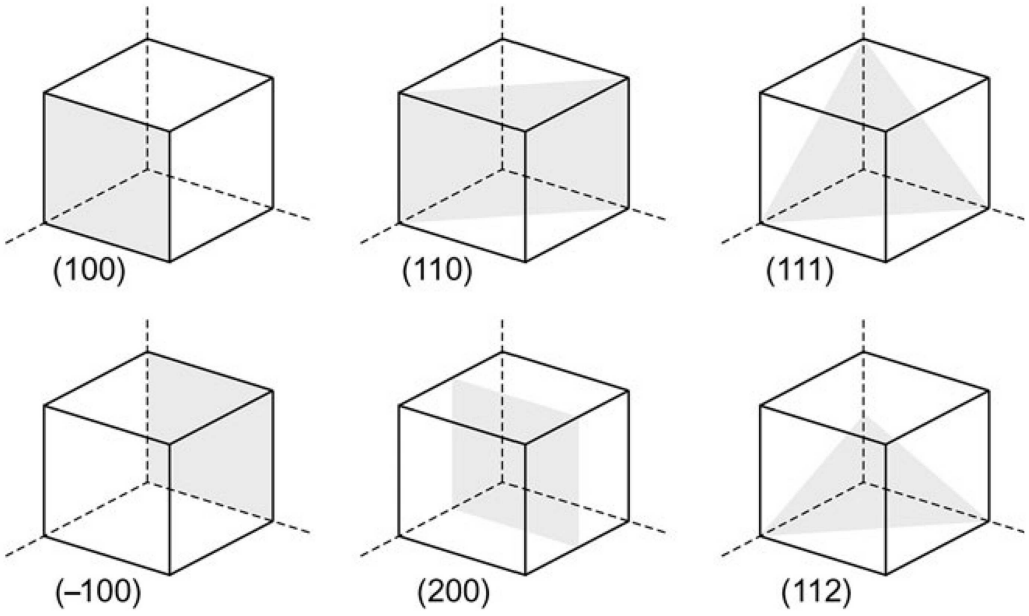


Figure A.2: Miller indices of important planes for the cubic lattice

reciprocal lattice points

$$\mathbf{G} = m_1\mathbf{b}_1 + m_2\mathbf{b}_2 + m_3\mathbf{b}_3, \tag{A.2}$$

where $m_i$ is any integer value, and $\mathbf{b}_1$, $\mathbf{b}_2$, and $\mathbf{b}_3$ are the primitive translation vectors of the reciprocal lattice which can be given directly in terms of the primitive translation vectors $\mathbf{a}_1$, $\mathbf{a}_2$, and $\mathbf{a}_3$ as

$$\begin{aligned} \mathbf{b}_1 &= \frac{2\pi}{\Omega}(\mathbf{a}_2 \times \mathbf{a}_3) \\ \mathbf{b}_2 &= \frac{2\pi}{\Omega}(\mathbf{a}_3 \times \mathbf{a}_1) \\ \mathbf{b}_3 &= \frac{2\pi}{\Omega}(\mathbf{a}_1 \times \mathbf{a}_2), \end{aligned} \tag{A.3}$$

where $\Omega$ is the volume of the unit cell and given as:

$$\Omega = |\mathbf{a}_1 \cdot (\mathbf{a}_2 \times \mathbf{a}_3)|. \tag{A.4}$$

For an arbitrary reciprocal lattice vector **G** and a vector **T** in direct space we find $\mathbf{G}\cdot\mathbf{T}=2\pi N$, where $N$ is always an integer. This relationship can serve to define one

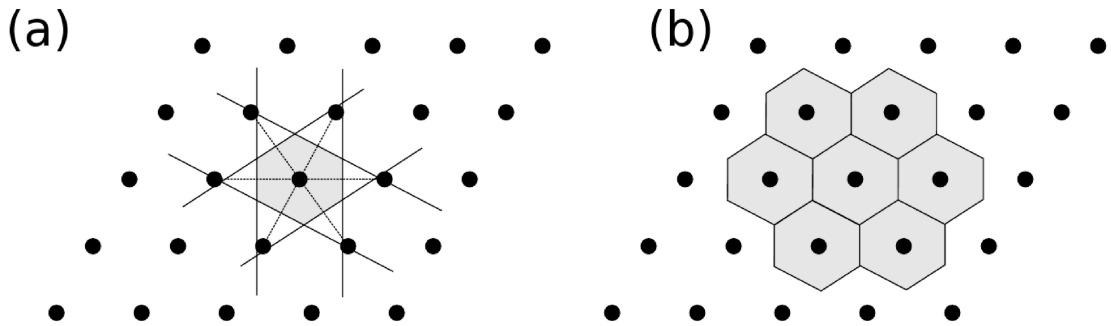


Figure A.3: (a) Construction of a two-dimensional Wigner-Seitz cell, (b) filling of space with WS cells.

set of vectors in terms of another set. This also gives

$$\exp(i\mathbf{G}\cdot\mathbf{T}) = 1 \tag{A.5}$$

for all **T** and **G** vectors. Any function that has the periodicity of the Bravis lattice can be written as

$$f(\mathbf{r}) = \sum_{\mathbf{G}} f(\mathbf{G}) e^{i\mathbf{G}\cdot\mathbf{r}}, \tag{A.6}$$

with *f*(**G**) the Fourier Transform component. Due to the periodicity of the lattice, any such function need only be studied for **r** within the primitive unit cell.

The unit cell of a reciprocal lattice is called Wigner-Seitz (WS) cell or the (first) Brillouin zone (BZ) which displays the full symmetry of the lattice. The construction of the WS is shown in Fig. A.3. The volume of a unit cell in the reciprocal lattice is inversely proportional to the volume of a unit cell in the direct lattice. The first Brillouin zone for a three-dimensional crystal lattice can be constructed by first drawing the reciprocal lattice vectors from a chosen reciprocal lattice point to all its nearest-neighboring reciprocal lattice points, and then drawing the bisecting planes perpendicular to each of these reciprocal lattice vectors. The smallest volume enclosed by these bisecting planes will normally form a polyhedron about the central reciprocal lattice point, and this polyhedron is called the first

Brillouin zone or the Wigner Seitz cell of the reciprocal lattice. The Brillouin zones for the most important lattices are shown in Fig. A.4.

The points of symmetry in the Brillouin zone are labelled with dedicated letters. The $\mathbf{\Gamma}$ point always denotes a zone centre. Electrons in a solid are perturbed by the potential of the crystal. The band structure of a solid gives the allowed energies of electrons as a function of $\mathbf{k}$ points. Therefore, points of high symmetry in the BZ have specific importance. Perhaps the most important, at least for optoelectronic devices, is at $k = 0$ which is known as the gamma point $\mathbf{\Gamma}$ [30]. There are three principal symmetry directions in the fcc BZ, which are the following:

$$\Delta \text{ direction: } \mathbf{\Gamma} \rightarrow \mathbf{X}\text{: } \mathbf{k} = \tfrac{2\pi}{a}(\eta, 0, 0) \text{ where } 0 \leq \eta \leq 1$$
$$\Sigma \text{ direction: } \mathbf{\Gamma} \rightarrow \mathbf{K}\text{: } \mathbf{k} = \tfrac{2\pi}{a}(\eta, \eta, 0) \text{ where } 0 \leq \eta \leq \tfrac{3}{4}$$
$$\Lambda \text{ direction: } \mathbf{\Gamma} \rightarrow \mathbf{L}\text{: } \mathbf{k} = \tfrac{2\pi}{a}(\eta, \eta, \eta) \text{ where } 0 \leq \eta \leq \tfrac{1}{2}.$$

### A.0.3 Cubic Crystal Structures

In three dimensions, we already know that the operations of the point group give us the fourteen 3D Bravais lattices that are categorized into seven crystal classes (trigonal, monoclinic, rhombic, tetragonal, cubic, rhombohedral and hexagonal). Here the important crystal structures for semiconductor physics will be discussed. These are diamond (C, Si, Ge) and zincblende (GaAs, InAs, ...) structures.

The space lattice of diamond is face-centered cubic (fcc) as shown in Fig. A.1. The base consists of two identical atoms at $(0, 0, 0)$ and $(\frac{1}{4}, \frac{1}{4}, \frac{1}{4})$. It has tetrahedral point symmetry. A symmetric set of primitive translation vectors can be taken to be

$$\begin{aligned} \mathbf{a}_1 &= \frac{a}{2}(0, 1, 1) \\ \mathbf{a}_2 &= \frac{a}{2}(1, 0, 1) \\ \mathbf{a}_3 &= \frac{a}{2}(1, 1, 0), \end{aligned} \tag{A.7}$$

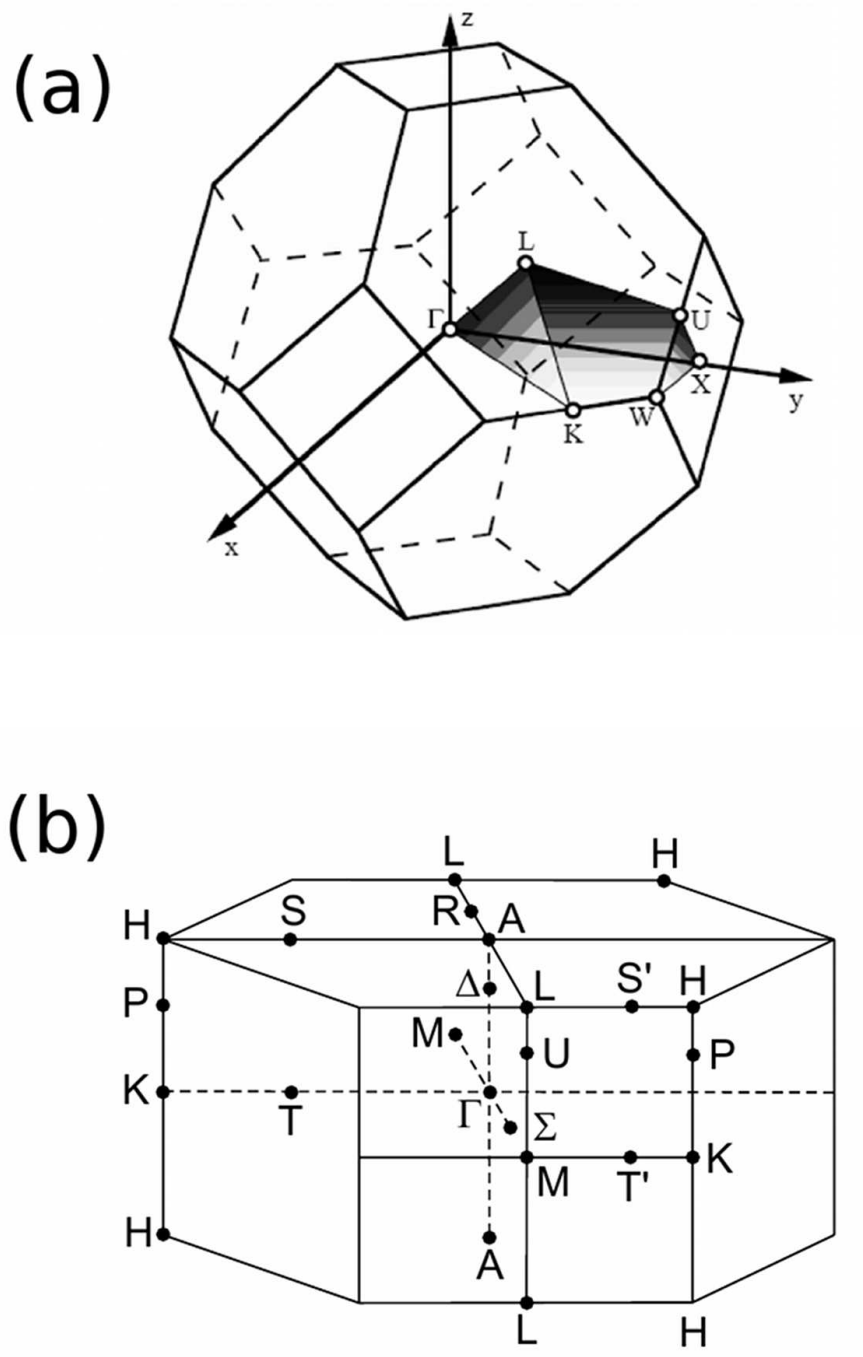


Figure A.4: Brillouin zones and special **k** points for (a) fcc lattice and (b) hcp lattice.

where $a$ is the cubic lattice constant and the volume of the primitive unit cell is $\Omega$=$a^3/4$. The diamond structure has an inversion center, located between the two atoms of the base. The materials that crystallize in the diamond lattice are C, Ge, Si and alfa-Sn.

Zincblende structure has the same geometry as the diamond crystal structure except that zinc blende crystals are binary or contains a diatomic base, such as ZnS. The atoms are tetrahedrally coordinated, a Zn atom is bonded to four S atoms and vice versa. However, there is no inversion centre in the zincblende structure. Many important III-V semiconductors, such as GaAs, InAs, AlAs, InP, GaP and their alloys, but also the II-VI compounds ZnS, ZnSe, ZnTe, HgTe, CdSe and CdTe crystallize in the zincblende structure.

### A.0.4 Bloch's Theorem

Many important physical and optical properties of a solid can be readily explained using its energy band structure. In general, the energy band structure of a solid can be constructed by solving the Schrödinger equation for electrons in a crystalline solids. In order to solve the Schrödinger equation, the first task is to find a potential distribution. Because of the periodic arrengment of atoms in the solids, the periodic potential is best suited for a calculation. This is firstly done by Bloch in 1928 [229, 230].

The Bloch theorem states that the most generalized solution for a one- electron Schrödinger equation in a periodic crystal lattice is given by

$$\Phi_k(\mathbf{r}) = u_k(\mathbf{r})e^{i\mathbf{k}\cdot\mathbf{r}}, \tag{A.8}$$

where $u_k(\mathbf{r})$ is the Bloch function, which has the spatial periodicity of the crystal potential, and $\mathbf{k}$ is the wave vector of the electron. The one-electron time-independent Schrödinger equation for which $\Phi_k(\mathbf{r})$ is a solution is given by

$$-\left(\frac{\hbar^2}{2m}\right)\nabla^2\Phi(\mathbf{r}) + V(\mathbf{r})\Phi(\mathbf{r}) = E\Phi(\mathbf{r}). \tag{A.9}$$

This equation can be rewritten as

$$-\left(\frac{\hbar^2}{2m}\right)\nabla^2\Phi_k(\mathbf{r}) + V(\mathbf{r})\Phi_k(\mathbf{r}) = E_k\Phi_k(\mathbf{r}), \tag{A.10}$$

where V(**r**) is the periodic crystal potential, which arises from the presence of ions at their regular lattice sites, and has the periodicity of the crystal lattice given by

$$V(\mathbf{r}+\mathbf{T}) = V(\mathbf{r}). \tag{A.11}$$

Therefore, the general solution of Eq. A.10 is given by Eq. A.8. From Eq. A.8, it is noted that the electron wave function in a periodic crystal lattice is a plane wave modulated by the Bloch function. The Bloch function $u_k(\mathbf{r})$ is invariant under translation. It should be pointed out here that the exact shape of $u_k(\mathbf{r})$ depends on the electron energy $E_k$ and the crystal potential V(**r**) of a crystalline solid. Thus, the Bloch theorem can be applied to solve the electron wave functions and energy band structures (i.e., $E_k$ vs. **k** relation) for the crystalline solids with periodic potential.

### A.0.5 Free Electron Band Structure

In the previous section, the solution of the Schrödinger equation was given by using the periodic potential for electrons in a crystalline solid. We now consider electrons which propagate freely, i.e., in a potential-free space. In other words, it is assumed that no "wall," i.e., no potential barrier ($V$), restricts the propagation of the electron wave. Therefore, the Schrödinger equation assumes the following form:

$$\nabla^2\Phi + \left(\frac{2m}{\hbar^2}\right)E\Phi = 0, \tag{A.12}$$

where $m$ is the electronic mass and $\hbar$ is the Planck's constant. The solution of this equation is

$$\Phi = Ae^{i\mathbf{k}\cdot\mathbf{r}}, \tag{A.13}$$

where

$$\mathbf{k} = \sqrt{\frac{2mE}{\hbar^2}}. \tag{A.14}$$

From the above equation, it follows that

$$E = \frac{\hbar^2}{2m}\mathbf{k}^2. \tag{A.15}$$

As the relation between $E$ and $\mathbf{k}$ is seen in Eq. A.15, the plot of $E$ versus $\mathbf{k}$ is a parabola. A band structure along one $\mathbf{k}$-direction can be displayed in various zone schemes. The most frequently used scheme is the reduced zone scheme. Using this scheme the Eq. A.15 can be rewritten as:

$$E(\mathbf{k}) = \frac{\hbar^2}{2m}(\mathbf{k} + \mathbf{G})^2. \tag{A.16}$$

Here $\mathbf{k}$ is the reduced wave vector confined to the first BZ and the $\mathbf{G}$ is the reciprocal lattice vectors. It should be mentioned that the band structures of actual solids are the result of extensive, computer aided calculations. Figure A.5 shows the calculated energy band structure of InAs and diamond. These bands are calculated using the density functional theory within the pseudopotential method, as explained later in chapter 2. The various investigators using different starting potentials arrive at slightly different band structures. Experimental investigations, such as measurements of the frequency dependence of the optical properties, can help determine which of the various calculated band structures are closest to reality.

### A.0.6 Density of States

One of the most fundamental properties of a material, which determines many of its properties, is its density of states. This refers to the number of states per unit energy in the band structure. The relation between the states and energy is given by,

$$N = \frac{V}{3\pi^2}\Big(\frac{2mE}{\hbar^2}\Big)^{3/2}, \tag{A.17}$$

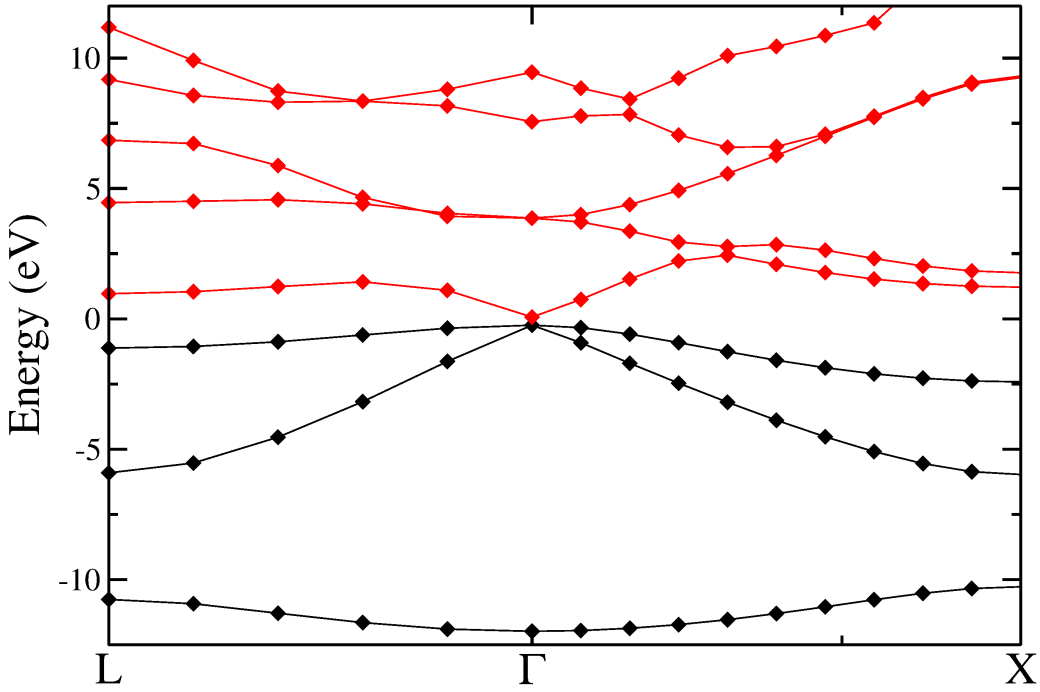


Figure A.5: Electronic band structure of bulk InAs, calculated by pseudopotential technique. Occupied and unoccupied states are shown by black and red curves, respectively. The symmetry points in the Brillouin zone are explained in section 1.2. Filled symbols represent the numerically calculated data and lines are joining to the data points.

where $N$ is the number of states, $E$ is the energy, and $V$ represents the volume of the crystal [223]. The differentiation of $N$ with respect to the energy $E$ provides the number of energy states per unit energy in the energy interval $dE$. However, the density of these states $D(E)$ per unit volume is given by

$$D(E) = \frac{1}{V}\frac{dN}{dE}. \tag{A.18}$$

Using Eqs. A.17 and A.18, we obtain the following within the free electron model:

$$D(E) = \frac{(2m)^{3/2}}{2\pi^2\hbar^3} \cdot E^{1/2}. \tag{A.19}$$

The density of states plotted versus the energy gives only a parabola for three dimensional solids. In actual crystals, however, the density of states is modified by the energy conditions within the first Brillouin zone. In Fig. A.6 (b) the DOS of bulk InAs is shown as an example. The DOS spectra can be measured [231] by different experimental techniques for instance photoemission experiments.

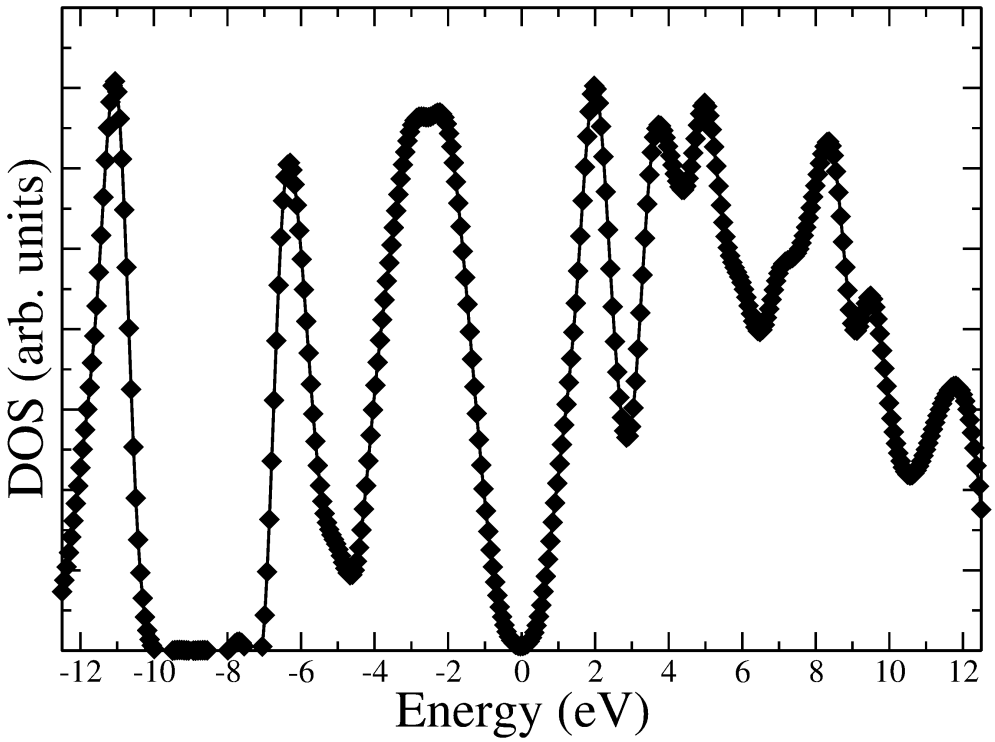


Figure A.6: Density of states $D(E)$ for bulk InAs. The zero energy in panel (b) presents the Fermi level and filled symbols are our numerically calculated datas. Curves are joining the data points

# Bibliography


[1] K. S. Novoselov, A. K. Geim, S. V. Morozov, D. Jiang, Y. Zhang, S. V. Dubonos, I. V. Grigorieva, and A. A. Firsov, *Electric Field Effect in Atomically Thin Carbon Films*, Science **306**, 666 (2004).

[2] Y. Zhang, J. P. Small, M. E. S. Amori, and P. Kim, *Electric Field Modulation of Galvanomagnetic Properties of Mesoscopic Graphite*, Phys. Rev. Lett. **94**, 176803 (2005).

[3] A. K. Geim and K. S. Novoselov, *The Rise of Graphene*, Nat. Mat. **6**, 183 (2007).

[4] K. S. Novoselov, A. K. Geim, S. V. Morozov, D. Jiang, M. I. K. I. V. Grigorieva, S. V. Dubonos, and A. Firsov, *Two-dimensional Gas of Massless Dirac Fermions in Graphene*, Nature **435**, 197 (2005).

[5] Y. Zhang, Y. W. Tan, H. L. Stormer, and P. Kim, *Experimental Observation of the Quantum Hall Effect and Berry's Phase in Graphene*, Nature **435**, 201 (2005).

[6] K. S. Novoselov, Z. Jiang, Y. Zhang, S. V. Morozov, H. L. Stormer, U. Zeitler, J. C. Maan, G. S. Boebinger, P. Kim, and A. K. Geim, *Room-Temperature Quantum Hall Effect in Graphene*, Science **315**, 5817 (2007).

[7] R. R. Nair, P. Blake, A. N. Grigorenko, K. S. Novoselov, T. J. Booth, T. Stauber, N. M. R. Peres, and A. K. Geim, *Fine Structure Constant Defines Visual Transparency of Graphene*, Science **320**, 5881 (2008).

[8] S. S. Zumdahl, *Chemistry* (D.C. Heath and Co., 1993).

[9] R. E. Peierls, *Quelques proprietes typiques des corpses solides*, Ann. I. H. Poincaré **5**, 177 (1935).

[10] L. D. Landau, *Zur Theorie der phasenumwandlungen II*, Phys. Z. Sowjetunion **11**, 26 (1937).

[11] *The Nobel Prize in Physics 2010* `http://nobelprize.org/nobel_prizes/physics/laureates/2010` (2010).

[12] A.K. Geim and K.S. Novoselov, *The rise of graphene*, Nat. Mater. **6**, 183 (2007).

[13] C. Berger, Z. Song, X. Li, X. Wu, N. Brown, C. Naud, D. Mayou, T. Li, J. Hass, A. N. Marchenkov, E. H. Conrad, P. N. First, and W. A. de Heer, *Electronic Confinement and Coherence in Patterned Epitaxial Graphene*, Science **312**, 5777 (2006).

[14] M. Sprinkle, P. Soukiassian, W. A. de Heer, C. Berger, E. H. Conrad, and W. M. K. Foundation, *Epitaxial Graphene: The Material for Graphene Electronics*, Phys. Status Solidi RRL **6**, A91 (2009).

[15] A. Mattausch and O. Pankratov, *Ab Initio Study of Graphene on SiC*, Phys. Rev. Lett. **99**, 076802 (2007).

[16] K. A. Ritter and J. W. Lyding, *The Influence of Edge Structure on the Electronic Properties of Graphene Quantum Dots and Nanoribbons*, Nat. Mater. **8**, 235 (2009).

[17] J. D. Caldwell, T. J. Anderson, J. C. Culbertson, G. G. Jernigan, K. D. Hobart, F. J. Kub, M. J. Tadjer, J. L. Tedesco, J. K. Hite, M. A. Mastro, R. Myers-Ward, C. R. Eddy, P. M. Campbell and D. K. Gaskill, *Technique for the Dry Transfer of Epitaxial Graphene onto Arbitrary Substrates*, ACS Nano **4**, 1108 (2010).

[18] P. Neugebauer, M. Orlita, C. Faugeras, A. L. Barra, and M. Potemski, *How Perfect Can Graphene Be?*, Phys. Rev. Lett. **103**, 136403 (2009).

[19] D. C. Elias, R. R. Nair, T. M. G. Mohiuddin, S. V. Morozov, P. Blake, M. P. Halsall, A. C. Ferrari, D. W. Boukhvalov, M. I. Katsnelson, A. K. Geim, and K. S. Novoselov, *Control of Graphene's Properties by Reversible Hydrogenation: Evidence for Graphane*, Science **323**, 610 (2009).

[20] S. Y. Zhou, G. H. Gweon, A. V. Fedorov, P. N. First, W. A. De Heer, D. H. Lee, F. Guinea, A. H. Castro Neto, and A. Lanzara, *Substrate-induced bandgap opening in epitaxial graphene*, Nature Mater. **6**, 770 (2007).

[21] G. Giovannetti, P. A. Khomyakov, G. Brocks, P. J. Kelly, and J. van den Brink, *Substrate-induced Band Gap in Graphene on Hexagonal Boron Nitride: Ab initio Density Functional Calculations*, Phys. Rev. B **76**, 073103 (2007).

[22] J. Berashevich and T. Chakraborty, *Tunable Band Gap and Magnetic Ordering by Adsorption of Molecules on Graphene*, Phys. Rev. B **80**, 033404 (2009).

[23] J. Hofrichter, B. N. Szafranek, M. Otto, T. J. Echtermeyer, M. Baus, A. Majerus, V. Geringer, M. Ramsteiner, and H. Kurz, *Synthesis of Graphene on Silicon Dioxide by a Solid Carbon Source*, Nano Lett. **10**, 36 (2010).

[24] D. Usachov, V. K. Adamchuk, D. Haberer, A. Grüneis, H. Sachdev, A. B. Preobrajenski, C. Laubschat, and D. V. Vyalikh, *Quasifreestanding Single-layer Hexagonal Boron Nitride as a Substrate for Graphene Synthesis*, Phys. Rev. B **82**, 075415 (2010).

[25] C. B. Duke, *Surface Science: The first thirty years*, Amsterdam; North-Holland, reprinted from Surf. Sci. **299/300**, (1994).

[26] C. B. Duke, *Semiconductor Surface Reconstruction: The Structural Chemistry of Two-Dimensional Surface Compounds*, Chem. Rev. **96**, 1237 (1996).

[27] D. J. Chadi, *(110) Surface States of GaAs: Sensitivity of Electronic Structure to Surface Structure*, Phys. Rev. B **18**, 1800 (1978).

[28] D. J. Chadi, *(110) Surface Atomic Structures of Covalent and Ionic Semiconductors*, Phys. Rev. B **19**, 2074 (1979).

[29] K. C. Pandey, *New $\pi$-Bonded Chain Model for Si(111)-(2$\times$1) Surface*, Phys. Rev. Lett **47**, 1913 (1981).

[30] G. P. Srivastava, *Theory of Semiconductor Surface Reconstruction*, Rep. Prog. Phys. **60**, 561 (1997).

[31] G. P. Srivastava, *Theoretical Modeling of Semicinductor Surfaces* (World Scientific, Singapore, 1999).

[32] W. G. Schmidt, F. Bechstedt, and G. P. Srivastava, *III-V(110) Surface Dynamics from an Ab initio Frozen-phonon Approach*, Phys. Rev. B **52**, 2001 (1995).

[33] W. G. Schmidt, F. Bechstedt, and G. P. Srivastava, *Adsorption of Group-V Elements on III-V (110) Surfaces*, Surf. Sci. Rep. **25**, 141 (1996).

[34] J. Neugebauer and M. Scheffler, *Adsorbate-Substrate and Adsorbate-Adsorbate Interactions of Na and K Adlayers on Al(111)*, Phys. Rev. B **46**, 16067 (1992).

[35] E. Kaxiras, *Atomic and Electronic Structure of Solids* (Cambridge University Press, Cambridge, 2003).

[36] J. Kohanoff, *Electronic Structure Calculations for Solids and Molecules: Theory and Computational Methods* (Cambridge University Press, Cambridge, 2006).

[37] M. Born and R. Oppenheimer, *Zur Quantentheorie der Molekeln*, Ann. Phys. **84**, 457 (1927).

[38] J. T. Devreese and P. V. Camp, *Electronic Structure, Dynamics, and Quantum Structural Properties of Condensed Matter*, Plenum Press, New York, 1985.

[39] G. P. Srivastava and D. Weaire, *The Theory of the Cohesive Energies of Solids*, Adv. Phys. **36**, 463 (1987).

[40] D. R. Hartree, *The Wave Mechanics of an Atom with a Non-Coulomb Central Field. Part I. Theory and Methods*, Proc. Cam. Phil. Soc. **24**, 89 (1928).

[41] J. C. Slater, *The Theory of Complex Spectra*, Phys. Rev. **34**, 1293 (1929).

[42] L. H. Thomas, *The Calculation of Atomic Fields*, Proc. Cambridge Philos. Soc. **23**, 542 (1927).

[43] E. Fermi, *Eine statistische Methode zur Bestimmung einiger Eigenschaften des Atoms und ihre Anwendung auf die Theorie des periodischen Systems der Elemente*, Z. Phys. **48**, 73 (1928).

[44] P. A. M. D. Dirac, *Note on Exchange Phenomena in the Thomas-Fermi Atom*, Phil. Roy. Soc. **26**, 376 (1930).

[45] P. Hohenberg and W. Kohn, *Inhomogeneous Electron Gas*, Phys. Rev. **136**, B864 (1964).

[46] W. Kohn and L. Sham, *Self-Consistent Equations Including Exchange and Correlation Effects*, Phys. Rev. **140**, A1133 (1965).

[47] R. Gáspár, *Über eine Approximation des Hartree-Fockschen Potentials Durch eine Universelle Potentialfunktion*, Acta. Phys. Hung. **3**, 263 (1954).

[48] E. P. Wigner, *On the Interaction of Electrons in Metals*, Phys. Rev. **46**, 1002 (1934).

[49] J. C. Slater, *The Self-consistent Field for Molecules and Solids* Vol 4 (McGraw-Hill,New York 1974).

[50] D. M. Ceperley and B. I. Alder, *Ground State of the Electron Gas by a Stochastic Method*, Phys. Rev. Lett. **45**, 566 (1980).

[51] J. P. Perdew and A. Zunger, *Self-interaction Correction to Density-Functional Approximations for Many-Electron Systems*, Phys. Rev. B **23**, 5048 (1981).

[52] J. P. Perdew, K. Burke, and M. Ernzerhof, *Generalized Gradient Approximation Made Simple*, Phys. Rev. Lett. **77**, 3865 (1996).

[53] A. Garcia, C. Elsasser, J. Zhu, S. G. Louie, and M. L. Cohen, *Use of Gradient-Corrected Functionals in Total-Energy Calculations for Solids* Phys. Rev. B **46**, 9829 (1992).

[54] A. D. Becke, *Density-functional Exchange-energy Approximation with Correct Asymptotic Behavior*, Phys. Rev. A **38**, 3098 (1992).

[55] E. Pehlke and M. Scheffler, *Theory of Adsorption and Desorption of $H_2$/Si(001)*, Phys. Rev. Lett. **74**, 952 (1995).

[56] P. Bagno, O. Jepsen, and O. Gunnarsson, *Ground-state Properties of Third-row Elements with Nonlocal Density Functionals*, Phys. Rev. B **40**, 1997 (1989).

[57] C. Flippi, D. J. Singh, and C. J. Umrigar, *All-electron Local-density and Generalized-gradient Calculations of the Structural Properties of Semiconductors*, Phys. Rev. B **50**, 14947 (1994).

[58] A. Dal Corso, A. Pasquarelo, A. Baldereschi, and R. Car, *Generalized-gradient Approximations to Density-functional Theory: A Comparative Study for Atoms and Solids*, Phys. Rev. B **53**, 1180 (1996).

[59] N. Ooi, A. Rairkar, and J. B. Adams, *Density Functional Study of Graphite Bulk and Surface Properties*, Carbon **44**, 231 (2006).

[60] L. A. Girifalco and M. Hodak, *Van der Waals Binding Energies in Graphitic Structures*, Phys. Rev. B. **65**, 125404 (2002).

[61] S. Kristyán and P. Pulay, *Can (Semi)Local Density Functional Theory Account for the London Dispersion Forces?*, Chem. Phys. Lett. **229**, 175 (1994).

[62] J. Pérez-Jordá and A. D. Becke, *A Density-functional Study of van der Waals Forces: Rare Gas Diatomics*, Chem. Phys. Lett. **233**, 134 (1995).

[63] L. Spanu, S. Sorella, and G. Galli, *Nature and Strength of Interlayer Binding in Graphite*, Phys. Rev. Lett. **103**, 196401 (2009).

[64] W. Kohn, Y. Meir, and D. E. Makarov, *van der Waals Energies in Density Functional Theory*, Phys. Rev. Lett. **80**, 4153 (1998).

[65] M. T. Yin and M. L. Cohen, *Theory of Static Structural Properties, Crystal Stability, and Phase Transformations: Application to Si and Ge*, Phys. Rev. B **26**, 5668 (1982).

[66] S. Froyen and M. L. Cohen, *High Pressure Phases of III–V Semiconductors: A Microscopic Theory*, Solid State Commun. **43**, 447 (1982).

[67] E. Wigner and F. Seitz, *On the Constitution of Metallic Sodium*, Phys. Rev. **43**, 804 (1933).

[68] J. C. Slater, *Wave Functions in a Periodic Potential*, Phys. Rev. **51**, 846 (1937).

[69] H. L. Skriver, *The LMTO Method-Miffin-Tin Orbitals and Electronic Structure*, Springer-Verlag, Berlin, (1984).

[70] E. Wimmer, H. Krakouer, M. Weinert, and A. J. Freeman, *Full-potential Self-Consistent Linearized-Augmented-Plane-Wave Method for Calculating the Electronic Structure of Molecules and Surfaces: $O_2$ Molecule*, Phys. Rev. B **24**, 864 (1981).

[71] S. H. Wei, H. Krakauer and M. Weinert, *Linearized Augmented-Plane-Wave Calculation of the Electronic Structure and Total Energy of Tungsten*, Phys. Rev. B **32**, 7792 (1985).

[72] J. C. Phillips and L. Kleinman, *New Method for Calculating Wave Functions in Crystals and Molecules*, Phys. Rev. **116**, 287 (1959).

[73] E. Antončik, *Approximate Formulation of the Orthogonalized Plane-Wave Method*, J. Phys. Chem. Solids **10**, 314 (1959).

[74] D. Vanderbilt, *Optimally Smooth Norm-Conserving Pseudopotentials*, Phys. Rev. B **32**, 8412 (1985).

[75] D. Vanderbilt, *Soft Self-Consistent Pseudopotentials in a Generalized Eigenvalue Formalism*, Phys. Rev. B **41**, 7892 (1990).

[76] D. R. Hamann and M. Schlüter, and C. Chiang, *Norm-Conserving Pseudopotentials*, Phys. Rev. Lett. **43**, 1494 (1979).

[77] G. B. Bachelet, D. R. Hamann and M. Schlüter, *Pseudopotentials that Work: From H to Pu*, Phys. Rev. B **26**, 4199 (1982).

[78] N. Troullier and J. L. Martins, *Efficient Pseudopotentials for Plane-Wave Calculations*, Phys. Rev. B **43**, 1993 (1991).

[79] L. Kleinman and D. M. Bylander, *Efficacious Form for Model Pseudopotentials*, Phys. Rev. Lett **48**, 1425 (1982).

[80] D. C. Allan and M. P. Teter, *Nonlocal Pseudopotentials in Molecular-Dynamical Density-Functional Theory: Application to $SiO_2$* Phys. Rev. Lett. **59**, 1136 (1987).

[81] X. Gonze, R. Stumpf, and M. Scheffler, *Analysis of separable potentials*, Phys. Rev. B **44**, 8503 (1991).

[82] G. Kresse and J. Hafner, *Norm-conserving and Ultrasoft Pseudopotentials for First-row and Transition Elements*, J. Phys. Condens. Matter **6**, 8245 (1994).

[83] W. E. Pickett, *Pseudopotential Methods in Condensed Matter Applications* , Comp. Phys. Rep. **9**, 115 (1989).

[84] A. Baldereschi, *Mean-Value Point in the Brillouin Zone*, Phys. Rev. B **7**, 5212 (1973).

[85] D. J. Chadi and M. L. Cohen, *Special Points in the Brillouin Zone*, Phys. Rev. B **8**, 5747 (1973).

[86] S. L. Cunningham, *Special Points in the Two-Dimensional Brillouin zone*, Phys. Rev. B **10**, 4988 (1874).

[87] H. J. Monkhorst and J. D. Pack, *Special Points for Brillouin-Zone Integrations*, Phys. Rev. B **13**, 5188 (1976).

[88] R. A. Evarestov and V. P. Smirnov, *Special points of the brillouin zone and their use in the solid state theory*, Phys. Status Solidi b **119**, 9 (1983).

[89] P. Bendt and A. Zunger, *Simultaneous Relaxation of Nuclear Geometries and Electric Charge Densities in Electronic Structure Theories*, Phys. Rev. Lett. **50** 1684 (1982).

[90] G. P. Srivastava, *Broyden's Method for Self-consistent Field Convergence Acceleration*, J. Phys. A: Math. Gen. **17**, L317 (1984).

[91] D. Singh, H. Krakauer, and C. S. Wang, *Accelerating the Convergence of Self-consistent Linearized Augmented-Plane-Wave Calculations*, Phys. Rev. B **34**, 8391 (1986).

[92] V. Eyert, *A Comparative Study on Methods for Convergence Acceleration of Iterative Vector Sequences*, J. Comput. Phys. **124**, 271 (1996).

[93] R. P. Feynman, *Forces in Molecules*, Phys. Rev. **56**, 340 (1939).

[94] P. Bendt and A. Zunger, *New Approach for Solving the Density-Functional Self-Consistent-Field Problem*, Phys. Rev. B **26**, 3114 (1983).

[95] R. Car and M. Parrinello, *Unified Approach for Molecular Dynamics and Density-Functional Theory*, Phys. Rev. Lett. **55**, 2471 (1985).

[96] M. C. Payne, M. P. Teter, D. C. Allan, T. A. Arias, and J. D. Joannopoulos, *Iterative Minimization Techniques for Ab Initio Total-Energy Calculations: Molecular Dynamics and Conjugate Gradients*, Rev. Mod. Phys. **64**, 1045 (1992).

[97] S. Grimme, *Semiempirical GGA-type Density Functional Constructed with a Long-range Dispersion Correction.*, J. Comput. Chem. **27**, 1787 (2006).

[98] A. Tkatchenko and M. Scheffler, *Accurate Molecular van der Waals Interactions from Ground-State Electron Density and Free-Atom Reference Data*, Phys. Rev. Lett. **102**, 073005 (2009).

[99] G. R. Victor, L. Wei, Z. Egbert, S. Matthias, and T. Alexandre, *Density-Functional Theory with Screened van der Waals Interactions for the Modeling of Hybrid Inorganic-Organic Systems*, Phys. Rev. Lett. **108**, 146103 (2012).

[100] M. Dion, H. Rydberg, E. Schröder, D. C. Langreth, and B. I. Lundqvist, *Van der Waals Density Functional for General Geometries*, Phys. Rev. Lett. **92**, 246401 (2004).

[101] L. Kyuho, D. M. Éamonn, K. Lingzhu, I. L. Bengt, and C. L. David, *Higher-Accuracy van der Waals Density Functional*, Phys. Rev. B. **82**, 081101 (2010).

[102] H. Ikutaro and O. Minoru, *Comparative van der Waals Density-Functional Study of Graphene on Metal Surfaces*, Phys. Rev. B. **82**, 153412 (2010).

[103] M. Vanin, J. J. Mortensen, A. K. Kelkkanen, J. M. Garcia-Lastra, K. S. Thygesen, and K. W. Jacobsen, *Graphene on Metals: A van der Waals Density Functional Study*, Phys. Rev. B. **81**, 081408(R) (2010).

[104] B. Carsten, L. Predrag, D. Rabie, C. Johann, G. Timm, A. Nicolae, C. Vasile, B. Radovan, T. N. Alpha, B. Stefan, Z. Jörg, and M .Thomas, *Graphene on Ir(111): Physisorption with Chemical Modulation*, Phys. Rev. Lett. **107**, 036101 (2011).

[105] R. Brako, D. Sokcevic, P. Lazic, and N. Atodiresei, *Graphene on the Ir(111) Surface: From van der Waals to Strong Bonding*, New J. Phys. **12**, 113016 (2010).

[106] Y. Fan, M. Zhao, Z. Wang, X. Zhang, and H. Zhang, *Tunable Electronic Structures of Graphene/Boron Nitride Heterobilayers*, Appl. Phys. Lett. **98**, 083103 (2011).

[107] B. Sachs, T. O. Wehling, M. I. Katsnelson, and A. I. Lichtenstein, *Adhesion and Electronic Structure of Graphene on Hexagonal Boron Nitride Substrates*, Phys. Rev. B **84**, 195414 (2011).

[108] F. Tournus and J. C. Charlier, *Ab Initio Study of Benzene Adsorption on Carbon Nanotubes*, Phys. Rev. B **71**, 165421 (2005).

[109] G. Binnig, H. Rohrer, Ch. Gerber, and E. Weibel, *Physisorption Kinetics from Mean-Field Theory: Compensation Effect near Monolayer Coverage*, Phys. Rev. Lett. **49**, 61 (1982).

[110] J. Tersoff and D. R. Hamann, *Theory and Application for the Scanning Tunneling Microscope*, Phys. Rev. Lett. **50**, 1998 (1983).

[111] J. Tersoff and D. R. Hamann, *Theory of the Scanning Tunneling Microscope*, Phys. Rev. B **31**, 805 (1985).

[112] R. S. Deacon, K. C. Chuang, R. J. Nicholas, K. S. Novoselov, and A. K. Geim, *Cyclotron resonance study of the electron and hole velocity in graphene monolayers*, Phys. Rev. B **76**, 081406(R) (2007).

[113] C. Berger, B. Z. Song, T. Li, X. Li, A. Y. Ogbazghi, R. Feng, Z. Dai, A. N. Marchenkov, E. H. Conrad, P. N. First, and W. A. D. Heer, *Ultrathin Epitaxial Graphite: 2D Electron Gas Properties and a Route toward Graphene-based Nanoelectronics*, J. Phys. Chem. **108**, 19912 (2004).

[114] P. R. Wallace, *The Band Theory of Graphite*, Phys. Rev. **71**, 622 (1947).

[115] J. W. McClure, *Band Structure of Graphite and de Haas-van Alphen Effect*, Phys. Rev. **108**, 612 (1957).

[116] J. C. Slonczewski and P. R. Weiss, *Band Structure of Graphite*, Phys. Rev. **109**, 272 (1958).

[117] P. R. M. Schroeder, S. Dresselhaus, and A. Javan, *Location of Electron and Hole Carriers in Graphite from Laser Magnetoreflection Data*, Phys. Rev. Lett. **20**, 1292 (1968).

[118] H. Rydberg, M. Dion, N. Jacobson, E. Schröder, P. Hyldgaard, S. I. Simak, D. C. Langreth, and B. I. Lundqvist, *Van der Waals Density Functional for Layered Structures*, Phys. Rev. Lett. **91**, 126402 (2003).

[119] Y. Zhao and D. Truhlar, *Density Functionals with Broad Applicability in Chemistry*, Acc. Chem. Res. **41**, 157 (2008).

[120] L. Goerigk and S. Grimme, *A Thorough Benchmark of Density Functional Methods For General Main Group Thermochemistry, Kinetics, and Noncovalent Interactions*, Phys. Chem. Chem. Phys. **13**, 6670 (2011).

[121] T. Ohta, A. Bostwick, J. McChesney, T. Seyller, K. Horn, and E. Rotenberg, *Interlayer Interaction and Electronic Screening in Multilayer Graphene Investigated with Angle-Resolved Photoemission Spectroscopy*, Phys. Rev. Lett. **98**, 206802 (2007).

[122] T. Eberlein, U. Bangert, R. R. Nair, R. Jones, M. Gass, A. L. Bleloch, K. S. Novoselov, A. Geim, and P. R. Briddon, *Plasmon spectroscopy of free-standing graphene films*, Phys. Rev. B **77**, 233406 (2008).

[123] S. Latil and L. Henrard, *Charge Carriers in Few-Layer Graphene Films*, Phys. Rev. Lett. **97**, 036803 (2006).

[124] M. Orlita, C. Faugeras, P. Plochocka, P. Neugebauer, G. Martinez, D. K. Maude, A. -L. Barra, M. Sprinkle, C. Berger, W. A. de Heer, and M. Potemski, *Approaching the Dirac Point in High-Mobility Multilayer Epitaxial Graphene*, Phys. Rev. Lett. **101**, 267601 (2008).

[125] Y. Zhang, Y. -W. Tan, H. L. Stormer, and P. Kim, *Experimental Observation of the Quantum Hall Effect and Berry's Phase in Graphene*, Nature **438**, 201 (2005).

[126] D. L. Miller, K. D. Kubista, G. M. Rutter, M. Ruan, W. A. de Heer, P. N. First, and J. A. Stroscio,*Observing the Quantization of Zero Mass Carriers in Graphene* Science **324**, 924 (2009).

[127] Z. Jiang, E. A. Henriksen, L. C. Tung, Y. J. Wang, M. E. Schwartz, M. Y. Han, P. Kim, and H. L. Stormer, *Infrared Spectroscopy of Landau Levels of Graphene*, Phys. Rev. Lett. **98**, 197403 (2007).

[128] R. Gillen and J. Robertson, *Density Functional Theory Screened-Exchange Approach for Investigating Electronical Properties of Graphene-Related Materials*, Phys. Rev. B **82**, 125406 (2010).

[129] P. E. Trevisanutto, C. Giorgetti, L. Reining, M. Ladisa, and V. Olevano, *Ab Initio GW Many-Body Effects in Graphene*, Phys. Rev. Lett. **101**, 226405 (2008).

[130] S. M. Choi, S. H. Jhi, and Y. W. Son, *Controlling Energy Gap of Bilayer Graphene by Strain*, Nano Lett. **10**, 3486 (2010).

[131] I. A. Lukýanchuk and Y. Kopelevich, *Phase Analysis of Quantum Oscillations in Graphite*, Phys. Rev. Lett. **93**, 166402 (2004).

[132] I. A. Lukýanchuk and Y. Kopelevich, *Dirac and Normal Fermions in Graphite and Graphene: Implications of the Quantum Hall Effect*, Phys. Rev. Lett. **97**, 256801 (2006).

[133] M. Koshino and E. McCann, *Gate-induced interlayer asymmetry in ABA-stacked trilayer graphene*, Phys. Rev. B **79**, 125443 (2009).

[134] M. Koshino and T. Ando, *Transport in bilayer graphene: Calculations within a self-consistent Born approximation*, Phys. Rev. B **73**, 245403 (2006).

[135] E. McCann and V. I. Fal'ko, *Landau-Level Degeneracy and Quantum Hall Effect in a Graphite Bilayer*, Phys. Rev. Lett. **96**, 086805 (2006).

[136] M. Aoki and H. Amawashi, *Dependence of band structures on stacking and field in layered graphene* , Solid State Commun. **142**, 123 (2007).

[137] M. F. Craciun, S. Russo, M. Yamamoto, J. B. Oostinga, A. F. Morpurgo, and S. Thrucha, *Trilayer graphene is a semimetal with a gate-tunable band overlap*, Nat. Nanotech. **4**, 383 (2009).

[138] K. F. Mak, J. Shan, and T. F. Heinz, *Electronic Structure of Few-Layer Graphene: Experimental Demonstration of Strong Dependence on Stacking Sequence*, Phys. Rev. Lett. **104**, 176404 (2010).

[139] F. Guinea, A. H. C. Neto, and N. M. R. Peres, *Electronic states and Landau levels in graphene stacks*, Phys. Rev. B **73**, 245426 (2006).

[140] R.S. Thompson, Y. C. Chang, and J. G. Lu, *Continuous-Distribution Puddle Model for Conduction in Trilayer Graphene*, Eur. Phys. J. B **85**, 13 (2012).

[141] R. C. Tatar and S. Rabii, *Electronic properties of graphite: A unified theoretical study*, Phys. Rev. B **25**, 4126 (1982).

[142] F. Rozploch, J. Patyk, and J. Stankowski, *Graphenes Bonding Forces in Graphite*, Acta. Phys. Pol. **112**, 557 (2007).

[143] D. E. Soule, *Change in Fermi Surfaces of Graphite by Dilute Acceptor Doping*, IBM J. Res. Dev. **8**, 268 (1964).

[144] M. Klintenberg, S. Lebégue, C. Ortiz, B. Sanyal, J. Fransson, and O. Eriksson, *Evolving properties of two-dimensional materials: from graphene to graphite*, J. Phys.: Condens. Matter **21**, 335502 (2009).

[145] W. Hua, B. Gao, S. Li, H. Ågren, and Y. Luo, *X-ray Absorption Spectra of Graphene From First-Principles Simulations*, Phys. Rev. B **82**, 155433 (2010).

[146] J. S. Bunch, Y. Yaish, M. Brink, K. Bolotin, and P. L. McEuen, *Coulomb Oscillations and Hall Effect in Quasi-2D Graphite Quantum Dots*, Nano Lett. **5**, 2887 (2005).

[147] K. S. Novoselov, D. Jiang, F. Schedin, T. J. Booth, V. V. Khotkevich, S. V. Morozov, and A. K. Geim, *Two-Dimensional Atomic Crystals*, Proc. Natl. Acad. Sci. **102**, 10451 (2005).

[148] W. J. Zhu, V. Perebeinos, M. Freitag, and P. Avouris, *Carrier Scattering, Mobilities, and Electrostatic Potential in Monolayer, Bilayer, and Trilayer Graphene*, Phys. Rev. B **80**, 235402 (2009).

[149] W. Z. Bao, Z. Zhao, H. Zhang, G. Liu, P. Kratz, L. Jing, J. Velasco, D. Smirnov, and C. N. Lau, *Magnetoconductance Oscillations and Evidence for Fractional Quantum Hall States in Suspended Bilayer and Trilayer graphene*, Phys. Rev. Lett. **105**, 246601 (2010).

[150] S. Ghosh, W. Z. Bao, D. L. Nika, S. Subrina, E. P. Pokatilov, C. N. Lau, and A. A. Balandin, *Dimensional Crossover of Thermal Transport in Few-layer Graphene*, Nat. Mater. **9**, 555 (2010).

[151] F. Guinea, A. H. Castro Neto, and N. M. R. Peres, *Electronic States and Landau Levels in Graphene Stacks*, Phys. Rev. B **73**, 245426 (2006).

[152] K. F. Mak, J. Shan, and T. F. Heinz, *Electronic Structure of Few-layer Graphene: Experimental Demonstration of Strong Dependence on Stacking Sequence*, Phys. Rev. Lett. **104**, 176404 (2010).

[153] S. Latil and L. Henrard, *Charge Carriers in Few-layer Graphene Films*, Phys. Rev. Lett. **97**, 036803 (2006).

[154] M. Aoki and H. Amawashi, *Dependence of Band Structures on Stacking and Field in Layered Graphene*, Solid State Comm. **142**, 123 (2007).

[155] W. Norimatsu and M. Kusunoki, *Selective Formation of ABC-stacked Graphene Layers on SiC(0001)*, Phys. Rev. B **81**, 161410 (2010).

[156] A. A. Avetisyan, B. Partoens, and F. M. Peeters, *Electric-field Control of the Band Gap and Fermi Energy in Graphene Multilayers by top and back Gates*, Phys. Rev. B **80**, 195401 (2009).

[157] E. McCann and M. Koshino, *Spin-orbit Coupling and Broken Spin Degeneracy in Multilayer Graphene*, Phys. Rev. B **81**, 241409 (2010).

[158] T. Ohta, A. Bostwick, T. Seyller, K. Horn, and E. Rotenberg, *Controlling the Electronic Structure of Bilayer Graphene*, Science **313**, 951 (2006).

[159] S. Yuan, H. de Raedt, and M. I. Katsnelson, *Electronic Transport in Disordered Bilayer and Trilayer Graphene*, Phys. Rev. B **82**, 235409 (2010).

[160] F. Guinea, A. H. Castro, and N. M. R. Peres, *Electronic Properties of Stacks of Graphene Layers*, Solid State Comm. **143**, 116 (2007).

[161] M. Nakamura and L. Hirasawa, *Electric Transport and Magnetic Properties in Multilayer Graphene*, Phys. Rev. B **77**, 045429 (2008).

[162] M. Koshino and E. McCann, *Gate-induced Interlayer Asymmetry in ABA-stacked Trilayer Graphene*, Phys. Rev. B **79**, 125443 (2009).

[163] M. Koshino and T. Ando, *Electronic Structures and Optical Absorption of Multilayer Graphenes*, Solid State Comm. **27**, 1123 (2009).

[164] M. Koshino and E. McCann, *Trigonal warping and Berry's phase $N\pi$ in ABC-stacked multilayer graphene*, Phys. Rev. B **80**, 165409 (2009).

[165] M. Koshino, *Interlayer Screening Effect in Graphene Multilayers with ABA and ABC Stacking*, Phys. Rev. B **81**, 125304 (2010).

[166] R. Zacharia, H. Ulbricht, and T. Hertel, *Interlayer Cohesive Energy of Graphite from Thermal Desorption of Polyaromatic Hydrocarbons*, Phys. Rev. B **69**, 155406 (2004).

[167] M. Koshino and T. Ando, *Transport in Bilayer Graphene: Calculations within a Self-consistent Born Approximation*, Phys. Rev. B **73**, 245403 (2006).

[168] W. Q. Han, L. Wu, Y. Zhu, K. Watanabe, and T. Taniguchi, *Structure of Chemically Derived Mono- and Few-atomic-layer Boron Nitride Sheets*, Appl. Phys. Lett. **93**, 223103 (2008).

[169] N. Alem, R. Erni, C. Kisielowski, M. D. Rossell, W. Gannett, and A. Zettl, *Atomically Thin Hexagonal Boron Nitride Probed by Ultrahigh-Resolution Transmission Electron Microscopy*, Phys. Rev. B **80**, 155425 (2009).

[170] J. Slawinska, I. Zasada, and Z. Klusek, *Energy Gap Tuning in Graphene on Hexagonal Boron Nitride Bilayer System*, Phys. Rev. B **81**, 155433 (2010).

[171] Y. Fan, M. Zhao, Z. Wang, X. Zhang, and H. Zhang, *Tunable Electronic Structures of Graphene/Boron Nitride Heterobilayers*, Appl. Phys. Lett. **98**, 083103 (2011).

[172] C. R. Dean, A. F. Young, I. Meric, C. Lee, L. Wang, S. Sorgenfrei, K. Watanabe, T. Taniguchi, P. Kim, K. L. Shepard, and J. Hone, *Boron Nitride Substrates for High-quality Graphene Electronics*, Nat. Nanotech. **5**, 722 (2010).

[173] C. R. Dean, A. F. Young, P. Cadden-Zimansky, L. Wang, H. Ren, K. Watanabe, T. Taniguchi, P. Kim, J. Hone, and K. L. Shepard, *Multicomponent Fractional Quantum Hall Effect in Graphene*, Nature Physics **7**, 693 (2011).

[174] D. Usachov, V. K. Adamchuk, D. Haberer, A. Gruneis, H. Sachdev, A. B. Preobrajenski, C. Laubschat, and D. V. Vyalikh, *Quasifreestanding Single-layer Hexagonal Boron Nitride as a Substrate for Graphene Synthesis*, Phys. Rev. B **82**, 075415 (2010).

[175] C. Bjelkevig, Z. Mi, J. Xiao, P. A. Dowben, L. Wang, W. N. Mei, and J. A. Kelber, *Electronic Structure of a Graphene/Hexagonal-BN Heterostructure Grown on Ru(0001) by Chemical Vapor Deposition and Atomic Layer Deposition: Extrinsically Doped Graphene.*, J. Phys.: Condens. Matter **22**, 302002 (2010).

[176] S. D. Sarma and E. H. Hwang, *Conductivity of Graphene on Boron Nitride Substrates*, Phys. Rev. B **83**, 121405 (2011).

[177] M. Kindermann, B. Uchoa, and D. L. Miller, *Zero-energy Modes and Gate-tunable Gap in Graphene on Hexagonal Boron Nitride*, Phys. Rev. B **86**, 115415 (2012).

[178] C. Ortix, L. Yang, and J. Brink, *Graphene on Incommensurate Substrates: Trigonal Warping and Emerging Dirac Cone Replicas with Halved Group Velocity*, Phys. Rev. B **86**, 081405(R) (2012).

[179] C. Yelgel and G. P. Srivastava, *Ab-initio Studies of Electronic and Optical Properties of Graphene and Graphene-BN Interface*, Appl. Surf. Sci. **258**, 8338 (2012).

[180] Y. Zhang, T. Tang, C. Girit, Z. Hao, M. C. Martin, A. Zett, M. F. Crommie, Y. R. Shen, and F. Wang, *Direct Observation of a Widely Tunable Band Gap in Bilayer Graphene*, Nature **459**, 820 (2009).

[181] E. V. Castro, K. S. Novoselov, S. V. Morozov, N. M. R. Peres, J. M. B. Lopes dos Santos, J. Nilsson, F. Guinea, A. K. Geim, and A. H. Castro Neto, *Electronic Properties of a Biased Graphene Bilayer*, J. Phys.: Condens. Matter **22**, 175503 (2010).

[182] Y. H. Kim, M. J. Heben, and S. B. Zhang, *Nanotube Wires on Commensurate InAs Surfaces: Binding Energies, Band Alignments, and Bipolar Doping by the Surfaces*, Phys. Rev. Lett. **92**, 176102 (2004).

[183] G. M. Rutter, J. N. Crain, N. P. Guisinger, T. Li, P. N. First, and J. A. Stroscio, *Scattering and Interference in Epitaxial Graphene*, Science **219**, 5835 (2007).

[184] M. Ishigami, J. H. Chen, W. G. Cullen, M. S. Fuhrer, and E. D. Williams, *Atomic Structure of Graphene on $SiO_2$*, Nano Lett. **6**, 1643 (2007).

[185] K. S. Novoselov, A. K. Geim, S. V. Morozov, D. Jiang, Y. Zhang, S. V. Dubonos, I. V. Grigorieva, and A. A. Firsov, *Electric Field Effect in Atomically Thin Carbon Films*, Science **666**, 5696 (2007).

[186] P. A. Khomyakov, G. Giovannetti, P. C. Rusu, G. Brocks, J. van den Brink, and P. J. Kelly, *First-principles Study of the Interaction and Charge Transfer between Graphene and Metals*, Phys. Rev. B **79**, 195425 (2009).

[187] S. Kim, J. Ihm, H. J. Choi, and Y. W. Son, *Origin of Anomalous Electronic Structures of Epitaxial Graphene on Silicon Carbide*, Phys. Rev. Lett. **100**, 176802 (2008).

[188] K. T. He, J. C. Koepke, S. Barraza-Lopez, and J. W. Lyding, *Separation-Dependent Electronic Transparency of Monolayer Graphene Membranes on III-V Semiconductor Substrates*, Nano Lett. **10**, 3446 (2010).

[189] L. B. Ruppalt and J. W. Lyding, *Charge Transfer between Semiconducting Carbon Nanotubes and their Doped GaAs(110) and InAs(110) Substrates Detected by Scanning Tunnelling Spectroscopy*, Nanotech. **18**, 215202 (2007).

[190] T. A. G. Eberlein, R. Jones, J. P. Goss, and P. R. Briddon, *Doping of Graphene: Density Functional Calculations of Charge Transfer between GaAs and Carbon Nanostructures*, Phys. Rev. B **78**, 045403 (2008).

[191] D. P. Andrade, R. H. Miwa, and G. P. Srivastava, *Graphene and Graphene Nanoribbons on InAs(110) and Au/InAs(110) surfaces: An Ab initio Study*, Phys. Rev. B **84**, 165322 (2011).

[192] R. C. Weast, *Handbook of Chemistry and Physics, 59th ed.* (Chemical Rubber, Cleveland 1978)

[193] D. J. Chadi, *Vacancy-Induced 2×2 Reconstruction of the Ga(111) Surface of GaAs*, Phys. Rev. Lett. **52**, 1911 (1984).

[194] G. P. Srivastava, *Theory of Semiconductor Surface Reconstruction*, Rep. Prog. Phys. **60**, 561 (1997).

[195] A. Taguchi and K. Kanisawa, *Stable Reconstruction and Adsorbates of InAs(111)A surface*, Appl. Surf. Sci. **252**, 5263 (2006).

[196] T. Nakada and T. Osaka, *Sb Trimer Structure of the InSb(111)B-(2×2) Surface as Determined by Transmission Electron Diffraction*, Phys. Rev. Lett. **67**, 2834 (1991).

[197] A. C. Ferraz and G. P. Srivastava, *Determination of the Surface Geometry of gaAs(110) by the Total Energy and Force Methods*, Surf. Sci. **182**, 161 (1987).

[198] Y. J. Kang, J. Kang, and K. J. Chang, *Electronic Structure of Graphene and Doping Effect on $SiO_2$*, Phys. Rev. B **78**, 115404 (2008).

[199] N. T. Cuong, M. Otani, and S. Okada, *Semiconducting Electronic Property of Graphene Adsorbed on (0001) Surfaces of $SiO_2$*, Phys. Rev. Lett. **106**, 106801 (2011).

[200] H. E. Romero, N. Shen, P. Joshi, H. R. Gutierrez, S. A. Tadigadapa, J. O. Sofo, and P. C. Eklund, *n-Type Behavior of Graphene Supported on Si/$SiO_2$ Substrates*, ACS Nano **2**, 2037 (2008).

[201] S. Berciaud, S. Ryu, L. E. Brus, and T. F. Heinz, *Probing the Intrinsic Properties of Exfoliated Graphene: Raman Spectroscopy of Free-Standing Monolayers*, Nano Lett. **9**, 346 (2009).

[202] S. M. Song and B. J. Cho, *Investigation of Interaction between Graphene and Dielectrics*, Nanotech. **21**, 335706 (2010).

[203] K. A. Ritter and J. W. Lyding, *Characterization of Nanometer-sized, Mechanically Exfoliated Graphene on the H-passivated Si(100) Surface Using Scanning Tunneling Microscopy*, Nanotech. **19**, 015704 (2008).

[204] T. Filleter, K. V. Emtsev, T. Seyller and R. Bennewitz, *Local Work Function Measurements of Epitaxial Graphene*, Appl. Phys. Lett. **93**, 133117 (2008).

[205] J. Martin, N. Akerman, G. Ulbricht, T. Lohmann, J. H. Smet, and K. V. Klitzing, *Observation of Electron-hole Puddles in Graphene Using a Scanning Single-electron Transistor*, Nat. Phys. **4**, 144 (2008).

[206] J. Wu, M. Agrawal, H. A. Becerril, Z. Bao, Z. Liu, Y. Chen, and P. Peumans, *Organic Light-Emitting Diodes on Solution-Processed Graphene Transparent Electrodes*, ACS Nano **4**, 43 (2010).

[207] F. Schedin, A. K. Geim, S. V. Morozov, E. W. Hill, P. Blake, M. I. Katsnelson, and K. S. Novoselov, *Detection of individual gas molecules adsorbed on graphene*, Nature Mater. **6**, 652 (2007).

[208] Y. Wu, Y. Ming Lin, A. A. Bol, K. A. Jenkins, F. Xia, D. B. Farmer, Y. Zhu, and P. Avouris, *High-frequency, scaled graphene transistors on diamond-like carbon*, Nature **472**, 74 (2011).

[209] K. S. Novoselov, A. K. Geim, S. V. Morozov, D. Jiang, M. I. Katsnelson, I. V. Grigorieva, S. V. Dubonos, and A. A. Firsov, *Two-dimensional gas of massless Dirac fermions in graphene*, Nature **438**, 197 (2005).

[210] C. R. Dean, A. F. Young, I. Meric, C. Lee, L. Wang, S. Sorgenfrei, K. Watanabe, T. Taniguchi, P. Kim, K. L. Shepard, and J. Hone, *Boron nitride substrates for high-quality graphene electronics*, Nature Nanotech. **5**, 722 (2010).

[211] X. Zhong, Y. K. Yap, R. Pandey, and S. P. Karna, *First-principles study of strain-induced modulation of energy gaps of graphene/BN and BN bilayers*, Phys. Rev. B **83**, 193403 (2011).

[212] K. Tang, R. Qin, J. Zhou, H. Qu, J. Zheng, R. Fei, H. Li, Q. Zheng, Z. Gao, and J. Lu, *Electric-Field-Induced Energy Gap in Few-Layer Graphene*, J. Phys. Chem. C **115**, 9458 (2011).

[213] E. Rotenberg, A. Bostwick, T. Ohta, J. L. McChesney, T. Seyller, and K. Horn-Rotenberg, *Origin of the energy bandgap in epitaxial graphene*, Nature Mater. **7**, 258 (2008).

[214] Y. Son, M.Cohen, and S. Louie, *Renormalization of Molecular Electronic Levels at Metal-Molecule Interfaces*, Phys. Rev. Lett. **97**, 216405 (2006).

[215] R. Balog, B. Jørgensen, J. Wells, E. Lægsgaard, P. Hofmann, F. Besenbacher, and L. Hornekæ, *Atomic Hydrogen Adsorbate Structures on Graphene*, J. Am. Chem. Soc. **131**, 8744 (2009).

[216] D. C. Elias, R. R. Nair, T. M. G. Mohiuddin, S. V. Morozov, P. Blake, M. P. Halsall, A. C. Ferrari, D. W. Boukhvalov, M. I. Katsnelson, A. K. Geim, and K. S. Novoselov, *Control of Graphene's Properties by Reversible Hydrogenation: Evidence for Graphane*, Science **323**, 610 (2009).

[217] F. Schwierz, *Graphene transistors*, Nat. Nanotech. **5**, 487 (2010).

[218] Y. Zhang, T. Tang, C. Girit, Z. Hao, M. C. Martin, A. Zettl, M. F. Crommie, Y. R. Shen, and F. Wang, *Direct observation of a widely tunable bandgap in bilayer graphene*, Nature **459**, 820 (2009).

[219] J. W. Yang, G. Lee, J. S. Kim, and K. S. Kim, *Gap Opening of Graphene by Dual $FeCl_3$-Acceptor and K-Donor Doping*, J. Phys. Chem. Lett. **2**, 2577 (2011).

[220] B. N. Szafranek, D. Schall, M. Otto, D. Neumaier, and H. Kurz, *High On/Off Ratios in Bilayer Graphene Field Effect Transistors Realized by Surface Dopants*, Nano Lett. **11**, 2640 (2011).

[221] W. J. Yu, L. Liao, S. H. Chae, Y. H. Lee, and X. F. Duan, *Toward Tunable Band Gap and Tunable Dirac Point in Bilayer Graphene with Molecular Doping*, Nano Lett. **11**, 4759 (2011).

[222] M. Yankowitz, F. Wang, C. N. Lau, and B. J. LeRoy, *Local spectroscopy of the electrically tunable band gap in trilayer graphene*, Phys. Rev. B 87, 165102 (2013).

[223] C. Kittel, *Introduction to Solid State Physics* (John Wiley & Sons, New York, 2004).

[224] N. W. Ashcroft and N. D. Mermin, *Solid State Physics* (Saunders College Publishing, New York, 1976).

[225] J. S. Blakemore, *Solid State Physics* (Cambridge University Press, Cambridge 1985).

[226] M. A. Omar, *Elementary Solid State Physics: Principles and Applications* (Addison-Wesley, 1975).

[227] G. F. Koster, *Solid State Physics*, Vol 5, (Ed F Seitz and D Turnbull, Academic Press, New York, 1957).

[228] G. Burns, *Solid State Physics* (Academic Press, New York, 1985).

[229] F. Bloch, *Über die Quantenmechanik der Elektronen in Kristallgittern*, Z. Phys. **52**, 555 (1928).

[230] F. Bloch, *Zum elektrischen Widerstandsgesetz bei tiefen Temperaturen*, Z. Phys. **59**, 208 (1930).

[231] J. R. Chelikowsky and M. L. Cohen, *Nonlocal Pseudopotential Calculations for the Electronic Structure of Eleven Diamond and Zinc-blende Semiconductors*, Phys. Rev. B **14**, 556 (1976).